Development of a Structure-Preserving Idealized Stochastic Climate Model

A

Dissertation

submitted to the Department of Mathematics
of the Faculty of Mathematics, Informatics and Natural Sciences
of the University of Hamburg

by

Kamal Kishor Sharma

Examination commission members:
Dr. Peter Korn (reviewer)
Prof. Dr. Jörn Behrens (reviewer)
Prof. Dr. Tobias Dyckerhoff (chair)
Prof. Dr. Philip Lederer (deputy chair)
Prof. Dr. Babette de Wolff (minute taker)

Date of oral defense: 19.09.2025

Hamburg, 2025

Abstract

This thesis investigates an idealized two-dimensional stochastic climate model consisting of coupled atmospheric and ocean components. The atmospheric component incorporates stochasticity using the stochastic advection by Lie transport (SALT) approach, while the ocean component remains deterministic. The model serves as a tool to study fundamental processes arising from ocean-atmosphere interactions and to quantify the uncertainty induced by unresolved small-scale dynamics.

We conduct numerical simulations of the climate model to evaluate the effectiveness of SALT in representing the impact of unresolved dynamics on large-scale flow behavior. Our methodology consists of three stages. First, we develop numerical schemes for the ocean component. Next, we perform a numerical investigation of an idealized stochastic atmosphere model. Finally, we combine these approaches to solve the full stochastic climate model. Additionally, we present numerical simulations of stochastic incompressible Navier-Stokes equations.

The stochastic noise terms are estimated using synthetic data from high-resolution deterministic simulations. While the temporal component of noise is typically modeled using a Gaussian process, we also explore an alternative approach based on Ornstein–Uhlenbeck (OU) processes. The latter method results in smoother temperature and vorticity fields and enhances uncertainty quantification performance.

Our results demonstrate that ensemble forecasts from the stochastic climate model exhibit good reliability, with ensemble spread proportional to the ensemble root mean square error over a significant time window. Comparisons between the stochastic and deterministic model forecasts, initialized from randomly perturbed initial conditions, reveal that the stochastic approach consistently outperforms the deterministic one throughout the simulation period. Overall, our findings indicate that (1) SALT parameterization improves ensemble performance and (2) modeling temporal noise with an OU process instead of a Gaussian process enhances prediction quality.

Zusammenfassung

Diese Dissertation untersucht ein idealisiertes zweidimensionales stochastisches Klimamodell, das aus gekoppelten atmosphärischen und ozeanischen Komponenten besteht. Die atmosphärische Komponente integriert Stochastizität mithilfe des Ansatzes der stochastischen Advektion durch Lie-Transport (SALT), während die ozeanische Komponente deterministisch bleibt. Das Modell dient als Werkzeug zur Untersuchung grundlegender Prozesse, die aus Wechselwirkungen zwischen Ozean und Atmosphäre entstehen, sowie zur Quantifizierung der Unsicherheiten, die durch nicht aufgelöste kleinskalige Dynamiken verursacht werden.
Wir führen numerische Simulationen des Klimamodells durch, um die Wirksamkeit von SALT bei der Darstellung der Auswirkungen nicht aufgelöster Dynamiken auf das großskalige Strömungsverhalten zu bewerten. Unsere Methodik besteht aus drei Phasen. Zunächst entwickeln wir numerische Schemata für die ozeanische Komponente. Anschließend führen wir eine numerische Untersuchung eines idealisierten stochastischen Atmosphärenmodells durch. Schließlich kombinieren wir diese Ansätze, um das vollständige stochastische Klimamodell zu lösen. Darüber hinaus präsentieren wir numerische Simulationen der stochastischen inkompressiblen Navier-Stokes-Gleichungen. Die stochastischen Rauschterme werden mithilfe synthetischer Daten aus hochauflösenden deterministischen Simulationen abgeschätzt. Während die zeitliche Komponente des Rauschens typischerweise durch einen Gaußschen Prozess modelliert wird, untersuchen wir auch einen alternativen Ansatz basierend auf Ornstein–Uhlenbeck-(OU)-Prozessen. Letzterer Ansatz führt zu glatteren Temperatur- und Vortizitätsfeldern und verbessert die Leistung der Unsicherheitsquantifizierung.
Unsere Ergebnisse zeigen, dass Ensemble-Vorhersagen des stochastischen Klimamodells eine gute Verlässlichkeit aufweisen, wobei die Ensemble-Streuung proportional zum ensemblebasierten mittleren quadratischen Fehler über ein signifikantes Zeitfenster ist. Vergleiche zwischen den stochastischen und deterministischen Modellvorhersagen, die aus zufällig gestörten Anfangsbedingungen initialisiert wurden, zeigen, dass der stochastische Ansatz den deterministischen über den gesamten Simulationszeitraum hinweg konsequent übertrifft. Insgesamt zeigen unsere Ergebnisse, dass (1) die SALT-Parametrisierung die Ensemble-Performance verbessert und (2) die Modellierung des zeitlichen Rauschens mit einem OU-Prozess anstelle eines Gaußschen Prozesses die Vorhersagequalität erhöht.

Acknowledgments

First and foremost, I would like to express my gratitude to my supervisor, Peter, for introducing me to this fascinating research topic. I am thankful for the academic freedom he gave me to explore my own research interests, while also ensuring that I remained focused on the core objectives of the project.

This project would not have been possible without the guidance and support of Wei, James, and Sagy. Thank you for always making time to answer my questions and help me navigate through various research challenges.

My heartfelt thanks to my friends and colleagues, Fabian and Ezra, for the countless technical and non-technical discussions we've shared over the past four years. Your presence across the office has been both intellectually stimulating and personally comforting.

Last but certainly not least, I would like to thank my parents, my brother, and my wonderful girlfriend for their love, support, and encouragement throughout this entire journey. Your belief in me has been my greatest source of strength.

Contents

Chapter 1

Introduction

Earth's oceans and atmosphere are characterized by a rich hierarchy of interacting processes that span a wide range of scales (Vallis, 2017; Fox-Kemper, 2018). The spatial scale of these processes typically ranges from a few millimeters to thousands of kilometers, whereas the temporal scale ranges from a few seconds to several decades (see Figure 1.1). In both media, small-scale motions coexist and interact with large-scale circulations, and these interactions are essential for energy transfer, mixing, and the overall dynamics of the climate system (Williams, 2005). For instance, mesoscale ocean eddies ($\sim$ 10–100 km) modulate the transport of heat and nutrients in basin-scale currents like the Gulf Stream (Holland, 1978), while atmospheric turbulence at the kilometer scale influences the structure of synoptic-scale ($\sim$ 1000 km) weather systems (Wyngaard, 2010).

Mathematical models are constructed to study such physical processes. These models are then solved numerically to gain further insights into the physical phenomena and predict the behavior of the atmosphere or the ocean in the future. Due to limited computational resources, however, it is practically impossible to capture all spatial and temporal scales in numerical simulations. Processes that occur at scales smaller than the grid resolution of the models remain unaccounted for or unresolved. The effect of small scales on large scales is therefore not captured by these models, which can lead to errors in predictions.

The representation of small scales is one of the most challenging aspects of numerical weather prediction and climate modeling. To account for the missing effect of unresolved/small scales, additional terms are added to the models. This process is known as parameterization or subgrid-scale modeling. Parameterization can be divided into two categories: deterministic parameterization and stochastic parameterization.

Deterministic parameterizations represent the effect of unresolved scales using fixed, predictable functions of the resolved variables. These methods often rely on empirical relationships or theoretical derivations (Zanna et al., 2017). On the other hand, stochastic parameterizations incorporate random (or probabilistic) components to represent the unpredictable or chaotic aspects of unresolved processes. Over the past two decades, the use of stochastic parameterizations in weather and climate models has gained

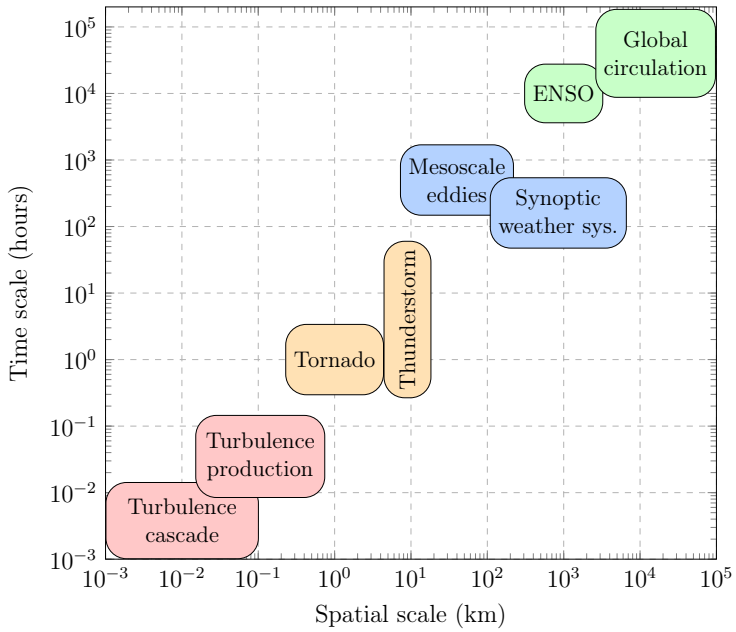

FIGURE 1.1: Spatial and temporal scales of various meteorological phenomena (Stull, 2017).

significant momentum. It offers several advantages over traditional (deterministic) approaches when modeling unresolved/subgrid-scale processes (Palmer, 2012; Berner et al., 2017). Subgrid processes are inherently unpredictable and intermittent in nature. Stochastic methods explicitly account for this randomness rather than providing a single, averaged outcome. This leads to a more realistic depiction of variability, particularly in ensemble forecasting. By introducing random fluctuations that mimic the variability of unresolved scales, stochastic parameterizations generate a broader range of outcomes. This enhanced ensemble spread better represents forecast uncertainty and improves probabilistic forecasts.

In this thesis, we investigate the use of a stochastic parameterization method known as stochastic advection by Lie transport (SALT) in modeling the effect of unresolved scales on the resolved scales and quantifying the uncertainty due to unresolved scales. The SALT method is a powerful way of introducing stochasticity into fluid dynamics equations while preserving their geometric structure, particularly the conservation laws and symmetries that arise from the deterministic version (Holm, 2015). Our aim is to simulate an idealized climate model which is parameterized using the SALT methodology.

1.1 Stochastic advection by Lie transport

A common approach to model the uncertainty due to unresolved scales is to add random forcing terms to the governing fluid dynamics equations. This approach is typically implemented post hoc i.e., after formulating a deterministic model, one adds noise with a chosen amplitude and correlation structure (Berner et al., 2012; Berner

et al., 2017). While such noise can improve ensemble spread or model variability, the resulting stochastic model may no longer preserve the fundamental conservation laws or symmetries of the fluid system. Moreover, the addition of noise, which is not based on physical principles, may lead to errors in the probability density functions of the system's dynamics (Brecht et al., 2021). The stochastic advection by Lie transport (SALT) framework addresses these limitations by introducing stochasticity through a variationally consistent and geometrically informed approach.

The idea behind SALT was introduced by Holm in the seminal paper Holm (2015). In fluid dynamics, equations of motion are derived starting from the assumption that fluid particles satisfy the equation

$$\frac{\mathrm{d}\boldsymbol{X}(a,t)}{\mathrm{d}t} = \mathbf{u}(\boldsymbol{X}(a,t),t), \quad \boldsymbol{X}(a,0) = a \in \mathbb{R}^2 \text{ or } \mathbb{R}^3, \tag{1.1}$$

where $\boldsymbol{X}(a,t)$ denotes the trajectory of a particle (with Lagrangian label a) at time t and $\mathbf{u}$ denotes the velocity field. In Holm (2015), one starts with the assumption that the Lagrangian particle paths follow a Stratonovich stochastic process given by

$$\mathrm{d}\boldsymbol{X}(a,t) = \overline{\mathbf{u}}(\boldsymbol{X}(a,t))\mathrm{d}t + \sum_i \boldsymbol{\xi}_i(\boldsymbol{X}(a,t)) \circ \mathrm{d}W_t^i \tag{1.2}$$

where $\overline{\mathbf{u}}$ denotes the mean flow velocity and $\sum_i \boldsymbol{\xi}_i(\boldsymbol{X}(a,t)) \circ \mathrm{d}W_t^i$ denotes a stochastic perturbation about the mean flow. The idea is to write fluid trajectories as a combination of a mean flow, representing large-scale dynamics, and noise terms representing the small-scale dynamics. In equation (1.2), W_t^i are independent Brownian motions whereas the vectors $\boldsymbol{\xi_i}$ represent the spatial correlation of the small-scale velocity fluctuations.

Equations for fluid dynamics (in Euler form) are then derived using the stochastic variational principle. The assumption (1.2) leads to the appearance of stochastic vector fields in the transport terms of fluid equations. The SALT approach can thus be viewed as a parameterization technique that models the uncertain transport behavior associated with small-scale/unresolved flow dynamics.

Cotter et al. (2017) showed that by using homogenization techniques, one can arrive at equation (1.2) starting from a multi-scale decomposition of the deterministic Lagrangian flow map into a slow large-scale mean and rapidly fluctuating small-scale map. The small-scale map can be represented by a stochastic process, if the time scale of the fluctuating map is sufficiently rapid in comparison to mean field dynamics and the fast dynamics is sufficiently chaotic. The Ansatz (1.2) for fluid particle trajectories was also used by Mémin (2014) to derive another class of stochastic fluid equations—known as modeling under Location Uncertainty (LU)—to model the effect of unresolved scales.

The motivation behind choosing a stochastic Lagrangian dynamics can be understood by examining the data from satellite observations of Earth's oceans. Figure 1.2 shows Lagrangian trajectories of drifters (floating oceanographic devices) on the ocean surface driven by the wind and ocean currents. Each color represents a different drifter.

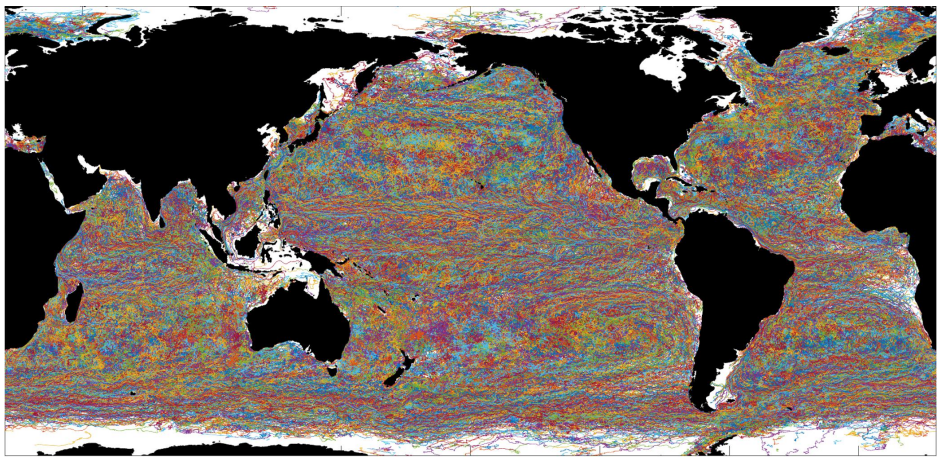

FIGURE 1.2: Trajectories of drifters in the ocean. Each color corresponds to a different drifter (Lilly, 2024). These data were compiled from satellite observations by the National Oceanic and Atmospheric Administration Global Drifter Program.

A careful look at the drifter paths reveals that they evolve under a combination of mean drift and rapid fluctuations.

The inclusion of stochasticity at the level of Lagrangian flow map (equation (1.2)) leads to stochastic fluid dynamics where the fundamental mathematical properties of the underlying deterministic equations are preserved (Crisan et al., 2019; Crisan et al., 2023a; Crisan and Lang, 2024). SALT-based models preserve Kelvin circulation, a fundamental property in fluid dynamics. The SALT framework also enables a new approach for sub-grid scale parameterization (Gay-Balmaz and Holm, 2018). The stochastic terms introduced by the SALT parameterization can be deduced from statistical analysis of high-resolution data (either observed, or numerically simulated).

We can use equations (1.1) and (1.2) to express the stochastic terms as the difference between Lagrangian particles advected by the true velocity field $\mathbf{u}$ and a coarse grained (averaged) version $\overline{\mathbf{u}}$,

$$\overline{\mathbf{u}}(\boldsymbol{X}(a,t))\mathrm{d}t + \sum_i \boldsymbol{\xi}_i(\boldsymbol{X}(a,t)) \circ \mathrm{d}W_t^i \approx \mathbf{u}(\boldsymbol{X}(a,t),t)\mathrm{d}t,$$

$$\sum_i \boldsymbol{\xi}_i(\boldsymbol{X}(a,t)) \circ \mathrm{d}W_t^i \approx \mathbf{u}(\boldsymbol{X}(a,t),t)\mathrm{d}t - \overline{\mathbf{u}}(\boldsymbol{X}(a,t),t)\mathrm{d}t.$$

The true velocity field $\mathbf{u}$ can be obtained from satellite observations or high-resolution simulations of deterministic models. Once $\mathbf{u}$ is obtained, one can obtain $\overline{\mathbf{u}}$ using standard filtering/averaging methods. Statistical methods like empirical orthogonal function (EOF), principal component analysis (PCA) or singular value decomposition (SVD) can then be applied to Lagrangian trajectory data $\mathbf{u}(\boldsymbol{X}(a,t),t)\mathrm{d}t - \overline{\mathbf{u}}(\boldsymbol{X}(a,t))\mathrm{d}t$ leading to the estimation of $\boldsymbol{\xi}_i$.

One of the first numerical implementations of stochastic fluid dynamics equations parameterized using SALT was carried out by Cotter et al. (2019). In this study, 2D

stochastic Euler equations were solved on coarse grids and the uncertainty arising from unresolved scales was quantified by performing several uncertainty quantification tests. The stochastic terms (which model the small-scale processes) were estimated using high-resolution simulations of the corresponding deterministic model. It was shown that the ensemble generated by the stochastic model could capture the large-scale behavior of the underlying deterministic system for a physically adequate period of time.

Similar observations were made by Cotter et al. (2020a) for a two-layer quasi-geostrophic model. In addition to uncertainty quantification tests, Cotter et al. (2020a) analyzed the reliability of the stochastic spread by studying the skill-spread relationship and found promising results. The results from the stochastic model were also compared with the corresponding deterministic model (without any parameterization). It was found that the stochastic spread captures the true solution at significantly more grid points and over longer time periods than the deterministic spread.

In both the above studies, the temporal evolution of stochastic terms (arising from small-scale dynamics) was modeled by Gaussian processes. Ephrati et al. (2023) extended the work of Cotter et al. (2019) by studying the performance of stochastic Euler equations for different modeling choices of time series associated with unresolved flow dynamics. Interestingly, it was found that the use of Ornstein–Uhlenbeck processes instead of Gaussian processes improves the quality of the coarse-grid predictions. In this thesis, we explore both modeling approaches for the stochastic terms.

The effectiveness of SALT parameterization for uncertainty quantification has been tested for several other geophysical fluid dynamics equations. Some notable examples are Crisan et al. (2023b) for shallow water equations and Resseguier et al. (2020) for a surface quasi-geostrophic model. In Crisan et al. (2023b), a new approach for noise calibration was developed. Their method used the entire solution field for estimating $\boldsymbol{\xi}_i$ instead of using Lagrangian trajectories of fluid parcels.

In all the above-mentioned works, one common feature of the stochastic model realizations is their ability to capture the true solution for a physically meaningful duration while maintaining sufficient ensemble spread. This property makes these stochastic models suitable for ensemble based data assimilation methods which can further improve the quality of solutions. Data assimilation combines observations with numerical model data to find the best possible model state. Particle filters, which are a type of ensemble based data assimilation methods, have been successfully combined with some of the stochastic models; Cotter et al. (2020b) combined the stochastic 2D Euler equation with a particle filter, Cotter et al. (2020c) showed data assimilation for quasi-geostrophic model, and Lang et al. (2022) presented a particle filter for the rotating shallow water model. In this thesis, we focus on numerical simulations of an idealized climate model without delving into particle filters. However, incorporating data assimilation would be a natural next step.

In recent years, the SALT framework has primarily been applied as a tool for quantifying uncertainty arising from unresolved scales in simplified geophysical fluid

dynamics models, such as the Euler equations, the shallow water equations, and quasi-geostrophic models. In the present study, we aim to extend the application of SALT to more complex fluid dynamics systems. Specifically, we investigate an idealized coupled ocean-atmosphere climate model formulated using the SALT approach.

Alongside testing SALT's capabilities for uncertainty quantification in this setting, we also look into different ways of modeling the stochastic noise terms, with the goal of improving the model's accuracy. In particular, we examine whether incorporating noise—intended to represent unresolved small-scale dynamics—can effectively guide large-scale processes toward the true solution, and how the performance of stochastic models compares to their deterministic counterparts.

Such an investigation is currently lacking in the literature, especially within the context of coupled ocean-atmosphere systems, and thus represents a novel contribution of this work.

1.2 Coupled ocean-atmosphere models

Many physical processes occur because of the close interaction between the ocean and the atmosphere. One famous example of such a process is the El Niño–Southern Oscillation (ENSO). ENSO is characterized by periodic variations in sea surface temperatures in the central and eastern tropical Pacific, with El Niño corresponding to unusually warm conditions and La Niña to unusually cool conditions (Cane and Zebiak, 1985). These fluctuations drive changes in atmospheric convection, leading to significant impacts on global weather patterns ranging from altered precipitation regimes and storm tracks to extreme temperature events across different regions of the world (Philander, 2001).

Such phenomena can only be effectively studied using coupled ocean–atmosphere models because their dynamics arise from the two-way feedbacks between oceanic and atmospheric processes. By incorporating the interactions between sea surface temperature anomalies, atmospheric convection, and wind stress on ocean currents, coupled models can capture the essential feedback mechanisms that drive phenomena like ENSO (McCreary Jr. and Anderson, 1991). This integrated approach has the potential to reduce systematic biases inherent in models that treat the ocean and atmosphere separately and enhance the simulation of overall climate variability.

In this thesis, we numerically solve an idealized coupled ocean-atmosphere model introduced by Crisan et al. (2023a) and quantify the uncertainty caused by running the model on coarse grids at low resolution. Such a model can be used to study some of the fundamental processes that occur due to interactions between the ocean and the atmosphere (ENSO for example). The atmosphere component of the coupled model is derived following the SALT approach (making it stochastic) whereas the ocean component is kept deterministic.

This choice is inspired by the stochastic climate model of Hasselmann (1976). Hasselmann proposed that the climate system can be divided into a fast component

(essentially the atmosphere) representing high-frequency weather fluctuations and a slow component (the ocean, land, etc.) that represents the long-term climatic variability. The fast processes act as a random, or stochastic, forcing on the slow climate variables. This separation into two distinct time scales is fundamental because it explains how short-term, seemingly chaotic weather events can collectively induce long-term, persistent climate variability (Lucarini and Chekroun, 2023).

The climate model of Crisan et al. (2023a), although resting on Hasselmann's paradigm in a general sense, incorporates stochasticity into the atmosphere model equations in a way that deviates from traditional methods. Instead of directly adding stochastic terms to the deterministic model equations, stochasticity is introduced at the level of Lagrangian fluid trajectories and then the model equations are derived. The deterministic version of the climate model introduced by Crisan et al. (2023a) can be described by

$$
\begin{aligned}
\text{Atmosphere}: \quad & \frac{\partial \mathbf{u}^a}{\partial t} + (\mathbf{u}^a \cdot \nabla)\mathbf{u}^a + \frac{1}{Ro^a}\hat{\mathbf{z}} \times \mathbf{u}^a + \frac{1}{C^a}\nabla\theta^a = \frac{1}{Re^a}\Delta \mathbf{u}^a, \\
& \frac{\partial \theta^a}{\partial t} + \nabla \cdot (\mathbf{u}^a \theta^a) = \gamma(\theta^a - \theta^o) + \frac{1}{Pe^a}\Delta\theta^a, \\
\text{Ocean}: \quad & \frac{\partial \mathbf{u}^o}{\partial t} + (\mathbf{u}^o \cdot \nabla)\mathbf{u}^o + \frac{1}{Ro^o}\hat{\mathbf{z}} \times \mathbf{u}^o + \frac{1}{Ro^o}\nabla p^o = \sigma(\mathbf{u}^o - \mathbf{u}^a_{sol}) + \frac{1}{Re^o}\Delta \mathbf{u}^o, \\
& \nabla \cdot \mathbf{u}^o = 0, \\
& \frac{\partial \theta^o}{\partial t} + \mathbf{u}^o \cdot \nabla\theta^o = \frac{1}{Pe^o}\Delta\theta^o,
\end{aligned}
\tag{1.3}
$$

where the vector variable $\mathbf{u}$ and the scalar variables θ and p (with superscripts for the atmosphere and ocean components) denote the velocity, potential temperature, and pressure fields, respectively. These variables are functions of the 2D spatial coordinate $\boldsymbol{x} = (x, y)$ and the time variable t. $\hat{\mathbf{z}}$ represents a unit vector in the z direction.

The atmosphere is modeled by the two-dimensional (2D) compressible Navier-Stokes equations which are coupled to a 2D advection-diffusion equation for the temperature θ^a. The atmospheric velocity field $\mathbf{u}^a$ transports the atmospheric temperature, and the gradient in the temperature field, in turn, alters the velocity. The atmospheric temperature is coupled to the ocean temperature through the term $\gamma\,(\theta^a - \theta^o)$ in the advection-diffusion equation. This term can be thought of as representing the transfer of heat from the ocean to the atmosphere.

The ocean is modeled by the 2D incompressible Navier-Stokes equations along with an equation for the ocean temperature θ^o, which is passively advected by the ocean velocity field $\mathbf{u}^o$. The atmosphere and ocean velocities are coupled through the term $\sigma(\mathbf{u}^o - \mathbf{u}^a_{sol})$ which models the shear stress exerted by atmospheric winds on the ocean surface. $\mathbf{u}^a_{sol}$ is the divergence-free part of the atmospheric velocity, $\mathbf{u}^a = \mathbf{u}^a_{sol} + \nabla q$. The divergence-free component is obtained by the Helmholtz decomposition,

$$\Delta q = \nabla \cdot \mathbf{u}^a.$$

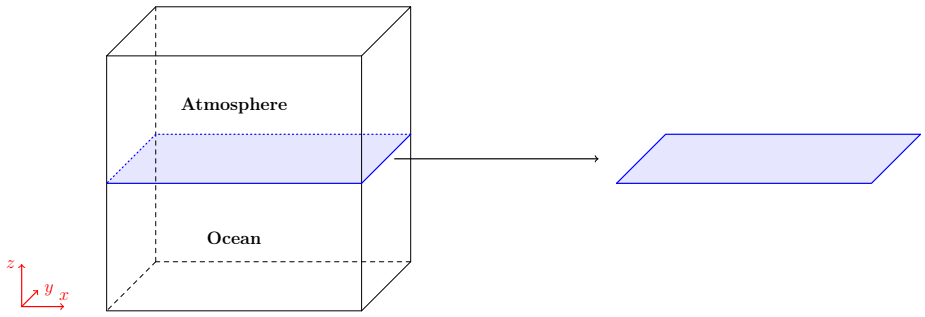

FIGURE 1.3: Schematic diagram of the 2D domain (in blue) on which the climate model equations are defined.

The strength of coupling is regulated by the magnitude of coupling constants $\gamma, \sigma < 0$. The constants Re, Pe, and Ro denote the Reynolds, Péclet, and the Rossby numbers, respectively. As a result of the non-dimensionalization, a new constant appears in the denominator of $\nabla\theta^a$. We denote this number by C^a.

Figure 1.3 shows a schematic diagram of the 2D domain on which the climate model equations are solved. The model (1.3) represents the fluid dynamics at the ocean-atmosphere interface (highlighted in blue) in the $x-y$ plane. One way to visualize such a 2D domain is to start with a 3D domain (as shown on the left in Figure 1.3) and take the average of all the relevant variables (such as ocean velocity, atmosphere velocity etc.) in the z direction up to the point of ocean-atmosphere interface. We can then obtain a 2D domain on which both the ocean and atmosphere variables are defined at each point.

1.2.1 The stochastic climate model

The introduction of stochasticity into the climate model (1.3) leads to the following stochastic climate model equations

$$
\begin{aligned}
\text{Atm.}: \; & \mathrm{d}\mathbf{u}^a + ((\mathbf{u}^a \mathrm{d}t + \sum_i \boldsymbol{\xi}_i \circ \mathrm{d}W^i)\cdot\nabla)\mathbf{u}^a + \frac{1}{Ro^a}\hat{\mathbf{z}}\times(\mathbf{u}^a \mathrm{d}t + \sum_i \boldsymbol{\xi}_i \circ \mathrm{d}W^i) \qquad (1.4)\\
& + \sum_i \left(\sum_{j=1}^{2} u_j^a \nabla \xi_{i,j} + \frac{1}{Ro^a}\nabla(\boldsymbol{\xi}_i \cdot \mathbf{R}) \right) \circ \mathrm{d}W^i = (-\frac{1}{C^a}\nabla\theta^a + \frac{1}{Re^a}\Delta\mathbf{u}^a)\mathrm{d}t,\\
& \mathrm{d}\theta^a + \nabla\cdot(\theta^a(\mathbf{u}^a \mathrm{d}t + \sum_i \boldsymbol{\xi}_i \circ \mathrm{d}W^i)) = (\gamma(\theta^a - \theta^o) + \frac{1}{Pe^a}\Delta\theta^a)\mathrm{d}t,\\
\text{Ocean}: \; & \frac{\partial \mathbf{u}^o}{\partial t} + (\mathbf{u}^o\cdot\nabla)\mathbf{u}^o + \frac{1}{Ro^o}\hat{\mathbf{z}}\times\mathbf{u}^o + \frac{1}{Ro^o}\nabla p^a = \sigma(\mathbf{u}^o - \mathbb{E}\mathbf{u}^a_{sol}) + \frac{1}{Re^o}\Delta\mathbf{u}^o,\\
& \nabla\cdot\mathbf{u}^o = 0,\\
& \frac{\partial\theta^o}{\partial t} + \mathbf{u}^o\cdot\nabla\theta^o = \frac{1}{Pe^o}\Delta\theta^o,
\end{aligned}
$$

where u_j^a and $\xi_{i,j}$ denote the jth components of atmosphere velocity $\mathbf{u}^a$ and the spatial correlation vectors $\boldsymbol{\xi}_i$, respectively.

The atmosphere component of the climate model is derived following the SALT approach resulting in additional noise terms in the equations. These noise terms describe the otherwise unmodeled effect of the small-scale processes on the large-scale dynamics. The ocean component equations are identical to their deterministic counterparts except in the coupling term, where the expected value of the divergence-free part of the atmospheric velocity $\mathbb{E}\mathbf{u}_{sol}^a$ is passed to the momentum equation instead of $\mathbf{u}_{sol}^a$. Our goal is to numerically solve this stochastic climate model.

1.3 Our approach

The climate model (1.4) poses certain technical challenges that must be addressed in order to confidently rely on the simulation results. Some of these challenges are unique to this model due to its coupled nature and therefore have not previously been encountered in the study of other stochastic models. We highlight three main challenges:

(1) We use Lagrangian trajectory data from high-resolution simulations of the deterministic climate model (1.3) to estimate/calibrate the vectors $\boldsymbol{\xi}_i$ for the stochastic climate model (1.4). However, this climate model was only recently introduced, and the literature therefore lacks a numerical analysis of the governing equations. A discretization scheme must be developed and tested to numerically solve the model equations.

(2) The calibration procedures presented in the literature (for example, in Cotter et al., 2019, Crisan et al., 2023b) are based on the assumption that the fluid is incompressible. However, the atmospheric component of the climate model we consider is compressible. Therefore, a new estimation method for $\boldsymbol{\xi}_i$ needs to be proposed that works in the compressible setting.

(3) The stochastic climate model equations involve an interaction between stochastic and deterministic variables. This setting makes it difficult to use traditional approaches, which have been effective for other stochastic models. A new discretization algorithm is therefore required to handle such coupled systems.

We approach the task of solving the stochastic climate model equations by breaking the problem into simpler sub-problems. We begin by investigating the deterministic climate model equations. We decouple the climate model into its constituent components (atmosphere and ocean) and analyze them separately. The ocean component consists of the incompressible Navier-Stokes equations and an advection-diffusion equation. These equations have been extensively studied in the literature and many numerical schemes

are available to solve them. We review relevant methods and choose an appropriate numerical method for their discretization.

Next, we study the atmosphere model equations. We test a new numerical scheme to solve these equations and check its accuracy by performing several numerical experiments. Finally, we combine the numerical schemes for the ocean and atmospheric components to arrive at a numerical discretization of the deterministic climate model.

The next step is the calibration of the stochastic climate model, followed by numerical simulations. However, due to the complexity of this model, we first investigate two simpler stochastic models:

(1) SALT-parameterized incompressible Navier-Stokes equations, and
(2) the atmosphere component of the stochastic climate model.

There are two main reasons for studying the stochastic incompressible Navier-Stokes equations:

(1) We want to assess the performance of SALT as a tool for quantifying the uncertainty arising from unresolved scales. The literature lacks such a study for the incompressible Navier-Stokes equations.
(2) These equations are relatively simpler to solve than the stochastic atmosphere model and therefore serve as an ideal precursor. Moreover, some of the algorithms developed during their numerical investigation can be reused in analyzing the atmosphere model.

After performing uncertainty quantification tests for the incompressible Navier-Stokes equations, we move on to the stochastic atmosphere model. We conduct several experiments with this model. In addition to uncertainty quantification tests, we also compare the stochastic model results with those of the non-parameterized deterministic model.

At the final stage, we solve the stochastic climate model equations. The insights gained from the earlier models help us to carefully design:

(1) a discretization scheme for the stochastic climate model,
(2) a calibration procedure to estimate $\boldsymbol{\xi}_i$, and
(3) numerical experiments for uncertainty quantification.

1.3.1 Thesis outline

The thesis is structured in the following manner. In Chapter 2, a numerical discretization scheme for the deterministic coupled ocean–atmosphere model is developed. The coupled model is first broken into its individual components (ocean and atmosphere), which are then analyzed separately.

Section 2.1 presents spatial and temporal discretization schemes for the Navier–Stokes equations and the advection–diffusion equation, which together form the ocean model. We use the finite element method for the spatial discretization of these equations. This section also briefly discusses the associated challenges, advantages, and limitations of using finite element methods for solving the ocean model equations.

Section 2.2 describes a numerical scheme for the atmospheric model equations. Results from several experiments are presented to test the accuracy of this scheme. Finally, in Section 2.3, an algorithm for solving the coupled model is presented, based on the numerical schemes developed for its individual components.

In Chapter 3, a calibration method for estimating the correlation vectors present in the SALT-parameterized models is proposed first. Then, the three stochastic models, namely, the stochastic Navier–Stokes model, the stochastic atmospheric model, and the stochastic climate model, are introduced along with their numerical discretizations.

Chapter 4 presents numerical simulation results for the three stochastic models introduced in Chapter 3. This is followed by Chapter 5, where the main results of this thesis are summarized and suggestions for future research directions are provided.

Chapter 2

Deterministic models

Overview

Our goal is to numerically solve (1.3) in high resolution and use the simulation data to calibrate the noise terms present in the stochastic model and ultimately solve the model on coarse grids. In order to achieve this, we first simplify the model by breaking it into an idealized ocean model and an idealized atmosphere model. Section 2.1 presents the numerical investigation of the idealized ocean model. We describe the numerical methods used to solve the incompressible Navier-Stokes equations and the advection-diffusion equation. In Section 2.2, we describe the numerical discretization of the atmosphere model equations. Finally, in Section 2.3, we describe the numerical scheme used to solve the climate model.

2.1 The ocean model

The ocean dynamics is described by 2D incompressible Navier-Stokes equations for the velocity and an advection diffusion equation for the temperature. The ocean model equations (after removing the coupling terms) can be written as

$$\begin{aligned} &\frac{\partial \mathbf{u}}{\partial t} + (\mathbf{u}\cdot\nabla)\mathbf{u} + \frac{1}{Ro}\hat{\mathbf{z}}\times\mathbf{u} + \frac{1}{Ro}\nabla p = \frac{1}{Re}\Delta\mathbf{u}, \\ &\nabla\cdot\mathbf{u} = 0, \\ &\frac{\partial\theta}{\partial t} + \mathbf{u}\cdot\nabla\theta = \frac{1}{Pe}\Delta\theta. \end{aligned} \tag{2.1}$$

In (2.1), the ocean temperature is passively advected by the velocity. The uncoupled nature of ocean variables (velocity and temperature) makes the process of discretizing these equations relatively straightforward. We can arrive at the discretized equations for the ocean model by combining the discrete versions of the Navier-Stokes equations with the advection-diffusion equation.

2.1.1 Navier-Stokes equations

The motion of fluid in a computational domain $\Omega \in \mathbb{R}^d,\ d = \{2, 3\}$ can be described by the incompressible Navier-Stokes equations (in dimensionless form) as

$$\begin{aligned} \partial_t \mathbf{u} + (\mathbf{u} \cdot \nabla)\, \mathbf{u} &= -\nabla p + \frac{1}{Re} \Delta \mathbf{u} + \mathbf{f}, \quad \text{in } (0, T] \times \Omega \\ \nabla \cdot \mathbf{u} &= 0, \end{aligned} \tag{2.2}$$

where $\mathbf{u}(\boldsymbol{x}, t)$ denotes the fluid velocity, $p(\boldsymbol{x}, t)$ denotes the pressure, $\mathbf{f}(\boldsymbol{x}, t)$ is the external force and Re is the Reynolds number (John, 2016). The above system of equations (2.2) is completed with an initial condition for velocity and appropriate conditions on the boundary. The initial velocity needs to be divergence-free,

$$\mathbf{u}(\boldsymbol{x}, 0) = \mathbf{u}_0,\ \nabla \cdot \mathbf{u}_0 = 0.$$

Different kinds of boundary conditions can be specified on the boundary $\partial\Omega$ for incompressible flows. We assume free-slip boundary conditions[1]

$$\begin{aligned} (\nabla \mathbf{u}\ \mathbf{n}) \cdot \tau &= 0 \quad \text{on } \partial\Omega, \\ \mathbf{u} \cdot \mathbf{n} &= 0 \quad \text{on } \partial\Omega, \end{aligned} \tag{2.3}$$

where $\mathbf{n}$ is the unit normal vector at $\boldsymbol{x} \in \partial\Omega$ and τ is the unit tangent vector.

Several methods exist for numerically solving the Navier-Stokes equations. Some of the popular ones are the Finite Difference Method, the Finite Volume Method and the Finite Element Method (FEM). We describe the use of FEM to solve (2.2).

Spatial discretization

The discretization process is split into spatial discretization and temporal discretization. In spatial discretization, the first step is to write the equations (2.2) in variational form. In this regard, we assume that the velocity $\mathbf{u}$ at any time instant belongs to the space

$$\mathbf{V} := H^1(\Omega)^d, \quad d = \{2, 3\}$$

and the pressure p at any time instant belongs to the space[2]

$$Q := L_0^2(\Omega) = \left\{ \psi : \psi \in L^2(\Omega) \text{ with } \int_\Omega \psi(\boldsymbol{x})\ \mathrm{d}\boldsymbol{x} = 0 \right\}.$$

[1] In the literature, the first part of free-slip boundary conditions is usually expressed as $(2\mathbb{D}\mathbf{u}\ \mathbf{n}) \cdot \tau = 0$, where $\mathbb{D}\mathbf{u} = \frac{1}{2}(\nabla \mathbf{u} + \nabla \mathbf{u}^T)$ is the symmetric gradient. However, for flat boundaries in 2D, it can be proven that $(\nabla \mathbf{u}^T\ \mathbf{n}) \cdot \tau = 0$ and hence one would get (2.3) as the free-slip boundary conditions.

[2] The notation $\mathrm{d}\boldsymbol{x}$ represents the integral over all the independent space variables. For example, in 2D, $\mathrm{d}\boldsymbol{x}$ represents $\mathrm{d}x \times \mathrm{d}y$

The variational form is obtained in the usual way by multiplying the equations in (2.2) with test functions, integrating the equations over Ω, and applying integration by parts to transfer derivatives from the solution to the test functions. The variational problem for (2.2) with boundary conditions (2.3) is to find, $(\mathbf{u}(\cdot,t), p(\cdot,t)) \in \mathbf{V} \times Q$ such that

$$\begin{aligned} \langle \partial_t \mathbf{u}, \mathbf{v} \rangle_\Omega + \langle (\mathbf{u} \cdot \nabla)\, \mathbf{u}, \mathbf{v} \rangle_\Omega &= \langle \nabla \cdot \mathbf{v}, p \rangle_\Omega - \frac{1}{Re} \langle \nabla \mathbf{u}, \nabla \mathbf{v} \rangle_\Omega + \langle \mathbf{f}, \mathbf{v} \rangle_\Omega, \\ \langle \nabla \cdot \mathbf{u}, \psi \rangle_\Omega &= 0, \end{aligned} \tag{2.4}$$

holds for all test functions, $(\mathbf{v}, \psi) \in \mathbf{V} \times Q$. The form $\langle \cdot, \cdot \rangle_\Omega$ denotes the standard L^2 inner product. Note that the choice of admissible spaces $\mathbf{V}$ and Q for velocity and pressure respectively is not arbitrary. It is governed by the well-posedness requirements for the problem (2.4). In fact, due to the inherent coupling between velocity and pressure, the spaces $\mathbf{V}$ and Q should satisfy the so called inf-sup condition (John, 2016) for the problem to be well posed.

In the next step of spatial discretization, one replaces the infinite-dimensional spaces $\mathbf{V}$ and Q by a finite-dimensional velocity space $\mathbf{V}_h$ and a finite-dimensional pressure space Q_h. The projection of equations in (2.4) onto finite-dimensional spaces $\mathbf{V} \times Q$ is considered which leads to approximations $\mathbf{u}_h$ and p_h of $\mathbf{u}$ and p, respectively. The semi-discrete variational formulation of (2.2) then becomes: find $(\mathbf{u}_h, p_h) \in \mathbf{V}_h \times Q_h$ such that

$$\begin{aligned} \langle \partial_t \mathbf{u}_h, \mathbf{v}_h \rangle_\Omega + \langle (\mathbf{u}_h \cdot \nabla)\, \mathbf{u}_h, \mathbf{v}_h \rangle_\Omega &= \langle \nabla \cdot \mathbf{v}_h, p_h \rangle_\Omega - \frac{1}{Re} \langle \nabla \mathbf{u}_h, \nabla \mathbf{v}_h \rangle_\Omega \\ &\quad + \langle \mathbf{f}_h, \mathbf{v}_h \rangle_\Omega, \\ \langle \nabla \cdot \mathbf{u}_h, \psi_h \rangle_\Omega &= 0, \end{aligned}$$

holds for all $(\mathbf{v}_h, \psi_h) \in \mathbf{V}_h \times Q_h$. One of the main steps involved in the Finite Element Method is the decomposition of computational domain into smaller entities called elements. In 2D, the domain is generally divided into triangles or quadrilaterals. We denote the discretized domain and the elements by $\mathcal{T}_h$ (where h represents the size of mesh elements) and K respectively. The Finite Element Method is called conforming, if $\mathbf{V}_h \subset \mathbf{V}$ and $Q_h \subset Q$, otherwise it is called non-conforming. Similar to the infinite dimensional case, the spaces $\mathbf{V}_h$ and Q_h should also satisfy (a discrete version of) the inf-sup condition so that the problem is well-posed.

One of the most popular choices for spaces $\mathbf{V}_h$, Q_h is the family of Taylor-Hood (TH) finite element spaces. The Taylor-Hood spaces[3] are given by $\mathbb{P}_k - \mathbb{P}_{k-1}$, $k \geq 2$, where $\mathbb{P}_k$ denotes the space of continuous piece-wise polynomials of degree k. The spaces $\mathbb{P}_k - \mathbb{P}_{k-1}$ satisfy the discrete inf-sup condition and hence leads to stable solutions. The spaces $\mathbb{P}_2 - \mathbb{P}_1$ are extensively used in practice due to their ease of implementation and low order. The Taylor-Hood spaces, however, have one significant drawback: their

[3]In the notation $\mathbb{P}_k - \mathbb{P}_{k-1}$, the first element $\mathbb{P}_k$ corresponds to the velocity space $\mathbf{V}_h$ while second element $\mathbb{P}_{k-1}$ corresponds to the pressure space Q_h.

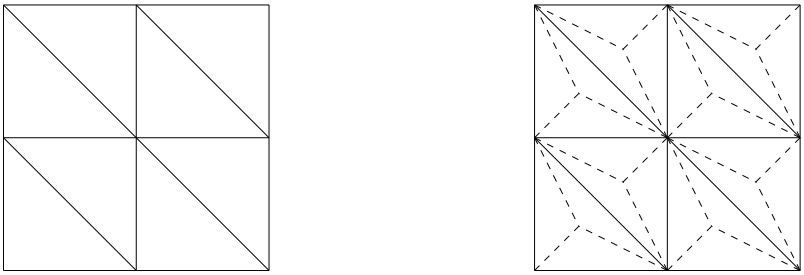

FIGURE 2.1: Barycentrically refined version (right) of a regular 2×2 mesh (left). A barycentric refinement is achieved by connecting the vertices of each triangle to the barycenter/centroid of the corresponding triangle.

poor mass conservation property. The mass conservation property is described by

$$\int_\Omega \nabla \cdot \mathbf{u}\ \psi\ \mathrm{d}\boldsymbol{x} = 0 \quad \forall \psi \in L_0^2(\Omega), \tag{2.5}$$

in the variational formulation (2.4). This implies that $\nabla \cdot \mathbf{u} = 0$ holds over the computational domain Ω in the L^2 sense. In the discrete problem, with finite element spaces $\mathbf{V}_h$ and Q_h for velocity and pressure, respectively, one obtains the variational equation

$$\int_\Omega \nabla \cdot \mathbf{u}_h\ \psi_h\ \mathrm{d}\boldsymbol{x} = 0, \quad \forall \psi_h \in Q_h.$$

Although, the function $\mathbf{u}_h$ is called discretely divergence-free, it generally does not imply $\nabla \cdot \mathbf{u}_h = 0$ in Ω in the L^2 sense since $Q_h \neq L_0^2(\Omega)$. This raises concerns about how well the finite element discretization conserves mass. One approach to alleviate mass conservation issues is to use the Scott-Vogelius finite element pair on Barycentrically refined mesh (see Figure 2.1).

The Scott-Vogelius (SV) finite element pair is defined as $\mathbb{P}_k - \mathbb{P}_{k-1}^{\text{disc}}$, where $k \geq d$. The velocity space for this pair is identical to that of the Taylor-Hood finite element pair. However, the pressure space differs; it consists of piecewise polynomials of degree $k-1$ that are not necessarily continuous across element boundaries.

For the SV pair $\mathbb{P}_k - \mathbb{P}_{k-1}^{\text{disc}}$, $k \geq d$, one can choose $\psi_h = \nabla \cdot \mathbf{u}_h + c$ in (2.5), where c is a constant selected such that $\int_\Omega \psi_h\ \mathrm{d}\boldsymbol{x} = 0$. Substituting this choice yields

$$\int_\Omega (\nabla \cdot \mathbf{u}_h)^2\ \mathrm{d}\boldsymbol{x} = 0,$$

which implies that the discrete velocity field is divergence-free. However, the SV pair generally leads to unstable solutions on standard meshes, as it does not satisfy the discrete inf-sup condition. To ensure stability, the mesh must be barycentrically refined, allowing the SV pair to meet the inf-sup condition (John, 2016).

The Scott-Vogelius finite element pair's ability to properly conserve mass, compared to Taylor-Hood elements, not only leads to more physically consistent solutions but also enhances the solution accuracy. Schroeder and Lube (2017) conducted several

experiments aimed at comparing the performance of Taylor-Hood method to the Scott-Vogelius methods. It was found that the solutions obtained using the SV pair exhibit considerably fewer artifacts compared to the TH pair. The experiments could also be run with higher Reynolds numbers without losing vortical characteristics when the SV pair was used. Moreover, the Scott-Vogelius FEM ran successfully on highly anisotropic meshes where Taylor-Hood elements failed to produce a converged solution.

The satisfaction of discrete divergence-free property is not unique to Scott-Vogelius finite elements. In fact, there are several other finite element pairs which lead to exactly divergence-free solutions. Popular examples are the Raviart-Thomas elements (RT) and the Brezzi-Douglas-Marini (BDM) elements. The use of these elements for discretization is called the $H(\text{div})-$conforming FEM. In Schroeder and Lube (2017), numerical experiments revealed that the Raviart-Thomas elements perform better than both the Taylor-Hood and the Scott-Vogelius finite elements. In our work, however, we prefer the use of Scott-Vogelius pair over other choices because of their relatively good performance, ease of implementation and satisfactory mass conservation properties. $H(\text{div})-$conforming finite elements are relatively difficult to implement. Moreover, they are nonconforming, which requires the addition of penalty terms in the discretization of the momentum equations (Farrell et al., 2021).

Time discretization

We discuss two approaches that are often used for the time discretization of the Navier-Stokes equations. The first approach is called the method of lines. In this approach, equations (2.4) are discretized in space first to obtain a nonlinear system of differential algebraic equations (DAEs). The DAEs are then discretized in time. In the second approach, discretization in time is applied first to equations (2.4), followed by space discretization. This approach is known as Rothe's method. In this section, we describe Rothe's method.

One of the most popular methods for time discretization is the ϑ(theta)-scheme. The $\vartheta-$scheme for (2.2) is of the form

$$\begin{aligned} \frac{\mathbf{u}^{n+1}-\mathbf{u}^{n}}{\Delta t} + \vartheta\left((\mathbf{u}^{n+1}\cdot\nabla)\mathbf{u}^{n+1} - \frac{1}{Re}\Delta\mathbf{u}^{n+1}\right) + \nabla p^{n+1} \\ = (1-\vartheta)\left(-(\mathbf{u}^{n}\cdot\nabla)\mathbf{u}^{n} + \frac{1}{Re}\Delta\mathbf{u}^{n}\right) + \vartheta\mathbf{f}^{n+1} + (1-\vartheta)\mathbf{f}^{n}, \\ \nabla\cdot\mathbf{u}^{n+1} = 0, \end{aligned} \tag{2.6}$$

where $\vartheta \in [0,1]$ and the time-step size $\Delta t = t^{n+1} - t^{n}$. These equations are solved for unknowns $\mathbf{u}^{n+1}, p^{n+1}$ at time t_{n+1}, given the velocity $\mathbf{u}^{n}$ at time t^{n}. Two well-known $\vartheta-$schemes are the Crank-Nicolson scheme (when $\vartheta = 0.5$) and the backward Euler scheme (when $\vartheta = 1$). The backward Euler scheme has a consistency order of 1 while the Crank-Nicolson scheme has a consistency order of 2. Both schemes are A-stable

(Gross and Reusken, 2011).
The variational form for (2.6) can be written as: find $(\mathbf{u}^{n+1}, p^{n+1}) \in \mathbf{V} \times Q$ such that

$$\begin{aligned}\left\langle \frac{\mathbf{u}^{n+1}-\mathbf{u}^n}{\Delta t}, \mathbf{v} \right\rangle_\Omega &+ \vartheta \left(\left\langle (\mathbf{u}^{n+1}\cdot\nabla)\mathbf{u}^{n+1}, \mathbf{v} \right\rangle_\Omega + \frac{1}{Re} \left\langle \nabla \mathbf{u}^{n+1}, \nabla \mathbf{v} \right\rangle_\Omega \right) \\ &- \langle p^{n+1}, \nabla\cdot\mathbf{v}\rangle_\Omega + \langle \nabla\cdot\mathbf{u}^{n+1}, \psi\rangle_\Omega \\ &= (1-\vartheta)\left(-\langle (\mathbf{u}^n\cdot\nabla)\mathbf{u}^n, \mathbf{v}\rangle_\Omega - \frac{1}{Re}\langle \nabla\mathbf{u}^n, \nabla\mathbf{v}\rangle_\Omega \right) \\ &+ \vartheta\langle \mathbf{f}^{n+1}, \mathbf{v}\rangle_\Omega + (1-\vartheta)\langle \mathbf{f}^n, \mathbf{v}\rangle_\Omega\end{aligned}$$

holds for all $(\mathbf{v}, \psi) \in \mathbf{V} \times Q$. Spatial discretization can be applied to this problem with spaces $\mathbf{V}_h \subset \mathbf{V}$, $Q_h \subset Q$ leading to a fully discrete problem.

In our work, we use the Scott-Vogelius pair $\mathbb{P}_2 - \mathbb{P}_1^{\text{disc}}$ on barycentrically refined meshes for spatial discretization and the Crank-Nicolson scheme for time discretization of the 2D incompressible Navier-Stokes equations. The fully discrete Navier-Stokes problem can be formulated as: given $\mathbf{u}_h^n \in \mathbb{P}_2$ at time t^n, find $(\mathbf{u}_h^{n+1}, p_h^{n+1}) \in \mathbb{P}_2 \times \mathbb{P}_1^{\text{disc}}$ at time $t^{n+1} = t^n + \Delta t$ such that

$$\begin{aligned}\left\langle \frac{\mathbf{u}_h^{n+1}-\mathbf{u}_h^n}{\Delta t}, \mathbf{v}_h \right\rangle_\Omega &+ \frac{1}{2}\left\langle \left(\mathbf{u}_h^{n+1}\cdot\nabla\right)\mathbf{u}_h^{n+1} + \left(\mathbf{u}_h^n\cdot\nabla\right)\mathbf{u}_h^n, \mathbf{v}_h \right\rangle_\Omega \\ &- \langle \nabla\cdot\mathbf{v}_h, p_h^{n+1}\rangle_\Omega + \frac{1}{2Re}\langle \nabla\mathbf{u}_h^{n+1} + \nabla\mathbf{u}_h^n, \nabla\mathbf{v}_h\rangle_\Omega \\ &- \frac{1}{2}\langle \mathbf{f}_h^{n+1} + \mathbf{f}_h^n, \mathbf{v}_h\rangle_\Omega + \langle \nabla\cdot\mathbf{u}_h^{n+1}, \psi_h\rangle_\Omega = 0,\end{aligned}$$

holds for all $(\mathbf{v}_h, \psi_h) \in \mathbb{P}_2 \times \mathbb{P}_1^{\text{disc}}$.

Remark 2.1.1 (Advection-dominated flows)**.** In applications, the advective term $(\mathbf{u}\cdot\nabla)\mathbf{u}$ often dominates the viscous term $\Delta\mathbf{u}/Re$. For advection-dominated flows, standard Finite Element Methods (as described above) lead to unstable solutions (John et al., 2018). The simulation results are polluted with artifacts or spurious oscillations. In order to counter these effects, additional stabilization terms need to be added to the variational formulation (see Gelhard et al., 2005; Burman and Linke, 2008 for more details).

2.1.2 Advection-diffusion equation

We consider the advection-diffusion equation

$$\partial_t\theta + \mathbf{u}\cdot\nabla\theta = \frac{1}{Pe}\Delta\theta \quad \text{in } (0,T]\times\Omega \tag{2.7}$$

in a computational domain $\Omega \in \mathbb{R}^d$, $d = \{2,3\}$, where $\theta(\boldsymbol{x}, t)$ denotes a scalar quantity (such as ocean temperature) which is being advected by a divergence-free velocity field

$\mathbf{u}(\boldsymbol{x}, t)$. Pe denotes the Péclet number

$$Pe = \frac{LU}{\eta},$$

where L is a characteristic length, and U is a characteristic velocity of the flow. The heat diffusion coefficient is denoted by η. Equation (2.7) needs to be equipped with an initial condition and appropriate boundary conditions for the problem to be well-posed. We assume an initial condition

$$\theta(\boldsymbol{x}, 0) = \theta_0$$

and the Neumann boundary condition

$$\mathbf{n} \cdot \nabla\theta = 0$$

for $\theta(\boldsymbol{x}, t)$.

In order to discretize equation (2.7), we follow Rothe's method as described in the last section. The time discretization form, using the Crank-Nicolson scheme, for the advection-diffusion equation can be written as

$$\frac{\theta^{n+1} - \theta^n}{\Delta t} + \frac{1}{2}\left(\mathbf{u}^{n+1} \cdot \nabla\theta^{n+1} + \mathbf{u}^n \cdot \nabla\theta^n\right) = \frac{1}{2Pe}\left(\Delta\theta^{n+1} + \Delta\theta^n\right) \tag{2.8}$$

with $\Delta t = t^{n+1} - t^n$. The variational problem corresponding to equation (2.8) can be posed as: find $\theta^{n+1} \in H^1(\Omega)$ such that

$$\begin{aligned}\left\langle \frac{\theta^{n+1} - \theta^n}{\Delta t}, \phi \right\rangle_\Omega + \frac{1}{2}\left\langle \mathbf{u}^{n+1} \cdot \nabla\theta^{n+1} + \mathbf{u}^n \cdot \nabla\theta^n, \phi \right\rangle_\Omega \\ + \frac{1}{2Pe}\left\langle \nabla\theta^{n+1} + \nabla\theta^n, \nabla\phi \right\rangle_\Omega = 0,\end{aligned} \tag{2.9}$$

holds for all test functions $\phi \in H^1(\Omega)$.

Spatial discretization is applied to the problem (2.9) with space $V_h \subset H^1(\Omega)$ leading to the following full discrete problem: given $\theta^n \in V_h$ at time t^n, find $\theta^{n+1} \in V_h$ at time $t^{n+1} = t^n + \Delta t$ such that

$$\begin{aligned}\left\langle \frac{\theta_h^{n+1} - \theta_h^n}{\Delta t}, \phi_h \right\rangle_\Omega + \frac{1}{2}\left\langle \mathbf{u}_h^{n+1} \cdot \nabla\theta_h^{n+1} + \mathbf{u}_h^n \cdot \nabla\theta_h^n, \phi_h \right\rangle_\Omega \\ + \frac{1}{2Pe}\left\langle \nabla\theta_h^{n+1} + \nabla\theta_h^n, \nabla\phi_h \right\rangle_\Omega = 0,\end{aligned}$$

holds for all $\phi_h \in V_h$. A typical choice for the finite element space V_h is $\mathbb{P}_2$ or $\mathbb{P}_1$. The use of a finite-dimensional subspace of $H^1(\Omega)$ (typically piecewise polynomials over a mesh) to approximate θ_h and ϕ_h is called the standard Galerkin finite element method.

A well-known challenge in solving the advection-diffusion equation arises when advection dominates diffusion. This is characterized by a high value of the Péclet

number, more specifically when the mesh Péclet number $Pe_h = \|\mathbf{u}\|_\infty h/\eta \gg 1$. For advection-dominated flows, the standard Galerkin method, although consistent, often produces nonphysical/spurious oscillations in the numerical solution (John et al., 2018). A characteristic feature of the solutions of equation (2.7) is the appearance of thin regions where the gradient of the solution is very high. The standard Galerkin method is not capable of resolving such regions, thus leading to the appearance of spurious oscillations in the solution (Franca et al., 2006). In order to avoid such numerical instabilities, finer meshes or stabilization methods are required.

Stabilization methods modify the Galerkin formulation by adding targeted artificial diffusion or residual-based terms to control oscillations while preserving consistency. Some of the popular stabilization methods are the streamline-upwind Petrov-Galerkin (SUPG) method (Brooks and Hughes, 1982; Bochev et al., 2004), continuous interior penalty (CIP) method (Burman and Hansbo, 2004), and the Galerkin/least-squares (GLS) method (Hughes et al., 1989).

Another class of methods used to improve accuracy and stability in advection-diffusion equations is the discontinuous Galerkin (DG) method (Ayuso and Marini, 2009). In DG, the solution is approximated by piecewise polynomials that are allowed to be discontinuous across element boundaries. Each element is coupled to its neighbors only through flux terms, which can be chosen to enforce stability (for example, using upwind fluxes for convective terms). This inherently provides a form of upwinding that controls oscillations without needing additional Petrov–Galerkin terms, making DG naturally suited for advection-dominated flows.

One of the main aims of this thesis is to develop numerical schemes for the stochastic models. These schemes are inherently complex due to the presence of noise terms in the model equations. In order to keep the numerical schemes as simple as possible, we refrain from using any stabilization method or the DG method to deal with spurious oscillations. Instead, we choose suitable mesh grid sizes that can resolve steep gradients of the solution resulting from advection-dominated flows.

2.2 The atmosphere model

The equations for the deterministic version of the uncoupled stochastic atmosphere model can be written as

$$\begin{aligned} &\frac{\partial \mathbf{u}}{\partial t} + (\mathbf{u}\cdot\nabla)\mathbf{u} + f\hat{\mathbf{z}}\times\mathbf{u} = -\kappa\nabla\theta + \nu\Delta\mathbf{u}, \\ &\frac{\partial \theta}{\partial t} + \nabla\cdot(\theta\mathbf{u}) = \eta\Delta\theta \end{aligned} \tag{2.10}$$

where ν is the kinematic viscosity, and η is the heat diffusion coefficient. The Coriolis force is denoted by $f\hat{\mathbf{z}}\times\mathbf{u}$ where $f = 2\Omega_E \sin\varphi$ is called the Coriolis parameter; Ω_E denotes the Earth's angular velocity and φ is the latitude. The constant κ takes the value, $\kappa = c_v(R/p_0)^{2/5}$ in which p_0 is the reference pressure level, c_p is specific heat at

constant pressure and R is the specific gas constant (Crisan et al., 2023a).

We assume a constant value for the Coriolis parameter (the f-plane approximation) throughout the computational domain and write the equations (2.10) in dimensionless form starting from the assumption that

$$\tilde{x} = \frac{x}{L}, \quad \tilde{y} = \frac{y}{L}, \quad \tilde{\theta} = \frac{\theta}{\Theta}, \quad \tilde{\mathbf{u}} = \frac{\mathbf{u}}{U}, \quad \tilde{t} = \frac{t}{L/U},$$

where L, U, and Θ are the characteristic length, characteristic velocity and characteristic potential temperature of the flow, respectively. The equations (2.10) after non-dimensionalization become

$$\begin{aligned} &\frac{U^2}{L}\frac{\tilde{\partial}\tilde{\mathbf{u}}}{\tilde{\partial}\tilde{t}} + \frac{U^2}{L}(\tilde{\mathbf{u}}\cdot\tilde{\nabla})\tilde{\mathbf{u}} + Uf\hat{\mathbf{z}}\times\tilde{\mathbf{u}} = -\frac{\kappa\Theta}{L}\tilde{\nabla}\tilde{\theta} + \frac{\nu U}{L^2}\tilde{\Delta}\tilde{\mathbf{u}}, \\ &\frac{U\Theta}{L}\frac{\tilde{\partial}\tilde{\theta}}{\tilde{\partial}\tilde{t}} + \frac{U\Theta}{L}\tilde{\nabla}\cdot(\tilde{\theta}\tilde{\mathbf{u}}) = \frac{\eta\Theta}{L^2}\tilde{\Delta}\tilde{\theta} \end{aligned} \tag{2.11}$$

With a slight abuse of notation, we rewrite (2.11) in a simplified manner by removing the *tilde* over the non-dimensionalized variables. The uncoupled atmosphere model equations in dimensionless form can be formulated as

$$\begin{aligned} &\frac{\partial\mathbf{u}}{\partial t} + (\mathbf{u}\cdot\nabla)\mathbf{u} + \frac{\hat{\mathbf{z}}\times\mathbf{u}}{Ro} + \frac{\nabla\theta}{C} = \frac{\Delta\mathbf{u}}{Re}, \\ &\frac{\partial\theta}{\partial t} + \nabla\cdot(\theta\mathbf{u}) = \frac{\Delta\theta}{Pe}, \end{aligned} \tag{2.12}$$

where,

$$Ro = \frac{U}{Lf}, \quad C = \frac{U^2}{\kappa\Theta}, \quad Re = \frac{LU}{\nu}, \quad Pe = \frac{LU}{\eta}.$$

For the geophysical processes considered in this thesis, the magnitude of Re, Pe is of the order of 10^{10}. The spatial resolution needed to compute smooth solutions corresponding to these values of Re, Pe is extremely high. We therefore introduce explicit diffusion/ eddy viscosity (in place of $\Delta\mathbf{u}/Re$ and $\Delta\theta/Pe$) in order to be able to solve the model in a reasonable amount of time with available computational resources. The non-dimensional model equations can then be reformulated as

$$\begin{aligned} &\frac{\partial\mathbf{u}}{\partial t} + (\mathbf{u}\cdot\nabla)\mathbf{u} + \frac{\hat{\mathbf{z}}\times\mathbf{u}}{Ro} + \frac{\nabla\theta}{C} = \nu_e\Delta\mathbf{u}, \\ &\frac{\partial\theta}{\partial t} + \nabla\cdot(\theta\mathbf{u}) = \eta_e\Delta\theta \end{aligned}$$

where ν_e denotes the eddy viscosity and η_e denotes the explicit diffusion coefficient.

We use the Finite Element Method to numerically solve the atmosphere model equations. The fully discrete variational formulation of (2.12) on a 2D bounded domain with free-slip boundary conditions for velocity and Neumann boundary conditions for temperature, can be posed as: find $\mathbf{u}^{n+1} \in \boldsymbol{V_1}$, $\theta^{n+1} \in V_2$ at time $t^{n+1} = t^n + \Delta t$ given

$\mathbf{u}^n, \theta^n$ at time t^n such that

$$\begin{aligned}
\left\langle \frac{\mathbf{u}^{n+1}-\mathbf{u}^n}{\Delta t}, \mathbf{v} \right\rangle_\Omega &+ \frac{1}{2}\left\langle \left(\mathbf{u}^{n+1}\cdot\nabla\right)\mathbf{u}^{n+1} + \left(\mathbf{u}^n\cdot\nabla\right)\mathbf{u}^n, \mathbf{v}\right\rangle_\Omega \\
&+ \frac{1}{2Ro}\left\langle \hat{\mathbf{z}}\times(\mathbf{u}^{n+1}+\mathbf{u}^n), \mathbf{v}\right\rangle_\Omega + \frac{1}{2C}\left\langle \theta^{n+1}+\theta^n, \nabla\cdot\mathbf{v}\right\rangle_\Omega \\
&+ \frac{\nu_e}{2}\left\langle \nabla\mathbf{u}+\nabla\mathbf{u}, \nabla\mathbf{v}\right\rangle_\Omega = 0, \\
\left\langle \frac{\theta^{n+1}-\theta^n}{\Delta t}, \phi \right\rangle_\Omega &- \frac{1}{2}\left\langle \theta^{n+1}\mathbf{u}^{n+1} + \theta^n\mathbf{u}^n, \nabla\phi\right\rangle_\Omega \\
&+ \frac{\eta_e}{2}\left\langle \nabla\theta^{n+1}+\nabla\theta^n, \nabla\phi\right\rangle_\Omega = 0,
\end{aligned}$$

holds for all $\mathbf{v} \in \boldsymbol{V_1}$, $\phi \in V_2$. The spaces $\boldsymbol{V_1}$ and V_2 are the finite-dimensional subspaces of $H^1(\Omega)^2$ and $H^1(\Omega)$, respectively. The Crank-Nicolson scheme is used for the temporal discretization. We choose the finite element spaces $\boldsymbol{V_1} = \mathbb{P}_1$, $V_2 = \mathbb{P}_1$ for the spatial discretization.

To the best of our knowledge, no benchmark tests are available in the literature to check the accuracy of our numerical scheme. The atmosphere model, however, has a strong resemblance to the viscous shallow-water equations (SWE) where the role of potential temperature is played by the height field. We can therefore, establish the accuracy of our numerical scheme by checking how it performs on the benchmark tests of shallow-water equations. We use the Galewsky benchmark test (Galewsky et al., 2004) for this purpose.

2.2.1 Galewsky test

Galewsky et al. (2004) proposed an initial-value problem for global viscous shallow-water equations

$$\begin{aligned}
\frac{\partial\mathbf{u}}{\partial t} + \left(\mathbf{u}\cdot\nabla\right)\mathbf{u} + f\hat{\mathbf{z}}\times\mathbf{u} &= -g\nabla h + \nu\Delta\mathbf{u}, \\
\frac{\partial h}{\partial t} + \nabla\cdot(\mathbf{u}h) &= \nu\Delta h,
\end{aligned} \tag{2.13}$$

where the prognostic variables are $\mathbf{u} = u_1\mathbf{i} + u_2\mathbf{j}$, the velocity vector tangent to the spherical surface (where $\mathbf{i}$ and $\mathbf{j}$ are the unit vectors in the eastward and northward directions, and u_1 and u_2 are the corresponding velocity components), and h is the thickness[4] of the fluid layer. The other notations are standard i.e. $f = 2\Omega_E\sin(\varphi)$ is the Coriolis parameter (φ denotes latitude), Ω_E is the angular velocity of the Earth, g is the acceleration due to gravity, and ν is the diffusion coefficient.

The Galewsky test is divided into two parts. In the first part, the model is run with an initial condition consisting of a basic zonal flow with a correspondingly balanced

[4]not to be confused with the mesh element size which is also denoted by h.

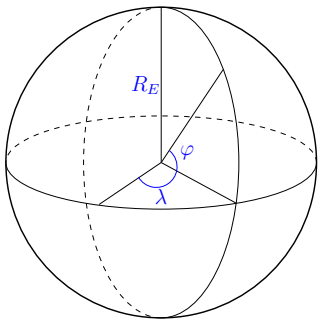

FIGURE 2.2: Illustration of the spherical coordinate symbols. R_E is the Earth's radius, φ is the latitude and λ is the longitude.

height field. In the second part, the height field is perturbed in order to initiate barotropic instability. This test case generates complex flow structures over time consisting of two distinct (slow and fast) time-scales.

The non-viscous shallow-water equations can be written in the spherical coordinate system as

$$\begin{aligned}
&\frac{\partial u_1}{\partial t} + \mathbf{u}\cdot\nabla u_1 - \left(f + \frac{u_1}{R_E}\tan\varphi\right)u_2 + \frac{g}{R_E\cos\varphi}\frac{\partial h}{\partial\lambda} = 0,\\
&\frac{\partial u_2}{\partial t} + \mathbf{u}\cdot\nabla u_2 + \left(f + \frac{u_1}{R_E}\tan\varphi\right)u_1 + \frac{g}{R_E}\frac{\partial h}{\partial\varphi} = 0,\\
&\frac{\partial h}{\partial t} + \mathbf{u}\cdot\nabla h + \frac{h}{R_E\cos\varphi}\left(\frac{\partial u_1}{\partial\lambda} + \frac{\partial u_2}{\partial\varphi}\cos\varphi\right) = 0,
\end{aligned}$$

where R_E is the Earth's radius and λ is the longitude in radians (see Figure 2.2).

The initial meridional velocity is set to zero ($u_2 = 0$) while the zonal velocity is defined as

$$u_1(\varphi) = \begin{cases} 0 & \text{for } \varphi \le \varphi_0,\\ \dfrac{u_{\max}}{e_{\mathrm{n}}}\exp\left(\dfrac{1}{(\varphi-\varphi_0)(\varphi-\varphi_1)}\right) & \text{for } \varphi_0 < \varphi < \varphi_1,\\ 0 & \text{for } \varphi \ge \varphi_1, \end{cases}$$

where $u_{\max} = 80\ \mathrm{ms}^{-1}$, $\varphi_0 = \pi/7$, $\varphi_1 = \pi/2 - \varphi_0$ and $e_{\mathrm{n}} = \exp(-4/(\varphi_1-\varphi_0)^2)$. The balanced height h is obtained by numerically integrating the balance equation

$$gh(\varphi) = gh_0 - \int^{\varphi} R_E u_1(\varphi')\left(f + u_1(\varphi')\frac{\tan(\varphi')}{R_E}\right)\mathrm{d}\varphi'.$$

Barotropic instability is initiated by perturbing the balanced height field by adding a localized bump to it which has the form

$$h'(\lambda,\varphi) = 120\cos(\varphi)e^{-(3\lambda)^2}e^{-(15(\pi/4-\varphi))^2} \quad \text{for } -\pi < \lambda < \pi.$$

The shallow-water equations (with $\nu = 0$), when integrated numerically with zonal jet and unperturbed, balanced height field as initial conditions should be able to hold the unperturbed zonal flow over a long time ($\approx$ 120 h). All fields should remain identical to the initial ones. When the same model is run with perturbed height field as initial condition, gravity waves should develop in the flow in the initial phase (see Figure 2 of Galewsky et al., 2004). In the later stages of the flow, complex vortical dynamics should appear (see Figure 4 and Figure 6 of Galewsky et al., 2004) in the flow.

2.2.2 2D viscous shallow water equations

In Galewsky et al. (2004), the shallow water equations (SWE) are solved on a spherical domain. We, however, solve the SWE on a 2D domain to avoid the complexities associated with discretizing spherical domains. The idea is to compare the qualitative behavior of our discrete model results with the results from the Galewsky test case. We first derive the model equations and the initial conditions of the Galewsky test for a 2D domain. We create test conditions on a 2D domain which are as close as possible to the Galewsky test conditions on the spherical domain.

In the Galewsky test problem, most of the flow dynamics occur in the Earth's northern hemisphere, especially in the region between 25° and 65° latitude. For our 2D domain, we take the domain length in the x direction to be $L_x = 2\pi R_E \cos(\pi/4)$ (R_E denotes Earth's average radius) so that it corresponds to a distance in the zonal direction around the globe at 45° latitude. The domain length in the y direction is taken to be $L_y = R_E(\varphi_e - \varphi_s)$ which corresponds to a distance on the Earth's surface in the Meridional direction. This domain size tries to capture the flow dynamics of the Earth's northern hemisphere between the latitudes φ_s and φ_e.

We enforce periodic boundary conditions in the x direction and free-slip conditions on the boundaries in y direction. Additionally, the β-plane approximation is assumed for the Coriolis parameter $f = f_0 + \beta y$, where $f_0 = 2\Omega_E \sin\varphi_s$, $\beta = 2\Omega_E \cos\varphi_s / R_E$ and Ω_E is the angular velocity of the Earth.
We define the dimensionless variables as

$$\tilde{x} = \frac{x}{L}, \quad \tilde{y} = \frac{y}{L}, \quad \tilde{\mathbf{u}} = \frac{\mathbf{u}}{U}, \quad \tilde{t} = \frac{t}{L/U}, \quad \tilde{h} = \frac{h}{H},$$

and non-dimensionalize the viscous shallow-water equations (2.13) leading to

$$\begin{aligned} &\frac{U^2}{L}\frac{\partial \tilde{\mathbf{u}}}{\partial \tilde{t}} + \frac{U^2}{L}\left(\tilde{\mathbf{u}}\cdot\tilde{\nabla}\right)\tilde{\mathbf{u}} + (f_0 + \beta L\tilde{y})\hat{\mathbf{z}}\times\tilde{\mathbf{u}} + \frac{gH}{L}\tilde{\nabla}\tilde{h} = \frac{\nu U}{L^2}\tilde{\Delta}\tilde{\mathbf{u}}, \\ &\frac{UH}{L}\frac{\partial \tilde{h}}{\partial \tilde{t}} + \frac{UH}{L}\tilde{\nabla}\cdot\left(\tilde{\mathbf{u}}\tilde{h}\right) = \frac{\nu H}{L^2}\tilde{\Delta}\tilde{h}. \end{aligned} \tag{2.14}$$

The equations (2.14) are further simplified by introducing the following dimensionless

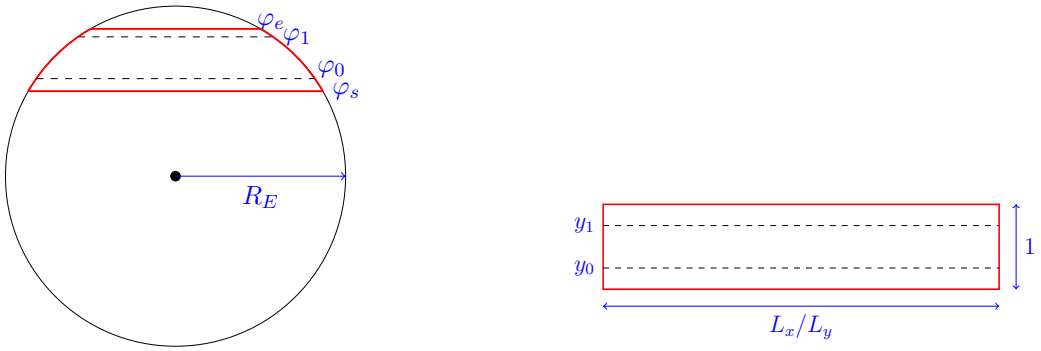

(A) (B)

FIGURE 2.3: Comparison between the domains used in Galewsky test problem (A), and our experiments (B). φ denotes the latitude and R_E denotes the Earth's radius. $L_x = 2\pi R_E \cos(\pi/4)$ and $L_y = R_E \Delta\varphi$, where $\Delta\varphi = \varphi_e - \varphi_s$.

quantities:

$$Ro = \frac{U}{Lf_0},\ \nu_e = \frac{\nu}{LU},\ C = \frac{U^2}{gH},\ B = \frac{L\beta}{f_0}.$$

The viscous shallow water equations after non-dimensionalization can be written as (we remove the *tilde* on top of non-dimensionalized variables for brevity)

$$\begin{aligned} &\frac{\partial \mathbf{u}}{\partial t} + (\mathbf{u}\cdot\nabla)\,\mathbf{u} + \frac{(1+By)}{Ro}\hat{\mathbf{z}}\times\mathbf{u} + \frac{1}{C}\nabla h = \nu_e \Delta \mathbf{u}, \\ &\frac{\partial h}{\partial t} + \nabla\cdot(\mathbf{u}h) = \nu_e \Delta h. \end{aligned} \tag{2.15}$$

After the non-dimensionalization, our domain has a size of $L_x/L_y \times 1$ (Figure 2.3). We take the characteristic length scale to be $L = L_x$, the characteristic velocity to be $U = 80$ ms^{-1} and the characteristic height to be $H = 10$ km for numerical simulations.

The initial zonal velocity u_1 in dimensionless form for our 2D domain can be formulated as

$$u_1(x,y) = \begin{cases} 0 & \text{for } y \le y_0 \\ \exp\left(\dfrac{\alpha^2}{(y-y_0)(y-y_1)}\right)\exp\left(\dfrac{4\alpha^2}{(y_1-y_0)^2}\right) & \text{for } y_0 < y < y_1 \\ 0 & \text{for } y \ge y_1 \end{cases} \tag{2.16}$$

where

$$\alpha = \frac{R_E}{L}, y_0 = \frac{\varphi_0 - \varphi_s}{\varphi_e - \varphi_s}, y_1 = \frac{\varphi_1 - \varphi_s}{\varphi_e - \varphi_s}.$$

The balanced height field h_{bal}, corresponding to the initial zonal flow, is obtained by

solving the equations

$$\frac{\partial h_g}{\partial x} = 0, \quad \frac{\partial h_g}{\partial y} = \frac{-C}{Ro}(1 + By)u_1. \tag{2.17}$$

where $h_{\text{bal}} = 1 + h_g$. The initial height for the test is chosen to be

$$h_i = h_{\text{bal}} + h_p,$$

where the last term

$$h_p = c_0 \cos\left(\frac{\pi y}{2}\right) e^{-c_1(x-x_0)^2} e^{-c_2(y-y_2)^2},$$

represents a perturbation field over the balanced height with parameters $c_0 = 0.01$, $c_1 = (3L/R_E)^2$, $c_2 = (15L/R_E)^2$, $x_0 = 0.5L_x/L_y$, and $y_2 = 0.5$. The values of these parameters are chosen so way that the height h_i is similar to the initial height field of the Galewsky test problem.

We assume periodic boundary conditions for velocity and height fields in the x-direction. At the boundaries $y = 0$ and $y = 1$, we apply free-slip boundary conditions for the velocity:

$$u_2 = 0, \quad \frac{\partial u_1}{\partial y} = 0,$$

and Neumann boundary conditions for the height:

$$\frac{\partial h}{\partial y} = 0,$$

The variational formulation for (2.15) can be posed as: find $\mathbf{u} \in H^1(\Omega)^2$ with $u_2 = 0$ at $y = 0, y = 1$ and $h \in H^1(\Omega)$ such that

$$\begin{aligned} \langle \partial_t \mathbf{u}, \mathbf{v} \rangle_\Omega + \langle (\mathbf{u} \cdot \nabla)\, \mathbf{u}, \mathbf{v} \rangle_\Omega + \frac{1}{Ro} \langle (1 + By)\hat{\mathbf{z}} \times \mathbf{u}, \mathbf{v} \rangle_\Omega \\ - \frac{1}{C} \langle h, \nabla \cdot \mathbf{v} \rangle_\Omega = -\nu_e \langle \nabla \mathbf{u}, \nabla \mathbf{v} \rangle_\Omega, \\ \langle \partial_t h, \phi \rangle_\Omega - \langle h\mathbf{u}, \nabla \phi \rangle_\Omega = -\nu_e \langle \nabla h, \nabla \phi \rangle_\Omega, \end{aligned} \tag{2.18}$$

holds for all $\mathbf{v} \in H^1(\Omega)^2$ with $v_2 = 0$ at $y = 0,\ y = 1$ and $\phi \in H^1(\Omega)$.

We use the Finite Element Method to discretize (2.18) for the spatial variable and the Crank-Nicolson time-stepping scheme to discretize equations for the temporal variable. The fully discrete variational problem then becomes; find $\mathbf{u}^{n+1} \in \boldsymbol{V_1}$, $h^{n+1} \in V_2$ at

TABLE 2.1: Model configuration of different experiments corresponding to the 2D Galewsky test case.

Parameters	**Experiment 1**	**Experiment 2**	**Experiment 3**
Number of elements, $N_x \times N_y$	448×128	448×128	896×256
Smallest element size, Δx	$1/128$ (~ 60 km)	$1/128$ (~ 60 km)	$1/256$ (~ 30 km)
Time-step size, Δt	0.01 (~ 16 min.)	0.01 (~ 16 min.)	0.005 (~ 8 min.)
Initial height	h_{bal}	$h_{\text{bal}} + h_p$	$h_{\text{bal}} + h_p$
Diffusion coefficient, ν_e	0	$1/(6 \times 10^3)$	$1/(6 \times 10^5)$

time $t^{n+1} = t^n + \Delta t$ given $\mathbf{u}^n,\ h^n$ at time t^n such that

$$\begin{aligned}
&\left\langle \frac{\mathbf{u}^{n+1} - \mathbf{u}^n}{\Delta t}, \mathbf{v} \right\rangle_\Omega + \frac{1}{2}\left\langle \left(\mathbf{u}^{n+1} \cdot \nabla\right)\mathbf{u}^{n+1} + \left(\mathbf{u}^n \cdot \nabla\right)\mathbf{u}^n, \mathbf{v} \right\rangle_\Omega \\
&\qquad + \frac{1}{2Ro}\left\langle (1 + By)(\hat{\mathbf{z}} \times \mathbf{u}^{n+1} + \hat{\mathbf{z}} \times \mathbf{u}^n), \mathbf{v} \right\rangle_\Omega \\
&\qquad + \frac{1}{2C}\left\langle h^{n+1} + h^n, \nabla \cdot \mathbf{v} \right\rangle_\Omega + \frac{\nu_e}{2}\left\langle \nabla\mathbf{u} + \nabla\mathbf{u}, \nabla\mathbf{v} \right\rangle_\Omega = 0, \\
&\left\langle \frac{h^{n+1} - h^n}{\Delta t}, \phi \right\rangle_\Omega - \frac{1}{2}\left\langle h^{n+1}\mathbf{u}^{n+1} + h^n\mathbf{u}^n, \nabla\phi \right\rangle_\Omega \\
&\qquad + \frac{\nu_e}{2}\left\langle \nabla h^{n+1} + \nabla h^n, \nabla\phi \right\rangle_\Omega = 0
\end{aligned}$$

for all $\mathbf{v} \in \boldsymbol{V_1},\ \phi \in V_2$. We choose $\boldsymbol{V_1} = \mathbb{P}_1,\ V_2 = \mathbb{P}_1$ for our numerical simulations.

2.2.3 Numerical experiments

Galewsky test case in 2D

Most of the flow dynamics resulting from the Galewsky test case take place in the northern Hemisphere. Therefore, we restrict our domain between $\varphi_s = \pi/18$ (10° latitude) and $\varphi_e = 8\pi/18$ (80° latitude). We choose $\varphi_0 = \pi/7$ and $\varphi_1 = 5\pi/14$, matching the Galewsky test case. This results in

$$y_0 = \frac{\varphi_0 - \varphi_s}{\varphi_e - \varphi_s} = \frac{11}{49},\ y_1 = \frac{\varphi_1 - \varphi_s}{\varphi_e - \varphi_s} = \frac{38}{49},\ \frac{L_x}{L_y} \approx 3.5$$

The characteristic length is $L = L_y = R_E\Delta\varphi \approx 7782$ km and the characteristic time scale is $T^* = L/U \approx 27$ hours. We conduct three different experiments in this test setup (Table 2.1).

In the first experiment, the model is run with $\nu = 0$ on a computational domain $\Omega = [0, 3.5] \times [0, 1]$ with a grid of size 448×128 elements. The initial height for this experiment is the unperturbed, balanced height field h_{bal} (see (2.17)) corresponding to the zonal jet (2.16). Figure 2.4 shows the plots for initial height and velocity fields. We aim to check whether our numerical scheme can keep the unperturbed zonal flow stable until $t = 120$ hours. A perfect numerical discretization would lead to a solution

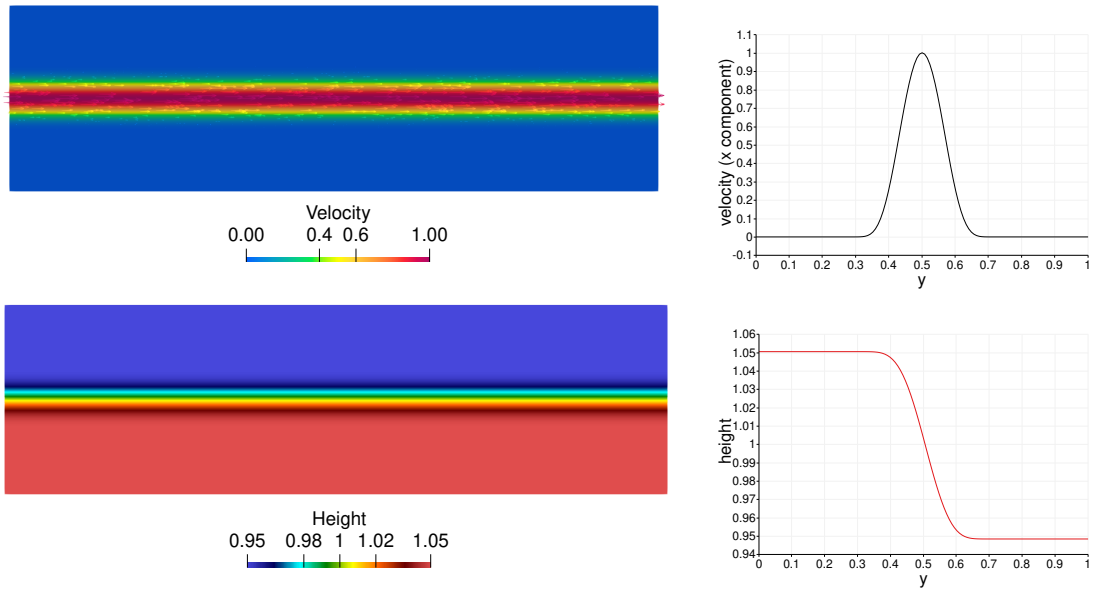

FIGURE 2.4: In the left column, plots of the initial velocity field and the corresponding balanced height field for the 2D Galewsky test are displayed. The variation of velocity (x component) and height along the y axis is plotted in the right (column).

where the values of initial velocity and height fields are maintained up to the machine precision at all times.

The velocity and height fields obtained from our simulation at $t = 120$ h are shown in Figure 2.5. We find that our numerical scheme is able to maintain the initial velocity and height profiles until $t = 120$ h. The magnitude of the difference between the fields at $t = 0$ and $t = 120$ h is, however, not equal to zero (up to machine precision) and instead is of the order of 10^{-5}.

In the second experiment, we perturb the balanced height field at $t = 0$ (Figure 2.6) and run the model until $t = 144$ hours on the grid of size 448×128. The diffusion coefficient is chosen to be $\nu = 10^5$ ($\nu_e = 1/(6 \times 10^3)$). The vorticity fields resulting from this experiment at times $t = 96$ hours, $t = 120$ hours and $t = 144$ hours are shown in Figure 2.7. The vorticity fields match the results shown in Figure 6 in Galewsky et al. (2004).

In the third experiment, we reduce the diffusion coefficient $\nu = 10^3$ ($\nu_e = 1/(6 \times 10^5)$) and run the model on a higher resolution grid, i.e., a grid of size 896×256 elements. The results are shown in Figure 2.7 where we also compare the vorticity fields obtained for this experiment with the vorticity fields of experiment 2. As expected, the reduction of diffusion leads to the formation of vortical structures with steep gradients. Our numerical scheme is able to resolve the steep gradients present in the solution. Moreover, the vortical dynamics resulting from this experiment becomes closer to the vortical dynamics achieved in the Galewsky test for the case $\nu = 0$ (see Figure 4 in Galewsky et al. (2004)).

For $\nu = 10^3$, we also plot the height and divergence fields during the initial phase

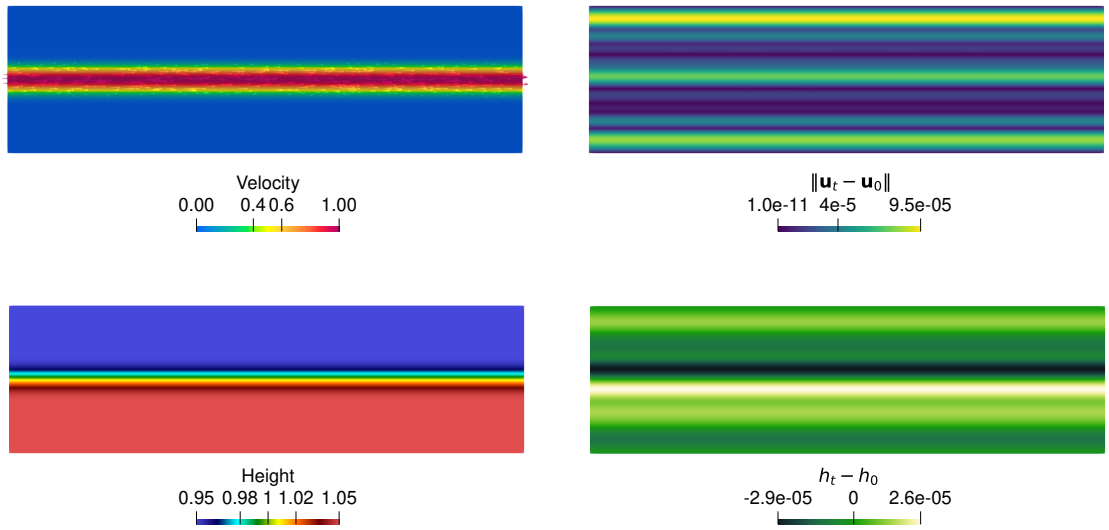

FIGURE 2.5: Velocity and height fields at $t = 120$ hours from experiment 1 are shown (left column). In addition, the difference between the velocity-fields/height-fields at $t = 0$ and $t = 120$ hours is displayed (right column).

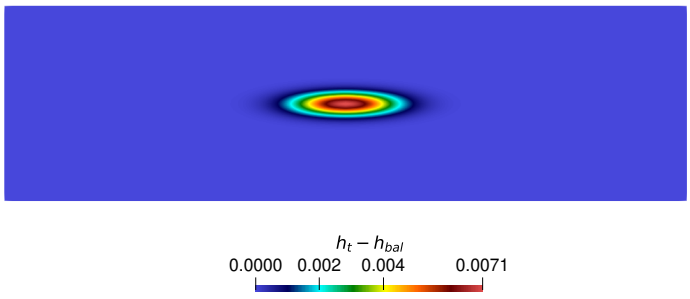

FIGURE 2.6: Plot of the perturbation field h_p, which is added to the balanced height field to induce barotropic instability.

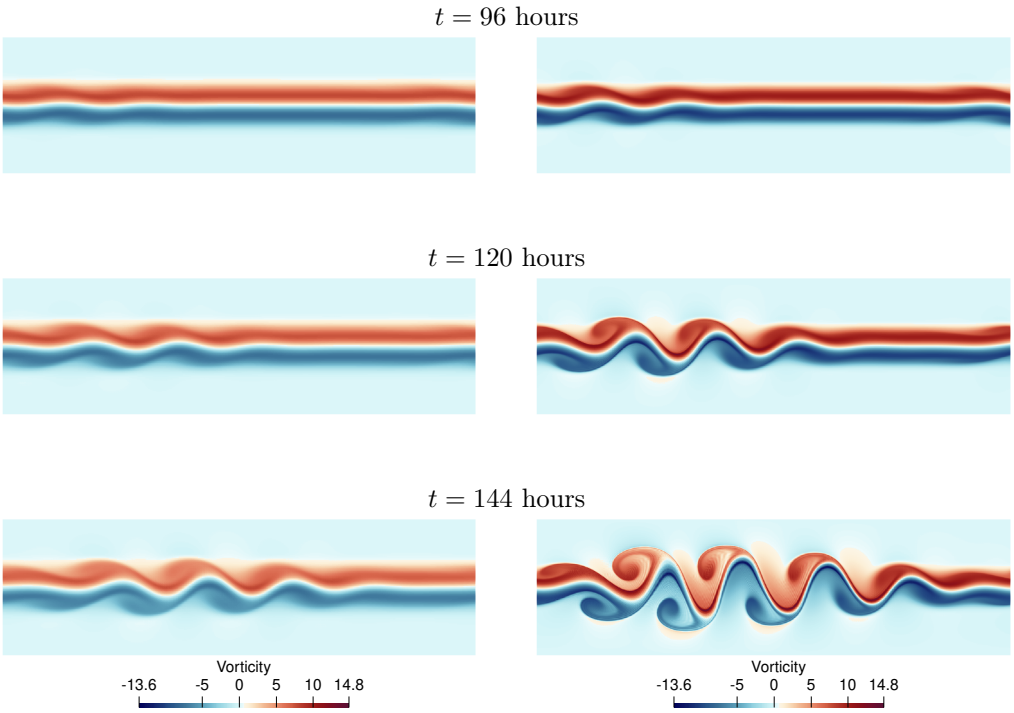

FIGURE 2.7: Plot of the vorticity field at different time instances for the 2D Galewsky test case. The simulation results correspond two different values of the diffusion coefficients: $\nu = 10^5$ (left column) and $\nu = 10^3$ (right column).

of the simulation (also known as the adjustment period). We want to check whether our solution exhibits the formation of gravity waves similar to the Galewsky test case.

Our simulation results are shown in Figure 2.8. We can observe the emergence of waves from the center of the initial perturbation similar to the results from the Galewsky test case (see Figure 2 of Galewsky et al. (2004) for comparison).

Long-term behavior

We re-run experiment 3 with slightly adjusted parameters. The new test parameters are shown in Table 2.2. Instead of observing the flow dynamics only until $t = 144$ hours, this time the simulation is performed until $t = 30$ days.

Figure 2.9 shows the vorticity plots at different stages of the simulation. The vorticity field develops complex flow dynamics after $t = 5$ days. A wide range of spatial scales can be observed, containing filament-like structures and a mix of eddies of different sizes. After a spin-up time of 15 to 20 days, the fluid seems to have attained a steady-state in the sense that the number of small, medium, and large-scale eddies does not change. This can be verified from the kinetic energy time series (Figure 2.10). The kinetic energy (KE) of the flow drops rapidly until $t = 16$ days before becoming relatively stable for a period of 10 days. From $t = 26$ days onwards, however, we observe a steep drop in KE again. This test serves as a starting point to explore similar initial conditions and parameter values for experiments carried out later in our study.

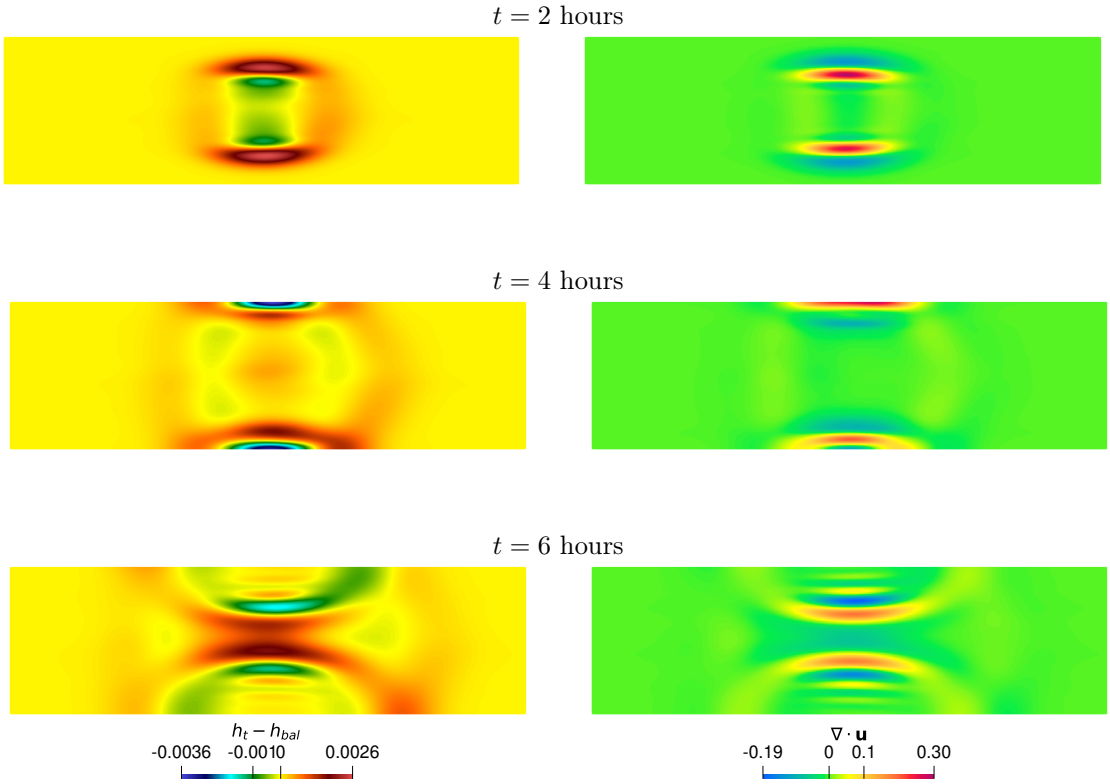

FIGURE 2.8: Plot of the height (left column) and the divergence fields (right column) during the adjustment process. The height is plotted as a difference between the instantaneous height (denoted by h_t) and the balanced, unperturbed, initial height $h_{\text{bal}} = 1 + h_g$ at time t.

TABLE 2.2: Model parameters of the Galewsky test case (experiment 3) and the long-term behavior test.

Parameters	**Galewsky test case, experiment 3**	**Long-term behavior test**
φ_s	$\pi/18$	$11\pi/72$
φ_e	$8\pi/18$	$25\pi/72$
φ_0	$\pi/7$	$\pi/6$
φ_1	$5\pi/14$	$\pi/3$
L_y	7782 km	3891 km
L_x/L_y	3.5	7
$N_x \times N_y$	896×256	1792×256
Δx	$1/256$ ($\sim$ 30 km)	$1/256$ ($\sim$ 15 km)
Δt	0.005 ($\sim$ 8 min.)	0.005 ($\sim$ 4 min.)
ν_e	$1/(6 \times 10^5)$	$1/(3 \times 10^5)$

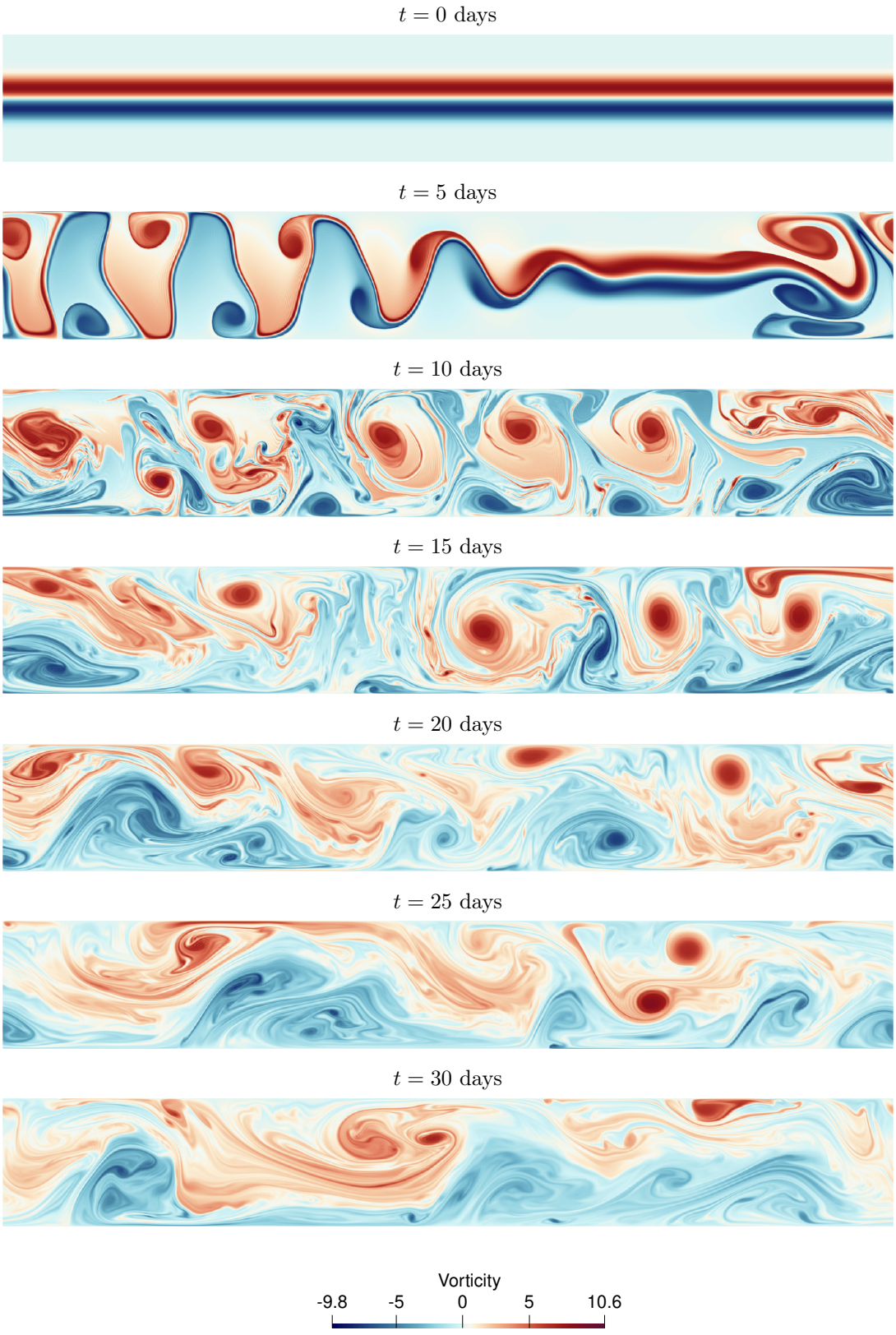

FIGURE 2.9: Evolution of vorticity field for the long-term behavior test. The model is run until $t = 30$ days.

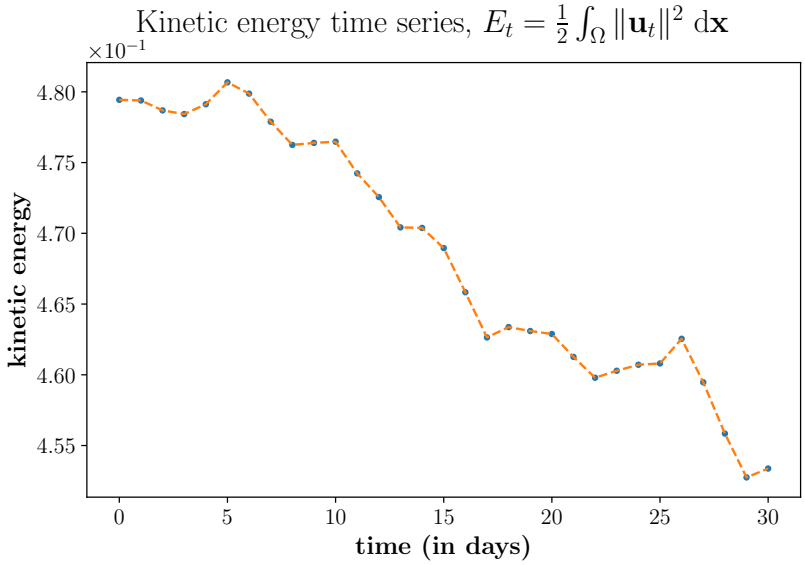

FIGURE 2.10: Kinetic energy time series plot for the long-term behavior test.

2.3 The climate model

We reintroduce the deterministic version of the climate model of Crisan et al. (2023a) as

$$
\begin{aligned}
\text{Atmosphere}: \quad & \frac{\partial \mathbf{u}^a}{\partial t} + (\mathbf{u}^a \cdot \nabla)\mathbf{u}^a + \frac{1}{Ro^a}\hat{\mathbf{z}} \times \mathbf{u}^a + \frac{1}{C^a}\nabla\theta^a = \nu^a \Delta \mathbf{u}^a, \\
& \frac{\partial \theta^a}{\partial t} + \nabla \cdot (\mathbf{u}^a \theta^a) = \gamma(\theta^a - \theta^o) + \eta^a \Delta \theta^a, \\
\text{Ocean}: \quad & \frac{\partial \mathbf{u}^o}{\partial t} + (\mathbf{u}^o \cdot \nabla)\mathbf{u}^o + \frac{1}{Ro^o}\hat{\mathbf{z}} \times \mathbf{u}^o + \frac{1}{Ro^o}\nabla p^o = \sigma(\mathbf{u}^o - \mathbf{u}^a_{sol}) + \nu^o \Delta \mathbf{u}^o, \\
& \nabla \cdot \mathbf{u}^o = 0, \\
& \frac{\partial \theta^o}{\partial t} + \mathbf{u}^o \cdot \nabla \theta^o = \eta^o \Delta \theta^o.
\end{aligned}
$$

Here, the viscous and diffusion terms are represented using artificial diffusion. The atmospheric velocity $\mathbf{u}^a$ is decomposed following the Helmholtz decomposition, $\mathbf{u}^a = \mathbf{u}^a_{sol} + \nabla q$ and its divergence-free part $\mathbf{u}^a_{sol}$ is passed on to the ocean component of the climate model.

2.3.1 Discretization

We solve the climate model equations on a rectangular computational domain Ω, which is periodic in the x direction. Free-slip boundary conditions are assumed for both the ocean and atmosphere velocities,

$$u_2 = 0, \quad \frac{\partial u_1}{\partial y} = 0$$

at the boundaries in the y direction. On the same boundaries, Neumann/insulated boundary conditions are assumed for the ocean and atmosphere temperatures,

$$\frac{\partial \theta}{\partial y} = 0.$$

We represent (with a slight abuse of notation) the discrete versions of atmosphere velocity and temperature by $\mathbf{u}^a$ and θ^a respectively. The variational formulation for the atmosphere component can be written as

$$\begin{aligned}
&\langle \partial_t \mathbf{u}^a, \mathbf{v}^a \rangle_\Omega + \langle (\mathbf{u}^a \cdot \nabla)\, \mathbf{u}^a, \mathbf{v}^a \rangle_\Omega + \frac{1}{Ro^a} \langle \hat{\mathbf{z}} \times \mathbf{u}^a, \mathbf{v}^a \rangle_\Omega \\
&\quad - \frac{1}{C^a} \langle \theta^a, \nabla \cdot \mathbf{v}^a \rangle_\Omega = -\nu^a \langle \nabla \mathbf{u}^a, \nabla \mathbf{v}^a \rangle_\Omega \,, \\
&\langle \partial_t \theta^a, \phi^a \rangle_\Omega - \langle \theta^a \mathbf{u}^a, \nabla \phi^a \rangle_\Omega = \langle \gamma(\theta^a - \theta^o), \phi^a \rangle_\Omega - \eta^a \langle \nabla \theta^a, \nabla \phi^a \rangle_\Omega \,,
\end{aligned}$$

where $\mathbf{v}^a$ and ϕ^a are the test functions corresponding to $\mathbf{u}^a$ and θ^a, respectively. We choose $\mathbf{u}^a, \theta^a \in \mathbb{P}_1$, i.e., piecewise continuous polynomials of degree 1.
The variational formulation for the ocean component is given by

$$\begin{aligned}
&\langle \partial_t \mathbf{u}^o, \mathbf{v}^o \rangle_\Omega + \langle (\mathbf{u}^o \cdot \nabla)\, \mathbf{u}^o, \mathbf{v}^o \rangle_\Omega + \frac{1}{Ro^o} \langle \hat{\mathbf{z}} \times \mathbf{u}^o, \mathbf{v}^o \rangle_\Omega \\
&\quad - \frac{1}{Ro^o} \langle p^o, \nabla \cdot \mathbf{v}^o \rangle_\Omega = \sigma \langle \mathbf{u}^o - (\mathbf{u}^a - \nabla q), \mathbf{v}^o \rangle_\Omega - \nu^o \langle \nabla \mathbf{u}^a, \nabla \mathbf{v}^a \rangle_\Omega \,, \\
&\langle \nabla \cdot \mathbf{u}^o, \psi \rangle_\Omega = 0, \\
&\langle \partial_t \theta^o, \phi^o \rangle_\Omega + \langle \mathbf{u}^o \cdot \nabla \theta^o, \nabla \phi^o \rangle_\Omega = -\eta^a \langle \nabla \theta^o, \nabla \phi^o \rangle_\Omega \,,
\end{aligned}$$

where $\mathbf{v}^o$, ψ, and ϕ^o are the test functions. We use the Scott-Vogelius finite element spaces, $\mathbf{u}^o, p^o \in \mathbb{P}_2 \times \mathbb{P}_1^{\text{disc}}$ to represent ocean velocity and pressure in order to strictly satisfy the variational incompressiblity condition. Both the ocean velocity and ocean pressure are defined on a barycentrically refined mesh. Similar to the atmospheric temperature, the ocean temperature is chosen to be in the space of piecewise continuous polynomials of degree 1 ($\theta^o \in \mathbb{P}_1$).

The divergence-free part of the atmospheric velocity is obtained by solving

$$\Delta q = \nabla \cdot \mathbf{u}^a, \tag{2.19}$$

for q and using the Helmholtz decomposition, $\mathbf{u}^a_{sol} = \mathbf{u}^a - \nabla q$. The weak formulation for (2.19) is shown in (2.20) where χ denotes the test function corresponding to q. We choose q to be in the space of piecewise continuous polynomials of degree 2 ($q \in \mathbb{P}_2$).

$$-\langle \nabla q, \nabla \chi \rangle_\Omega = \langle \nabla \cdot \mathbf{u}^a, \chi \rangle_\Omega \tag{2.20}$$

We use the Crank-Nicolson time-stepping scheme for time discretization. Our numerical implementation procedure is summarized in Algorithm 1.

Algorithm 1 Solver algorithm for the deterministic climate model

1: Let Δt and Δx be the time discretization step and the spatial discretization step respectively. Let $\mathbf{u}_0^a, \mathbf{u}_0^o$ and θ_0^a, θ_0^o be initial velocity and temperature variables, respectively of the coupled model at $t = 0$.

2: Solve

$$-\langle \nabla q_0, \nabla \chi \rangle_\Omega = \langle \nabla \cdot \mathbf{u}_0^a, \chi \rangle_\Omega$$

to obtain q_0 and set $\mathbf{u}_{sol,0}^a = \mathbf{u}_0^a - \nabla q_0$.

3: **for** $t_i = i\Delta t$, $i = 0, 1, 2 \ldots, N-1$, with $t_N = T$ **do**

4: Set $\mathbf{u}_n^a = \mathbf{u}_i^a,\ \theta_n^a = \theta_i^a,\ \theta_n^o = \theta_i^o, \mathbf{u}_{sol,n}^a = \mathbf{u}_{sol,i}^a$

5: Solve the atmosphere component

$$\begin{aligned}
\left\langle \mathbf{u}_{n+1}^a - \mathbf{u}_n^a, \mathbf{v}^a \right\rangle_\Omega &+ \frac{\Delta t}{2} \left\langle \left(\mathbf{u}_n^a \cdot \nabla\right) \mathbf{u}_n^a + \left(\mathbf{u}_{n+1}^a \cdot \nabla\right) \mathbf{u}_{n+1}^a, \mathbf{v}^a \right\rangle_\Omega \\
&+ \frac{\Delta t}{2Ro^a} \left\langle \hat{\mathbf{z}} \times (\mathbf{u}_n^a + \mathbf{u}_{n+1}^a), \mathbf{v}^a \right\rangle_\Omega - \frac{\Delta t}{2C^a} \left\langle \theta_n^a + \theta_{n+1}^a, \nabla \cdot \mathbf{v}^a \right\rangle_\Omega \\
&+ \frac{\Delta t\ \nu^a}{2} \left\langle \nabla \mathbf{u}_n^a + \nabla \mathbf{u}_{n+1}^a, \nabla \mathbf{v}^a \right\rangle_\Omega = 0, \\
\left\langle \theta_{n+1}^a - \theta_n^a, \phi^a \right\rangle_\Omega &- \frac{\Delta t}{2} \left\langle \theta_n^a \mathbf{u}_n^a + \theta_{n+1}^a \mathbf{u}_{n+1}^a, \nabla \phi^a \right\rangle_\Omega - \Delta t\ \gamma \left\langle \frac{\theta_n^a + \theta_{n+1}^a}{2} - \theta_n^o, \phi^a \right\rangle_\Omega \\
&+ \frac{\Delta t\ \eta^a}{2} \left\langle \nabla \theta_n^a + \nabla \theta_{n+1}^a, \nabla \phi^a \right\rangle_\Omega = 0,
\end{aligned}$$

to obtain $\mathbf{u}_{n+1}^a$ and θ_{n+1}^a.

6: Solve

$$-\langle \nabla q_{n+1}, \nabla \chi \rangle_\Omega = \left\langle \nabla \cdot \mathbf{u}_{n+1}^a, \chi \right\rangle_\Omega$$

to obtain q_{n+1} and set $\mathbf{u}_{sol,n+1}^a = \mathbf{u}_{n+1}^a - \nabla q_{n+1}$.

7: Solve the ocean component

$$\begin{aligned}
\left\langle \mathbf{u}_{n+1}^o - \mathbf{u}_n^o, \mathbf{v}^o \right\rangle_\Omega &+ \frac{\Delta t}{2} \left\langle \left(\mathbf{u}_n^o \cdot \nabla\right) \mathbf{u}_n^o + \left(\mathbf{u}_{n+1}^o \cdot \nabla\right) \mathbf{u}_{n+1}^o, \mathbf{v}^o \right\rangle_\Omega \\
&+ \frac{\Delta t}{2Ro^o} \left\langle \hat{\mathbf{z}} \times (\mathbf{u}_n^o + \mathbf{u}_{n+1}^o), \mathbf{v}^o \right\rangle_\Omega - \frac{\Delta t}{2Ro^o} \left\langle p_{n+1}, \nabla \cdot \mathbf{v}^o \right\rangle_\Omega \\
&- \frac{\Delta t\ \sigma}{2} \left\langle \mathbf{u}_n^o + \mathbf{u}_{n+1}^o - (\mathbf{u}_{sol,n}^a + \mathbf{u}_{sol,n+1}^a), \mathbf{v}^o \right\rangle_\Omega \\
&+ \frac{\Delta t \nu^o}{2} \left\langle \nabla \mathbf{u}_n^o + \nabla \mathbf{u}_{n+1}^o, \nabla \mathbf{v}^o \right\rangle_\Omega + \Delta t \left\langle \nabla \cdot \mathbf{u}_{n+1}^o, \psi \right\rangle_\Omega = 0, \\
\left\langle \theta_{n+1}^o - \theta_n^o, \phi^o \right\rangle_\Omega &+ \frac{\Delta t}{2} \left\langle \mathbf{u}_n^o \cdot \nabla \theta_n^o + \mathbf{u}_{n+1}^o \cdot \nabla \theta_{n+1}^o, \phi^o \right\rangle_\Omega \\
&+ \frac{\Delta t\ \eta^o}{2} \left\langle \nabla \theta_n^o + \nabla \theta_{n+1}^o, \nabla \phi^o \right\rangle_\Omega = 0,
\end{aligned}$$

to obtain $\mathbf{u}_{n+1}^o,\ p_{n+1}$ and θ_{n+1}^o.

8: Set $\mathbf{u}_{i+1}^a = \mathbf{u}_{n+1}^a,\ \theta_{i+1}^a = \theta_{n+1}^a,\ \mathbf{u}_{sol,i+1}^a = \mathbf{u}_{sol,n+1}^a,\ \mathbf{u}_{i+1}^o = \mathbf{u}_{n+1}^o,\ \theta_{i+1}^o = \theta_{n+1}^o$.

9: **end for**

Chapter 3

Inclusion of stochasticity

Overview

In this chapter, we present discretization schemes for three stochastic models: the stochastic Navier-Stokes model, the stochastic atmosphere model, and the stochastic climate model. The stochastic models must be well calibrated to ensure good performance. Therefore, before presenting the discretization of the models, we illustrate our methodology for calibration. In our work, we use (synthetic) data from high-resolution simulations of deterministic models to calibrate the corresponding stochastic models. The calibration methodology presented in this section, however, can also be easily applied to observational/satellite data.

3.1 Stochastic model calibration

We estimate $\boldsymbol{\xi}_i$ from the difference between Lagrangian trajectories of the high resolution velocity field $\mathbf{u}$ and the coarse-grained velocity field $\overline{\mathbf{u}}$ evaluated on a coarse grid,

$$\sum_i \boldsymbol{\xi}_i(\boldsymbol{X}(a,t)) \circ \mathrm{d}W_t^i \approx \mathbf{u}(\boldsymbol{X}(a,t),t)\mathrm{d}t - \overline{\mathbf{u}}(\boldsymbol{X}(a,t))\mathrm{d}t.$$

For small time-step size Δt, we can rewrite the above equation in Eulerian form as

$$\sum_i \boldsymbol{\xi}_i(\boldsymbol{x}) \circ \Delta W_n^i \approx (\mathbf{u}(\boldsymbol{x},t) - \overline{\mathbf{u}}(\boldsymbol{x},t))\Delta t,$$

where $\boldsymbol{x}$ denotes standard Euclidean coordinates on the computational domain and ΔW^i is a Gaussian process with mean zero and variance equal to Δt. This equation can be further modified to make the Gaussian process dimensionless,

$$\sum_i \boldsymbol{\xi}_i \circ \Delta B_n^i \approx (\mathbf{u} - \overline{\mathbf{u}})\sqrt{\Delta t},$$

where $\Delta B_n^i \sim \mathcal{N}(0,1)$.

We obtain the coarse-grained velocity by first spatially averaging the velocity on the fine grid (by applying the Helmholtz operator[1] (Cotter et al., 2020b; Ephrati et al., 2023)) and then projecting the averaged field onto the coarse grid. The average velocity is therefore obtained by solving

$$\overline{\mathbf{u}} - c^2 \Delta \overline{\mathbf{u}} = \mathbf{u},$$

with appropriate boundary conditions for $\overline{\mathbf{u}}$. The choice of c is determined by the smallest element size in the coarse grid. The action of the Helmholtz operator averages out the velocity field $\mathbf{u}$ in a box of size $c \times c$ throughout the mesh. This way, length scales smaller than the size of a coarse grid element are filtered out.
The following steps are involved in the estimation of $\boldsymbol{\xi}_i$:

1. Create a data matrix by calculating $(\mathbf{u} - \overline{\mathbf{u}})\Delta t$ for all the coarse-grid points at different time instances. We denote this data matrix by $\Delta \boldsymbol{X}$. If we have data from (let's say) m time instances and p points in the domain, $\Delta \boldsymbol{X}$ would be a $m \times 2p$ matrix. The first p columns would contain $(u_1 - \overline{u}_1)\Delta t$ data while the remaining columns would contain data from $(u_2 - \overline{u}_2)\Delta t$.

2. Rescale the data matrix:
$$F' = \frac{\Delta \boldsymbol{X}}{\sqrt{\Delta t}}.$$
The rescaled matrix is denoted by F'.

3. Subtract the column-mean from each entry of F':
$$F = \left(I_m - \frac{1}{m} \mathbf{1}_m \mathbf{1}_m^T \right) F',$$
where I_m is the $m \times m$ identity matrix and $\mathbf{1}_m = (1, \ldots, 1)^T$ is a column vector of length m containing only ones (Hannachi et al., 2007). This step is necessary to satisfy the assumption that $\Delta B^i \sim \mathcal{N}(0, 1)$.

4. Apply the singular value decomposition (SVD) algorithm to decompose F:
$$\mathrm{SVD}(F) = U \Lambda V^T,$$
where U is $m \times r$ matrix, Λ is $r \times r$ diagonal matrix, and V^T is $r \times 2p$ matrix in which
$$r = \mathrm{rank}(F) \leq \min(m, 2p).$$
The diagonal entries $\lambda_i = \Lambda_{ii}$ of matrix Λ are known as the singular values of F. The matrices U and V are unitary and form a set of orthonormal vectors,
$$U^T U = I_r, \quad V^T V = I_r$$

[1] not to be confused with the standard Helmholtz equation which has a different formulation.

The columns $\mathbf{u}_1, \ldots, \mathbf{u}_r$ of U are a basis for the columns space of F and the columns $\mathbf{v}_1, \ldots, \mathbf{v}_r$ of V are a basis for the row space of F. Moreover, the columns of U have zero mean (since columns of F have zero mean). These properties make $\mathbf{u}_i$ good candidates to approximate the Gaussian processes ΔB^i. However, the columns need to be rescaled to match their variance with that of ΔB^i.

5. The covariance between the column entries of U is given by:

$$\text{Cov}(U) := \frac{U^T U}{m-1} = \frac{I_r}{m-1}.$$

Each column has a variance of $1/(m-1)$. We re-express the matrix F as

$$F = \overline{U}\ \overline{V}^T, \quad \text{where} \quad \overline{U} = \sqrt{m-1}\ U \text{ and } \overline{V}^T = \frac{\Lambda}{\sqrt{m-1}} V^T.$$

The columns $\sqrt{m-1}\ \mathbf{u}_i$ of $\overline{U}$ have zero mean and unit variance, and therefore are assumed to model ΔB^i.

6. The vectors $\boldsymbol{\xi}_i$ are obtained from the rows of $\overline{V}^T$:

$$\boldsymbol{\xi}_i = \frac{\lambda_i}{\sqrt{m-1}} \mathbf{v}_i^T.$$

The vectors $\boldsymbol{\xi}_i$ represent the spatial correlations of unresolved/small-scale velocity. This is clear if we compute the covariance between the columns of matrix F. We denote the spatial covariance tensor by R,

$$\begin{aligned} R :&= \frac{F^T F}{m-1} \\ &= \frac{V \Lambda^T U^T U \Lambda V^T}{m-1} = \frac{V \Lambda^2 V^T}{m-1}, \\ RV &= V \frac{\Lambda^2}{m-1} \end{aligned}$$

The columns $\mathbf{v}_i$ (of matrix V) are the eigenvectors of R with corresponding eigenvalues $\alpha_i^2 := \lambda_i^2/(m-1)$. The vectors $\boldsymbol{\xi}_i$ can therefore be obtained from eigenvectors of spatial covariance tensor. This procedure of obtaining $\boldsymbol{\xi}_i$ is called the empirical orthogonal function (EOF) analysis (Hannachi et al., 2007). The ith EOF is simply the ith eigenvector $\mathbf{v}_i$. The eigenvalues of the covariance tensor R provide a measure of the variance accounted for by the corresponding eigenvectors. Generally, the amount of variance explained by a spatial correlation vector $\boldsymbol{\xi}_i$ is expressed as a percentage:

$$\frac{\alpha_i^2}{\sum_{i=1}^r \alpha_i^2} \times 100.$$

3.2 Stochastic Navier-Stokes equations

A stochastic version of the 2D incompressible Navier-Stokes equations is presented in Goodair and Crisan (2024). The stochastic Navier-Stokes equations can be written as

$$\begin{aligned} \mathrm{d}\mathbf{u} + (\mathbf{u}\cdot\nabla)\,\mathbf{u}\,\mathrm{d}t + \sum_{i=1}^{N}[(\mathcal{L}_i + \mathcal{A}_i)\mathbf{u}] \circ \mathrm{d}W^i &= -\nabla p\,\mathrm{d}t + \frac{1}{Re}\Delta\mathbf{u}\,\mathrm{d}t + \mathbf{f}\,\mathrm{d}t, \\ \nabla\cdot\mathbf{u} &= 0 \end{aligned} \tag{3.1}$$

where $\mathcal{L}_i := (\boldsymbol{\xi}_i\cdot\nabla)\mathbf{u}$, $\mathcal{A}_i\mathbf{u} := \sum_{j=1}^{2} u_j\nabla\xi_{i,j}$ (in which $\xi_{i,j}$ denotes the jth component of $\boldsymbol{\xi}_i$) and $\boldsymbol{\xi}_i$ are divergence-free and time-independent vector fields. We present the numerical discretization of equations (3.1) for a unit-square domain Ω with free-slip boundary conditions

$$(\mathbb{D}\mathbf{u}\ \mathbf{n})\cdot\tau = 0, \quad \mathbf{u}\cdot\mathbf{n} = 0,$$

on the boundary $\partial\Omega$.

3.2.1 Discretization

We discretize the equations (3.1) for the temporal variable first using the stochastic version of the Crank-Nicolson scheme (Zhang et al., 2013). The Brownian motion terms $\mathrm{d}W^i$ are approximated by $w_i\sqrt{\Delta t}$, where $w_i \sim \mathcal{N}(0,1)$ are independent and identically distributed (i.i.d.) samples from a Gaussian distribution with mean zero and unit variance. The stochastic system then becomes

$$\begin{aligned} \mathbf{u}^{n+1} - \mathbf{u}^n = &\left(-\frac{(\mathbf{u}^{n+1}\cdot\nabla)\mathbf{u}^{n+1} + (\mathbf{u}^n\cdot\nabla)\mathbf{u}^n}{2} - \nabla p^{n+1}\right)\Delta t \\ &+ \left(\frac{1}{2Re}(\Delta\mathbf{u}^{n+1} + \Delta\mathbf{u}^n) + \mathbf{f}\right)\Delta t \\ &- \sum_i \left(\frac{(\boldsymbol{\xi}_i w_i\cdot\nabla)\mathbf{u}^{n+1} + (\boldsymbol{\xi}_i w_i\cdot\nabla)\mathbf{u}^n}{2}\right)\sqrt{\Delta t} \\ &- \sum_i \left(\frac{(u_1^{n+1} + u_1^n)}{2}\nabla(\xi_{i,1}w_i) + \frac{(u_2^{n+1} + u_2^n)}{2}\nabla(\xi_{i,2}w_i)\right)\sqrt{\Delta t}, \\ \nabla\cdot\mathbf{u}^{n+1} = 0, & \end{aligned} \tag{3.2}$$

where $\mathbf{u}^{n+1}$ and $\mathbf{u}^n$ denote the velocity fields at time t^{n+1} and t^n respectively. The time-step size is denoted by $\Delta t = t^{n+1} - t^n$. We simplify these equations further by denoting the noise components as

$$\sum_i \boldsymbol{\xi}_i w_i = \left(\sum_i \xi_{i,1}w_i, \sum_i \xi_{i,2}w_i\right) = (\tilde{u}_1, \tilde{u}_2) = \tilde{\mathbf{u}}.$$

Similar to the spatial discretization of the deterministic equations, we discretize the stochastic system (3.2) using the Scott-Vogelius pair on barycentrically refined meshes. The variational formulation for the equations (3.2) is posed as: given $\mathbf{u}_h^n \in \mathbb{P}_2$ at time t^n, find $(\mathbf{u}_h^{n+1}, p_h^{n+1}) \in \mathbb{P}_2 \times \mathbb{P}_1^{\text{disc}}$ at time $t^{n+1} = t^n + \Delta t$ such that

$$\begin{aligned}
\left\langle \mathbf{u}_h^{n+1} - \mathbf{u}_h^n, \mathbf{v}_h \right\rangle_\Omega &+ \Delta t \left\langle \frac{(\mathbf{u}_h^{n+1} \cdot \nabla)\mathbf{u}_h^{n+1} + (\mathbf{u}_h^n \cdot \nabla)\mathbf{u}_h^n}{2}, \mathbf{v}_h \right\rangle_\Omega - \Delta t \left\langle \nabla \cdot \mathbf{v}_h, p_h^{n+1} \right\rangle_\Omega \\
&+ \frac{\Delta t}{Re} \left\langle \frac{\nabla \mathbf{u}_h^{n+1} + \nabla \mathbf{u}_h^n}{2}, \nabla \mathbf{v}_h \right\rangle_\Omega - \Delta t \left\langle \mathbf{f}_h, \mathbf{v}_h \right\rangle_\Omega \\
&+ \Delta t \left\langle \nabla \cdot \mathbf{u}_h^{n+1}, \psi_h \right\rangle_\Omega + \sqrt{\Delta t} \left\langle \frac{(\tilde{\mathbf{u}}^n \cdot \nabla)(\mathbf{u}_h^{n+1} + \mathbf{u}_h^n)}{2}, \mathbf{v}_h \right\rangle_\Omega \\
&+ \sqrt{\Delta t} \left\langle \frac{(u_{1,h}^{n+1} + u_{1,h}^n)}{2} \nabla \tilde{u}_{1,h}^n, \mathbf{v}_h \right\rangle_\Omega \\
&+ \sqrt{\Delta t} \left\langle \frac{(u_{2,h}^{n+1} + u_{2,h}^n)}{2} \nabla \tilde{u}_{2,h}^n, \mathbf{v}_h \right\rangle_\Omega = 0,
\end{aligned}$$

holds for all $(\mathbf{v}_h, \psi_h) \in \mathbb{P}_2 \times \mathbb{P}_1^{\text{disc}}$.

3.3 Stochastic atmosphere model

We consider the stochastic version of the uncoupled atmosphere model introduced in Section 2.2. The stochastic model equations are written as (Crisan et al., 2023a)

$$\begin{aligned}
&\mathrm{d}\mathbf{u} + ((\mathbf{u}\mathrm{d}t + \sum_i \boldsymbol{\xi}_i \circ \mathrm{d}W^i) \cdot \nabla)\mathbf{u} + f\hat{\mathbf{z}} \times (\mathbf{u}\mathrm{d}t + \sum_i \boldsymbol{\xi}_i \circ \mathrm{d}W^i) \\
&\quad + \sum_{i=1}^{N} \left(\sum_{j=1}^{2} u_j \nabla \xi_{i,j} + \nabla(\boldsymbol{\xi}_i \cdot \mathbf{R}) \right) \circ \mathrm{d}W^i = (-\kappa \nabla \theta + \nu \Delta \mathbf{u})\mathrm{d}t, \\
&\mathrm{d}\theta + \nabla \cdot \left(\theta(\mathbf{u}\mathrm{d}t + \sum_i \boldsymbol{\xi}_i \circ \mathrm{d}W^i) \right) = \eta \Delta \theta \mathrm{d}t.
\end{aligned} \tag{3.3}$$

New parameterization terms $\hat{\mathbf{z}} \times \sum_i \boldsymbol{\xi}_i \circ \mathrm{d}W^i + \sum_{i=1}^N \nabla(\boldsymbol{\xi}_i \cdot \mathbf{R}) \circ \mathrm{d}W^i$ appear in equations (3.3) that are absent in the stochastic Navier-Stokes equations. These terms account for the rotation in the deterministic atmosphere model (Holm and Luesink, 2021). The vector field $\mathbf{R}$ is a vector potential of the Coriolis parameter: $\mathrm{curl}(\mathbf{R}) = f\hat{\mathbf{z}}$.

Similar to the deterministic case, we derive the non-dimensional form of (3.3). The equations for the non-dimensionalized stochastic atmosphere model (after removing *tilde* over the non-dimensionalized variables and introducing eddy viscosity and artificial

diffusion terms) can be formulated as

$$\begin{aligned}
&\mathrm{d}\mathbf{u} + \left((\mathbf{u}\ \mathrm{d}t + \sum_i \boldsymbol{\xi}_i \circ \mathrm{d}W^i)\cdot\nabla\right)\mathbf{u} + \frac{1}{Ro}\hat{\mathbf{z}}\times(\mathbf{u}\ \mathrm{d}t + \sum_i \boldsymbol{\xi}_i \circ \mathrm{d}W^i) \\
&\quad + \sum_{i=1}^{N}\left(\sum_{j=1}^{2} u_j\nabla\xi_{i,j} + \frac{1}{Ro}\nabla(\boldsymbol{\xi}_i\cdot\mathbf{R})\right)\circ\mathrm{d}W^i = \left(-\frac{1}{C}\nabla\theta + \nu_e\Delta\mathbf{u}\right)\mathrm{d}t, \\
&\mathrm{d}\theta + \nabla\cdot\left(\theta\left(\mathbf{u}\mathrm{d}t + \sum_i \boldsymbol{\xi}_i\circ\mathrm{d}W^i\right)\right) = \eta_e\Delta\theta\ \mathrm{d}t.
\end{aligned}$$

In our study, we assume that the vector fields $\boldsymbol{\xi}_i$ are divergence-free. In addition to that, we neglect the parameterization terms which account for the rotation. These assumptions lead to the following stochastic model

$$\begin{aligned}
&\mathrm{d}\mathbf{u} + \left(\mathbf{u}\mathrm{d}t + \sum_i \boldsymbol{\xi}_i\circ\mathrm{d}W^i\right)\cdot\nabla\mathbf{u} + \frac{1}{Ro}\hat{\mathbf{z}}\times\mathbf{u}\mathrm{d}t + \sum_i\left(\sum_{j=1}^{2} u_j\nabla\xi_{i,j}\right)\circ\mathrm{d}W^i \\
&\quad = \left(-\frac{1}{C}\nabla\theta + \nu_e\Delta\mathbf{u}\right)\mathrm{d}t, \\
&\mathrm{d}\theta + \nabla\cdot(\theta\mathbf{u})\ \mathrm{d}t + \sum_i(\boldsymbol{\xi}_i\circ\mathrm{d}W^i)\cdot\nabla\theta = \eta_e\Delta\theta\ \mathrm{d}t.
\end{aligned} \tag{3.4}$$

3.3.1 Discretization

In this section, we explain the discretization procedure for equations (3.4). First, we discretize the equations for the temporal variable using stochastic Crank-Nicolson scheme. The Brownian motion terms $\mathrm{d}W^i$ are approximated by Gaussian processes $w_i\sqrt{\Delta t}$, where $w_i \sim \mathcal{N}(0,1)$. The SPDEs can then be written as

$$\begin{aligned}
\mathbf{u}^{n+1} - \mathbf{u}^n &= \left(-\frac{(\mathbf{u}^{n+1}\cdot\nabla)\mathbf{u}^{n+1} + (\mathbf{u}^n\cdot\nabla)\mathbf{u}^n}{2} - \frac{1}{Ro}\hat{\mathbf{z}}\times\frac{\mathbf{u}^{n+1}+\mathbf{u}^n}{2}\right)\Delta t \\
&\quad + \left(-\frac{1}{C}\frac{\nabla\theta^{n+1}+\nabla\theta^n}{2} + \nu_e\frac{\Delta\mathbf{u}^{n+1}+\Delta\mathbf{u}^n}{2}\right)\Delta t \\
&\quad - \sum_i(\boldsymbol{\xi}_i w_i\cdot\nabla)\frac{\mathbf{u}^{n+1}+\mathbf{u}^n}{2}\sqrt{\Delta t} \\
&\quad - \sum_i\left(\frac{u_1^{n+1}+u_1^n}{2}\nabla(\xi_{i,1}w_i) + \frac{u_2^{n+1}+u_2^n}{2}\nabla(\xi_{i,2}w_i)\right)\sqrt{\Delta t}, \\
\theta^{n+1} - \theta^n &= \left(-\frac{\nabla\cdot(\theta^{n+1}\mathbf{u}^{n+1}) + \nabla\cdot(\theta^n\mathbf{u}^n)}{2} + \eta_e\frac{\Delta\theta^{n+1}+\Delta\theta^n}{2}\right)\Delta t \\
&\quad - \sum_i \boldsymbol{\xi}_i w_i\cdot\frac{\nabla\theta^{n+1}+\nabla\theta^n}{2}\sqrt{\Delta t}.
\end{aligned} \tag{3.5}$$

We simplify the equations further by defining

$$\sum_i \boldsymbol{\xi}_i w_i = \left(\sum_i \xi_{i,1} w_i, \sum_i \xi_{i,2} w_i \right) := (\tilde{u}_1, \tilde{u}_2) = \tilde{\mathbf{u}}.$$

We discretize the stochastic system of equations (3.5) using the finite element spaces for velocity and temperature that were used for the deterministic model. The discrete variational problem for the uncoupled stochastic atmosphere model can be posed as: given $\mathbf{u}^n \in \mathbb{P}_1,\ \theta^n \in \mathbb{P}_1$ at time t^n, find $(\mathbf{u}^{n+1}, \theta^{n+1}) \in \mathbb{P}_1 \times \mathbb{P}_1$ at time $t^{n+1} = t^n + \Delta t$ such that

$$\begin{aligned}
\left\langle \mathbf{u}^{n+1} - \mathbf{u}^n, \mathbf{v} \right\rangle_\Omega &+ \frac{\Delta t}{2} \left\langle \left(\mathbf{u}^{n+1} \cdot \nabla\right) \mathbf{u}^{n+1} + \left(\mathbf{u}^n \cdot \nabla\right) \mathbf{u}^n, \mathbf{v} \right\rangle_\Omega \\
&+ \frac{\Delta t}{2Ro} \left\langle \hat{\mathbf{z}} \times (\mathbf{u}^{n+1} + \mathbf{u}^n), \mathbf{v} \right\rangle_\Omega + \frac{\Delta t}{2C} \left\langle \theta^{n+1} + \theta^n, \nabla \cdot \mathbf{v} \right\rangle_\Omega \\
&+ \frac{\nu_e \Delta t}{2} \left\langle \nabla \mathbf{u}^{n+1} + \nabla \mathbf{u}^n, \nabla \mathbf{v} \right\rangle_\Omega + \frac{\sqrt{\Delta t}}{2} \left\langle (\tilde{\mathbf{u}} \cdot \nabla)(\mathbf{u}^{n+1} + \mathbf{u}^n), \mathbf{v} \right\rangle_\Omega \\
&+ \frac{\sqrt{\Delta t}}{2} \left\langle (u_1^{n+1} + u_1^n) \nabla \tilde{u}_1 + (u_2^{n+1} + u_2^n) \nabla \tilde{u}_2, \mathbf{v} \right\rangle_\Omega = 0, \\
\left\langle \theta^{n+1} - \theta^n, \phi \right\rangle_\Omega &- \frac{\Delta t}{2} \left\langle \theta^{n+1} \mathbf{u}^{n+1} + \theta^n \mathbf{u}^n, \nabla \phi \right\rangle_\Omega + \frac{\eta_e \Delta t}{2} \left\langle \nabla \theta^{n+1} + \nabla \theta^n, \nabla \phi \right\rangle_\Omega \\
&+ \frac{\sqrt{\Delta t}}{2} \left\langle \tilde{\mathbf{u}} \cdot (\nabla \theta^{n+1} + \nabla \theta^n), \phi \right\rangle_\Omega = 0,
\end{aligned}$$

for all $(\mathbf{v}, \phi) \in \mathbb{P}_1 \times \mathbb{P}_1$.

3.4 Stochastic climate model

The stochastic atmosphere model introduced earlier is coupled to an idealized ocean model. This leads to the following equations for the coupled ocean-atmosphere model

$$\begin{aligned}
\text{Atmosphere}: \ & \mathrm{d}\mathbf{u}^a + ((\mathbf{u}^a \mathrm{d}t + \sum_i \boldsymbol{\xi}_i \circ \mathrm{d}W^i) \cdot \nabla)\mathbf{u}^a + \frac{1}{Ro^a} \hat{\mathbf{z}} \times \mathbf{u}^a \mathrm{d}t \\
&\qquad + \sum_i (u_1^a \nabla \xi_{i,1} + u_2^a \nabla \xi_{i,2}) \circ \mathrm{d}W^i = (-\frac{1}{C^a} \nabla \theta + \nu^a \Delta \mathbf{u}^a) \mathrm{d}t, \\
& \mathrm{d}\theta^a + \nabla \cdot (\theta^a \mathbf{u}^a) \mathrm{d}t + \sum_i (\boldsymbol{\xi}_i \circ \mathrm{d}W^i) \cdot \nabla \theta^a = (\gamma(\theta^a - \theta^o) + \nu^a \Delta \theta) \mathrm{d}t, \\
\text{Ocean}: \ & \frac{\partial \mathbf{u}^o}{\partial t} + (\mathbf{u}^o \cdot \nabla)\mathbf{u}^o + \frac{1}{Ro^o} \hat{\mathbf{z}} \times \mathbf{u}^o + \frac{1}{Ro^o} \nabla p^a = \sigma(\mathbf{u}^o - \mathbb{E}\mathbf{u}^a_{sol}) + \nu^o \Delta \mathbf{u}^o, \\
& \nabla \cdot \mathbf{u}^o = 0, \\
& \frac{\partial \theta^o}{\partial t} + \mathbf{u}^o \cdot \nabla \theta^o = \eta^o \Delta \theta^o.
\end{aligned} \tag{3.6}$$

Unlike in the deterministic case, the ocean model here is driven by the expected value of the divergence-free part of the atmospheric velocity. Due to this coupling, it is not possible to solve for all the unknowns in equations (3.6) simultaneously. As a result, we are restricted to solving the individual components separately. We combine the discretization schemes developed for the atmosphere and ocean components in the previous sections to arrive at a numerical scheme for the stochastic climate model.

Algorithm 2 summarizes our numerical procedure for solving the stochastic climate model equations. This algorithm is implemented using the Firedrake finite element package. We use Firedrake's parallelization feature to run each ensemble member on a separate CPU core; steps 2 to 4 and steps 7 to 11 of the algorithm are performed on different cores.

Algorithm 2 Solver algorithm for the stochastic climate model

1: Let Δt and Δx be the time discretization step and the spatial discretization step, respectively. Let $\mathbf{u}_0^o$ and θ_0^o be the initial velocity and temperature fields of the ocean component of the model at $t = 0$. Let $\mathbf{u}_{0,j}^a$ and $\theta_{0,j}^a$ (where $j = 1, 2, \ldots, N_p$) be the initial atmospheric velocity and temperature for each particle in the ensemble.

2: **for** $j = 1, 2 \ldots, N_p$ **do**

3: Solve

$$-\langle \nabla q_{0,j}, \nabla \chi \rangle_\Omega = \left\langle \nabla \cdot \mathbf{u}_{0,j}^a, \chi \right\rangle_\Omega$$

to obtain $q_{0,j}$, and set $\mathbf{u}_{sol,0,j}^a = \mathbf{u}_{0,j}^a - \nabla q_{0,j}$.

4: **end for**

5: **for** $t_k = k\Delta t$, $k = 0, 1, 2 \ldots, M-1$, with $t_M = T$ **do**

6: Set $\mathbf{u}_{n,j}^a = \mathbf{u}_{k,j}^a$, $\theta_{n,j}^a = \theta_{k,j}^a$, $\mathbf{u}_{sol,n,j}^a = \mathbf{u}_{sol,k,j}^a$, $\mathbf{u}_n^o = \mathbf{u}_k^o$, $\theta_n^o = \theta_k^o$.

7: **for** $j = 1, 2 \ldots, N_p$ **do**

8: Let

$$\sum_i \boldsymbol{\xi}_i w_i := \left(\sum_i \xi_{i,1} w_i, \sum_i \xi_{i,2} w_i \right) = (\tilde{u}_1, \tilde{u}_2) = \tilde{\mathbf{u}} \quad \text{for i.i.d. } w_i \in \mathcal{N}(0,1).$$

9: Solve the atmosphere component

$$\begin{aligned}
\left\langle \mathbf{u}_{n+1,j}^a - \mathbf{u}_{n,j}^a, \mathbf{v}^a \right\rangle_\Omega &+ \frac{\Delta t}{2} \left\langle \left(\mathbf{u}_{n+1,j}^a \cdot \nabla\right) \mathbf{u}_{n+1,j}^a + \left(\mathbf{u}_{n,j}^a \cdot \nabla\right) \mathbf{u}_{n,j}^a, \mathbf{v}^a \right\rangle_\Omega \\
&+ \frac{\Delta t}{2Ro^a} \left\langle \hat{\mathbf{z}} \times (\mathbf{u}_{n+1,j}^a + \mathbf{u}_{n,j}^a), \mathbf{v}^a \right\rangle_\Omega \\
&+ \frac{\Delta t}{2C^a} \left\langle \theta_{n+1,j}^a + \theta_{n,j}^a, \nabla \cdot \mathbf{v}^a \right\rangle_\Omega \\
&+ \frac{\nu^a \Delta t}{2} \left\langle \nabla \mathbf{u}_{n+1,j}^a + \nabla \mathbf{u}_{n,j}^a, \nabla \mathbf{v}^a \right\rangle_\Omega \\
&+ \frac{\sqrt{\Delta t}}{2} \left\langle (\tilde{\mathbf{u}} \cdot \nabla)(\mathbf{u}_{n+1,j}^a + \mathbf{u}_{n,j}^a), \mathbf{v}^a \right\rangle_\Omega \\
&+ \frac{\sqrt{\Delta t}}{2} \left\langle (u_{1,n+1,j}^a + u_{1,n,j}^a) \nabla \tilde{u}_1, \mathbf{v}^a \right\rangle_\Omega \\
&+ \frac{\sqrt{\Delta t}}{2} \left\langle (u_{2,n+1,j}^a + u_{2,n,j}^a) \nabla \tilde{u}_2, \mathbf{v}^a \right\rangle_\Omega = 0, \\
\left\langle \theta_{n+1,j}^a - \theta_{n,j}^a, \phi^a \right\rangle_\Omega &+ \frac{\Delta t}{2} \left\langle \theta_{n+1,j}^a \mathbf{u}_{n+1,j}^a + \theta_{n,j}^a \mathbf{u}_{n,j}^a, \nabla \phi^a \right\rangle_\Omega \\
&- \gamma \ \Delta t \left\langle \frac{\theta_{n,j}^a + \theta_{n+1,j}^a}{2} - \theta_n^o, \phi^a \right\rangle_\Omega \\
&+ \frac{\eta^a \Delta t}{2} \left\langle \nabla \theta_{n+1,j}^a + \nabla \theta_{n,j}^a, \nabla \phi^a \right\rangle_\Omega \\
&+ \frac{\sqrt{\Delta t}}{2} \left\langle \tilde{\mathbf{u}} \cdot (\nabla \theta_{n+1,j}^a + \nabla \theta_{n,j}^a), \phi^a \right\rangle_\Omega = 0,
\end{aligned}$$

to obtain the updated values $\mathbf{u}_{n+1,j}^a$ and $\theta_{n+1,j}^a$.

10: Solve

$$-\left\langle \nabla q_{n+1,j}, \nabla \chi \right\rangle_\Omega = \left\langle \nabla \cdot \mathbf{u}^a_{n+1,j}, \chi \right\rangle_\Omega$$

to obtain $q_{n+1,j}$, and set $\mathbf{u}^a_{sol,n+1,j} = \mathbf{u}^a_{n+1,j} - \nabla q_{n+1,j}$.

11: **end for**

12: Set

$$\mathbf{u}^a_{sol,n} = \frac{1}{N_p}\sum_{j=1}^{N_p} \mathbf{u}^a_{sol,n,j} \quad \text{and} \quad \mathbf{u}^a_{sol,n+1} = \frac{1}{N_p}\sum_{j=1}^{N_p} \mathbf{u}^a_{sol,n+1,j}$$

13: Solve the ocean component

$$\begin{aligned}
\left\langle \mathbf{u}^o_{n+1} - \mathbf{u}^o_n, \mathbf{v}^o \right\rangle_\Omega &+ \frac{\Delta t}{2}\left\langle \left(\mathbf{u}^o_n \cdot \nabla\right)\mathbf{u}^o_n + \left(\mathbf{u}^o_{n+1} \cdot \nabla\right)\mathbf{u}^o_{n+1}, \mathbf{v}^o \right\rangle_\Omega \\
&+ \frac{\Delta t}{2Ro^o}\left\langle \hat{\mathbf{z}} \times (\mathbf{u}^o_n + \mathbf{u}^o_{n+1}), \mathbf{v}^o \right\rangle_\Omega - \frac{\Delta t}{2Ro^o}\left\langle p_{n+1}, \nabla \cdot \mathbf{v}^o \right\rangle_\Omega \\
&- \frac{\Delta t\ \sigma}{2}\left\langle \mathbf{u}^o_n + \mathbf{u}^o_{n+1} - (\mathbf{u}^a_{sol,n} + \mathbf{u}^a_{sol,n+1}), \mathbf{v}^o \right\rangle_\Omega \\
&+ \frac{\Delta t \nu^o}{2}\left\langle \nabla \mathbf{u}^o_n + \nabla \mathbf{u}^o_{n+1}, \nabla \mathbf{v}^o \right\rangle_\Omega + \Delta t \left\langle \nabla \cdot \mathbf{u}^o_{n+1}, \psi \right\rangle_\Omega = 0, \\
\left\langle \theta^o_{n+1} - \theta^o_n, \phi^o \right\rangle_\Omega &+ \frac{\Delta t}{2}\left\langle \mathbf{u}^o_n \cdot \nabla \theta^o_n + \mathbf{u}^o_{n+1} \cdot \nabla \theta^o_{n+1}, \phi^o \right\rangle_\Omega \\
&+ \frac{\Delta t\ \eta^o}{2}\left\langle \nabla \theta^o_n + \nabla \theta^o_{n+1}, \nabla \phi^o \right\rangle_\Omega = 0,
\end{aligned}$$

to obtain $\mathbf{u}^o_{n+1}$, p_{n+1} and θ^o_{n+1}.

14: Set $\mathbf{u}^a_{k+1,j} = \mathbf{u}^a_{n+1,j}$, $\theta^a_{k+1,j} = \theta^a_{n+1,j}$, $\mathbf{u}^a_{sol,k+1,j} = \mathbf{u}^a_{sol,n+1,j}$, $\mathbf{u}^o_{k+1} = \mathbf{u}^o_{n+1}$, and $\theta^o_{k+1} = \theta^o_{n+1}$.

15: **end for**

Chapter 4

Numerical simulations

Overview

In this chapter, we present results from the numerical simulations of three stochastic models. The first stochastic model is a SALT parameterized version of the 2D Navier-Stokes equations. The calibration procedure described in the previous chapter is used to estimate the stochastic terms in the model. We present results from several tests to quantify the uncertainty introduced by running the model on coarse grids. The second stochastic model is an idealized stochastic atmosphere model. We present an extensive numerical investigation of this model since it forms an integral part of the climate model. Finally, we present the simulation results for the stochastic climate model.

4.1 Stochastic Navier-Stokes equations

In this section, we evaluate the effectiveness of SALT (stochastic advection by Lie transport) parameterization in capturing the uncertainty introduced by unresolved transport phenomena in the Navier-Stokes equations. The 2D stochastic incompressible Navier-Stokes equations can be written as

$$\begin{aligned} \mathrm{d}\mathbf{u} + (\mathbf{u}\mathrm{d}t + \sum_i \boldsymbol{\xi}_i \circ \mathrm{d}W^i)\cdot\nabla\mathbf{u} &= -\sum_i (u_1\nabla\xi_{i,1} + u_2\nabla\xi_{i,2}) \circ \mathrm{d}W^i \\ &\quad - \nabla p\ \mathrm{d}t + \frac{1}{Re}\Delta\mathbf{u}\ \mathrm{d}t + \mathbf{f}\ \mathrm{d}t, \\ \nabla\cdot\mathbf{u} &= 0 \end{aligned} \tag{4.1}$$

These equations represent the stochastic counterpart of the deterministic Navier-Stokes equations

$$\begin{aligned} \partial_t\mathbf{u} + (\mathbf{u}\cdot\nabla)\,\mathbf{u} &= -\nabla p + \frac{1}{Re}\Delta\mathbf{u} + \mathbf{f}, \\ \nabla\cdot\mathbf{u} &= 0. \end{aligned} \tag{4.2}$$

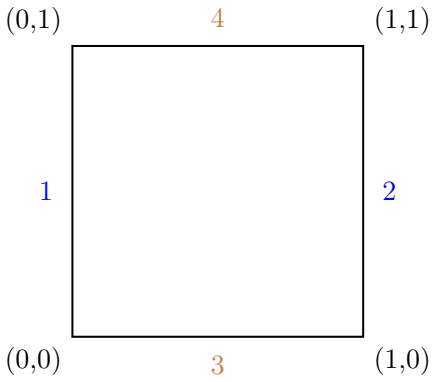

FIGURE 4.1: Computational domain (with labeled boundaries) on which the Navier-Stokes equations are solved.

TABLE 4.1: The value of grid parameters for Navier-Stokes model simulation

Parameter	**Fine grid**	**Coarse grid 1**	**Coarse grid 2**
Number of elements, $N_x \times N_y$	256×256	64×64	32×32
Element size, Δx	$1/256$	$1/64$	$1/32$
Time-step size, Δt	0.025	0.1	0.2
Reynolds number, Re	8×10^4	4×10^4	2×10^4

We solve these equations on a two-dimensional unit-square domain Ω (Figure 4.1) with free-slip boundary conditions

$$(\nabla \mathbf{u}\ \mathbf{n}) \cdot \tau = 0, \quad \mathbf{u} \cdot \mathbf{n} = 0 \quad \text{on } \partial\Omega,$$

which, due to the domain geometry, simplify to

$$\begin{aligned} u_1 = 0,\ \partial_x u_2 = 0 \quad &\text{on boundaries 1 and 2,} \\ u_2 = 0,\ \partial_y u_1 = 0 \quad &\text{on boundaries 3 and 4.} \end{aligned}$$

The external force $\mathbf{f}$ is defined as

$$\mathbf{f}(x, y) = (\alpha y \sin(\beta\pi x),\ \alpha \sin(\beta\pi x) \sin(\beta\pi y)),$$

where the parameters α and β control the intensity and frequency of the forcing, respectively.

Our goal is to calibrate the stochastic model for coarse grid simulations using data from high-resolution deterministic model runs and to perform uncertainty quantification tests. We consider three different mesh configurations (see Table 4.1). The aim is to extract the small-scale flow information from simulations on 256×256 grid and use it to run the stochastic model on 64×64 and 32×32 grids and quantify the uncertainty of coarse grid simulations.

4.1.1 Fine grid simulation

We run the deterministic model (4.2) on the fine grid of size 256×256 starting from the initial condition

$$\mathbf{u}(t = 0) = (0, 0),$$

and forcing parameters $\alpha = 0.01,\ \beta = 8$.

Figure 4.2 shows the evolution of fluid velocity, pressure, and vorticity fields over time. We identify a time window during which the numerical solutions attain statistical equilibrium. This is important for effective calibration of the stochastic model, which is derived on the assumption that the velocity-velocity correlation of the unresolved dynamics is stationary or time-independent.

We observe from Figure 4.3 and the kinetic energy plot (Figure 4.4) that the flow has reached energy equilibrium after an initial spin-up time of approximately 50 time units.

Stochastic model calibration

We estimate the correlation eigenvectors $\boldsymbol{\xi}_i$ using the Lagrangian trajectory data obtained from the fine grid velocity field $\mathbf{u}$ and its coarse-grained counterpart $\overline{\mathbf{u}}$ on the coarse grid. The coarse-grained velocity is calculated by first spatially averaging the fine grid velocity and then projecting the averaged field onto the coarse grid. The average velocity is obtained by solving

$$\overline{\mathbf{u}} - c^2 \Delta \overline{\mathbf{u}} = \mathbf{u} \quad \text{in } \Omega,$$

with free-slip conditions on the boundary. We choose $c = 1/64$ for the 64×64 grid and $c = 1/32$ for the 32×32 grid.

Figure 4.5 shows the result of coarse graining on the high-resolution velocity field corresponding to time $t = 50$. The velocity field for the 64×64 grid loses information about sharp gradients when compared to the fine grid. The effect of coarse graining is even more noticeable for 32×32 grid. Figure 4.5 also displays the vorticity fields corresponding to coarse-grained velocity fields.

We record the fine grid velocity $\mathbf{u}$ from $t = 50$ to $t = 110$ time units at an interval of Δt (the coarse grid time-step) and apply the calibration procedure described in Section 3.1. Applying this procedure yields a data matrix $\Delta \boldsymbol{X}$ of size 600×98818 and 300×24834 for grids of size 64×64 and 32×32, respectively.

Figure 4.6 shows the plots for the EOF normalized spectrum for both coarse grids. We find that for 64×64 grid, 32 EOFs/$\boldsymbol{\xi}_i$ can capture 90% of the total variability in $\Delta \boldsymbol{X}$. For 32×32 grid, 90% of the total variability in $\Delta \boldsymbol{X}$ is captured by just 23 EOFs. Table 4.2 shows the number of EOFs required by the coarse grids for capturing different levels of variability in data.

Figures 4.7 and 4.8 show some of the estimated $\boldsymbol{\xi}_i$ for coarse grids 64×64 and

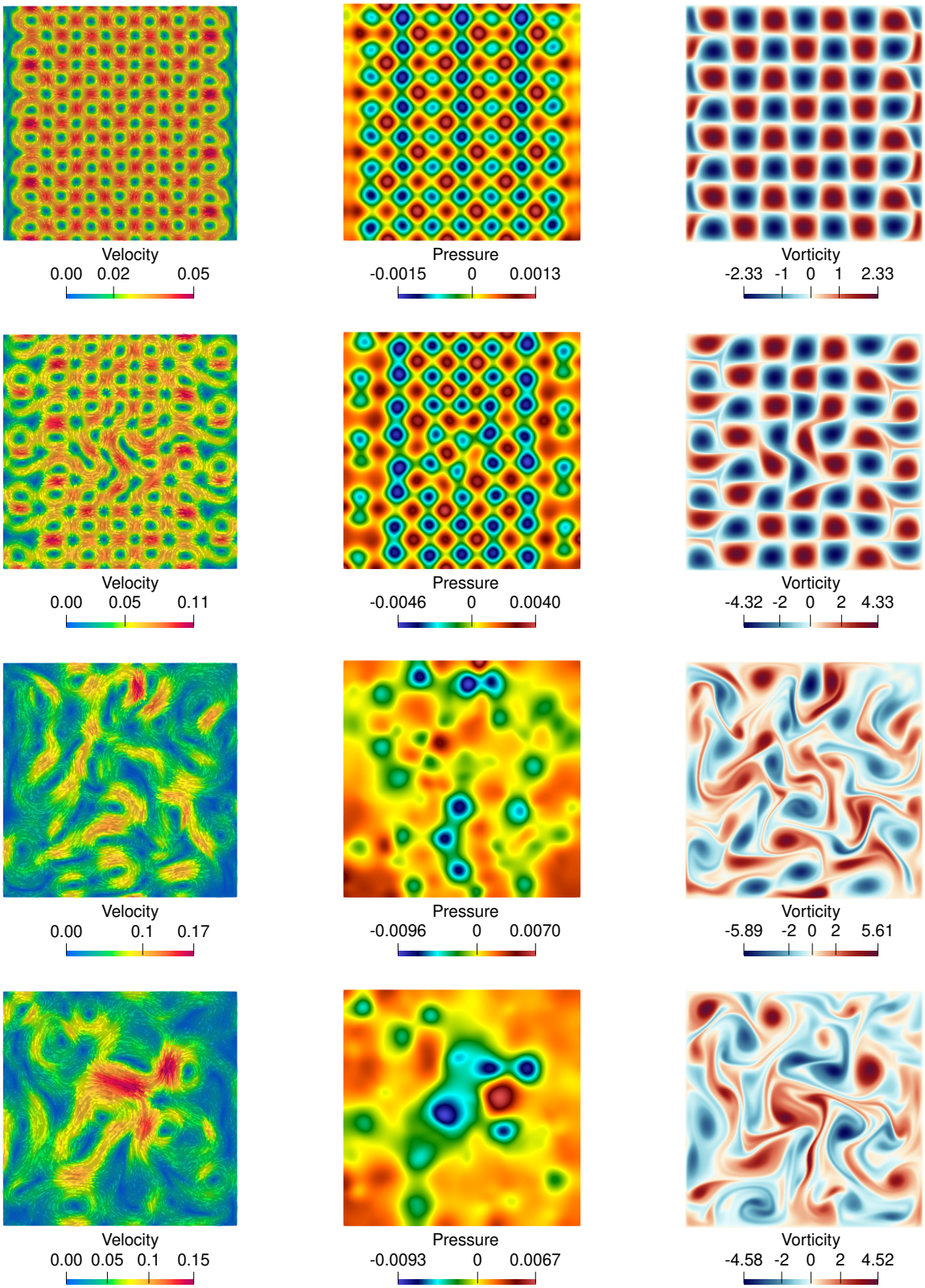

FIGURE 4.2: Velocity (left column), pressure (middle column), and vorticity (right column) fields at $t = 10$ (top), $t = 20$, $t = 30$, and $t = 40$ (bottom). The fields are obtained by solving the deterministic model (4.2) on the fine grid.

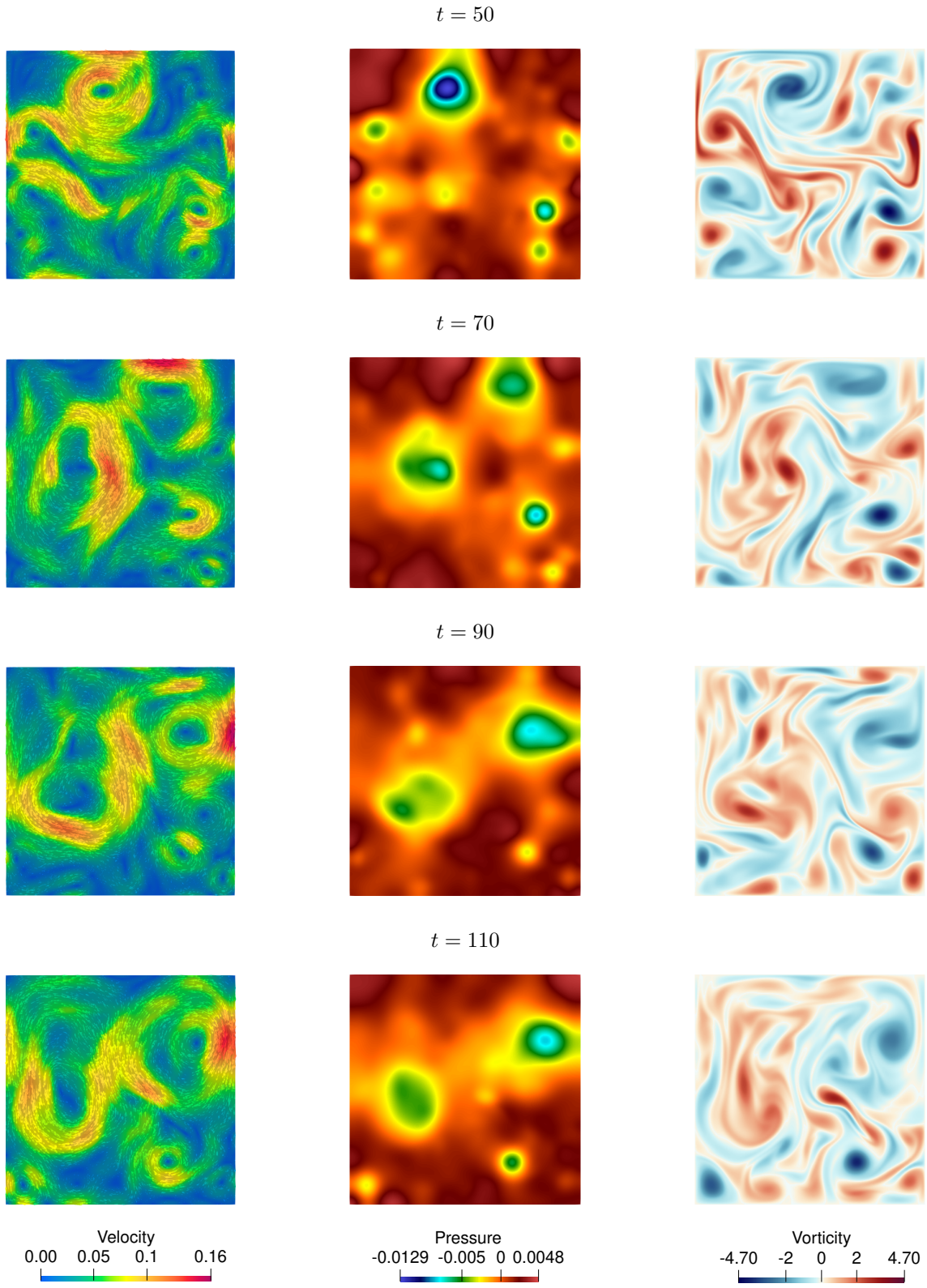

FIGURE 4.3: Velocity (left column), pressure (middle column), and vorticity (right column) fields at $t = 50$, $t = 70$, $t = 90$, and $t = 110$ (bottom). The fields are obtained by solving the deterministic model (4.2) on the fine grid. The color scales are kept the same across all time snapshots.

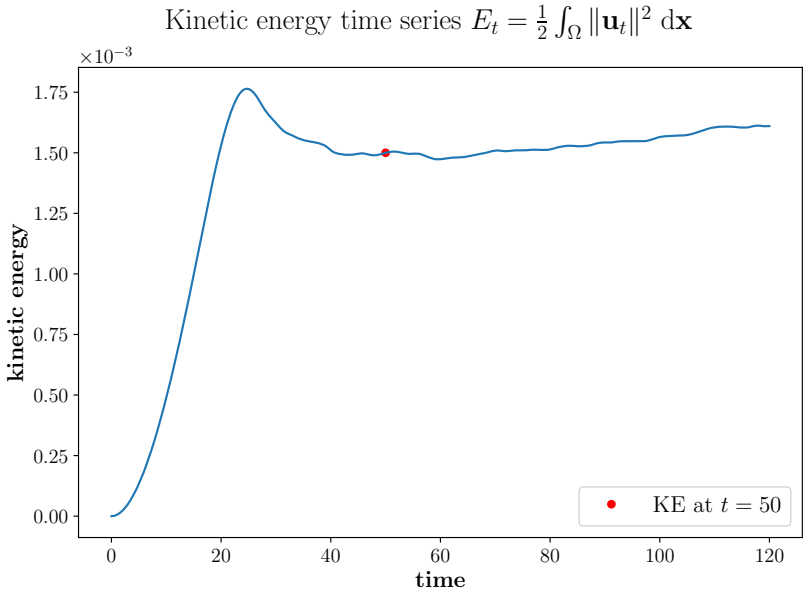

FIGURE 4.4: Evolution of kinetic energy of the deterministic model solution on 256×256 grid over time.

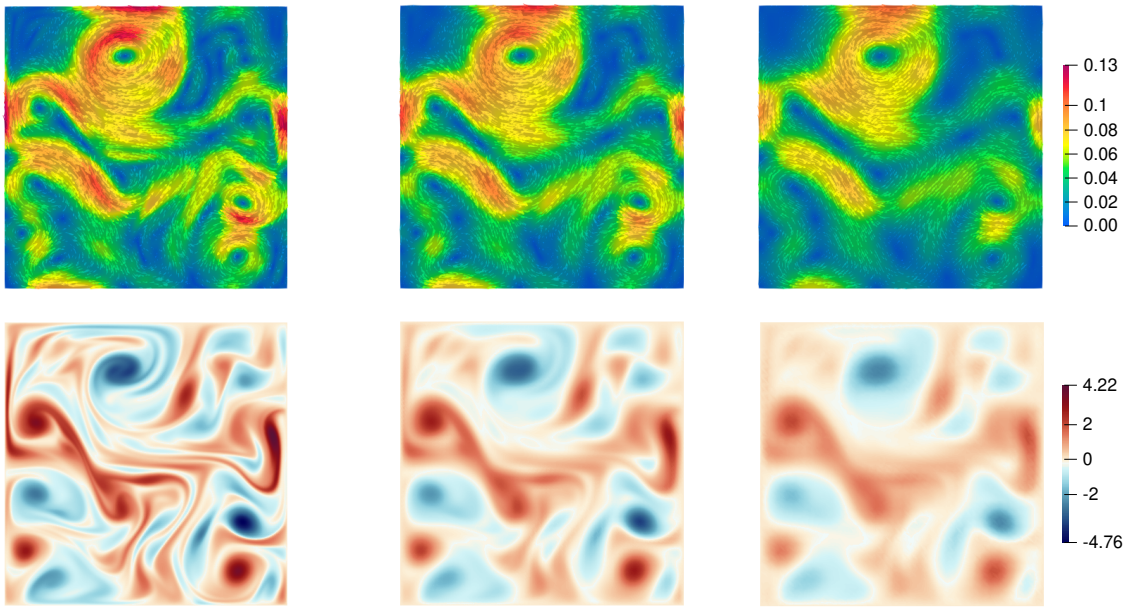

FIGURE 4.5: Coarse-grained velocity and vorticity fields for grids of size 64×64 (middle) and 32×32 (right). The coarse-grained fields are obtained by applying the Helmholtz operator to the fine-grid velocity field (left) at time $t = 50$. The first row shows the velocity fields; the second row shows the corresponding vorticity fields.

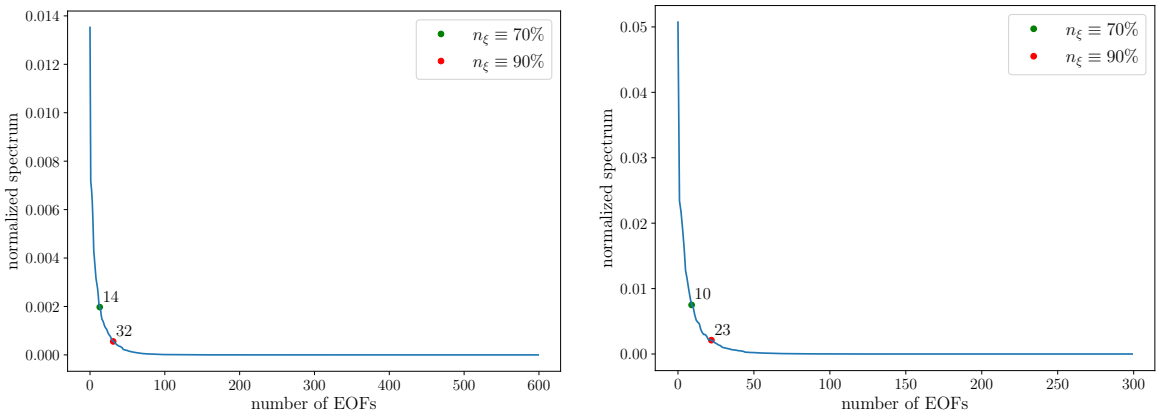

FIGURE 4.6: EOF normalized spectrum for coarse grids of size 64×64 (left) and 32×32 (right).

TABLE 4.2: Number of $\boldsymbol{\xi}_i$ (denoted by n_ξ) needed to explain different levels of variance in the data $\Delta \boldsymbol{X}$ for grids 64×64 and 32×32.

	90% variance	70% variance	50% variance
n_ξ, 64×64 grid	75	32	14
n_ξ, 32×32 grid	56	23	10

32×32, respectively. We observe from the figures that the first $\boldsymbol{\xi}_i$ exhibit large-scale flow patterns, whereas the later modes contain small-scale patterns. Similar observations were also made by Crisan et al. (2023b) in their study of the stochastic shallow water equations.

4.1.2 Stochastic model simulation

We use the $\boldsymbol{\xi}_i$ obtained after the calibration procedure to run the SPDE (4.1) on coarse grids of size 64×64 and 32×32. The initial condition for all the independent realizations of the SPDE is chosen to be the coarse-grained initial velocity at time $t = 50$. The SPDE is integrated for a time period of 20 units i.e., until $t = 70$.

For uncertainty quantification, we analyze the SPDE solution at 9 observation points inside the computational domain (Figure 4.9). Figure 4.10 shows the evolution of velocity (x and y components) at the observations points. This result is obtained from 30 independent realizations of the SPDE on the 64×64 grid. The noise term in the SPDE is modeled using first 32 EOFs ($n_\xi = 32$) capturing 90% of the total variance present in the calibration data.

Along with the SPDE solution, Figure 4.10 also shows the coarse-grained high-resolution solution (denoted as the truth). We can observe that the ensemble spread remains closer to the truth (on most of the observation points) for 5 to 6 time units before diverting. At a few observation points, however, the ensemble fails to capture the true solution from the start.

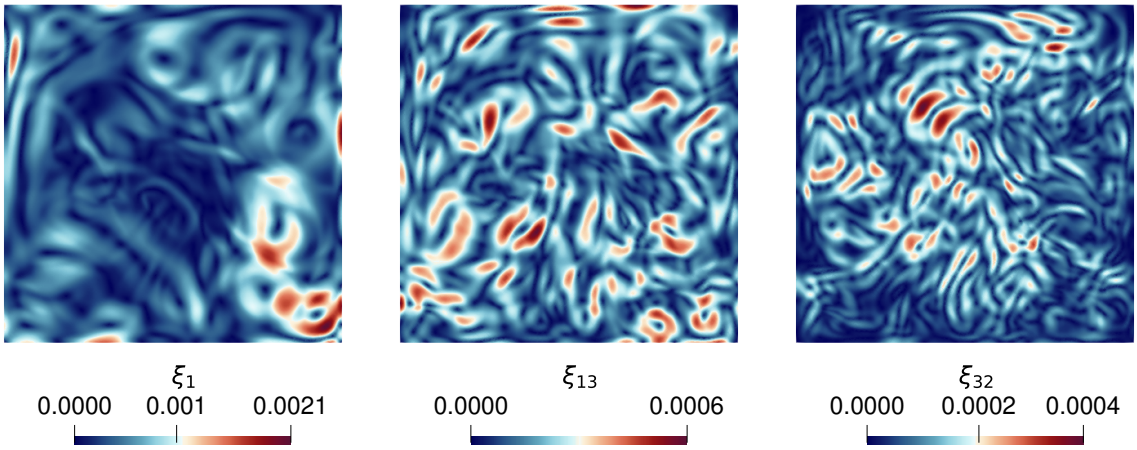

FIGURE 4.7: Estimated $\boldsymbol{\xi}_i$ for the coarse grid of size 64×64. The 1st, 14th, and 32nd $\boldsymbol{\xi}_i$ are shown. For 64×64 grid, the first 32 EOFs explain 90% of the variance in the data.

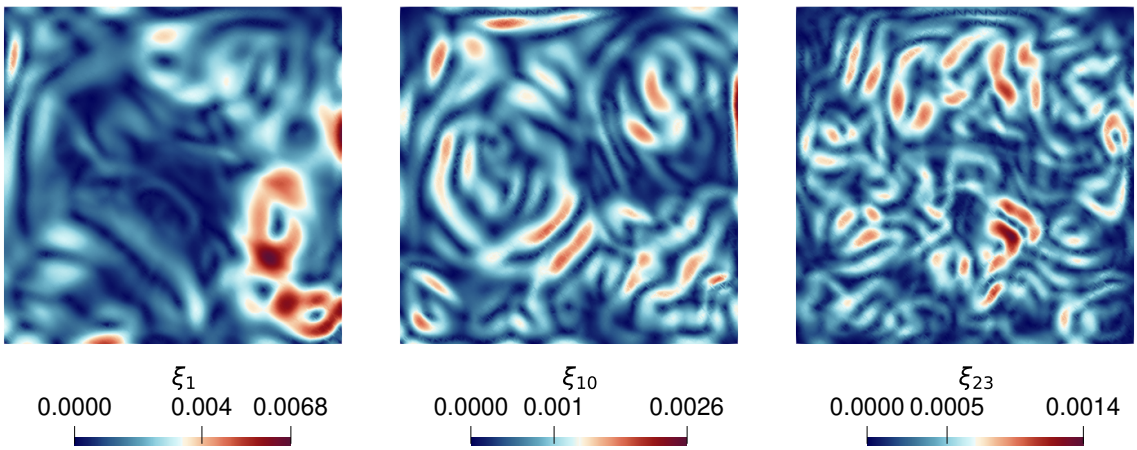

FIGURE 4.8: Estimated $\boldsymbol{\xi}_i$ for the coarse grid of size 32×32. The 1st, 10th, and 23rd $\boldsymbol{\xi}_i$ are shown. For 32×32 grid, the first 23 EOFs explain 90% of the variance in the data.

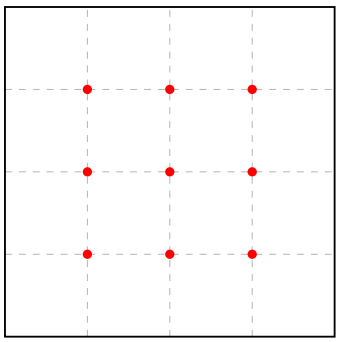

FIGURE 4.9: Observation points (red dots) within the domain where the SPDE solution is analyzed for uncertainty quantification.

SALT parameterization and hence the resulting stochastic terms in the model do not account for the discretization errors, it only models the unresolved transport dynamics. Therefore, it is better to compare the ensemble results with a reference solution which accounts for the discretization error. We follow Ephrati et al. (2023) to define such a reference solution.

Adapted reference solution

In the SALT approach, the information about the unresolved scales is supplied to the deterministic model as a stochastic forcing $\sum_i \boldsymbol{\xi}_i \Delta W_n^i$. This forcing term can be written as an approximation of a function $\mathbf{g}(\boldsymbol{x}, t)$ such that

$$\mathbf{g}(\boldsymbol{x}, t)\sqrt{\Delta t} = (\mathbf{u} - \overline{\mathbf{u}})\Delta t \approx \sum_i \boldsymbol{\xi}_i \Delta W_n^i.$$

In the calibration process, the function $\mathbf{g}(\boldsymbol{x}, t)$ is obtained from SVD decomposition of the Lagrangian trajectory data, where the stochastic process W_n^i is modeled by the Gaussian noise. The forcing $\mathbf{g}$ acts as a correction to $\overline{\mathbf{u}}$, which is a part of high-resolution velocity $\mathbf{u}$ that can be resolved on a coarse grid. The application of the SVD algorithm on $(\mathbf{u} - \overline{\mathbf{u}})\sqrt{\Delta t}$ measurement data yields

$$\mathbf{g}(\boldsymbol{x}, t) = \boldsymbol{\xi}_0 + \sum_i^N a_i(t)\boldsymbol{\xi}_i(\boldsymbol{x}), \tag{4.3}$$

where $\boldsymbol{\xi}_0(\boldsymbol{x})$ is the time-mean of the measurement data and $a_i(t)$ are the time series corresponding to each correlation vector $\boldsymbol{\xi}_i(\boldsymbol{x})$. The stochastic model is generally calibrated by utilizing only the rescaled EOF modes $\boldsymbol{\xi}_i$. The time-mean $\boldsymbol{\xi}_0(\boldsymbol{x})$ is neglected and the time series $a_i(t)$ is approximated as i.i.d. samples of a standard normal distribution.

Instead of approximating the correction term using stochastic forcing, we utilize the full information contained in $(\mathbf{u} - \overline{\mathbf{u}})\Delta t$ and apply it as deterministic forcing $\mathbf{g}$. The resulting solution from such deterministic forcing is denoted by adapted reference solution.

The adapted reference solution serves as a benchmark for comparing the results of stochastic model simulations on coarse grids. In fact, it is a better measure for evaluating the results from the stochastic model than the coarse-grained high-resolution fields since it contains the effect of discretization errors when the model is run on coarse grids. This effect is missing in the solution obtained from coarse-graining the high-resolution solution.

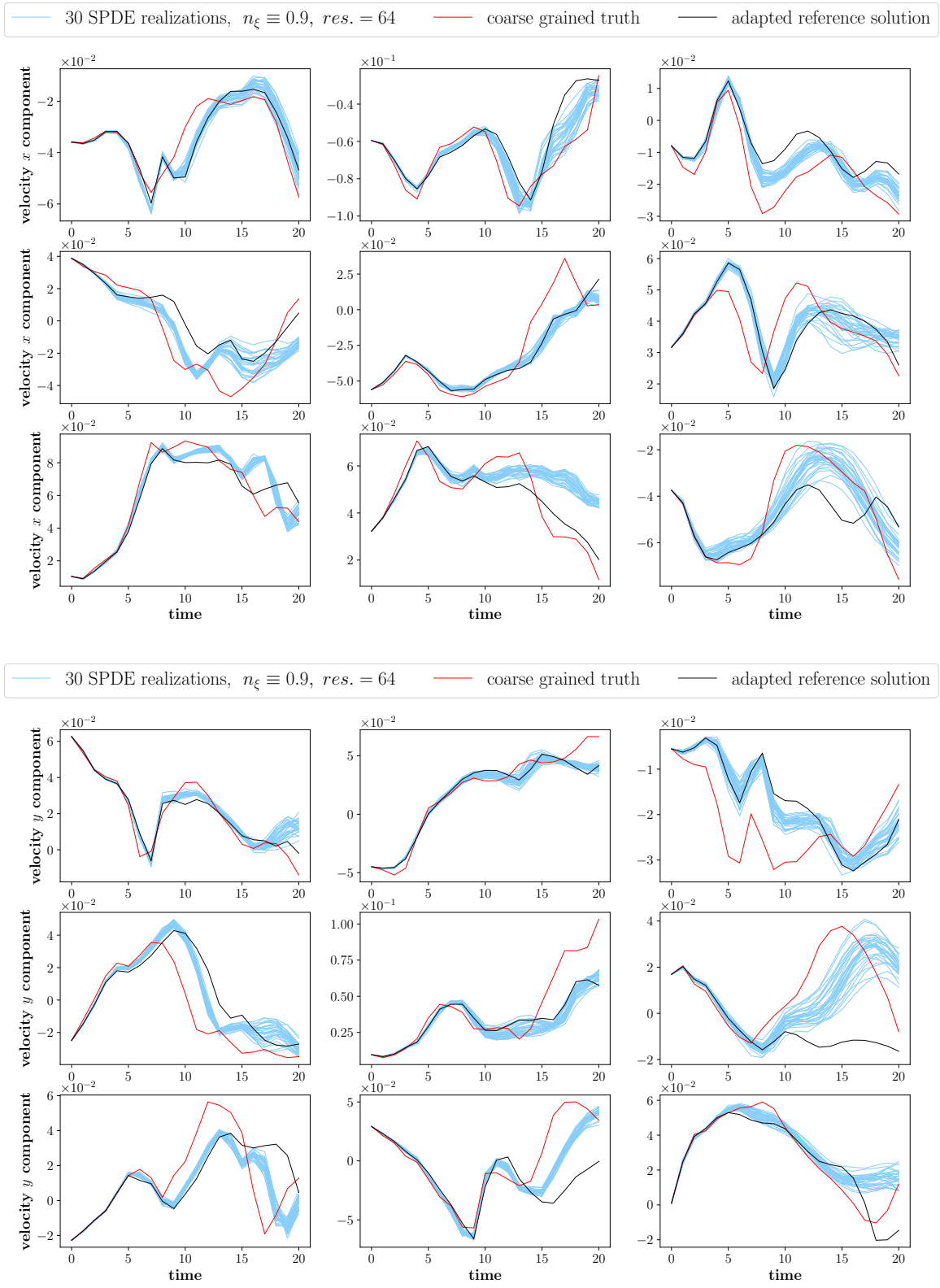

FIGURE 4.10: Evolution of the velocity components (x and y) over time at 9 observation points, illustrating the comparison between the ensemble spread, the truth, and the adapted reference solution.

We obtain the adapted reference solution by solving the following discrete in-time equations

$$\begin{aligned}
\mathbf{u}^{n+1} - \mathbf{u}^n = & \left(-\frac{(\mathbf{u}^{n+1} \cdot \nabla)\mathbf{u}^{n+1} + (\mathbf{u}^n \cdot \nabla)\mathbf{u}^n}{2} - \nabla p^{n+1} \right) \Delta t \\
& + \left(\frac{1}{2Re}(\Delta \mathbf{u}^{n+1} + \Delta \mathbf{u}^n) + \mathbf{f} \right) \Delta t \\
& - \left(\frac{(\mathbf{g}^{n+1} \cdot \nabla)\mathbf{u}^{n+1} + (\mathbf{g}^n \cdot \nabla)\mathbf{u}^n}{2} \right) \sqrt{\Delta t} \\
& - \left(\frac{u_1^{n+1} \nabla g_1^{n+1} + u_1^n \nabla g_1^n}{2} + \frac{u_2^{n+1} \nabla g_2^{n+1} + u_2^n \nabla g_2^n}{2} \right) \sqrt{\Delta t} \\
\nabla \cdot \mathbf{u}^{n+1} = & \, 0.
\end{aligned}$$

In our study, for the calculation of adapted reference solution, we always use the amount of $\boldsymbol{\xi}_i$ which explains 90% of the variance in the calibration data.

In Figure 4.10, we plot the adapted reference solution (x and y components of velocity) at observation points and compare it with the ensemble solution and the coarse-grained truth. We can observe that at all locations, the ensemble spread captures the adapted reference solution for longer time-periods in comparison to the coarse-grained solution. This observation is further substantiated by visible inspection of the velocity, pressure and vorticity fields at $t = 70$ (see Figures 4.11 and 4.12). The stochastic model realizations are not able to accurately capture the large-scale flow patterns of the coarse-grained solution after running for 20 time units (Figure 4.12). However, the SPDE results are remarkably closer to the adapted reference solution (Figure 4.11).

Uncertainty quantification

In this section, we show the uncertainty quantification test results. We denote the independent realizations of our SPDE by "particles" following the data-assimilation vocabulary. We first evaluate the effect of a using different number of particles N_p, different number of EOFs n_ξ, and different levels of mesh refinement on one standard deviation region about the mean of SPDE solutions (we call it the ensemble spread) at 9 observation points on the domain.

For 64×64 grid, with $n_\xi \equiv 0.9$ (i.e. the number of EOFs capturing 90% variance) fixed, we compare the differences due to changing the number of particles in the ensemble: $N_p = 30$ versus $N_p = 60$. The results are shown in Figure 4.13. Varying the number of EOFs shows no significant effect on the ensemble spread size within the observed time frame. We analyze the impact of using a different number of EOFs by fixing $N_p = 60$ and comparing the ensemble results for different number of EOFs: $n_\xi \equiv 0.9$ (32 EOFs capturing 90% variance) versus $n_\xi \equiv 0.7$ (14 EOFs capturing 70% variance). The results are shown in Figure 4.14. The use of different number of EOFs

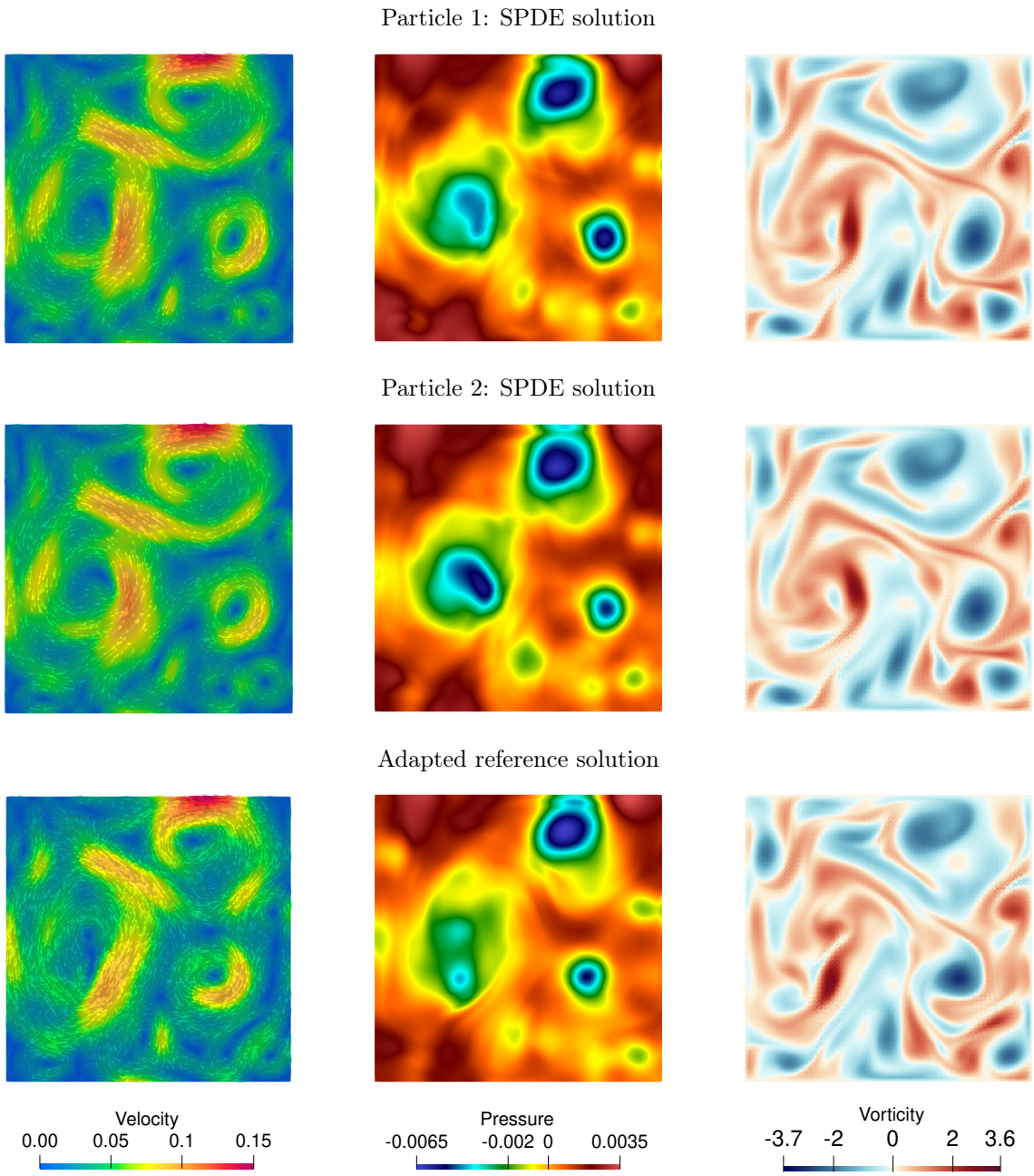

FIGURE 4.11: Velocity (left column), pressure (middle column), and vorticity (right column) fields corresponding to the adapted reference solution (bottom row) and two independent realizations of the SPDE (top two rows) on 64×64 grid at time $t = 70$.

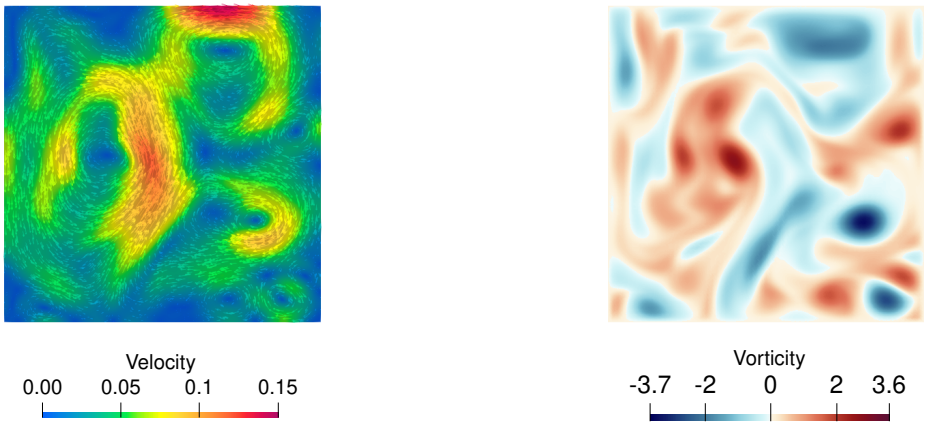

FIGURE 4.12: Coarse-grained velocity and vorticity fields for the grid of size 64×64 at time $t = 70$.

also does not seem to have an effect on the ensemble spread size. Ideally, the ensemble spread size should increase when the number of EOFs or the number of particles are increased. However, the differences shown in Figures 4.13 and 4.14 are negligible. Similar observations were made by Cotter et al. (2019) in their study of the stochastic 2D Euler equations.

In order to study the impact of mesh grid size on the ensemble spread, we fix the variance level and the number of ensemble particles ($n_\xi \equiv 0.9,\ N_p = 60$) and run the SPDE on a coarser grid of size 32×32. Figure 4.15 shows the results where the ensemble spread is compared for velocity fields at 9 observation points for two different mesh resolutions. It can be observed that the ensemble spread for the 64×64 grid is narrower than the ensemble spread for 32×32 grid. When we compare the SPDE solutions with the reference solutions, it is clear that the spread generated by 64×64 grid is more accurate than the spread of 32×32 grid. The spread for the 64×64 grid captures the reference solution for longer time intervals in comparison to the 32×32 grid. In this sense, the SALT parameterization is consistent under mesh refinement.

Figures 4.13–4.15 highlight the effect of using different number of particles, variance levels, and mesh refinement levels on the ensemble spread size only at certain observation points on the grid. In order to quantify the impact of these parameters on the whole domain, we investigate relative L^2 distance between the stochastic model realizations and the coarse-grained truth. The relative L^2 error for velocity is defined by

$$\frac{\|\mathbf{u}(t) - \mathbf{u}_{\text{truth}}(t)\|_{L^2(\Omega)}}{\|\mathbf{u}_{\text{truth}}\|_{L^2(\Omega)}}.$$

Figure 4.16 compares the ensemble mean relative L^2 error for different model configurations. The use of different number of $\boldsymbol{\xi}_i$ or the number of particles has negligible effect on the L^2 error. The effect of mesh refinement on the L^2 error is, however, quite visible. The L^2 error grows much more rapidly for the 32×32 grid than for the 64×64 grid.

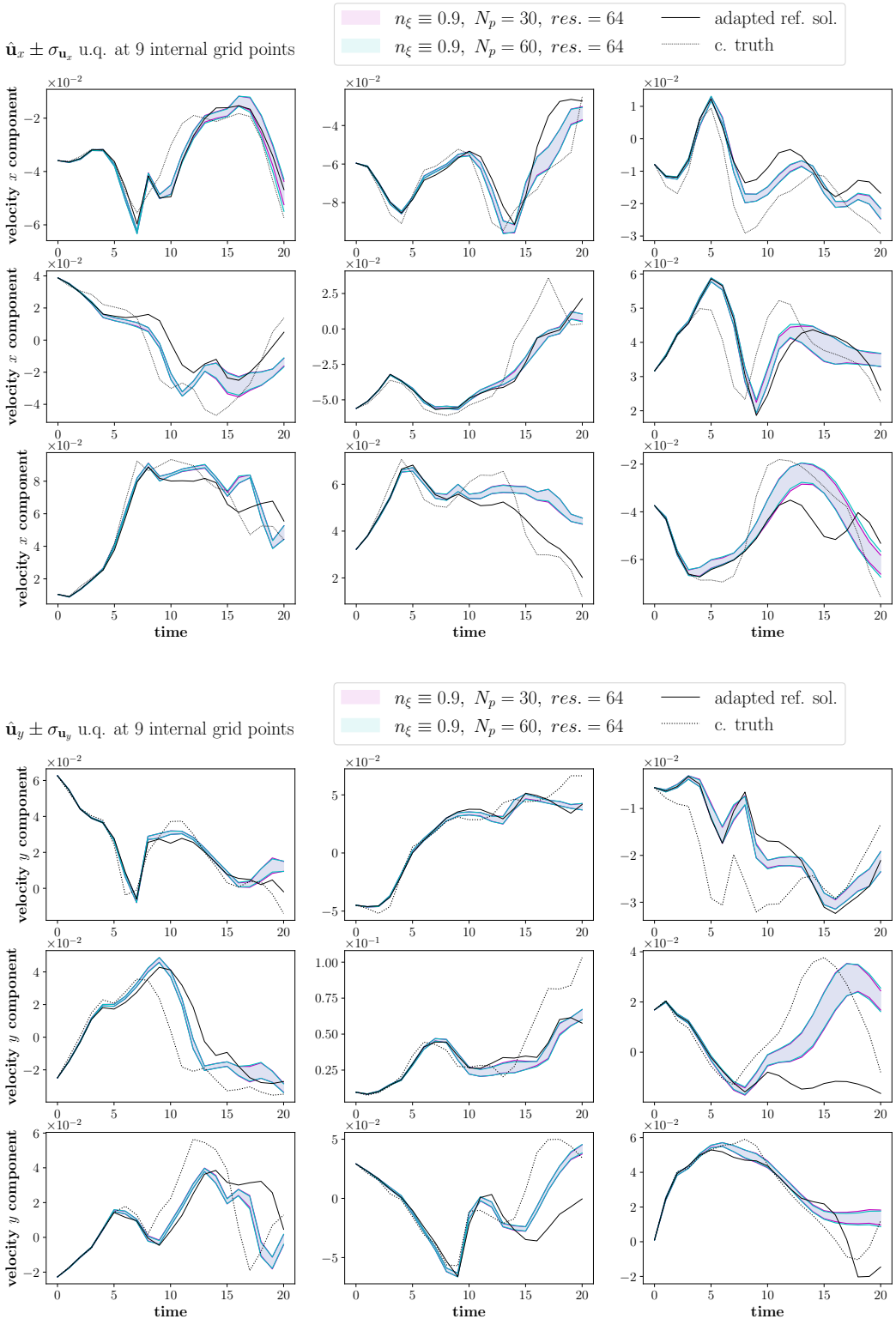

FIGURE 4.13: Uncertainty quantification results comparing the effect of using different number of particles (in the SPDE ensemble) on the ensemble spread for velocity field at 9 observation points.

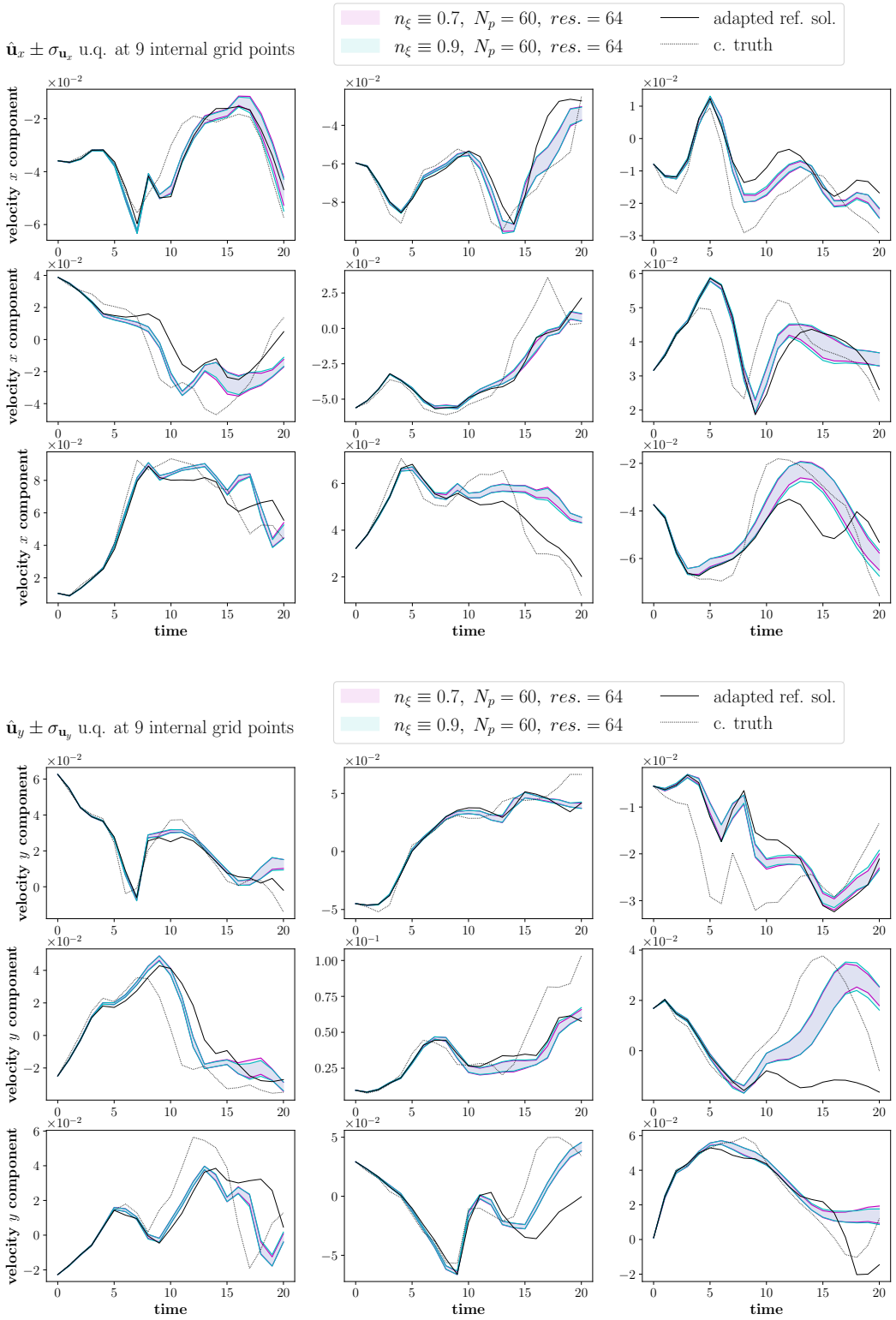

FIGURE 4.14: Uncertainty quantification results comparing the effect of using different number of EOFs (in the SPDE) on the ensemble spread for velocity field at 9 observation points.

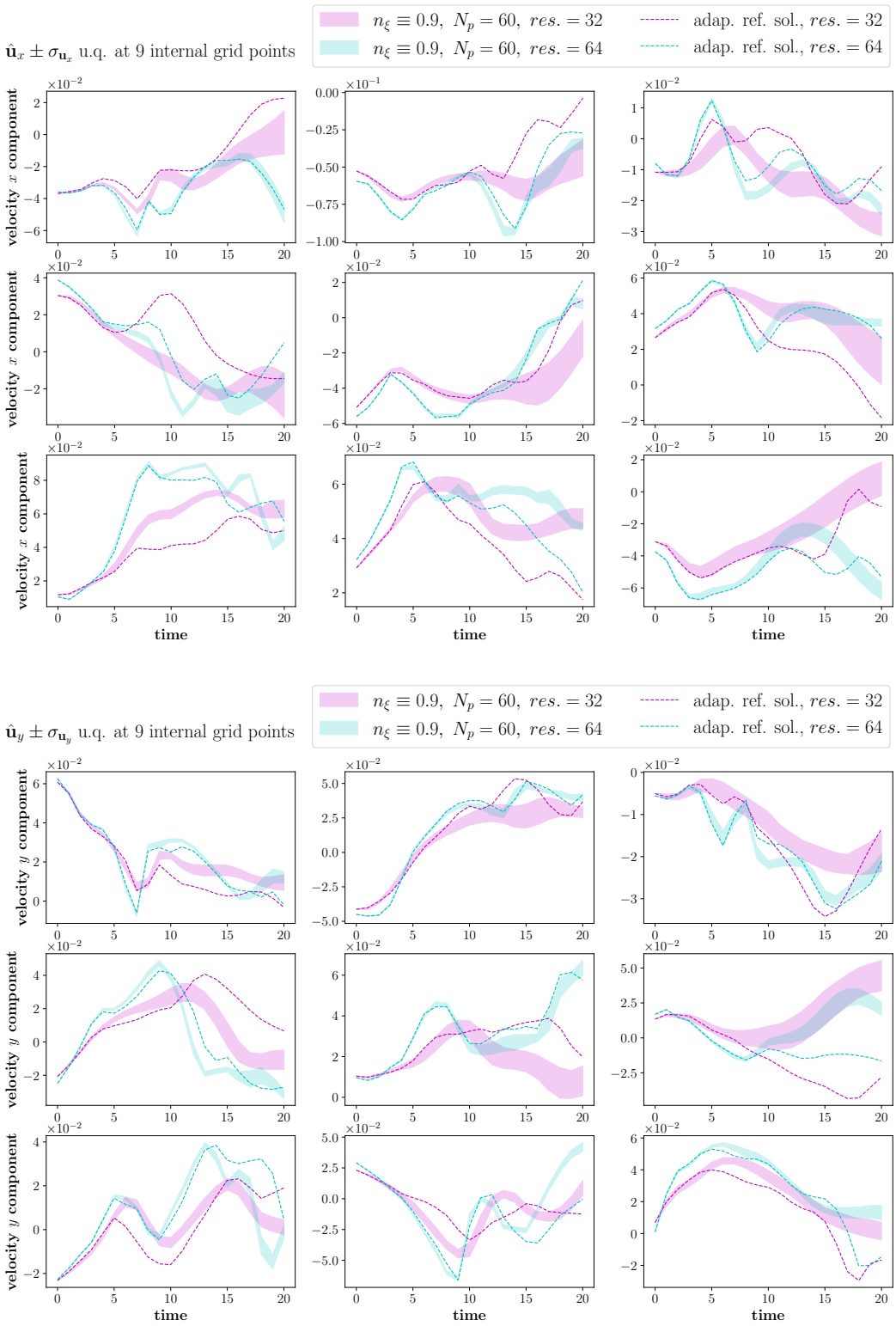

FIGURE 4.15: Uncertainty quantification results comparing the effect of using different mesh resolutions on the ensemble spread for velocity field at 9 observation points.

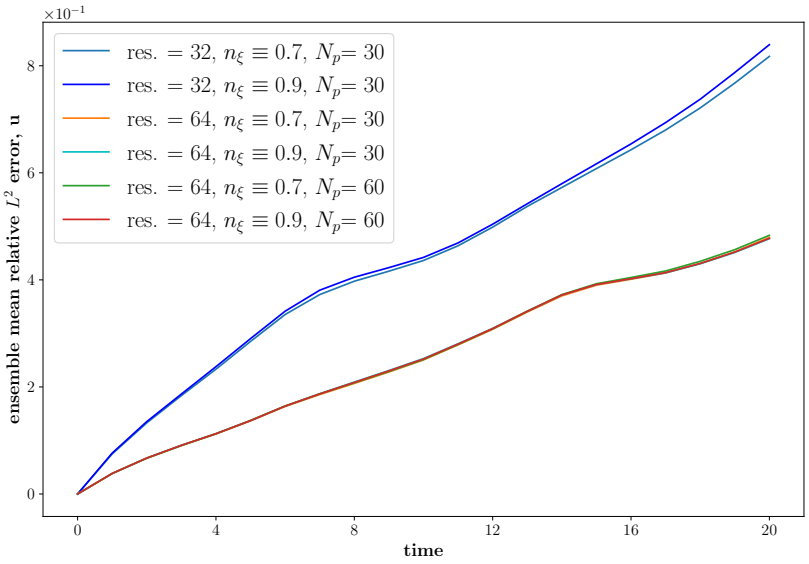

FIGURE 4.16: Relative L^2 distance between the SPDE ensemble and the truth for velocity, averaged over all ensemble members. Results are shown for different model configurations.

Figure 4.17 shows the L^2 error of the stochastic model ($n_\xi \equiv 0.9,\ N_p = 60$) solution along with the L^2 error of the deterministic model solution for different mesh resolutions. Instead of plotting the mean L^2 error, this time we plot one standard deviation regions around the ensemble mean. We find that the L^2 error of the stochastic model solution (on both coarse grids) is similar to the deterministic model solution. This suggests that parameterizing the deterministic models offers no apparent advantage in this case. However, the main advantage of the stochastic model is its ability to generate an ensemble of solutions whose spread size is proportional to the solution bias. This ability helps in quantifying the uncertainty in the model solution. The bias in the stochastic model solution, which indicates how far the ensemble mean is from the true solution, can be corrected using data assimilation techniques like particle filters. In Figure 4.17, the increase in spread size over time indicates decreased confidence of the stochastic model solution. This is reflected in the values of L^2 errors which gradually increase over time. Moreover, the ensemble spread size for 64×64 grid is consistently smaller than the spread size for 32×32 grid indicating an increase in confidence of the SPDE solution as the mesh gets more refined.

4.1.3 Discussion and outlook

SALT parameterized Navier-Stokes model exhibits certain desirable features. We have seen that the stochastic parameterization is consistent under mesh refinement. The stochastic model solution on the 64×64 grid has both a smaller ensemble spread size and a smaller relative L^2 error in comparison to the grid of size 32×32 (see Figure 4.16). In addition to this, the ensemble generated by the stochastic model is able to capture the reference solution for a few time units (see Figure 4.15). However, certain expected

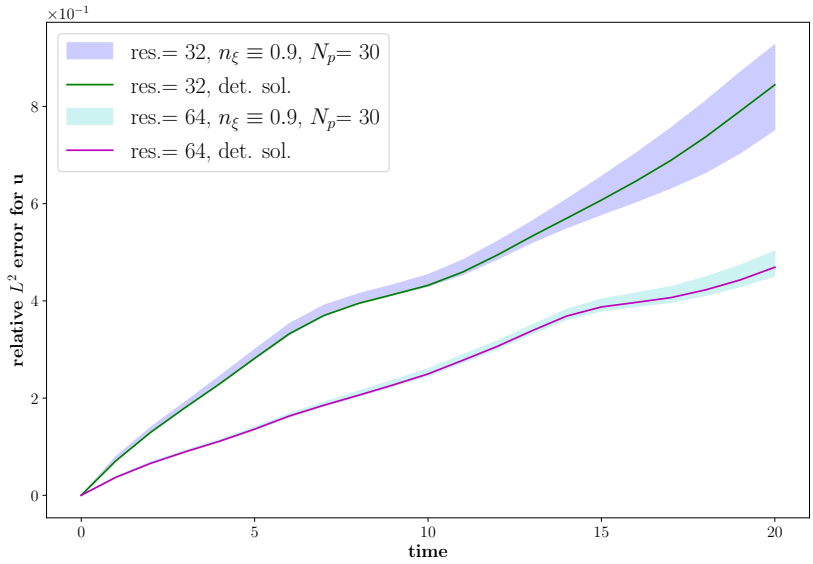

FIGURE 4.17: Relative L^2 errors of the stochastic and deterministic model solutions. The colored bands represent one standard deviation regions around the ensemble mean of L^2 errors of stochastic model solutions.

properties of a SALT parameterized model are not exhibited by our model. First, we did not observe growth in the ensemble spread size with an increase in either the number of particles or the number of EOFs/$\boldsymbol{\xi}_i$. Second, the accuracy of the stochastic model is not better than the deterministic model (without parameterization)in terms of the relative L^2 errors (Figure 4.17). We suspect these shortcomings might be linked to an improper modeling of the noise term $\sum_i \boldsymbol{\xi}_i \circ \mathrm{d}W^i$.

The noise term $\sum_i \boldsymbol{\xi}_i \circ \mathrm{d}W^i$ is approximated using the results from SVD decomposition of the Lagrangian trajectory data $(\mathbf{u} - \overline{\mathbf{u}})\Delta t$. The SVD decomposition results in two matrices; one matrix contains the EOFs and the other matrix contains the time series data corresponding to each EOF. The EOFs are used directly as $\boldsymbol{\xi}_i$ for numerical simulations while the time series data are approximated using standard normal distributions. We analyzed the time series data and found that, the time series corresponding only to the last few EOFs or $\boldsymbol{\xi}_i$ exhibit Gaussian-like distribution. The elements in the time series corresponding to the first few EOFs—which explain the majority of variance in observation data and hence contribute the most to the noise term $\sum_i \boldsymbol{\xi}_i \circ \mathrm{d}W^i$)—are highly correlated. Figure 4.18 displays the plots of time series data for the grid of size 64×64. It can be observed that the time series corresponding to $\boldsymbol{\xi}_{73}$, $\boldsymbol{\xi}_{74}$, and $\boldsymbol{\xi}_{75}$ (denoted by a_{73}, a_{74}, and a_{75} respectively) closely match an independent realization of the standard normal distribution. On the other hand, the time series a_1, a_2, and a_3 do not resemble a random or Gaussian process. In order to make a more quantitative comparison, we plot the autocorrelation function (ACF) for time series data and compare it to the ACF of a normally distributed Gaussian process.

The autocorrelation function gives a measure of similarity between a time series and its delayed copy over successive time periods or lag times (Park, 2018). Mathematically,

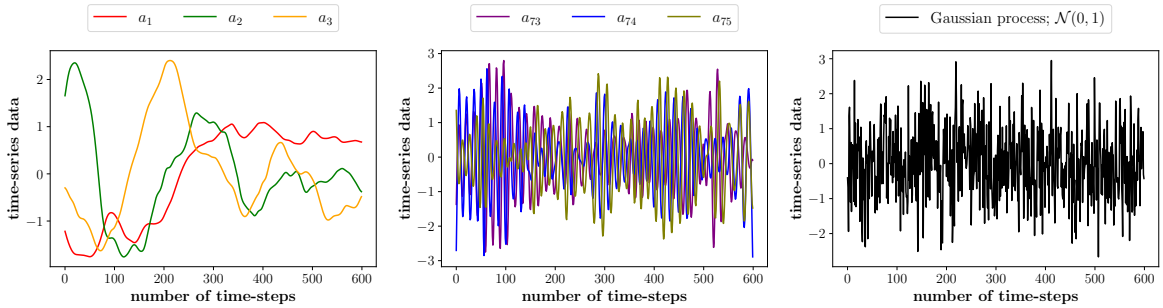

FIGURE 4.18: Time series plots corresponding to $\boldsymbol{\xi}_1$, $\boldsymbol{\xi}_2$, $\boldsymbol{\xi}_3$ (left) and $\boldsymbol{\xi}_{73}$, $\boldsymbol{\xi}_{74}$, $\boldsymbol{\xi}_{75}$ (middle) for a coarse grid of size 64×64. For comparison, the time series generated by a Gaussian process is shown (right).

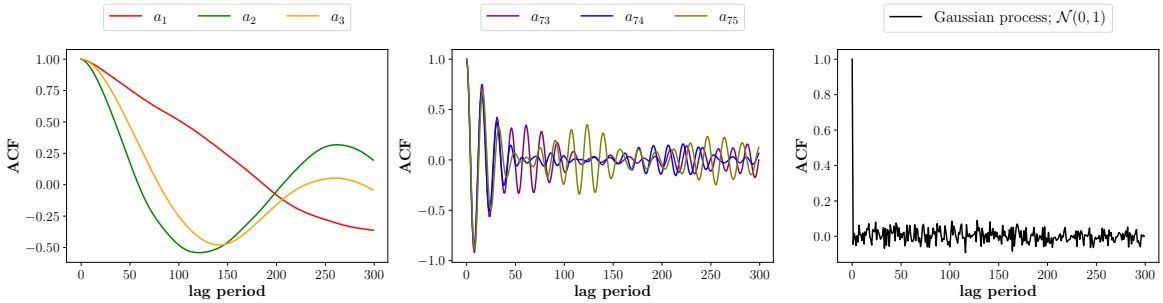

FIGURE 4.19: Autocorrelation function (ACF) plots for the time series data corresponding to $\boldsymbol{\xi}_1$, $\boldsymbol{\xi}_2$, $\boldsymbol{\xi}_3$ (left) and $\boldsymbol{\xi}_{73}$, $\boldsymbol{\xi}_{74}$, $\boldsymbol{\xi}_{75}$ (middle) for coarse grid of size 64×64. For comparison, the ACF plot for time series generated by a Gaussian process is shown (right).

ACF is denoted by ρ_k, where k represents the lag time or the number of time-steps between the observations. For a time series dataset (say X_n where n denotes a time instance), the ACF at lag k is given by (Toboga, 2021)

$$\rho_k = \frac{\frac{1}{N-k}\sum_{n=1}^{N-k}(X_n - \mu)(X_{n+k} - \mu)}{\frac{1}{N}\sum_{n=1}^{N}(X_n - \mu)^2},$$

where N denotes the number of data points in the time series, and μ is the sample mean.

Figure 4.19 shows the ACF plots for the time series data at different lag times. The independence or decorrelation between the realizations of a Gaussian process is indicated by a sudden drop of ACF value from 1 to 0 for lag times of one or more time-steps. This trend is closely followed by the time series a_{73}, a_{74} and a_{75}. The ACF values corresponding to the time series of first three EOFs, on the other hand, takes at least 50 times steps to get closer to zero, thus suggesting very strong correlation between the data points. We believe that a better approximation of the time series data can improve the accuracy of stochastic model solution.

4.2 Stochastic atmosphere model

This section investigates the effectiveness of SALT parameterization in modeling the effect of unresolved/small scales on the resolved/large-scale flow dynamics. The stochastic parameterization results in an ensemble of solutions, and hence it can also be used to quantify the uncertainty generated by solving the model on coarse grids. We present a numerical investigation of the idealized stochastic atmosphere model introduced in the previous chapter. When coupled with an ocean component, this model yields a coupled ocean-atmosphere system suitable for studying some fundamental processes that occur due to the interaction between the ocean and the atmosphere.

The governing equations for the atmosphere model are

$$\begin{aligned} &\mathrm{d}\mathbf{u} + \left(\mathbf{u}\mathrm{d}t + \sum_i \boldsymbol{\xi}_i \circ \mathrm{d}W^i\right)\cdot\nabla\mathbf{u} + \frac{1}{Ro}\hat{\mathbf{z}}\times\mathbf{u}\ \mathrm{d}t + \sum_i\left(\sum_{j=1}^{2} u_j\nabla\xi_{i,j}\right)\circ\mathrm{d}W^i \\ &\quad = \left(-\frac{1}{C}\nabla\theta + \nu_e\Delta\mathbf{u}\right)\mathrm{d}t, \\ &\mathrm{d}\theta + \nabla\cdot(\theta\mathbf{u})\ \mathrm{d}t + \sum_i(\boldsymbol{\xi}_i\circ\mathrm{d}W^i)\cdot\nabla\theta = \eta_e\Delta\theta\ \mathrm{d}t. \end{aligned} \tag{4.4}$$

These equations represent a stochastic extension of the deterministic two-dimensional model

$$\begin{aligned} &\frac{\partial\mathbf{u}}{\partial t} + (\mathbf{u}\cdot\nabla)\mathbf{u} + \frac{\hat{\mathbf{z}}\times\mathbf{u}}{Ro} + \frac{\nabla\theta}{C} = \nu_e\Delta\mathbf{u}, \\ &\frac{\partial\theta}{\partial t} + \nabla\cdot(\theta\mathbf{u}) = \eta_e\Delta\theta. \end{aligned} \tag{4.5}$$

We solve models (4.4) and (4.5) on a 2D domain with periodic boundary conditions applied in the zonal (East-West) direction (see Figure 4.20 and Figure 4.21). This configuration approximates mid-latitude atmospheric flow between 27.5° and 62.5° north latitude. Along the meridional (North–South) boundaries, we impose free-slip conditions on velocity:

$$u_2 = 0, \quad \frac{\partial u_1}{\partial y} = 0,$$

and insulated boundary conditions for temperature:

$$\frac{\partial\theta}{\partial y} = 0.$$

Three different mesh configurations are considered for the numerical experiments (see Table 4.3). The idea is to run the deterministic model on the fine grid with size 1792×256 and use the high-resolution velocity data to calibrate the stochastic model which can later be run on coarser grids.

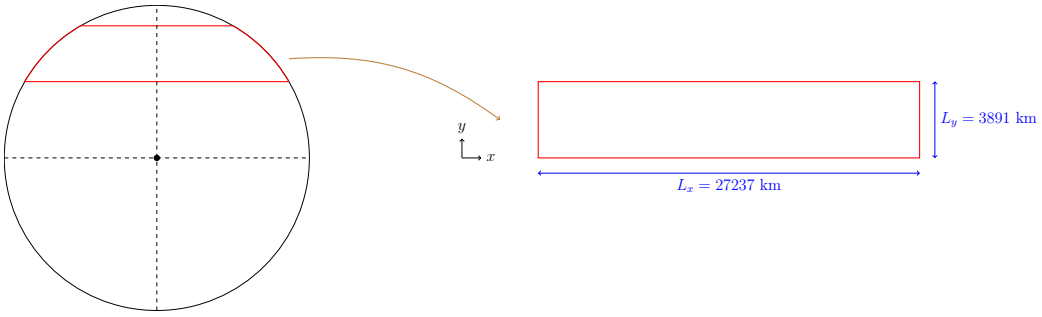

FIGURE 4.20: Schematic representation of the 2D domain (right) on which the atmosphere model is simulated.

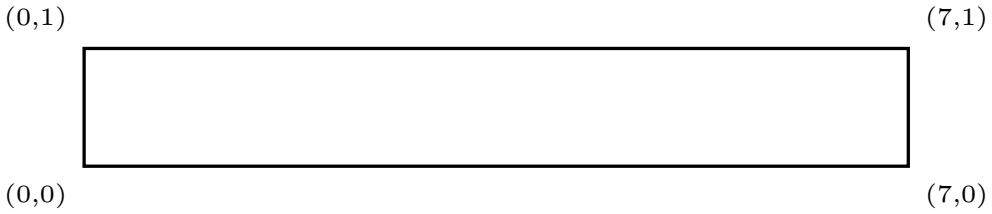

FIGURE 4.21: Computational domain (after non-dimensionalization) for the atmosphere model simulation.

TABLE 4.3: Values of grid parameters for different configurations of the atmosphere model.

Parameter	**Fine grid**	**Coarse grid 1**	**Coarse grid 2**
Number of elements, $N_x \times N_y$	1792×256	448×64	224×32
Smallest element size, Δx	$1/256$ (~ 15 km)	$1/64$ (~ 60 km)	$1/32$ (~ 120 km)
Time-step size, Δt	0.005 (~ 4 min.)	0.02 (~ 16 min.)	0.04 (~ 32 min.)
Eddy viscosity, ν_e	$1/(3 \times 10^5)$	$1/(3 \times 10^4)$	$1/10^4$
Diffusion coefficient, η_e	$1/(3 \times 10^5)$	$1/(3 \times 10^4)$	$1/10^4$
Rossby number, Ro	0.3	0.3	0.3
C	0.02	0.02	0.02

4.2.1 Fine grid simulation

The initial conditions for the deterministic model (2.12) are designed to resemble the Galewsky test-case (Galewsky et al., 2004). The initial zonal velocity profile is given by

$$u_1(x,y) = \begin{cases} 0 & \text{for } y \leq y_0, \\ \exp\left(\dfrac{\alpha^2}{(y-y_0)(y-y_1)}\right)\exp\left(\dfrac{4\alpha^2}{(y_1-y_0)^2}\right) & \text{for } y_0 < y < y_1, \\ 0 & \text{for } y \geq y_1, \end{cases}$$

where $\alpha = 1.64$, $y_0 = 1/14$, and $y_1 = 13/14$. The corresponding temperature field consists of a balanced state plus a perturbation:

$$\theta = 1 + \theta_b + \hat{\theta}\cos(\pi y/2)e^{-c_1(x-x_0)^2}e^{-c_2(y-y_2)^2},$$

where $\hat{\theta} = 0.01$, $c_1 = 4$, $c_2 = 81$, $x_0 = 3.5$, and $y_2 = 0.5$. The balanced temperature θ_b satisfies

$$\frac{\partial \theta_b}{\partial y} = -\frac{C}{Ro}u_1, \quad \frac{\partial \theta_b}{\partial x} = 0.$$

The model is integrated for 54 time units (approximately 30 days). Figures 4.22–4.28 illustrate the evolution of temperature, velocity, and vorticity fields. An initial temperature perturbation triggers the development of turbulence, which gradually decays. After approximately 27 time units, the flow stabilizes. This is also evident from the kinetic energy plot (Figure 4.29) which reveals that the rate of kinetic energy loss reduces over time. We consider the flow from $t = 27$ to $t = 45$ for further analysis. The vorticity plots show that the flow contains a mix of small, medium and large-scale vortices from $t = 27$ to $t = 45$. We use the velocity data obtained from this time-period for stochastic model calibration.

Stochastic model calibration

We use the difference between the Lagrangian trajectories generated by the high-resolution (1792×256 grid) velocity field $\mathbf{u}$ and its coarse-grained/filtered version $\overline{\mathbf{u}}$ at different time-instances to estimate $\boldsymbol{\xi}_i$. The SALT parameterization is based on the assumption that

$$(\mathbf{u} - \overline{\mathbf{u}})\Delta t \approx \sum_i \boldsymbol{\xi}_i \Delta W_n^i,$$

where ΔW^i are samples from a Gaussian distribution with zero mean and a standard deviation of $\sqrt{\Delta t}$. The coarse grid time-step size is denoted by Δt. The difference in the Lagrangian trajectories, $(\mathbf{u} - \overline{\mathbf{u}})\Delta t$, is evaluated at the coarse grid nodes. The procedure for obtaining the coarse-grained velocity consists of two steps. In the first

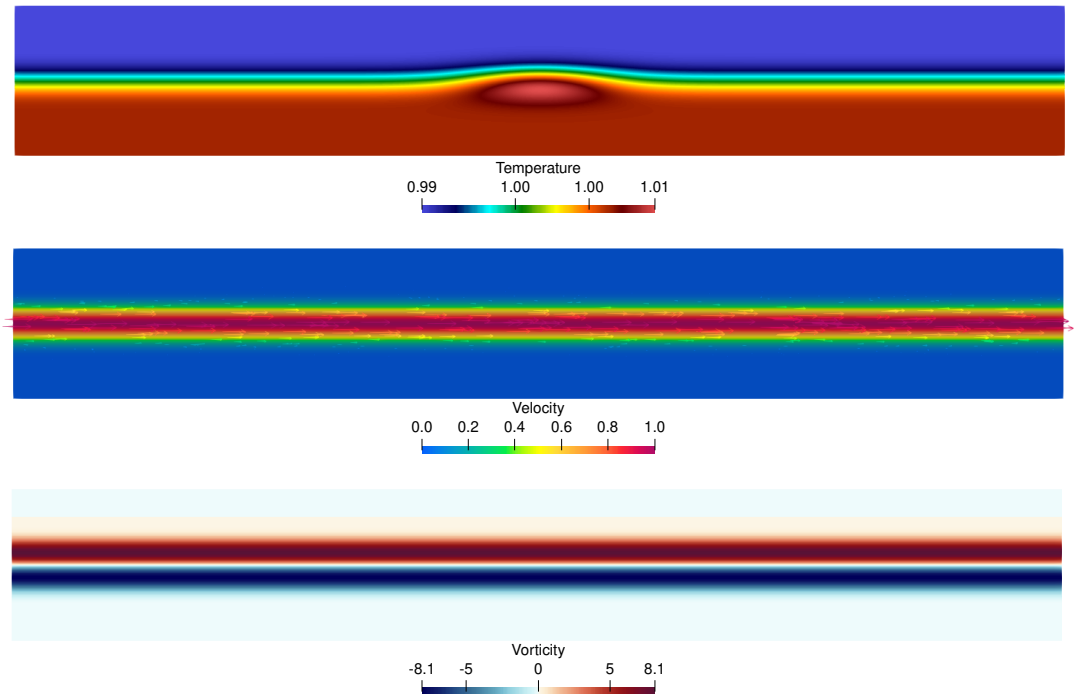

FIGURE 4.22: Temperature (top), velocity (middle), and vorticity (bottom) fields at $t = 0$ from the deterministic model simulation on a 1792×256 grid.

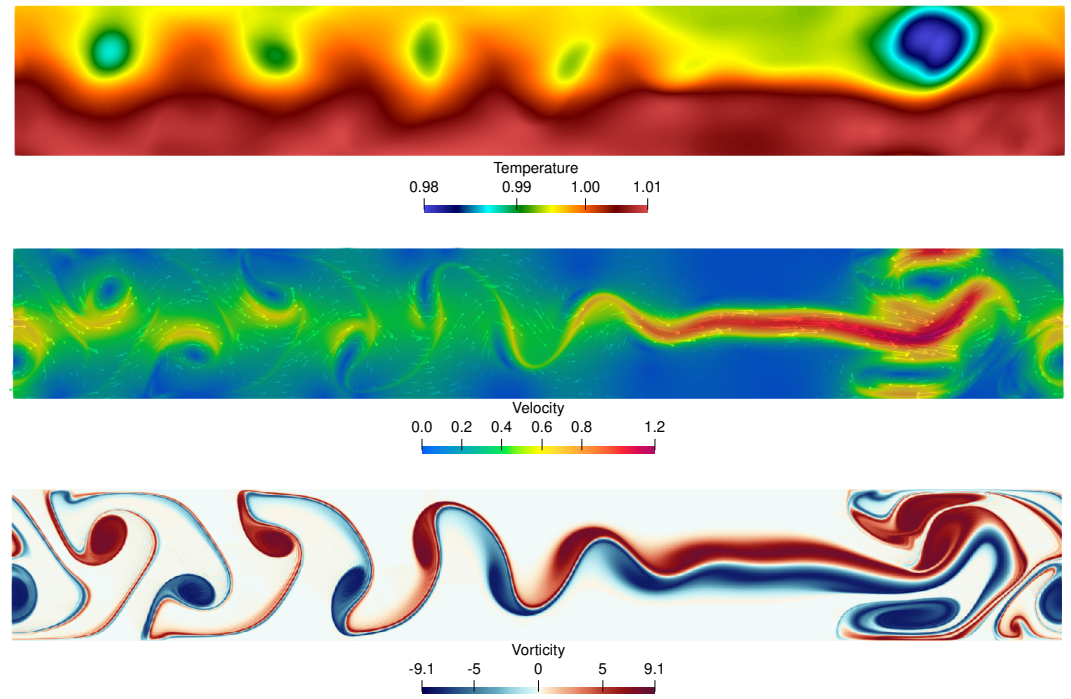

FIGURE 4.23: Temperature (top), velocity (middle), and vorticity (bottom) fields at $t = 9$ ($\sim$ 5 days) from the deterministic model simulation on a 1792×256 grid.

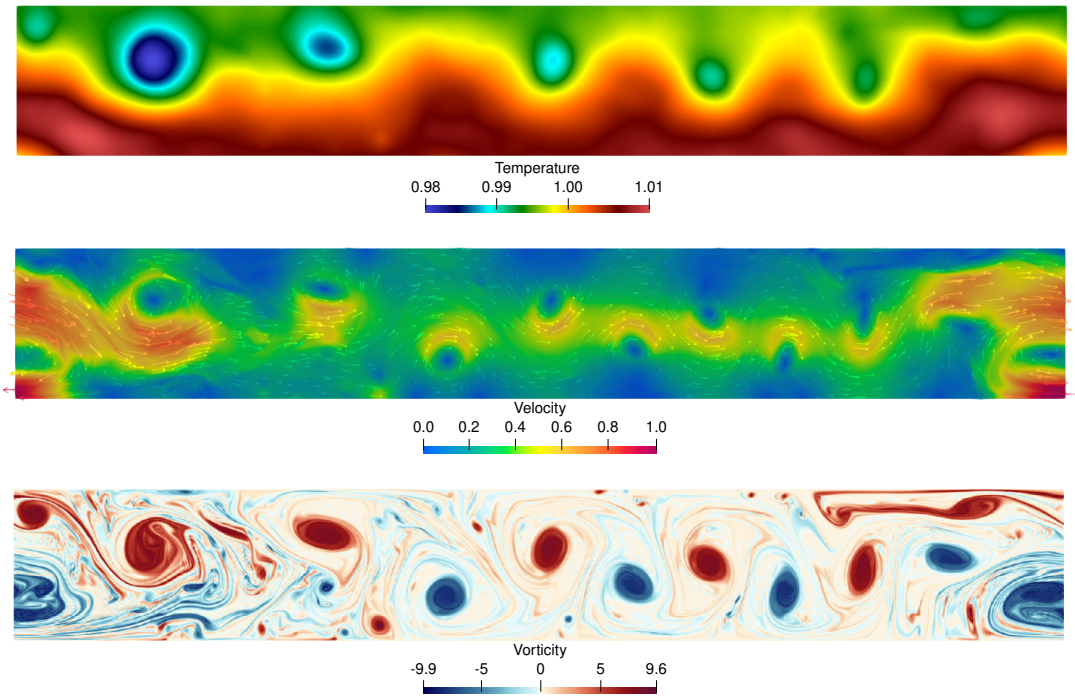

FIGURE 4.24: Temperature (top), velocity (middle), and vorticity (bottom) fields at $t = 18$ (~ 10 days) from the deterministic model simulation on a 1792×256 grid.

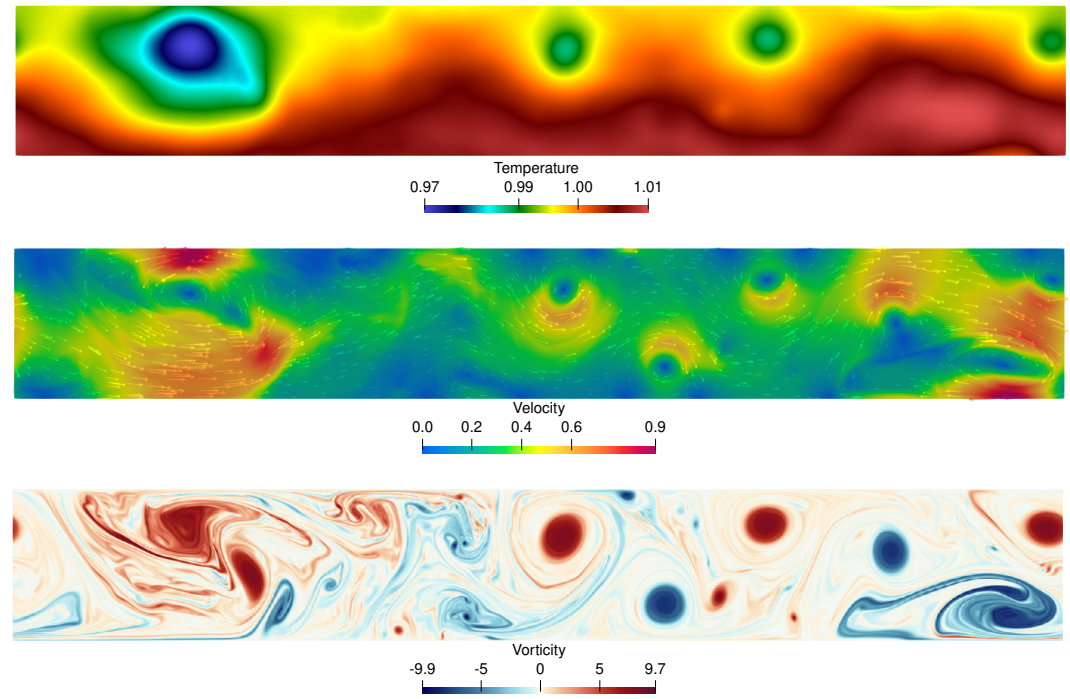

FIGURE 4.25: Temperature (top), velocity (middle), and vorticity (bottom) fields at $t = 27$ (~ 15 days) from the deterministic model simulation on a 1792×256 grid.

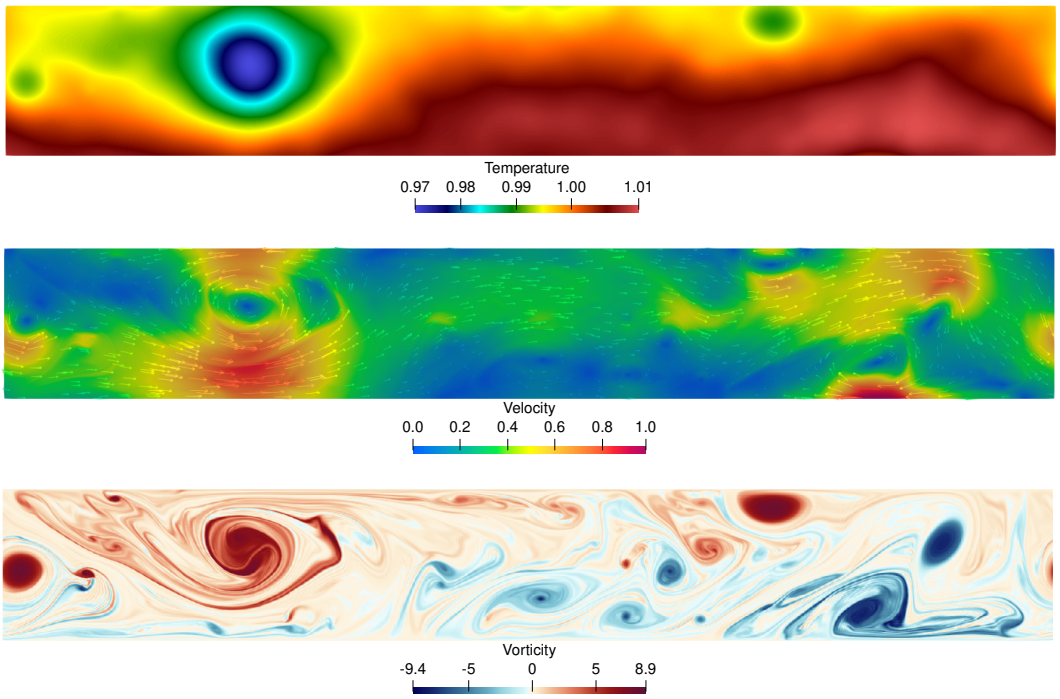

FIGURE 4.26: Temperature (top), velocity (middle), and vorticity (bottom) fields at $t = 36$ (~ 20 days) from the deterministic model simulation on a 1792×256 grid.

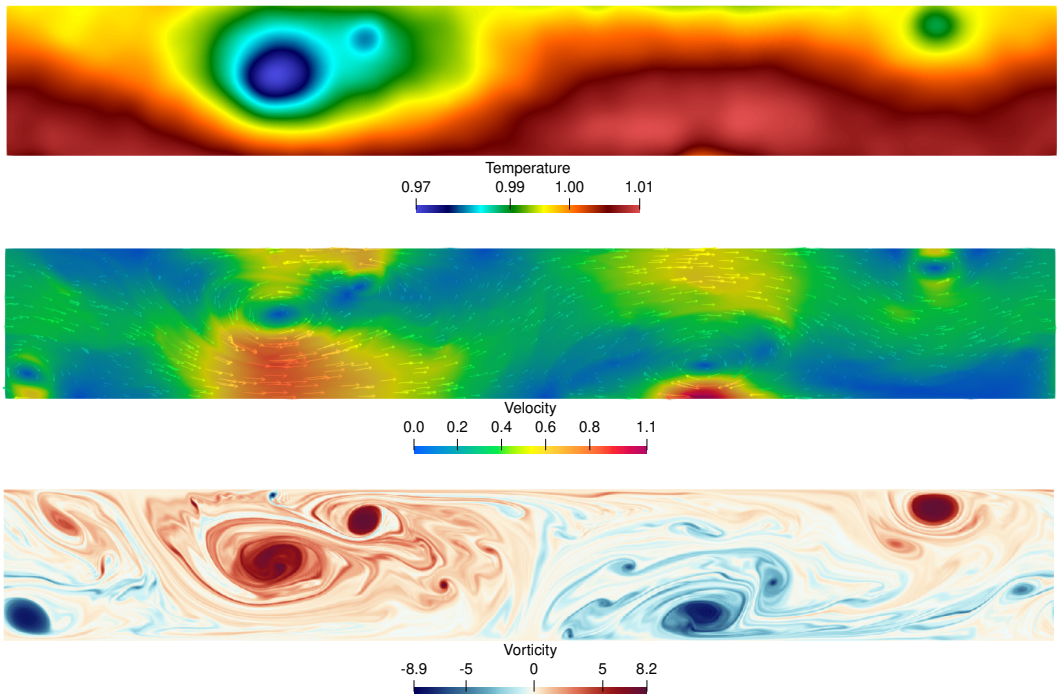

FIGURE 4.27: Temperature (top), velocity (middle), and vorticity (bottom) fields at $t = 45$ (~ 25 days) from the deterministic model simulation on a 1792×256 grid.

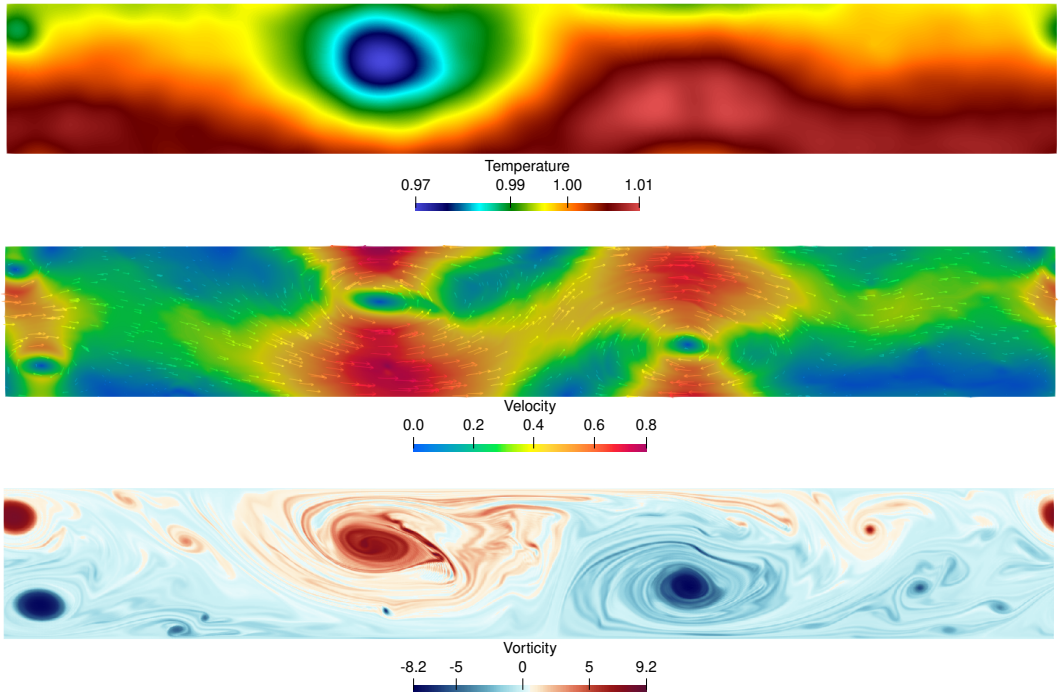

FIGURE 4.28: Temperature (top), velocity (middle), and vorticity (bottom) fields at $t = 54$ (~ 30 days) from the deterministic model simulation on a 1792×256 grid.

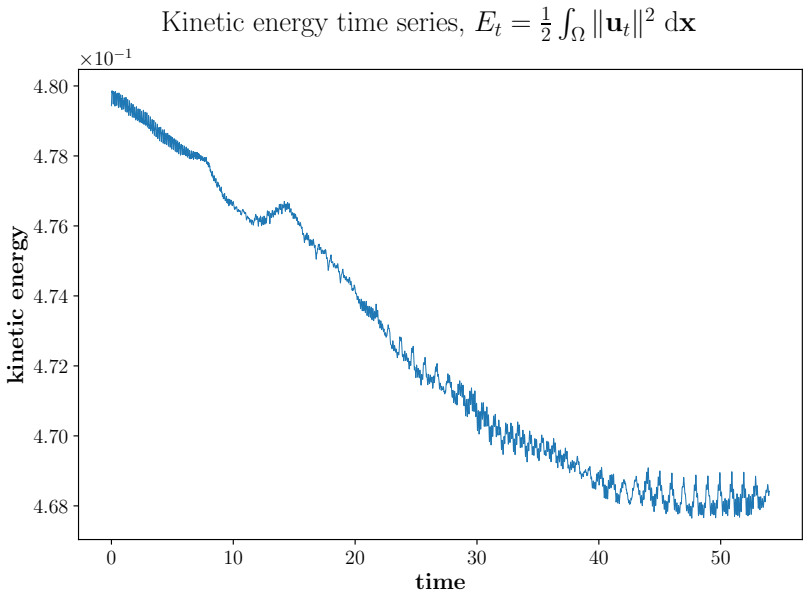

FIGURE 4.29: Time series plot of kinetic energy from the deterministic atmosphere model simulation on a grid of size 1792×256 for 54 time units (~ 30 days).

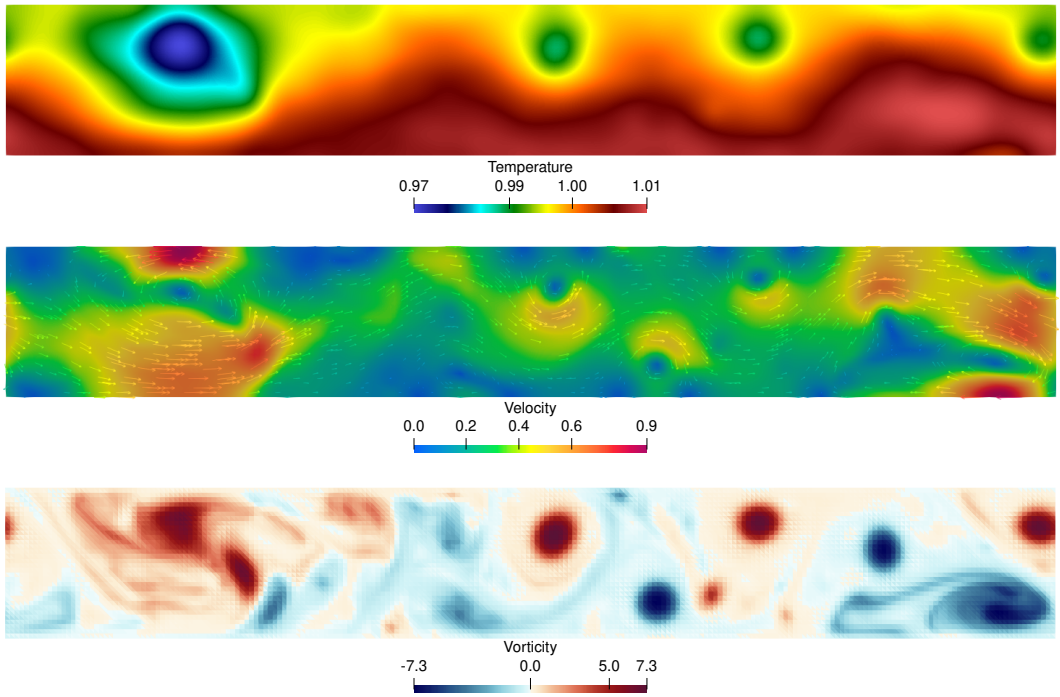

FIGURE 4.30: Coarse-grained temperature (top), velocity (middle), and vorticity (bottom) fields at time $t = 27$ for the coarse grid of size 224×32.

step, we solve (on a fine grid of size 1792×256)

$$\mathbf{u}_{\text{avg}} - c^2 \Delta \mathbf{u}_{\text{avg}} = \mathbf{u},$$

with periodic boundary conditions on the East and West boundaries and free-slip boundary conditions on the North and South boundaries to calculate the spatially averaged velocity $\mathbf{u}_{\text{avg}}$. The coarse-grained velocity is obtained in the second step by projecting the spatially averaged velocity on a coarse grid. The value of parameter c is governed by the smallest element size of the coarse grid ($c = 1/32$ for 224×32 grid and $c = 1/64$ for 448×64 grid).

Figures 4.30 and 4.31 show the coarse-grained fields calculated at time $t = 27$ for grids with sizes 224×32 and 448×64, respectively. The coarse-grained temperature fields are calculated from fine grid (1792×256) temperature fields following the coarse-graining procedure described earlier for velocity. The coarse-grained vorticity is obtained from coarse-grained velocity, $\overline{\omega} := \nabla \times \overline{\mathbf{u}}$. The effect of coarse-graining (which removes the small-scale features from the fine grid solution) is more visible when one looks at the vorticity plots.

We record the fine grid velocity $\mathbf{u}$ from $t = 27$ to $t = 45$ time units at an interval of Δt (the coarse grid time-step) and apply the calibration procedure described in Section 3.1. For the grid with size 224×32, SVD decomposition results in 450 EOFs/ $\boldsymbol{\xi}_i$. We find that out of 450 EOFs, 51 EOFs can explain 90% of the total variance present in the data matrix $\Delta \boldsymbol{X}$. 21 EOFs are needed explain 70% of the total variance. For

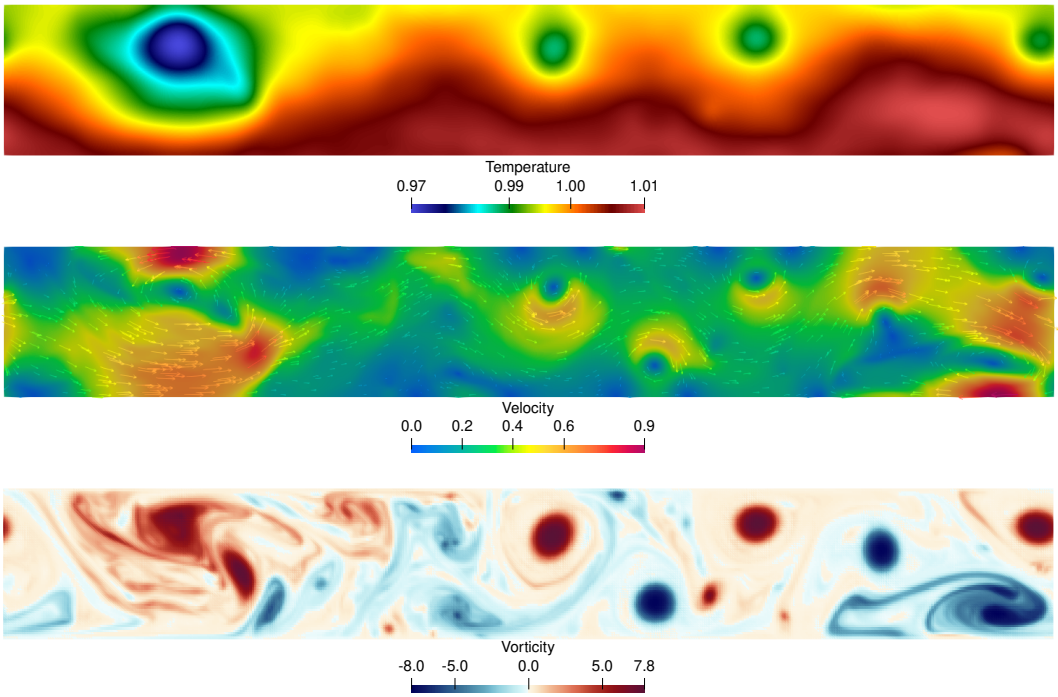

FIGURE 4.31: Coarse-grained temperature (top), velocity (middle), and vorticity (bottom) fields at time $t = 27$ for the coarse grid of size 448×64.

TABLE 4.4: Number of $\boldsymbol{\xi}_i$ (denoted by n_ξ) needed to explain different levels of variance in the observation data $\Delta \boldsymbol{X}$ for 64×64 and 32×32 grids.

	90% variance	70% variance	50% variance
n_ξ, 448×64 grid	94	39	18
n_ξ, 224×32 grid	51	21	10

the grid with size 448×64, the SVD decomposition results in 900 EOFs. In order to capture 90% and 70% of the total variability in $\Delta \boldsymbol{X}$, number of EOFs required are 94 and 39, respectively. Table 4.4 summarizes the results obtained from the calibration procedure.

Figures 4.32 and 4.33 show the plots of some of the calculated $\boldsymbol{\xi}_i$ for grids of size 224×32 and 448×64 respectively. It can be observed that for both coarse grids, the first EOF contains large-scale features whereas the last EOF contains small-scale features. Note that we observed similar flow features for the EOFs obtained in the analysis of the stochastic Navier-Stokes equations.

4.2.2 Impact of parameterization

The SALT parameterization is designed to model the effect of unresolved (small-scale) components on the resolved (large-scale) components of the flow. The stochastic parameterization leads to an ensemble of solutions which can be further used to probe

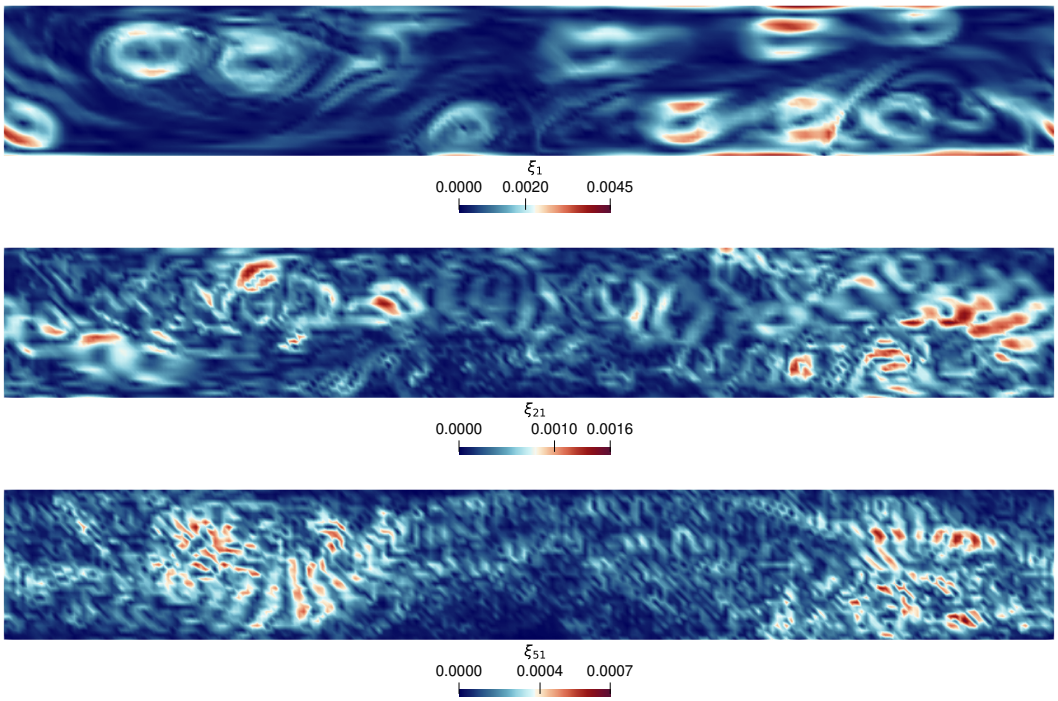

FIGURE 4.32: Estimated $\boldsymbol{\xi}_i$ for the coarse grid of size 224×32. The 1st (top), 21st (middle), and 51st (bottom) $\boldsymbol{\xi}_i$ are shown. The first 51 EOFs explain 90% of the total variance present in the observation data.

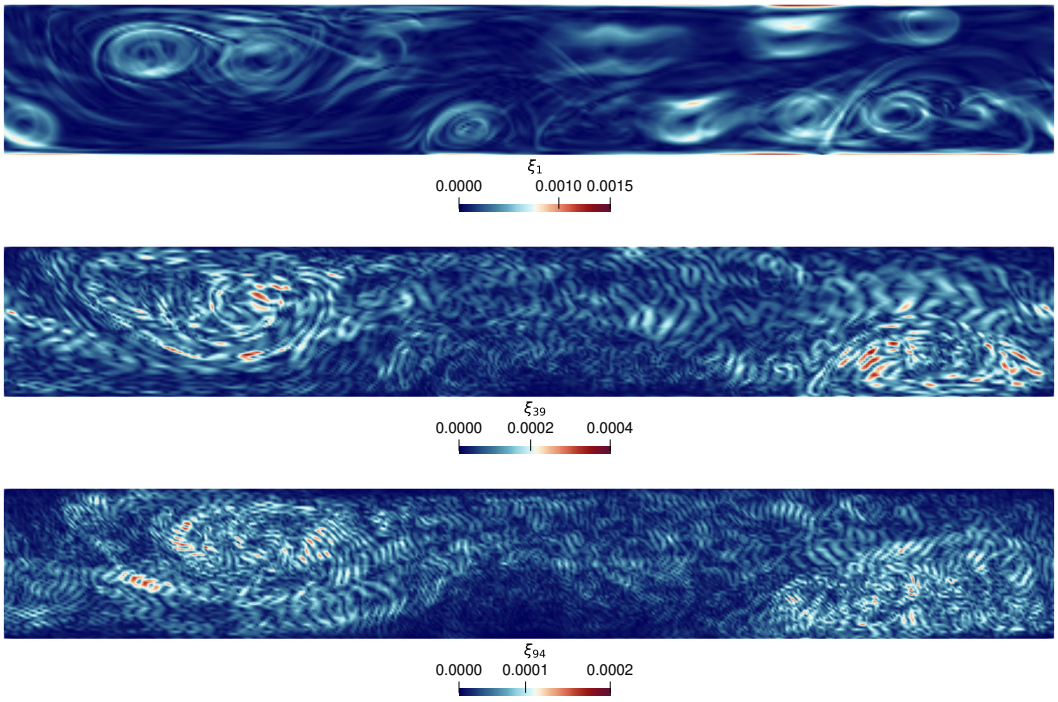

FIGURE 4.33: Estimated $\boldsymbol{\xi}_i$ for the coarse grid of size 448×64. The 1st (top), 39th (middle), and 94th (bottom) $\boldsymbol{\xi}_i$ are shown. The first 94 EOFs explain 90% of the total variance present in the observation data.

the uncertainty resulting from running the model on coarse grids. In this section, we evaluate the effectiveness of SALT parameterization in nudging the large-scale features of the flow towards the coarse-grained high-resolution solution (henceforth referred to as the "truth") when the model is run on coarser grids.

We first run the deterministic model on a coarse grid with coarse-grained high-resolution fields at $t = 27$ as initial conditions. The idea is to see how the large-scale flow patterns evolve on the coarse grid (which does not include the effect of small scales) in comparison to the high-resolution simulation. We compare the temperature, velocity and the vorticity fields for 224×32 grid with the coarse-grained high-resolution fields.

Figures 4.34 and 4.35 show the simulation results at time $t = 36$ and $t = 45$, respectively. At $t = 36$, we can observe slight differences in the deterministic model solution and the coarse-grained fields. The difference in flow patterns is more apparent when one compares the vorticity field plots. At $t = 45$, significant differences (especially in the vorticity fields) can be observed between the two solutions. In Figure 4.35, we can see that the deterministic model solution fails to capture the locations of most of the vortices. The deterministic model solution also cannot retain the total number of vortices in the flow. For the deterministic model, the vortices seem to combine and form big vortices much earlier in comparison to the truth. We can attribute these observations to two main factors:

(1) The deterministic model does not contain any information about the small-scale processes at the start of simulation (due to coarse-graining). The effect of small scales on the large scales is also absent in the deterministic PDE since it has not been parameterized with any sub-grid closure model yet.

(2) The model is run on a coarse grid and therefore the solution inherently contains discretization errors which accumulate over time resulting in large difference between the model solution and the coarse-grained field at $t = 45$.

The SALT parameterization is designed to tackle the first factor i.e. the effect of small (unresolved) scales on large (resolved) scales. The information about the unresolved scales is supplied to the deterministic model as a stochastic forcing $\sum_i \boldsymbol{\xi}_i \Delta W_n^i$. We can write this stochastic forcing as an approximation of a function $\mathbf{g}(\boldsymbol{x}, t)$ such that

$$\mathbf{g}(\boldsymbol{x}, t)\sqrt{\Delta t} = (\mathbf{u} - \overline{\mathbf{u}})\Delta t \approx \sum_i \boldsymbol{\xi}_i \Delta W_n^i.$$

The function $\mathbf{g}(\boldsymbol{x}, t)$ is obtained from SVD decomposition of the Lagrangian trajectory data in the calibration procedure. The application of SVD algorithm on the $(\mathbf{u} - \overline{\mathbf{u}})\sqrt{\Delta t}$ measurement data yields

$$\mathbf{g}(\boldsymbol{x}, t) = \boldsymbol{\xi}_0 + \sum_i^N a_i(t)\boldsymbol{\xi}_i(\boldsymbol{x}), \tag{4.6}$$

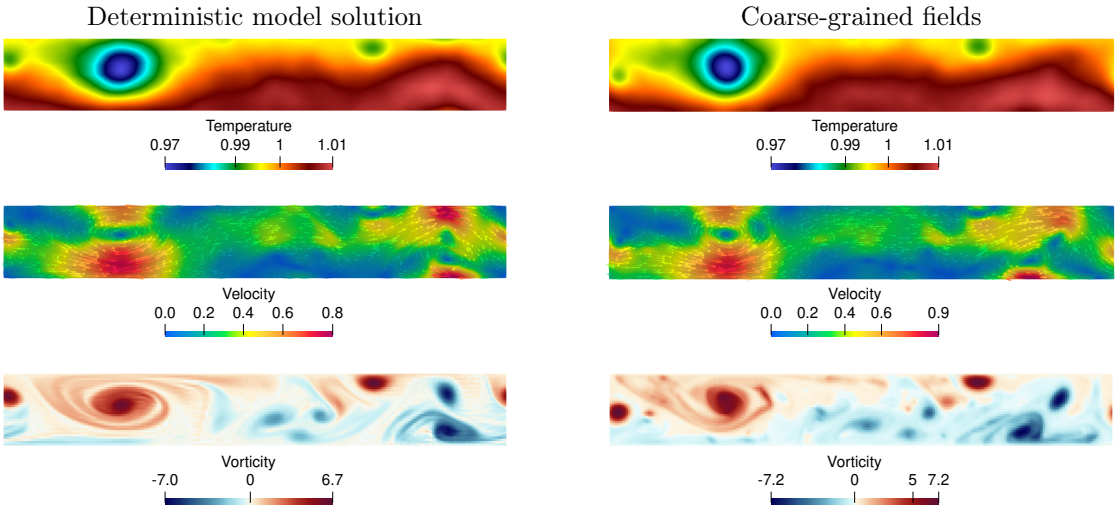

FIGURE 4.34: Comparison between the deterministic model simulation results (left) and the coarse-grained high-resolution fields for the 224×32 grid. The plots correspond to temperature (top), velocity (middle,) and vorticity (bottom) fields at time $t = 36$.

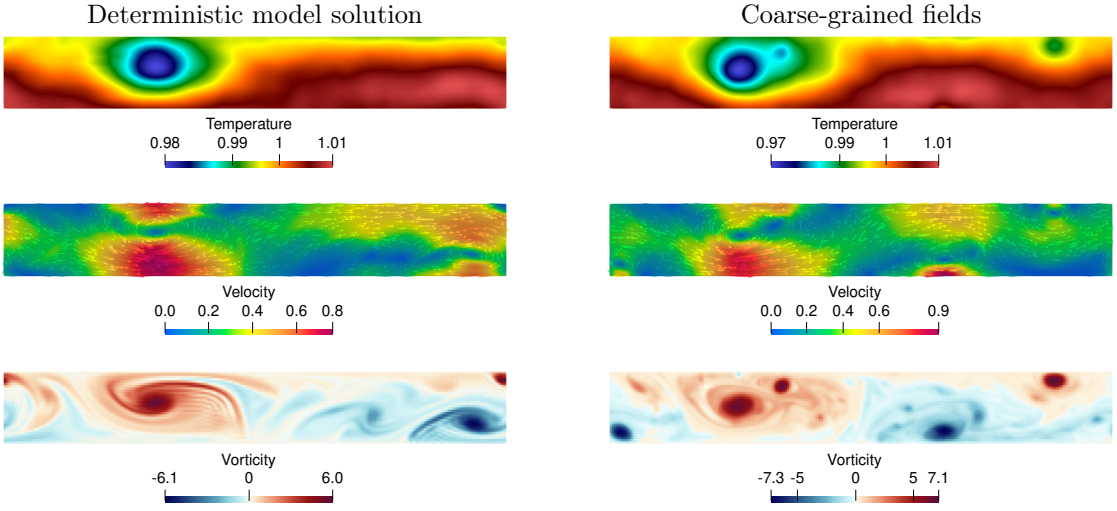

FIGURE 4.35: Comparison between the deterministic model simulation results (left) and the coarse-grained high-resolution fields for the 224×32 grid. The plots correspond to temperature (top), velocity (middle,) and vorticity (bottom) fields at time $t = 45$.

where $\boldsymbol{\xi}_0(\boldsymbol{x})$ is the time-mean of the measurement data and $a_i(t)$ are the time series corresponding to each correlation vector $\boldsymbol{\xi}_i(\boldsymbol{x})$. The stochastic model is calibrated by utilizing only the rescaled EOF modes $\boldsymbol{\xi}_i$. The time-mean $\boldsymbol{\xi}_0(\boldsymbol{x})$ is neglected and the time series $a_i(t)$ is approximated as i.i.d. samples of a standard normal distribution.

Instead of approximating the correction term by a stochastic forcing, we can use all the information contained in $(\mathbf{u} - \overline{\mathbf{u}})\Delta t$ and force the model with a deterministic forcing $\mathbf{g}(\boldsymbol{x}, t)$. The resulting solution from such a deterministic forcing is denoted by the adapted reference solution. The discrete in-time equations which lead to the adapted reference solution for the atmosphere model are

$$
\begin{aligned}
\mathbf{u}^{n+1} - \mathbf{u}^n = &- \left(\frac{(\mathbf{u}^{n+1} \cdot \nabla)\mathbf{u}^{n+1} + (\mathbf{u}^n \cdot \nabla)\mathbf{u}^n}{2} + \frac{1}{2Ro}\hat{\mathbf{z}} \times (\mathbf{u}^{n+1} + \mathbf{u}^n) \right) \Delta t \\
&- \frac{1}{2C}\left(\nabla\theta^{n+1} + \nabla\theta^n\right)\Delta t + \frac{\nu_e}{2}(\Delta\mathbf{u}^{n+1} + \Delta\mathbf{u}^n)\Delta t \\
&- \frac{(\mathbf{g}^{n+1} \cdot \nabla)\mathbf{u}^{n+1} + (\mathbf{g}^n \cdot \nabla)\mathbf{u}^n}{2}\sqrt{\Delta t} \\
&- \left(\frac{u_1^{n+1}\nabla g_1^{n+1} + u_1^n \nabla g_1^n}{2} + \frac{u_2^{n+1}\nabla g_2^{n+1} + u_2^n \nabla g_2^n}{2} \right) \sqrt{\Delta t}, \\
\theta^{n+1} - \theta^n = &- \left(\frac{\nabla \cdot (\theta^{n+1}\mathbf{u}^{n+1}) + \nabla \cdot (\theta^n \mathbf{u}^n)}{2} \right) \Delta t \\
&+ \frac{\eta_e}{2}(\Delta\theta^{n+1} + \Delta\theta^n)\Delta t \\
&- \left(\frac{\mathbf{g}^{n+1} \cdot \nabla\theta^{n+1} + \mathbf{g}^n \cdot \nabla\theta^n}{2} \right) \sqrt{\Delta t}.
\end{aligned}
\tag{4.7}
$$

We obtain the adapted reference solution after solving equations (4.7) from time $t = 27$ to $t = 45$ on a grid of size 224×32. We use 51 EOFs for estimating the deterministic function $\mathbf{g}(\boldsymbol{x}, t)$. Figures 4.36 and 4.37 show a comparison between the adapted reference solution and the coarse-grained fields at $t = 36$ and $t = 45$ respectively. It is clearly visible from the plots that the adapted reference solution is closer to the truth than the deterministic solution (see Figure 4.34 and Figure 4.35). Figure 4.38 shows vorticity plots at $t = 45$ for the adapted reference solution, the deterministic model solution and the coarse-grained fine solution. The adapted reference solution is able to capture some of the flow patterns which are missed by the deterministic model solution. For example, a vortex in the bottom-left corner of the domain is absent in the deterministic model solution but is captured by the adapted reference solution. In order to make a more quantitative comparison, we investigate relative L^2 distance between the deterministic model solution or the adapted reference solution and the coarse-grained truth. The relative L^2 error can be defined as

$$
\frac{\|\theta(t) - \theta_{\text{truth}}(t)\|_{L^2(\Omega)}}{\|\theta_{\text{truth}}(t)\|_{L^2(\Omega)}}
$$

for temperature and similarly for velocity and vorticity fields. This error provides a

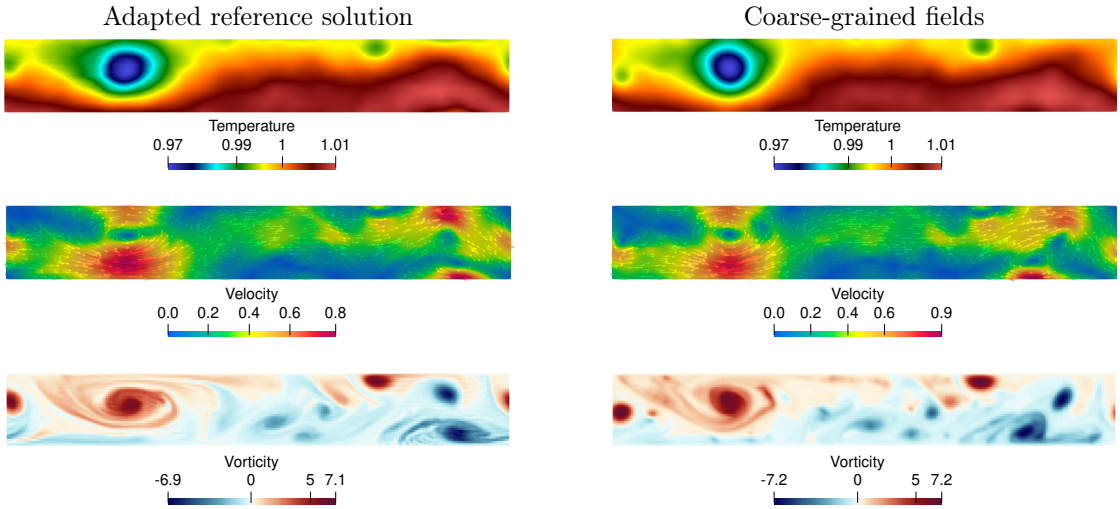

FIGURE 4.36: Comparison between the adapted reference solution (left) and the coarse-grained high-resolution fields for the 224×32 grid. The plots correspond to temperature (top), velocity (middle,) and vorticity (bottom) fields at time $t = 36$.

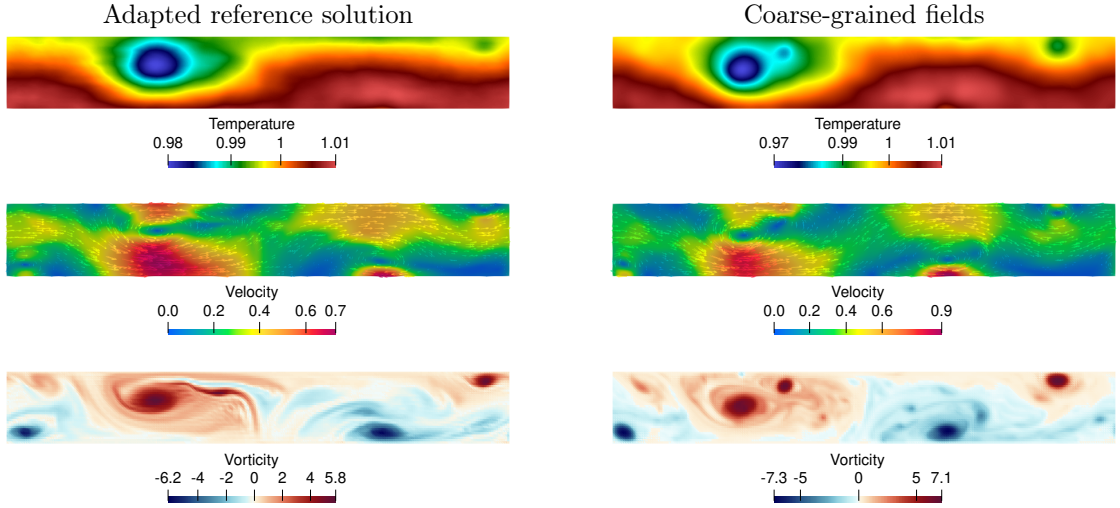

FIGURE 4.37: Comparison between the adapted reference solution (left) and the coarse-grained high-resolution fields for the 224×32 grid. The plots correspond to temperature (top), velocity (middle,) and vorticity (bottom) fields at time $t = 45$.

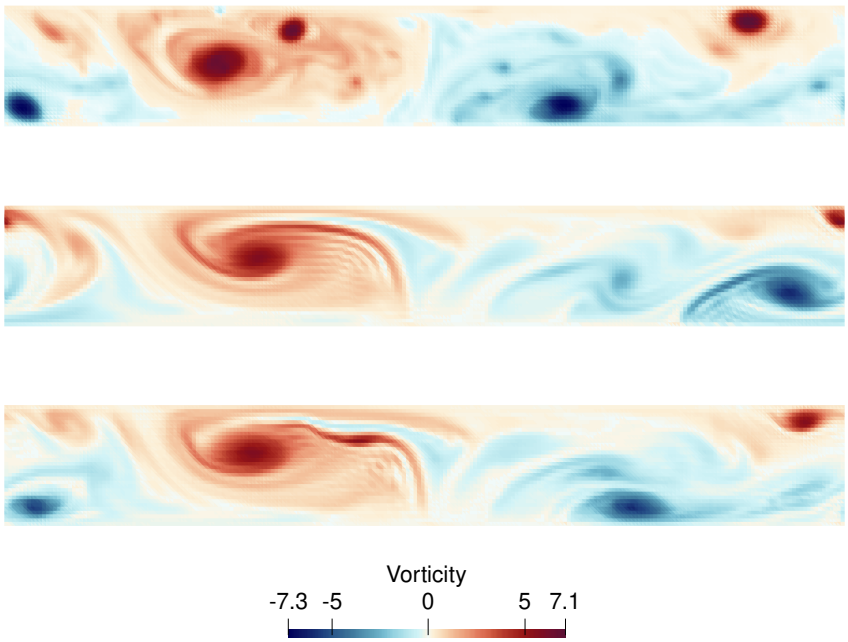

FIGURE 4.38: Vorticity fields at $t = 45$ from the coarse-grained fine-grid solution (top), deterministic model simulation (middle), and adapted reference solution (bottom) for the 224×32 grid.

global measure for comparing the solutions at different time instances. Figure 4.39 shows an evolution of relative L^2 errors for the deterministic model solution and the adapted reference solution from $t = 27$ to $t = 45$. The velocity and vorticity L^2 errors for both solutions remain fairly close to each other for the first 9 time units i.e., until $t = 36$. After $t = 36$, the L^2 error for the deterministic model overtakes the adapted model. The temperature L^2 error for the deterministic model remains lower than the adapted model for most of the simulation window but it too surpasses the L^2 error of the adapted model after approximately 15 time units. The qualitative and quantitative assessment clearly shows an advantage of parameterization for the deterministic model. We expect to get similar results from the SPDE (parameterized by SALT) ensemble in capturing the effect of small scales on large scales since it is an approximation (or stochastic version) of the adapted reference solution.

4.2.3 SPDE ensemble

In this section, we analyze the simulation results of the stochastic atmosphere model. The stochastic model (4.4) is simulated on a coarse grid of size 224×32 from $t = 27$ to $t = 45$. Each independent realization of the SPDE is initialized with the same initial conditions. The initial velocity and temperature fields for the SPDE ensemble are obtained from coarse-graining of high-resolution (1792×256) velocity and temperature fields at $t = 27$. We use 51 EOFs (explaining 90% variability in the data) to generate the noise terms in the SPDE. The evolution of velocity and temperature fields are

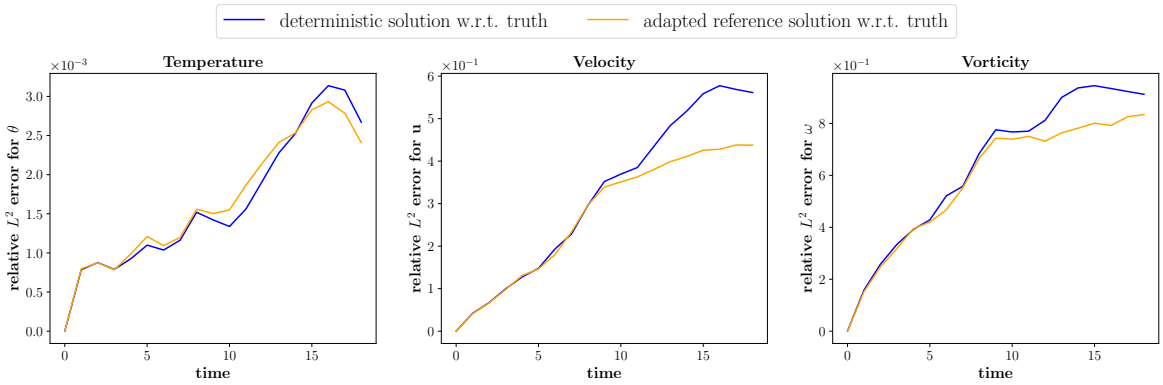

FIGURE 4.39: Relative L^2 errors for the deterministic model solution (blue) and the adapted reference solution (orange) over 18 time units ($t = 27$ to $t = 45$). Errors are shown for temperature (left), velocity (center), and vorticity (right).

monitored for 50 ensemble particles at three internal grid points $(1.75, 0.5), (3.5, 0.5)$, and $(5.25, 0.5)$ in the domain.

Figure 4.40 shows the evolution of one standard deviation region about the ensemble mean for velocity (x and y components) and temperature fields with time. The SPDE results are compared with the adapted reference solution. Preliminary analysis suggests that the SPDE ensemble is able to capture the adapted reference solution for a major part of the simulation time window. This is particularly true for the temperature field where the adapted solution stays inside the ensemble spread for all times. The spread generated by the SPDE solution is higher for temperature in comparison to velocity suggesting more variability or uncertainty in the coarse grid temperature fields. At first glance, these results appear promising in the sense that the SPDE solution exhibits a spread whose size gradually increases over time as expected. The ensemble spread also captures the reference solution for extended time periods signifying an accurate approximation of the noise terms. A deeper analysis of the SPDE results, however, reveals some serious issues.

Figures 4.41 and 4.42 compare the velocity, temperature and vorticity fields of one independent realization of the SPDE with the adapted reference solution at $t = 36$ and $t = 45$, respectively. At $t = 36$, although the velocity and vorticity fields from the SPDE solution show a great resemblance to the adapted reference solution, the temperature field differs substantially. The temperature field is very noisy and has a lot of artifacts. These artifacts stay in the temperature field throughout the simulation time window.

In Figure 4.43, we compare the vorticity fields for three independent realizations of the SPDE with the deterministic model solution and the adapted reference solution at $t = 45$ (i.e. after 18 time units). Vorticity fields obtained from the SPDE solution are noisier than both the deterministic solution and the adapted reference solution. Large-scale flow patterns in the SPDE solution resemble the deterministic model solution more than the adapted reference solution flow patterns. Moreover, we can not observe

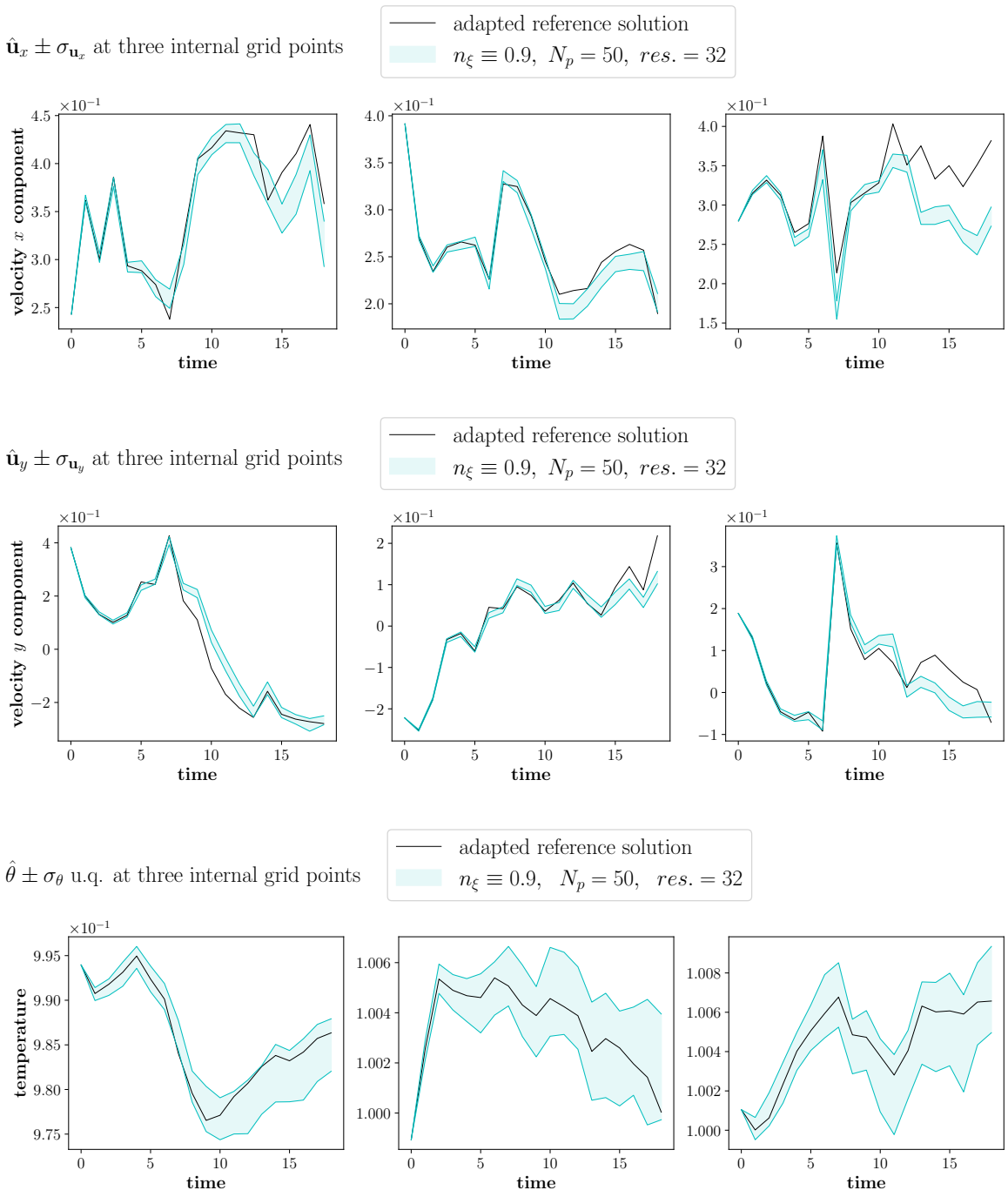

FIGURE 4.40: One-standard-deviation bands about the ensemble mean for velocity (x and y components) and temperature, compared with the adapted reference solution at three internal grid points in the domain. The black solid line represents the adapted reference solution; colored bands indicate ensemble spread.

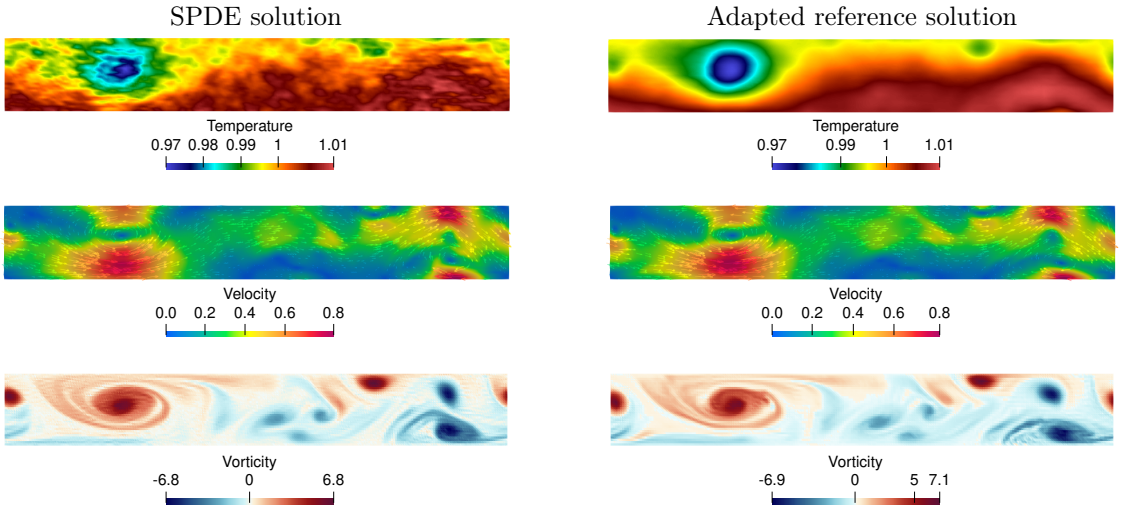

FIGURE 4.41: Comparison between one independent realization of the SPDE and the adapted reference solution for the 224×32 grid. The plots show temperature (top), velocity (middle), and vorticity (bottom) fields at $t = 36$.

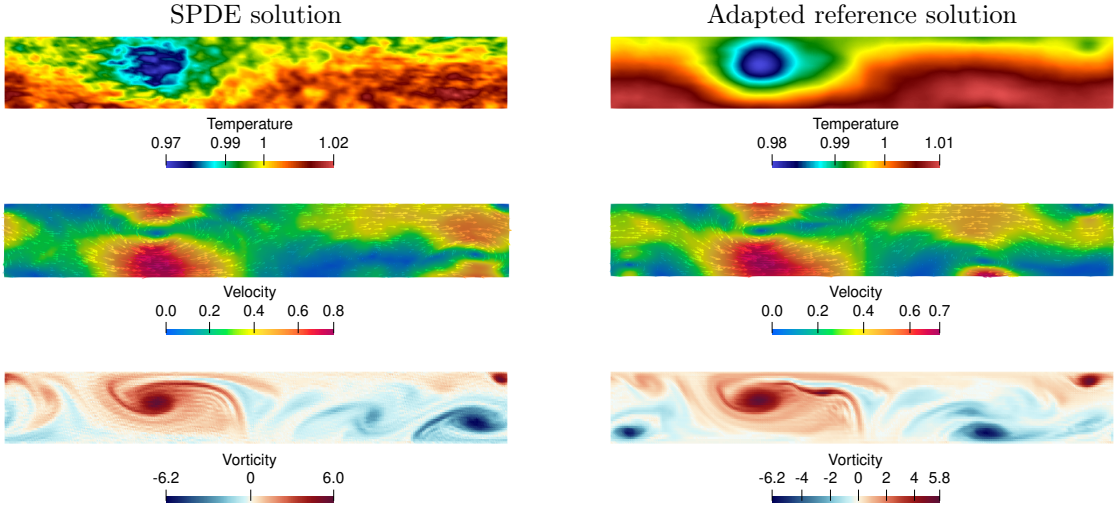

FIGURE 4.42: Comparison between one independent realization of the SPDE and the adapted reference solution for the 224×32 grid. The plots show temperature (top), velocity (middle), and vorticity (bottom) fields at $t = 45$.

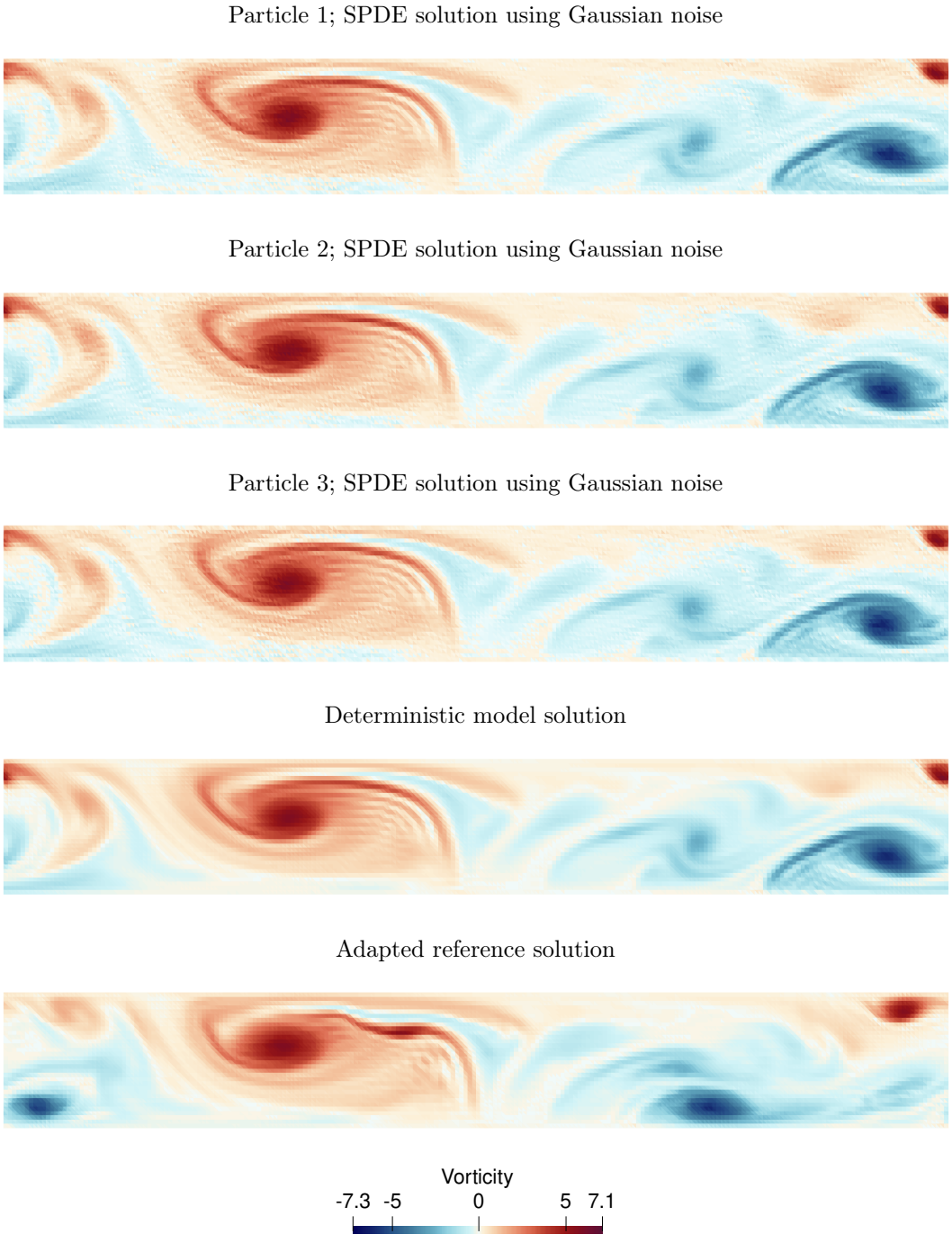

FIGURE 4.43: Comparison of vorticity fields at $t = 45$ for three independent SPDE realizations, deterministic model solution, and adapted reference solution on the 224×32 grid.

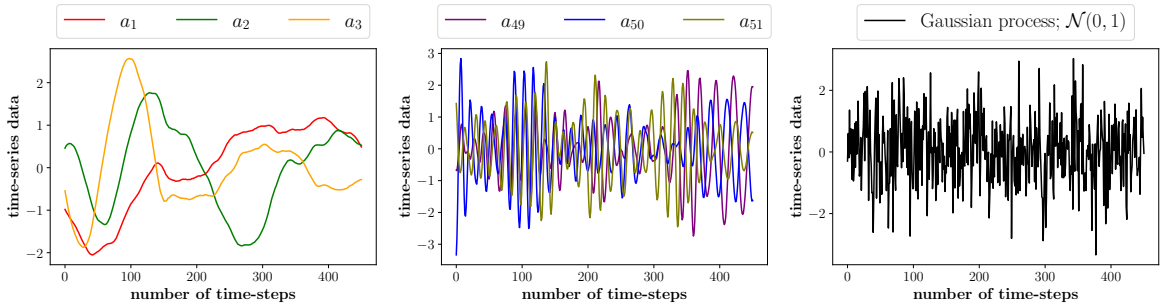

FIGURE 4.44: Time series data corresponding to $\boldsymbol{\xi}_1$, $\boldsymbol{\xi}_2$, $\boldsymbol{\xi}_3$ (left) and $\boldsymbol{\xi}_{49}$, $\boldsymbol{\xi}_{50}$, $\boldsymbol{\xi}_{51}$ (middle) for coarse grid of size 224×32. The time series generated by a Gaussian process is shown on the right.

any variability in large-scale flow patterns of independent realizations of the SPDE (Figure 4.43 shows results for 4 members in the 50 particle ensemble). The stochastic parameterization appears to add only random noise to the flow rather than producing different flow states. The spread exhibited by the independent realizations of SPDE can thus be attributed to random noise in the solution rather than to different large-scale flow patterns. We conclude that the noise generated by SALT parameterization neither induces variability in the flow nor steers the large-scale flow towards the truth. We suspect that approximating the time series $a_i(t)$ (in (4.6)) with a Gaussian distribution may be the reason why the SPDE solution does not match the adapted reference solution. We investigate this further in the next section.

Gaussian noise versus OU process

The time series $a_i(t)$ is modeled by a Gaussian process $\mathcal{N}(0,1)$. Although the time series $a_i(t)$ has zero mean and unit standard deviation, it is possible that its elements are not uncorrelated. Figure 4.44 presents time series plots corresponding to the first three and last three EOFs obtained for a 224×32 grid. For this grid, 51 EOFs capture 90% of the total variance in observation data. It is clear from this figure that the time series plots for a_1, a_2 and, a_3 do not resemble a Gaussian process. The time series plots for a_{49}, a_{50} and, a_{51} however do look similar to a Gaussian process. Nevertheless, the first few EOFs explain the most variance present in the data and if the time series corresponding to those EOFs are not modeled accurately, the parameterization may not have the desired effect on the large-scale flows. We make a more quantitative assessment by plotting the autocorrelation function (ACF) for a_i.

Figure 4.45 shows the ACF plots for time series data corresponding to some EOFs. Ideally, the ACF values for all the time series a_i should start at 1 and drop to 0 for a lag time-period of more than 1 time-step. We observe that, only the time series of last few EOFs follow this pattern. We can thus conclude that the time series are highly correlated. The approximation of $a_i(t)$ using a Gaussian process, therefore, may not be a good modeling choice.

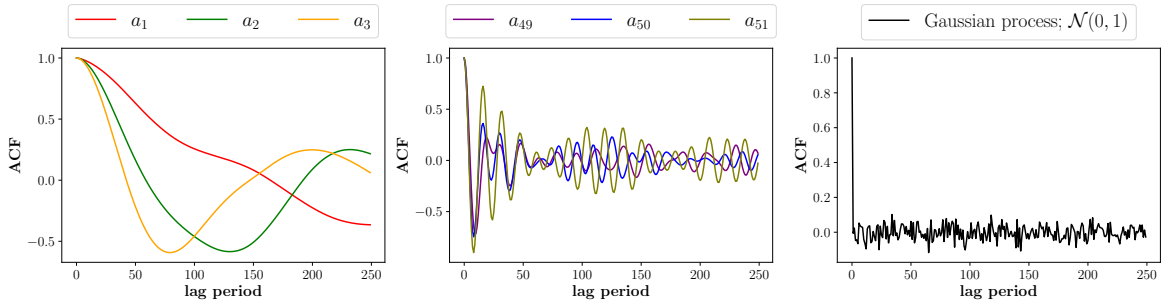

FIGURE 4.45: Autocorrelation function (ACF) plots for time series data corresponding to $\boldsymbol{\xi}_1$, $\boldsymbol{\xi}_2$, $\boldsymbol{\xi}_3$ (left) and $\boldsymbol{\xi}_{49}$, $\boldsymbol{\xi}_{50}$, $\boldsymbol{\xi}_{51}$ (middle) for coarse grid of size 224×32. The ACF plot for time series generated by a Gaussian process is shown on the right.

The Ornstein-Uhlenbeck (OU) process presents a good alternative to the Gaussian process in modeling time series data which is highly correlated (Ephrati et al., 2023). The noise generated using the OU process can mimic the temporal correlation of the measured time series. Ephrati et al. (2023), in their study of stochastic 2D Euler equations, demonstrated that the ensemble generated by OU noise provides better uncertainty quantification than the ensemble generated by Gaussian noise.

We approximate the time series $a_i(t)$ in (4.3) using the discrete analog of OU process, known as the autoregressive model of order 1 (AR(1) model), see Maller et al., 2009. The AR(1) model is a stochastic process defined as

$$X_t = \varphi X_{t-1} + \epsilon_t,$$

where X_t is the value of the process at time t, φ is the autoregressive coefficient, and $\epsilon_t \sim \mathcal{N}(0, \sigma^2)$ is a white-noise process with zero mean and a constant variance of σ^2. This process satisfies

$$\mathbb{E}(X_t) = 0, \ \ \mathrm{Var}(X_t) = \frac{\sigma^2}{1-\varphi^2},$$

and the correlation between X_t and X_{t+1} is

$$\mathrm{Corr}(X_t, X_{t+1}) = \frac{\mathrm{Cov}(X_t, X_{t+1})}{\mathrm{var}(X_t)} = \varphi,$$

where $\mathrm{var}(X_t)$ denotes the variance of X_t and $\mathrm{cov}(X_t, X_{t+1})$ is the covariance between X_t and X_{t+1}.

Our method for generating a discrete OU process corresponding to the time series $a_i(t)$ is presented in Algorithm 3. Figure 4.46 shows the generated discrete OU processes corresponding to time series of six different $\boldsymbol{\xi}_i$. We can clearly observe similarities between the observation data time series $a_i(t)$ and the AR(1) model generated time series $o_i(t)$. The OU processes, denoted by $o_i(t)$), do not match the time series $a_i(t)$ at each time instance; rather, they replicate only the general behavior or pattern of $a_i(t)$. This discrepancy arises because the AR(1) model is initialized using a random draw

from $\mathcal{N}(0,1)$ rather than the actual value of $a_i(i)$ at $t = 0$.

Algorithm 3 Algorithm for generating discrete OU processes using the AR(1) model

1: Let $a_i(t_k)$ be a time series corresponding to the correlation vector $\boldsymbol{\xi}_i$ where $t_k = k\Delta t,\ k = 0, 1, 2, \ldots, M-1$ and $t_M = T$. We know that

$$\mathrm{Var}(a_i) = 1, \quad \mathbb{E}(a_i) = 0.$$

2: Calculate the parameter φ where

$$\varphi = \frac{\mathrm{Cov}(a_i(t_k), a_i(t_{k+1}))}{\mathrm{Var}(a_i)} = \frac{1}{M}\sum_{k=0}^{M-1} a_i(t_k) \times a_i(t_{k+1}).$$

3: Use φ to calculate σ,

$$\sigma = \sqrt{1-\varphi^2}.$$

4: Initialize the discrete OU time series $X(t)$ corresponding to $a_i(t)$,

$$X(t_0) \sim \mathcal{N}(0,1).$$

5: **for** $j = 0, 1, 2 \ldots, M-1$ **do**
6: $\quad X(t_{j+1}) = \varphi X(t_j) + \sigma r_j \quad$ where $r_j \sim \mathcal{N}(0,1)$
7: **end for**

Figure 4.47 presents a comparison of ensemble spread sizes (one standard deviation region around the ensemble mean) generated by 50 independent realizations of the SPDE using Gaussian noise and OU processes. The SPDE with the OU process exhibits slightly larger spread sizes for velocity compared to the SPDE realizations using Gaussian noise. However, the spread for temperature is significantly reduced when Gaussian noise is replaced by OU processes.

To further investigate this observation, we plot the temperature fields resulting from the Gaussian noise SPDE and the OU process SPDE at $t = 36$ and $t = 45$. The results are shown in Figure 4.48 and Figure 4.49. It is evident that the use of OU processes results in smoother temperature fields. Interestingly, artifacts present in the temperature fields of Gaussian noise SPDE are completely eliminated when we switch to OU process SPDE. Moreover, the temperature fields from the SPDE using the OU process exhibit a closer resemblance to the adapted reference solution compared to those generated with Gaussian noise. To provide a quantitative comparison, we analyze the relative L^2 distance between the SPDE solution (produced using Gaussian noise and, separately, using the OU process) and the adapted reference solution.

Figure 4.50 presents a comparison of the one-standard-deviation regions around the ensemble mean of relative L^2 errors for the SPDE solutions using Gaussian noise and the OU process. For the temperature field, the ensemble relative L^2 errors with Gaussian noise are significantly higher than those with the OU process. In contrast, the magnitudes of L^2 errors for velocity and vorticity fields are similar for both SPDE

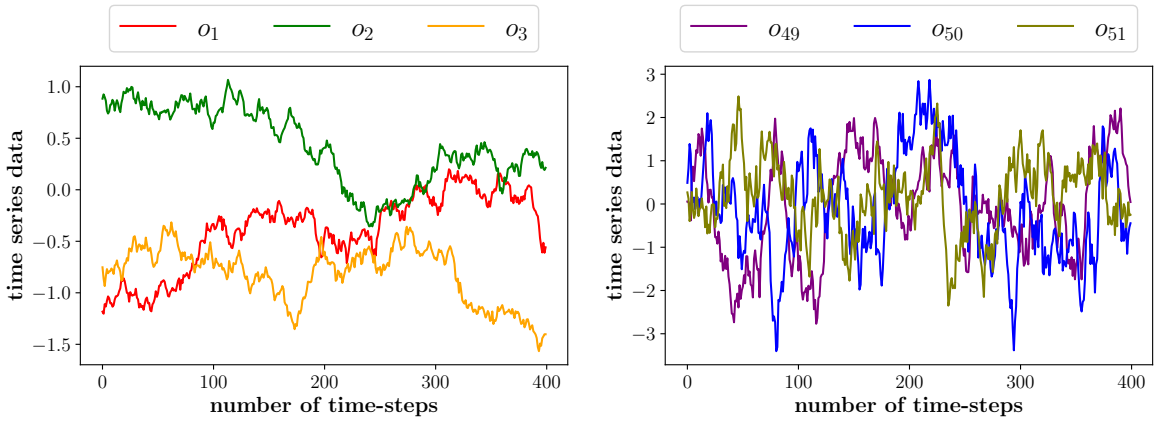

FIGURE 4.46: Time series plots generated using the AR(1) model corresponding to $\boldsymbol{\xi}_1$, $\boldsymbol{\xi}_2$, $\boldsymbol{\xi}_3$ (left) and $\boldsymbol{\xi}_{49}$, $\boldsymbol{\xi}_{50}$, $\boldsymbol{\xi}_{51}$ (right) for the coarse grid of size 224×32. The AR(1) model is initialized with a random sample from the standard normal distribution.

solutions. However, the OU process results in a larger spread than Gaussian noise, indicating greater variability in the solution as the L^2 error increases. This characteristic makes ensembles generated using OU processes more suitable for data assimilation than those using Gaussian processes.

Figure 4.51 shows vorticity plots for four randomly selected members (particles) of the SPDE ensemble generated using OU processes at $t = 45$. Clear differences in the large-scale flow patterns among these four particles can be observed. This variability is entirely absent in the ensemble members generated using Gaussian noise (see Figure 4.43). These observations suggest that OU processes can meaningfully influence large-scale flow patterns rather than merely introducing random noise, as is the case with Gaussian noise.

We conclude that the OU process is a more suitable choice for modeling the time series $a_i(t)$ (see (4.6)) than Gaussian noise. Since the data exhibits correlation, it is essential to incorporate this information into the stochastic model. The stochastic model using OU processes produces more accurate temperature fields, which are smoother and exhibit lower L^2 errors compared to the model with Gaussian noise. Furthermore, the use of OU processes improves uncertainty quantification, as the increasing L^2 error of the solution over time is reflected in the growing ensemble spread size.

4.2.4 Uncertainty quantification

This section focuses on the uncertainty quantification of stochastic model ensemble predictions. The SPDE is simulated for 18 time units, and the solution is compared with the truth (coarse-grained fine-grid solution) and the adapted reference solution. Each independent realization of the SPDE begins with the same initial condition, namely, the coarse-grained fine-grid solution at $t = 27$.

We analyze the effect of different model parameters on the ensemble spread of

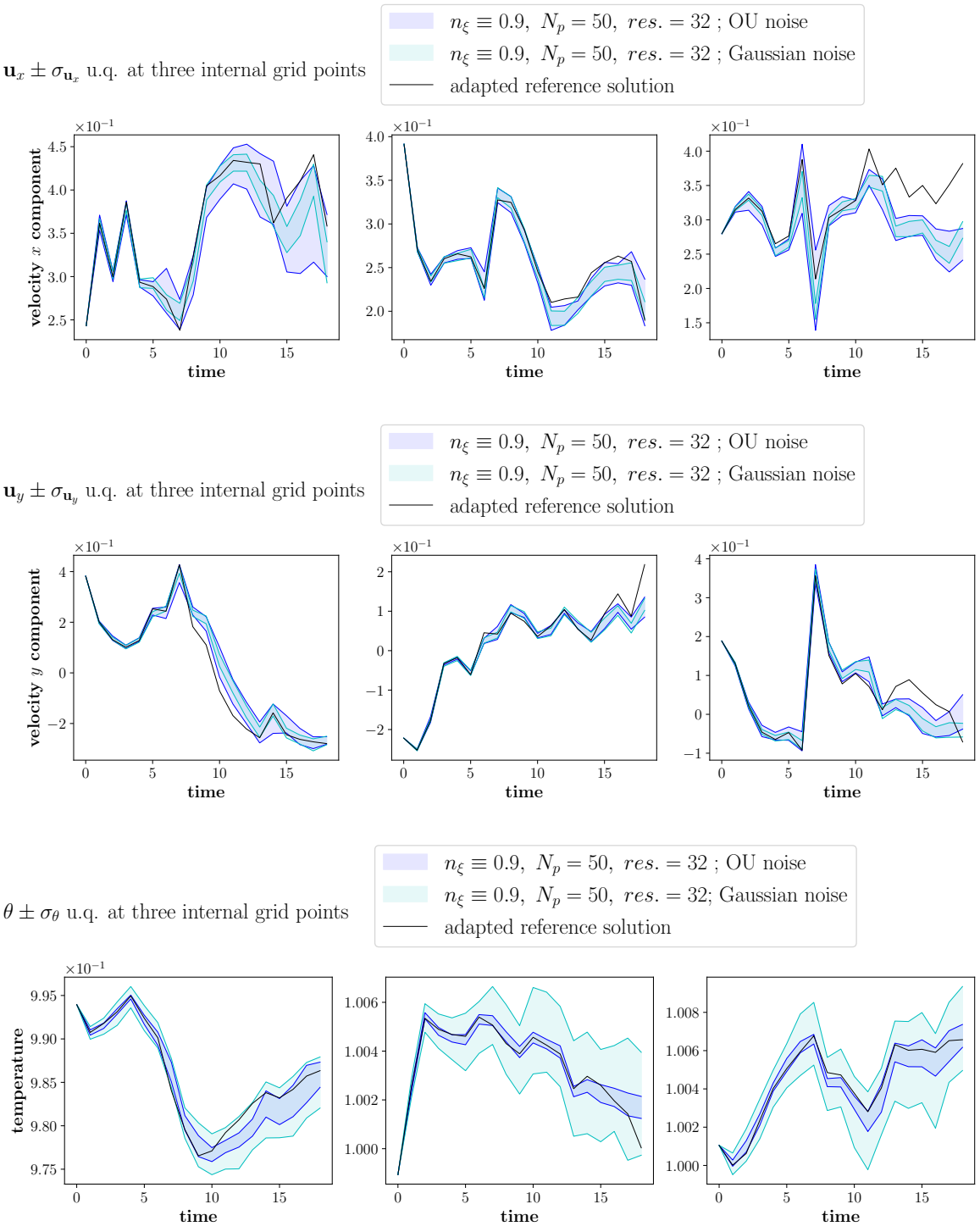

FIGURE 4.47: Comparison of one standard deviation bands generated by the SPDE using Gaussian noise and the OU process for velocity (x and y components) and temperature. Results are compared to the adapted reference solution (black solid line) at three internal grid points. Colored regions indicate the ensemble spread.

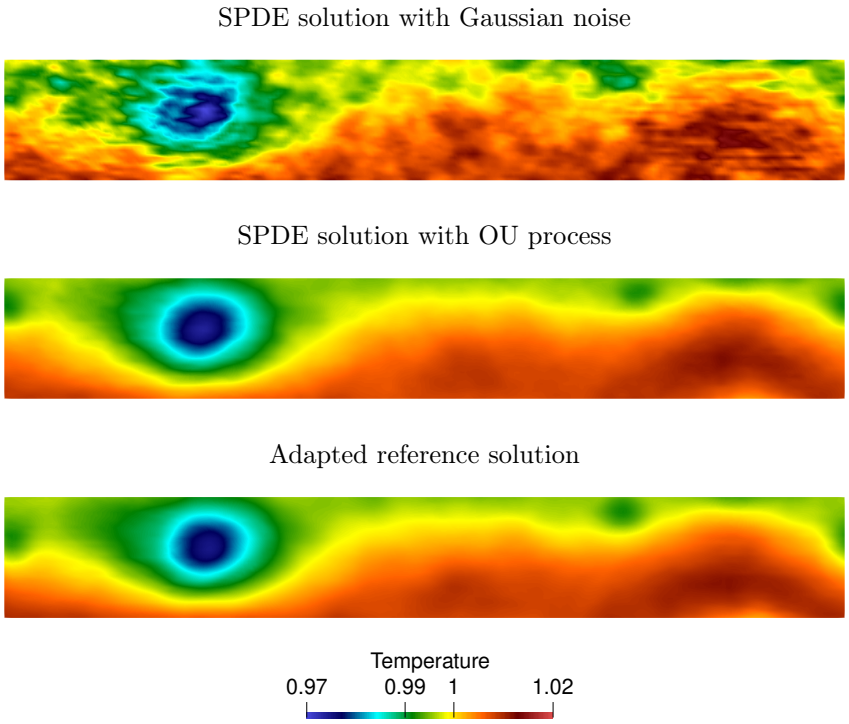

FIGURE 4.48: Temperature fields from SPDE simulations using Gaussian noise (top) and the OU process (center) at $t = 36$, with the adapted reference solution (bottom) shown for comparison.

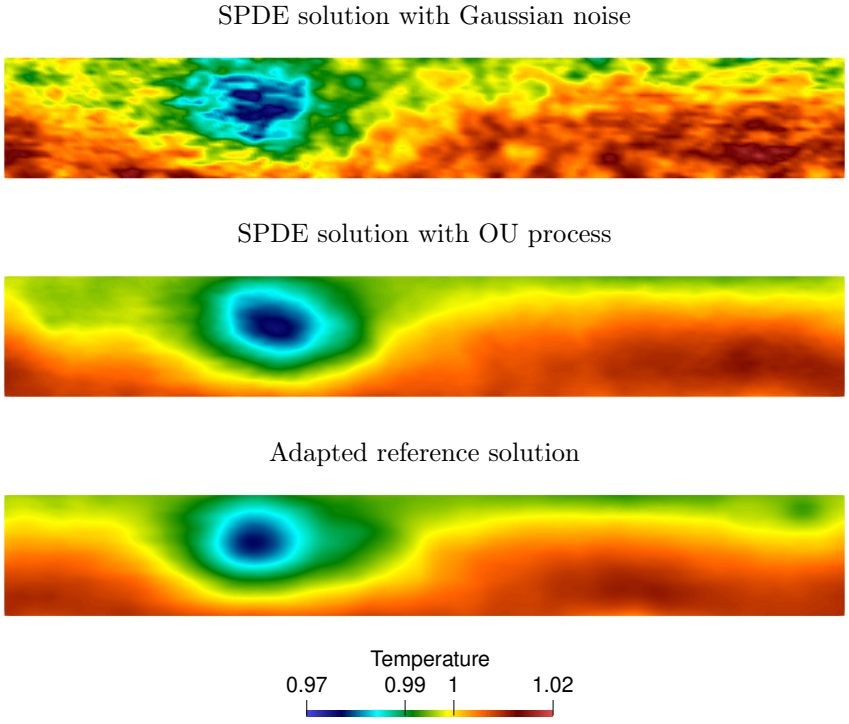

FIGURE 4.49: Temperature fields from SPDE simulations using Gaussian noise (top) and the OU process (center) at $t = 45$, with the adapted reference solution (bottom) shown for comparison.

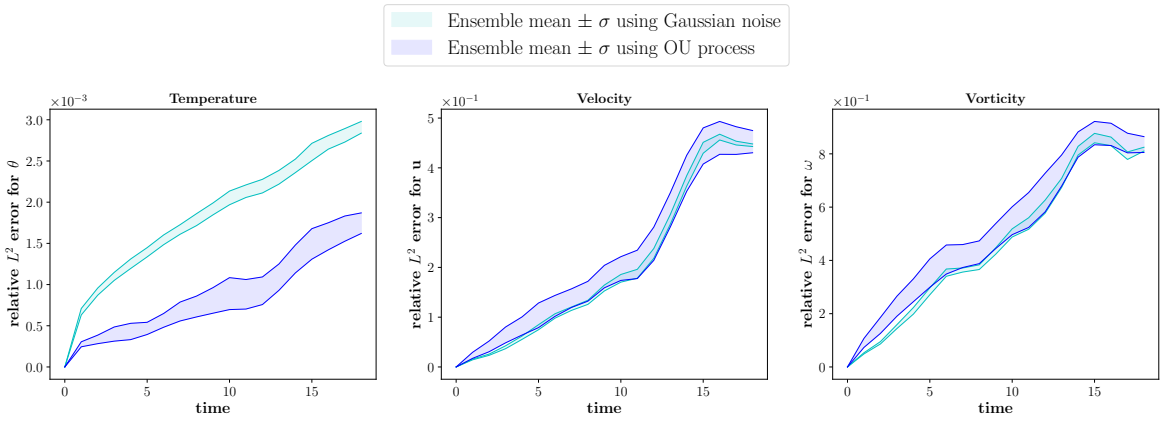

FIGURE 4.50: Relative L^2 error between the SPDE ensembles and the adapted reference solution for temperature (left), velocity (center), and vorticity (right). Colored bands represent one standard deviation around the ensemble mean. The cyan band corresponds to Gaussian noise SPDE and the blue band corresponds to OU process SPDE.

stochastic solutions. Keeping the number of ensemble particles fixed at $N_p = 50$, we examine differences in the one-standard-deviation regions around the ensemble mean solution at three internal grid points when different numbers of EOFs are used: $n_\xi \equiv 0.9$ versus $n_\xi \equiv 0.5$.

Figure 4.52 presents the results for velocity and temperature fields. The plots indicate that varying the number of particles has a negligible effect on the spread size. For velocity, the truth remains within the ensemble spread for approximately 4 to 5 time units before deviating. However, the SPDE ensemble performs poorly for the temperature field, as the truth deviates from the ensemble spread after just 1 or 2 time units. In contrast, the adapted reference solution remains within the ensemble spread for a significantly longer duration (roughly 10 time units). This is expected, as the adapted reference solution accounts for discretization errors, which are not considered when calculating the truth. Additionally, the plots show that the spread size increases over time, indicating growing uncertainty in the stochastic model forecast for longer time periods.

Next, we fix the number of EOFs at $n_\xi \equiv 0.9$ and compare the one-standard-deviation regions for different ensemble sizes: $N_p = 50$ versus $N_p = 100$. Figure 4.53 presents the results, where velocity and temperature values are plotted for three internal grid points. The use of different ensemble sizes has a negligible effect on the spread size.

Figures 4.52 and 4.53 correspond to SPDE solutions computed on a grid of size 224×32. To further investigate uncertainty quantification, we examine the effect of different mesh resolutions. Keeping the number of particles and the variance level fixed ($n_\xi \equiv 0.9, N_p = 50$), we repeat the uncertainty quantification tests on a finer grid of size 448×64. The results are shown in Figure 4.54, where the SPDE ensemble spread is compared with the coarse-grained high-resolution solution corresponding to each

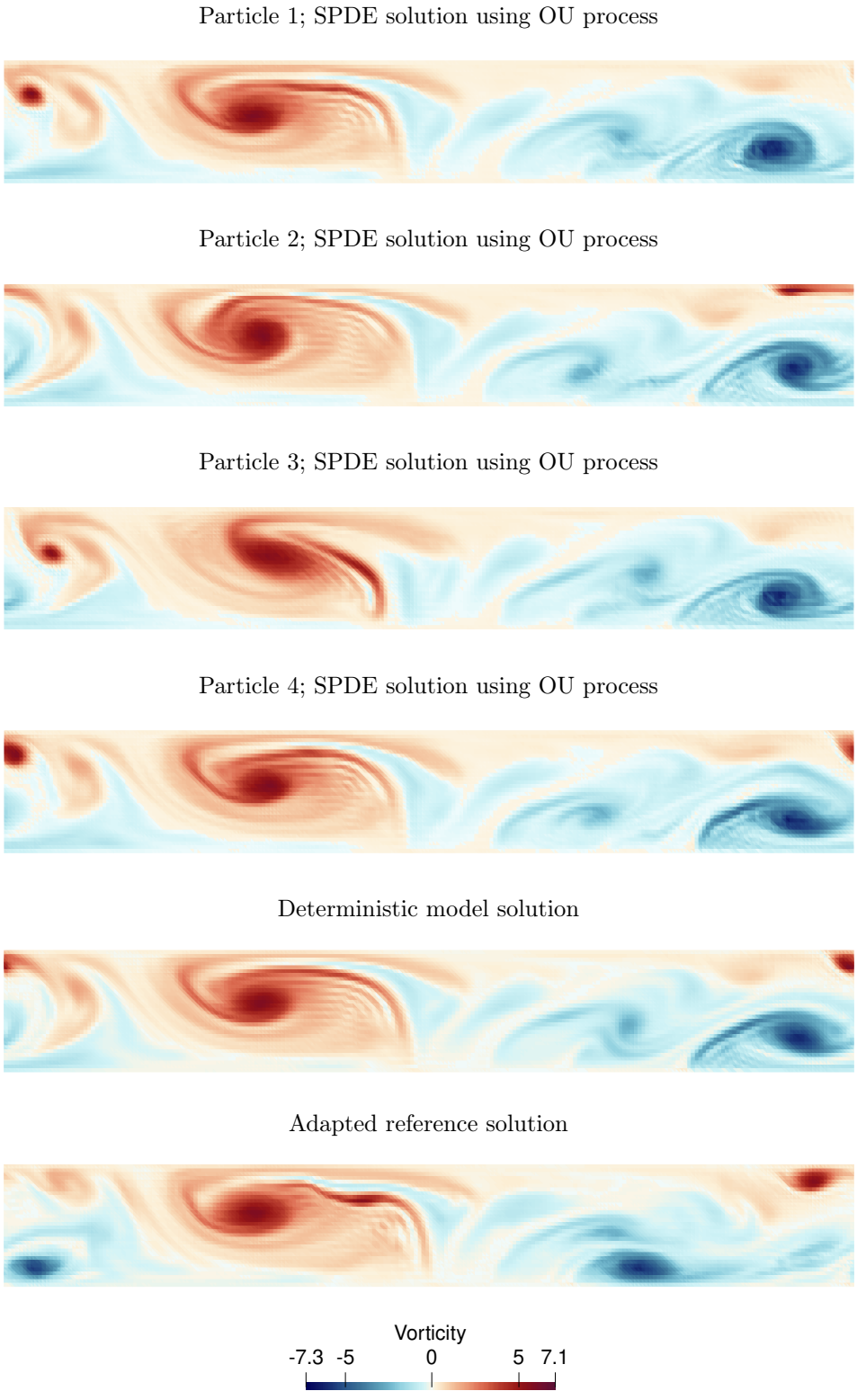

FIGURE 4.51: Vorticity field comparison between four independent realizations of SPDE (using OU processes), deterministic model solution and the adapted reference solution at $t = 45$.

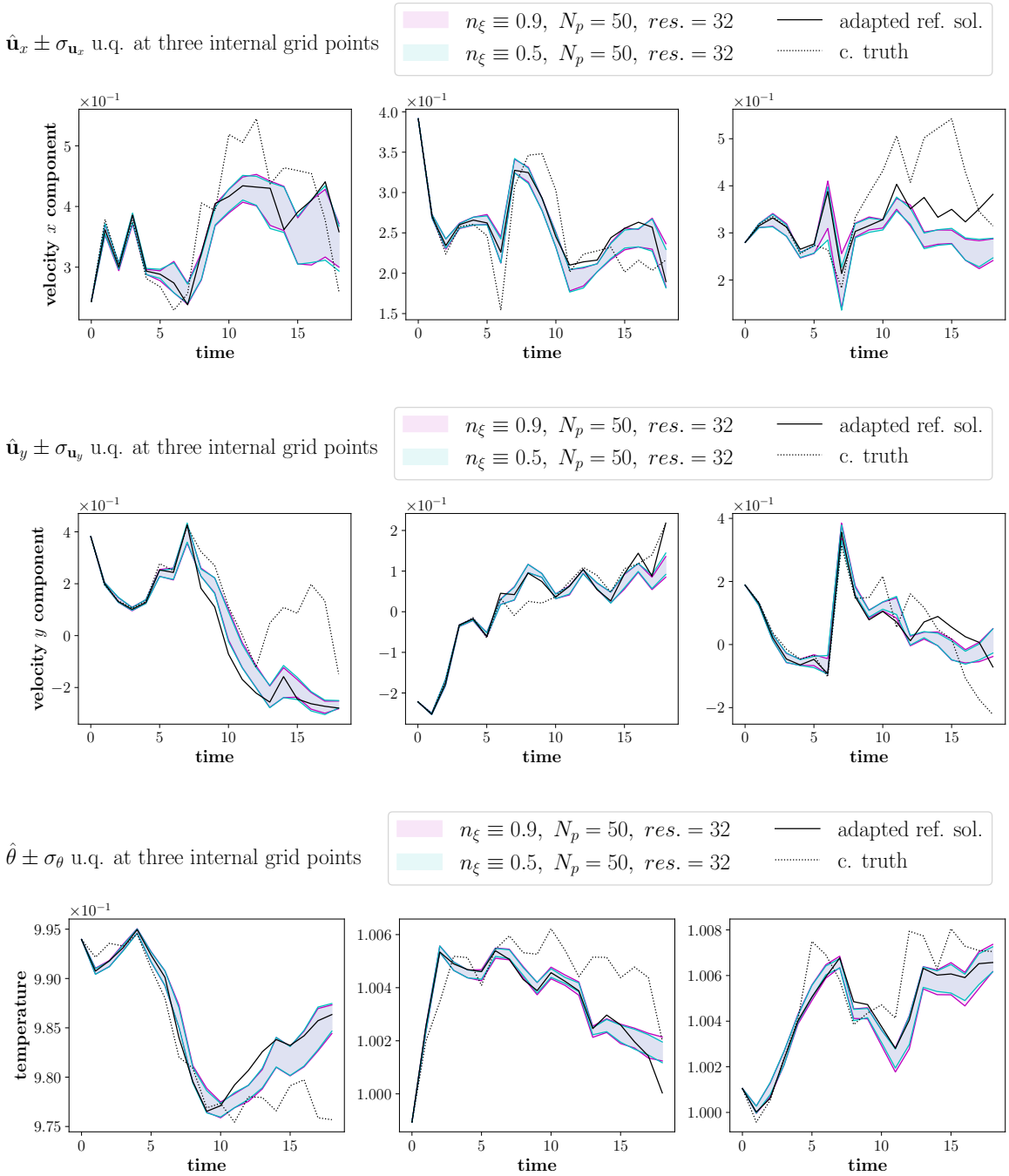

FIGURE 4.52: Uncertainty quantification plots comparing one standard deviation bands about the ensemble mean with the truth and adapted reference solution at three internal grid points on the 224×32 grid. For a fixed ensemble size ($N_p = 50$), spread sizes are shown for different numbers of EOFs: $n_\xi \equiv 0.9$ (magenta) and $n_\xi \equiv 0.5$ (cyan).

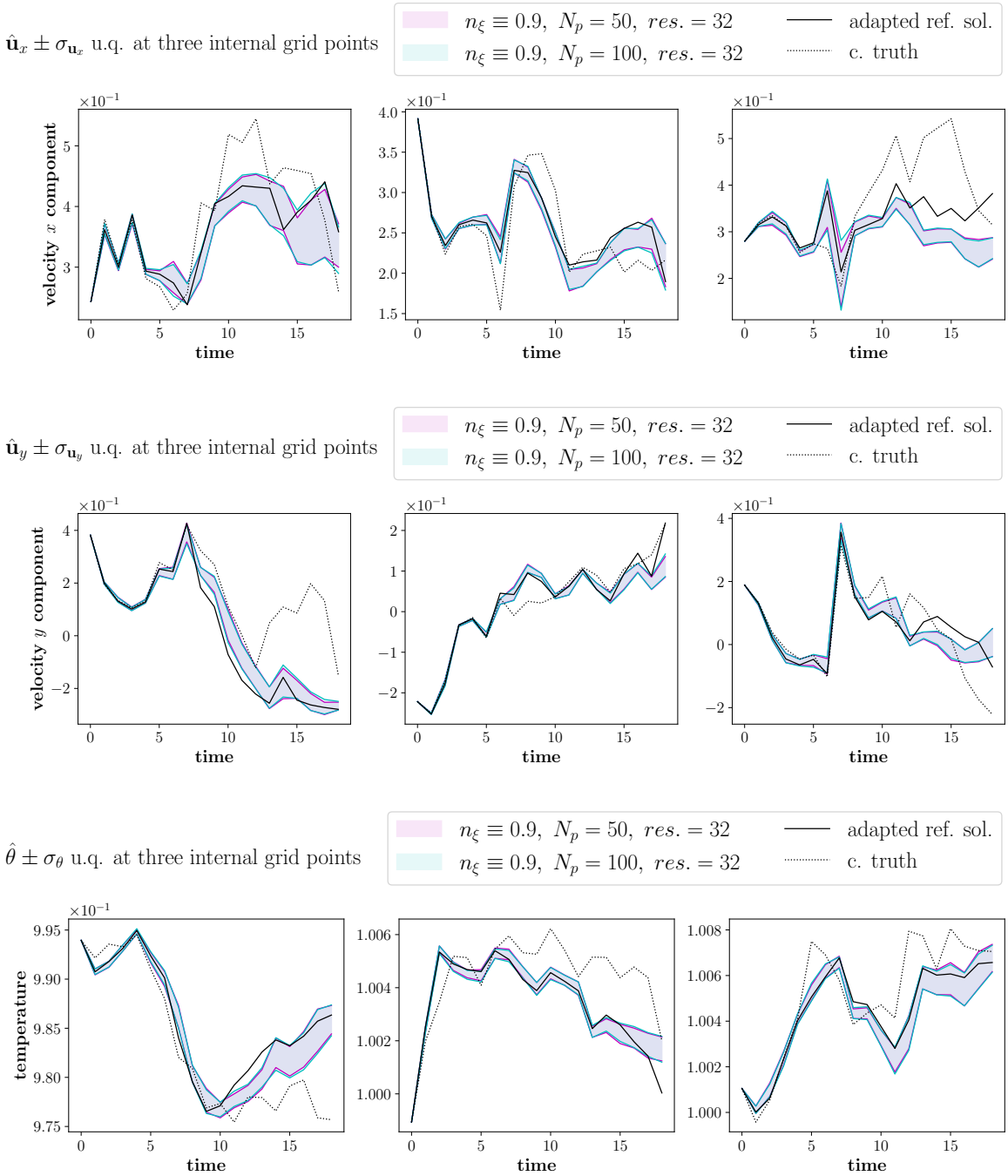

FIGURE 4.53: Uncertainty quantification plots comparing one standard deviation bands about the ensemble mean with the truth and adapted reference solution at three internal grid points on the 224×32 grid. For a fixed number of EOFs ($n_\xi \equiv 0.9$), spread sizes are shown for different ensemble sizes: $N_p = 50$ (magenta) and $N_p = 100$ (cyan).

mesh resolution.

In the uncertainty quantification plots, the effect of mesh refinement on spread size is evident. The SPDE solution on the 448×64 grid produces narrower spread sizes for both velocity and temperature fields. Additionally, the truth remains within the ensemble spread for a longer duration on the 448×64 grid compared to the 224×32 grid. These observations suggest that the stochastic parameterization remains consistent under grid refinement.

Global comparison

The plots in Figures 4.52–4.54 illustrate the impact of different model parameters (n_ξ, N_p, mesh resolution) on the ensemble spread at three internal grid points. These plots also provide insight into the accuracy of the SPDE solution, as they include both the adapted reference solution and the true solution. However, this evaluation is limited to only three locations in the grid. Moreover, assessing the effect of different model parameters on model accuracy solely from these plots is difficult. To facilitate a more quantitative and global comparison, this section examines the relative L^2 errors of SPDE realizations for different model parameters.

Figure 4.55 presents the ensemble mean of relative L^2 distances between the SPDE solution and the coarse-grained solution. The left plot displays the relative L^2 errors for temperature, while the right plot shows the relative L^2 errors for velocity. The results indicate that varying the ensemble size and the number of EOFs has no significant effect on the L^2 errors for either coarse grid. However, a substantial reduction in L^2 error is observed when increasing the grid resolution from 224×32 to 448×64. Additionally, the rate of increase in L^2 error is lower for the 448×64 grid compared to the 224×32 grid. These findings further confirm the consistency of stochastic parameterization under grid refinement.

4.2.5 Deterministic model versus stochastic model

To compare the performance of the stochastic model relative to the deterministic model, we compute the relative L^2 errors of ensemble members and the deterministic model with respect to the truth. The results are shown in Figure 4.56, which also includes the relative L^2 errors of the adapted reference solution for different mesh resolutions.

For velocity, the L^2 error of the adapted reference solution on both mesh resolutions is lower than that of the corresponding deterministic model solution, in particular towards the end of the simulation window. This can be attributed to the inclusion of unresolved scales in the adapted reference solution, which helps maintain closer agreement with the coarse-grained fine-grid solution. However, the advantage of the adapted reference solution over the deterministic model is less evident for the temperature field. The deterministic model exhibits lower L^2 errors than the adapted reference solution (on both meshes) for most of the simulation. The L^2 error of the

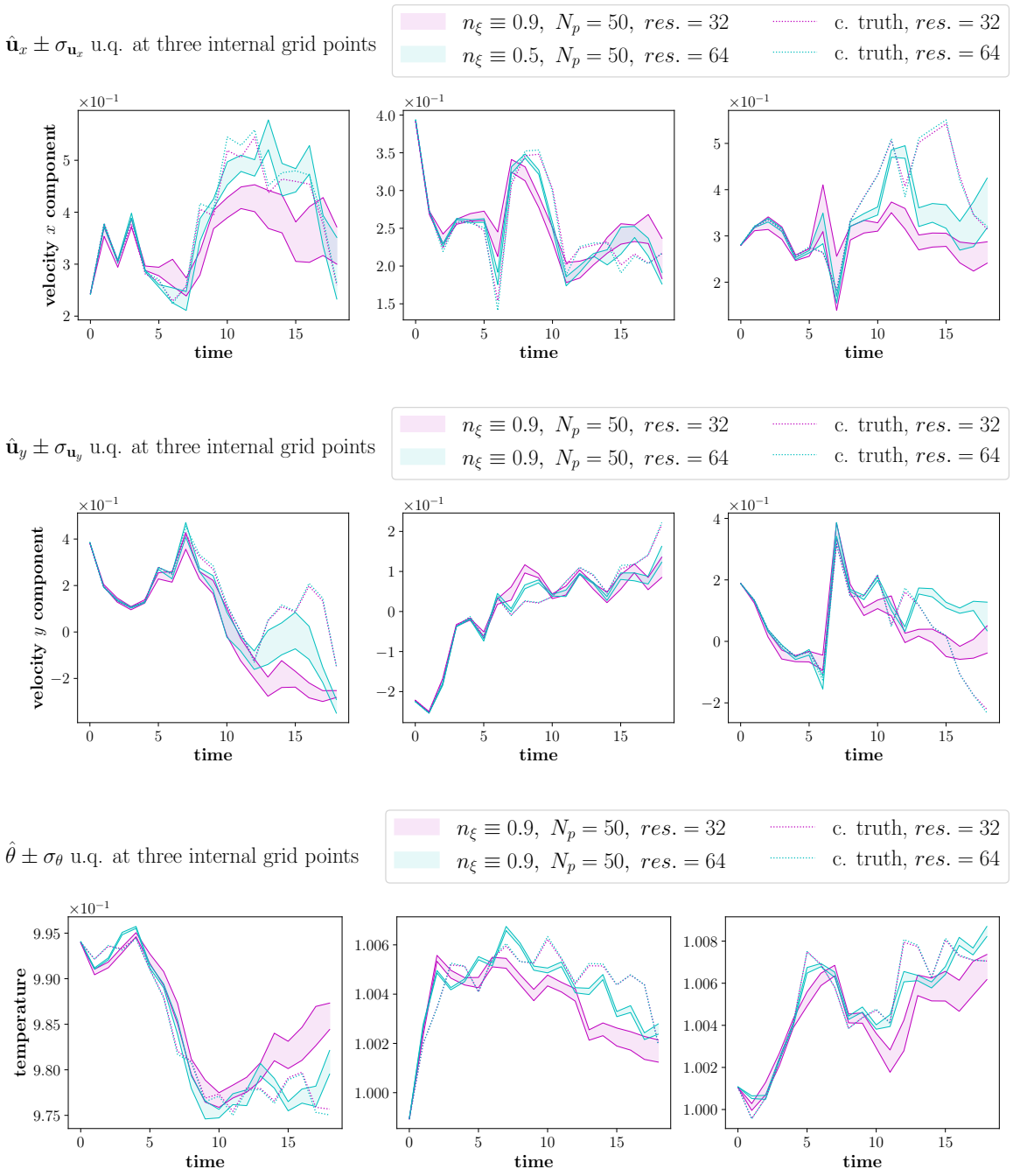

FIGURE 4.54: Uncertainty quantification plots comparing one standard deviation bands about the ensemble mean with the truth at three internal grid points. For a fixed number of EOFs ($n_\xi \equiv 0.9$) and ensemble size ($N_p = 50$), spread sizes are shown for different grid resolutions: 224×32 (magenta) and 448×64 (cyan).

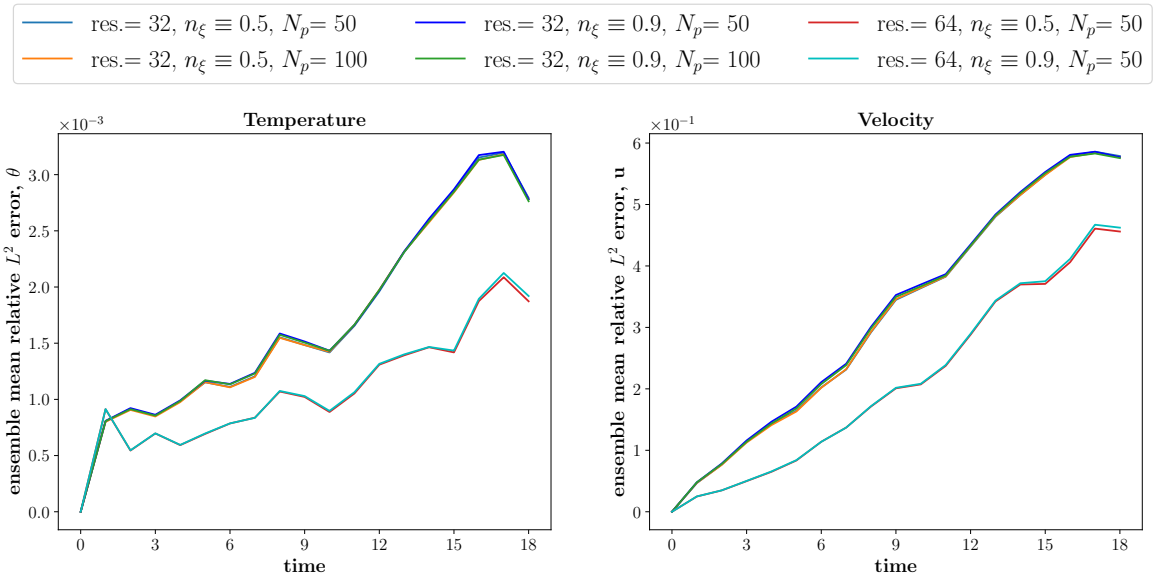

FIGURE 4.55: Relative L^2 distance between SPDE ensemble and truth for temperature (left) and velocity (right) averaged over all ensemble members. The results are shown for different model configurations.

adapted reference solution drops below that of the deterministic model only after approximately 14 to 16 time units. Nevertheless, this reduction in L^2 error is a positive indication of the effectiveness of the stochastic parameterization.

Since the stochastic model is an approximation of the adapted reference solution, we expect the L^2 errors of ensemble members to behave similarly to those of the adapted reference solution. In Figure 4.56, the colored bands represent the one-standard-deviation region around the ensemble mean of the relative L^2 error. Interestingly, these bands follow the deterministic solution more closely than the adapted reference solution. This suggests that, on average, the stochastic model does not offer a significant advantage over the deterministic model, as the L^2 error of a typical ensemble member is comparable to that of the deterministic solution.

However, the stochastic model generates an ensemble of solutions, and some ensemble members may achieve lower L^2 errors than the deterministic model. To investigate this further, we compute the L^2 errors for individual ensemble members averaged over all time steps and identify the ensemble member with the lowest L^2 error. The results, shown in Figure 4.57, reveal that the best-performing ensemble member consistently has a lower L^2 error than the deterministic model solution at all time steps on both grids (224×32 and 448×64).

To further assess model accuracy, we compare the vorticity field of the best-performing ensemble member with the deterministic solution and the truth at $t = 45$ (after 18 time units). Figures 4.58 and 4.59 present the results for the 224×32 and 448×64 grids, respectively. On the 224×32 grid, notable differences emerge between the deterministic and stochastic model solutions. While both models fail to fully

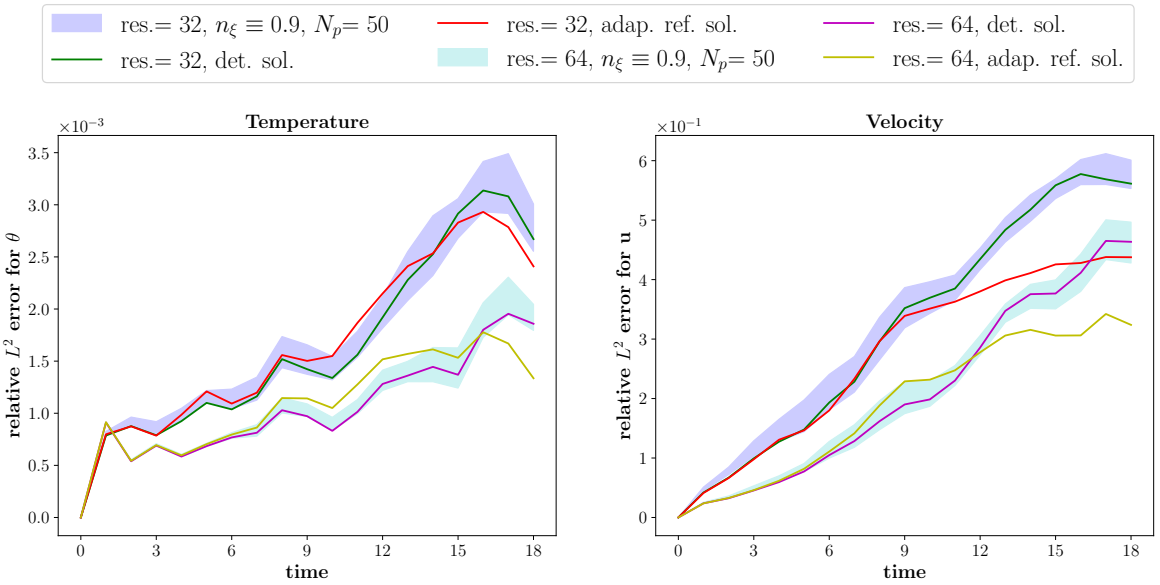

FIGURE 4.56: Comparison of relative L^2 errors between the stochastic model solution, adapted reference solution, and deterministic model solution. The colored bands represent one standard deviation regions around the ensemble mean of L^2 errors of stochastic model solution.

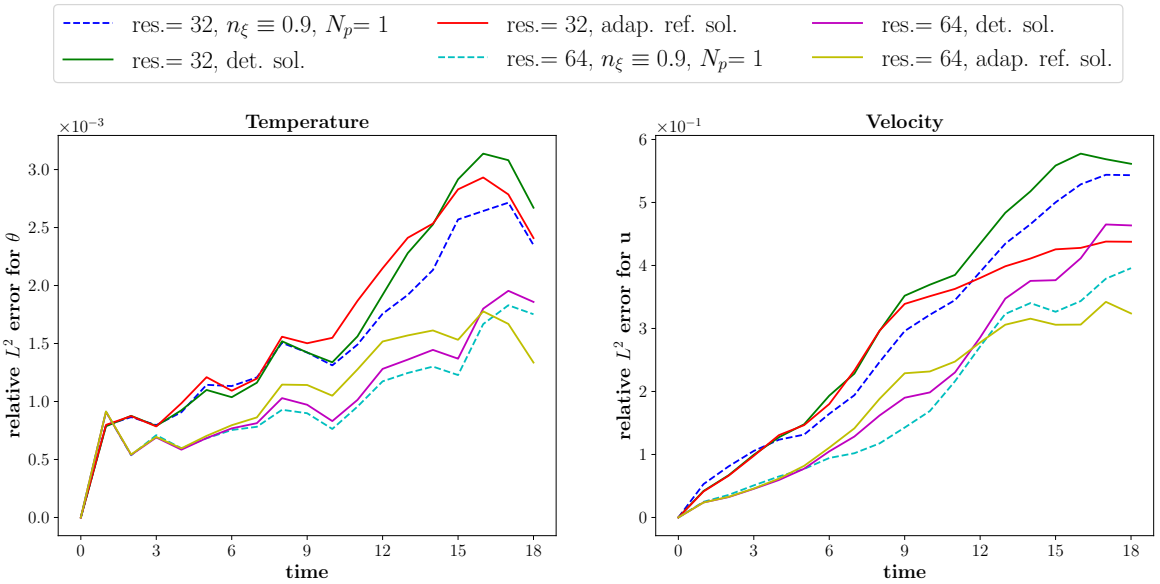

FIGURE 4.57: Comparison of relative L^2 errors for the best-performing SPDE ensemble member, the adapted reference solution, and the deterministic model solution. Dashed lines indicate the ensemble member with the lowest L^2 error among all SPDE realizations.

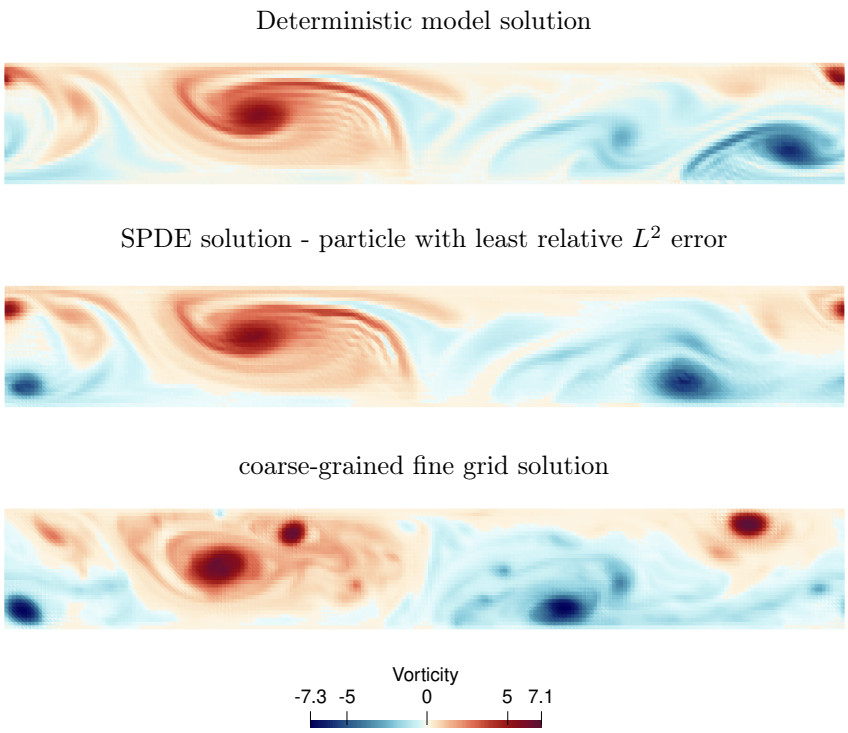

FIGURE 4.58: Vorticity fields at $t = 45$ from the best-performing SPDE ensemble member, the deterministic model solution, and the coarse-grained fine-grid solution on the 224×32 grid.

capture certain large-scale flow features, the stochastic model solution appears visibly closer to the truth.

The accuracy of both models improves significantly when the grid resolution is increased to 448×64. However, as observed in the 224×32 case, the stochastic model continues to outperform the deterministic model. The stochastic model solution successfully captures most of the large-scale flow structures present in the coarse-grained solution, whereas the deterministic model still fails to reproduce some vortical flow structures. For instance, the vortex in the lower-left corner (see Figure 4.59) is better captured by the stochastic model, further demonstrating its advantage over the deterministic approach.

4.2.6 Discussion and outlook

One of the main findings of our work is that the SPDE with OU noise outperforms the SPDE with Gaussian noise. We have shown that the approximation of times series data using discrete OU processes instead of standard normal distribution leads to better uncertainty quantification. The use of OU processes lead to an increased ensemble spread size and, smoother and more accurate temperature fields.

Time series resulting from the SVD decomposition of the observation data $(\mathbf{u} - \overline{\mathbf{u}})\Delta t$ are found to be highly correlated. This indicates that the observation data are also

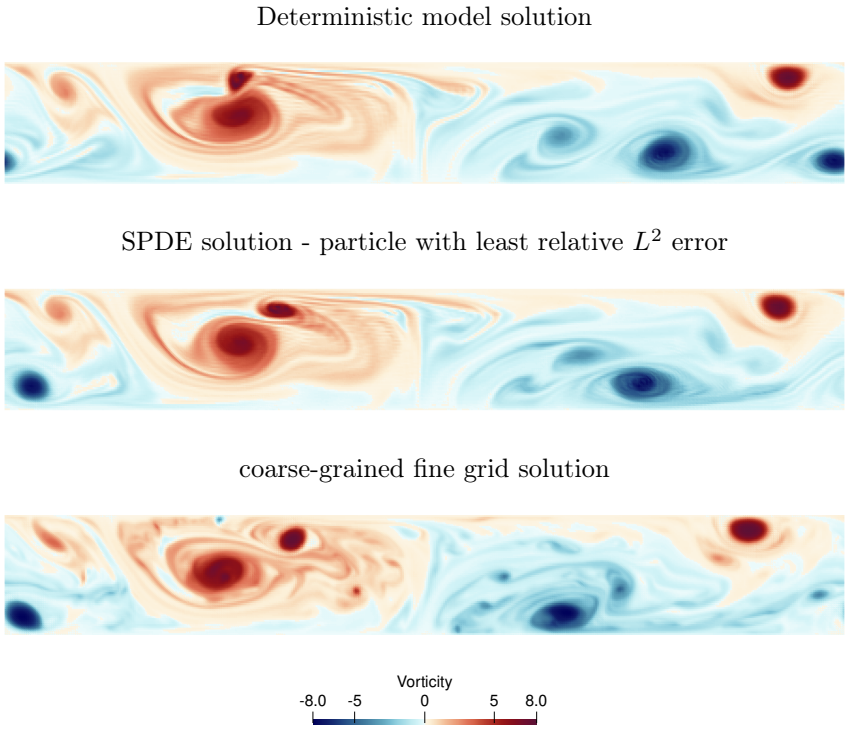

FIGURE 4.59: Vorticity fields at $t = 45$ from the best-performing SPDE ensemble member, the deterministic model solution, and the coarse-grained fine-grid solution on the 448×64 grid.

highly correlated in time. Figure 4.60 shows the ACF plots of observation data $(\mathbf{u}-\overline{\mathbf{u}})\Delta t$ at 100 different nodes for the 224×32 grid. The figure also presents the mean of ACF values over all nodes in the grid. It can be observed that the mean ACF value drops to zero only for a lag period of more than 50 time steps. These results indicate that the average decorrelation time is at least 50 Δt.

The fact that the consecutive column entries of data matrix $\Delta \boldsymbol{X}$ are correlated is not surprising. We created the matrix $\Delta \boldsymbol{X}$ by recording the Lagrangian trajectory differences $(\mathbf{u} - \overline{\mathbf{u}})\Delta t$ at an interval of size Δt. For a small value of Δt, the length of an increment of a Lagrangian flow path is proportional to the velocity and to the time step size Δt (Resseguier et al., 2020). The residual flow path $(\mathbf{u} - \overline{\mathbf{u}})\Delta t$ begins to act as a Brownian motion only when the time interval between the recordings $(\mathbf{u} - \overline{\mathbf{u}})\Delta t$ becomes larger than the correlation time of the small-scale Lagrangian velocities $(\mathbf{u} - \overline{\mathbf{u}})$ (Resseguier et al., 2020).

The ACF plots in Figure 4.60 show that the residual flow paths become decorrelated only after 50 time steps. If we reformulate the data matrix $\Delta \boldsymbol{X}$ by considering only every 50th data entry of the original data matrix, its SVD should lead to a time series whose values are decorrelated and hence closely matching a Gaussian distribution. This approach was also followed by Crisan et al. (2023b) in their study of stochastic shallow water equations for model calibration and considered only decorrelated $(\mathbf{u} - \overline{\mathbf{u}})\Delta t$

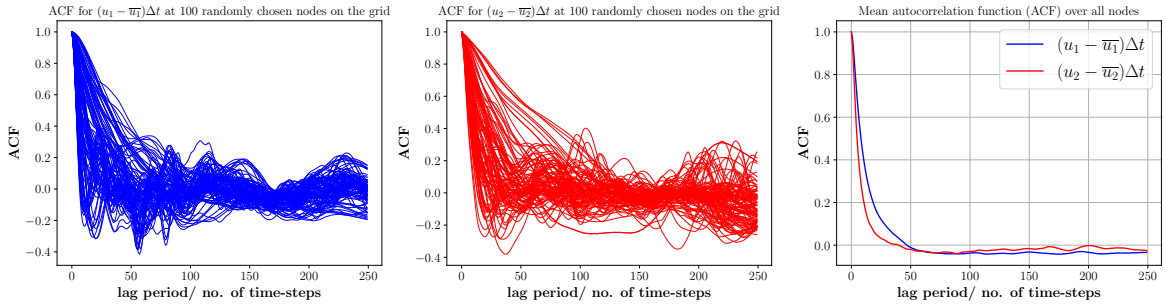

FIGURE 4.60: ACF plots of the observation data $(\mathbf{u} - \overline{\mathbf{u}})\Delta t$ for the 224×32 grid. The first two plots corresponds to the ACF values (at different lag times) for x and y components of the flow increments $(\mathbf{u} - \overline{\mathbf{u}})\Delta t$ at 100 randomly selected nodes, respectively. The third plot shows the mean of ACF values over all grid nodes.

values in the data matrix $\Delta \boldsymbol{X}$ for estimation of $\boldsymbol{\xi}_i$.

The calculation of $\boldsymbol{\xi}_i$ using decorrelated data did not lead to better results for our model (results not shown here). The temperature fields still contained many artifacts and there was no change in the ensemble spread sizes (for both velocity and temperature fields). This limitation likely stems from the insufficient quantity of observation data available for the SVD. For the grid of size 224×32, the observation data matrix $\Delta \boldsymbol{X}$ has a size 451×14784. The selection of every 50th row entry reduces the matrix size to 10×14784. The SVD of this matrix results in a times series matrix of size 10×10 and an EOF matrix of size 10×14784. The number of elements (10) in the time series matrix are not enough to model a Gaussian distribution accurately. The SVD of observation matrix $\Delta \boldsymbol{X}$ (with decorrelated data entries in the rows) can lead to a time matrix with decorrelated time series only if the number of rows are large enough.

One possible solution to the problem of insufficient data in the matrix $\Delta \boldsymbol{X}$ is to record the Lagrangian trajectory data for longer periods of time. However, this may be difficult to achieve in practice. It is possible that after a certain period of time the unresolved velocity is not stationary anymore. For example, in our test case, even though we had Lagrangian trajectory data from $t = 27$ to $t = 54$, we only used the data from $t = 27$ to $t = 35$ for model calibration. This is because the unresolved velocity does not remain stationary after approximately $t = 35$. For such situations, we believe that modeling the time series using OU processes is a better solution.

The numerical investigation of stochastic atmosphere model presented here is limited in scope. In our analysis, we neglected the parameterization terms which account for the rotation. These terms are $\hat{\mathbf{z}} \times \sum_i \boldsymbol{\xi}_i \circ \mathrm{d}W^i + \sum_{i=1}^{N} \nabla(\boldsymbol{\xi} \cdot \mathbf{R}) \circ \mathrm{d}W^i$. In addition to this, we also assumed that the vector fields $\boldsymbol{\xi}_i$ are divergence-free. To see the impact of these assumptions on the stochastic model performance, we did two preliminary tests. In the first test, we did numerical simulation of the stochastic model which included the rotation parameterization terms. The vector field $\boldsymbol{R}$ is a vector potential of the Coriolis parameter, $\mathrm{curl}(\mathbf{R}) = f\hat{\mathbf{z}}$. We assumed the vector field $\boldsymbol{R}$ to be $\mathbf{R} = (-yf, 0)$. In the second test, we removed the divergence-free constraint for the correlation vectors

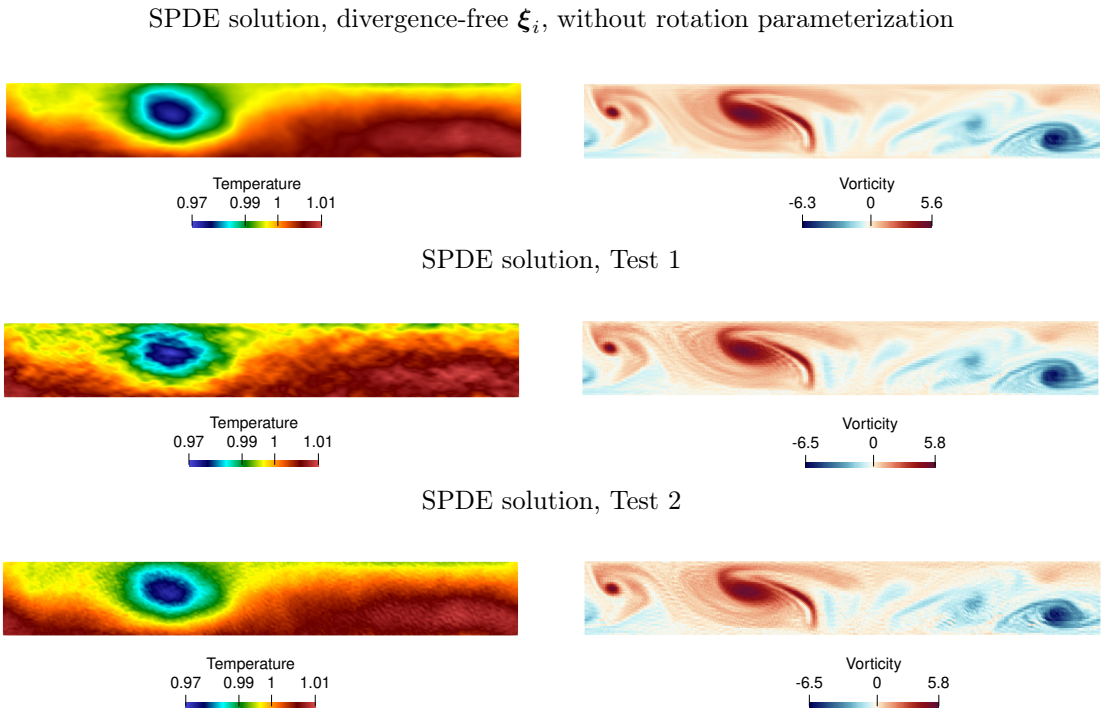

FIGURE 4.61: Comparison of temperature and vorticity fields at $t = 45$ on the 224×32 grid. The top row shows the SPDE solution with divergence-free $\boldsymbol{\xi}_i$ and no rotation parameterization. Test 1 (middle) includes rotation parameterization terms but assumes divergence-free $\boldsymbol{\xi}_i$. Test 2 (bottom) removes the divergence-free constraint on $\boldsymbol{\xi}_i$ but excludes rotation parameterization.

$\boldsymbol{\xi}_i$ and ran the stochastic model.

Figure 4.61 presents the temperature and vorticity fields at $t = 45$ from these tests on 224×32 grid. The inclusion of rotation parameterization terms or removal of divergence-free constraint on $\boldsymbol{\xi}_i$ leads to noisy solutions, particularly in the temperature fields. The inclusion of rotation parameterization seems to make the solution noisier. This is also reflected in the ensemble spread sizes of the SPDE solution (see Figure 4.62). The ensemble spread size for the temperature fields have increased in size for both tests. The velocity fields on the other hand still exhibits the same ensemble spread size. Further analysis is warranted to fully understand the effects of including rotation parameterization and relaxing the divergence-free assumption on model accuracy and stability.

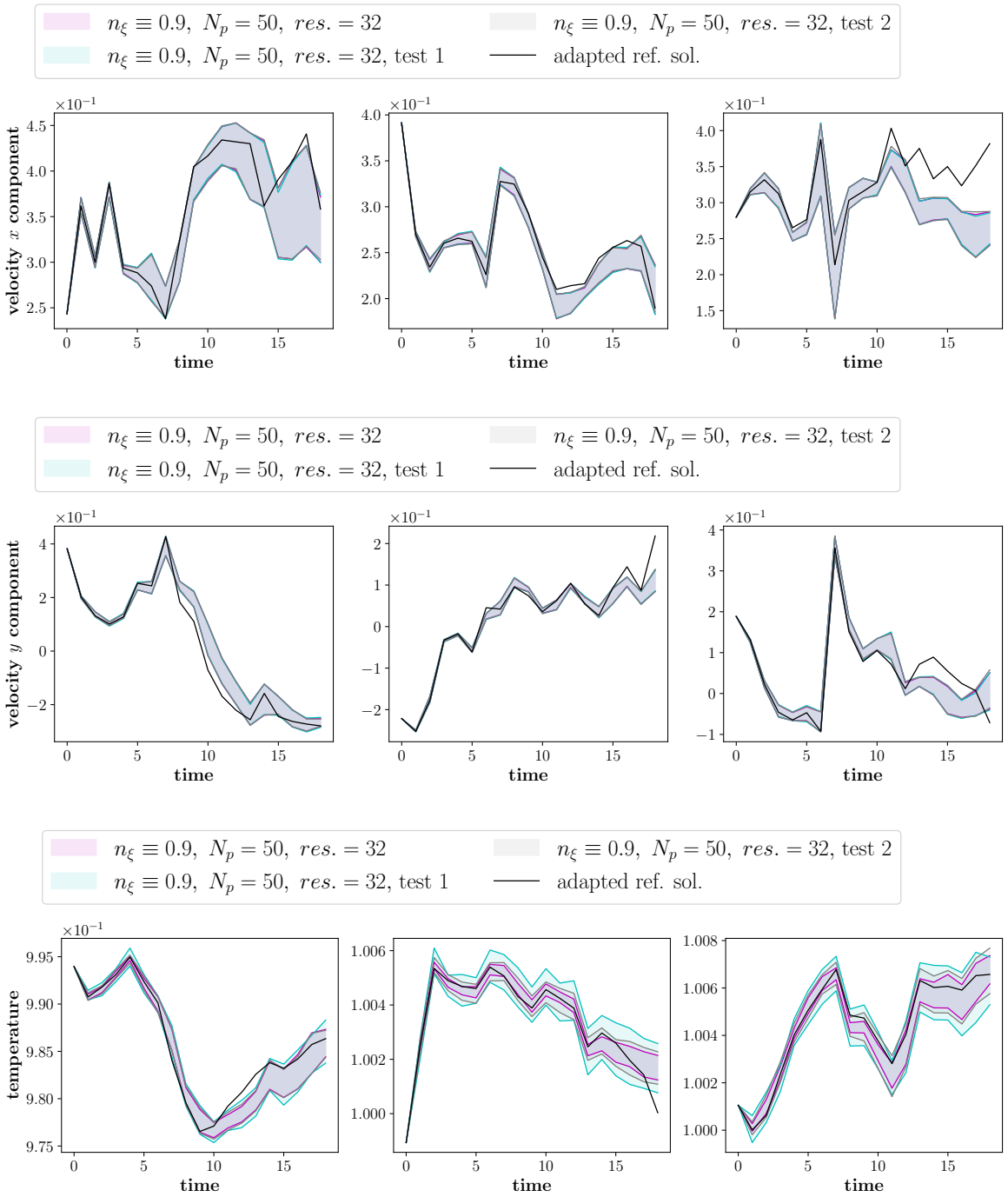

FIGURE 4.62: Uncertainty quantification plots comparing one standard deviation bands about the ensemble mean with the truth and adapted reference solution at three internal grid points on the 224×32 grid. For a fixed ensemble size ($N_p = 50$) and number of EOFs ($n_\xi \equiv 0.9$), the impact of rotation parameterization and the divergence-free assumption on $\boldsymbol{\xi}_i$ is assessed.

4.3 Stochastic climate model

Crisan et al. (2023a) derived a stochastic coupled ocean-atmosphere climate model using a stochastic variational principle based on Hasselmann's paradigm for stochastic climate models. In this formulation, stochasticity is introduced into the atmospheric component via stochastic Lie transport, while the ocean component remains deterministic. The governing equations of the model are

$$
\begin{aligned}
\text{Atmosphere}: \; & \mathrm{d}\mathbf{u}^a + (\mathbf{u}^a \mathrm{d}t + \sum_i \boldsymbol{\xi}_i \circ \mathrm{d}W^i) \cdot \nabla \mathbf{u}^a + \frac{1}{Ro^a} \hat{\mathbf{z}} \times \mathbf{u}^a \mathrm{d}t \\
& \qquad + \sum_i (u_1^a \nabla \xi_{i,1} + u_2^a \nabla \xi_{i,2}) \circ \mathrm{d}W^i = (-\frac{1}{C^a} \nabla \theta + \nu^a \Delta \mathbf{u}^a) \mathrm{d}t, \\
& \mathrm{d}\theta^a + \nabla \cdot (\theta^a \mathbf{u}^a) \mathrm{d}t + \sum_i (\boldsymbol{\xi}_i \circ \mathrm{d}W^i) \cdot \nabla \theta^a = (\gamma(\theta^a - \theta^o) + \nu^a \Delta \theta) \mathrm{d}t, \\
\text{Ocean}: \; & \frac{\partial \mathbf{u}^o}{\partial t} + (\mathbf{u}^o \cdot \nabla)\mathbf{u}^o + \frac{1}{Ro^o} \hat{\mathbf{z}} \times \mathbf{u}^o + \frac{1}{Ro^o} \nabla p^a = \sigma(\mathbf{u}^o - \mathbb{E}\mathbf{u}^a_{sol}) + \nu^o \Delta \mathbf{u}^o, \\
& \nabla \cdot \mathbf{u}^o = 0, \\
& \frac{\partial \theta^o}{\partial t} + \mathbf{u}^o \cdot \nabla \theta^o = \eta^o \Delta \theta^o.
\end{aligned}
\tag{4.8}
$$

In this section, we present numerical simulation results for this model (equations (4.8)). The correlation vectors $\boldsymbol{\xi}_i$ of the unresolved transport dynamics are obtained using high-resolution simulations of the deterministic version of the climate model. The equations for the deterministic climate model can be formulated as

$$
\begin{aligned}
\text{Atmosphere}: \; & \frac{\partial \mathbf{u}^a}{\partial t} + (\mathbf{u}^a \cdot \nabla)\mathbf{u}^a + \frac{1}{Ro^a} \hat{\mathbf{z}} \times \mathbf{u}^a + \frac{1}{C^a} \nabla \theta^a = \nu^a \Delta \mathbf{u}^a, \\
& \frac{\partial \theta^a}{\partial t} + \nabla \cdot (\mathbf{u}^a \theta^a) = \gamma(\theta^a - \theta^o) + \eta^a \Delta \theta^a, \\
\text{Ocean}: \; & \frac{\partial \mathbf{u}^o}{\partial t} + (\mathbf{u}^o \cdot \nabla)\mathbf{u}^o + \frac{1}{Ro^o} \hat{\mathbf{z}} \times \mathbf{u}^o + \frac{1}{Ro^o} \nabla p^o = \sigma(\mathbf{u}^o - \mathbf{u}^a_{sol}) + \nu^o \Delta \mathbf{u}^o, \\
& \nabla \cdot \mathbf{u}^o = 0, \\
& \frac{\partial \theta^o}{\partial t} + \mathbf{u}^o \cdot \nabla \theta^o = \eta^o \Delta \theta^o.
\end{aligned}
\tag{4.9}
$$

We solve both climate model formulations ((4.8) and (4.9)) on a rectangular domain Ω, with periodic boundary conditions in the x direction. The physical dimensions of the domain are 27237 km (in x) and 3891 km (in y), which, after non-dimensionalization, correspond to $\Omega = [0, 7] \times [0, 1]$ (see Figure 4.63).

The atmosphere and ocean variables are both non-dimensionalized using the same characteristic velocity (denoted by U) and characteristic length (denoted by L). The

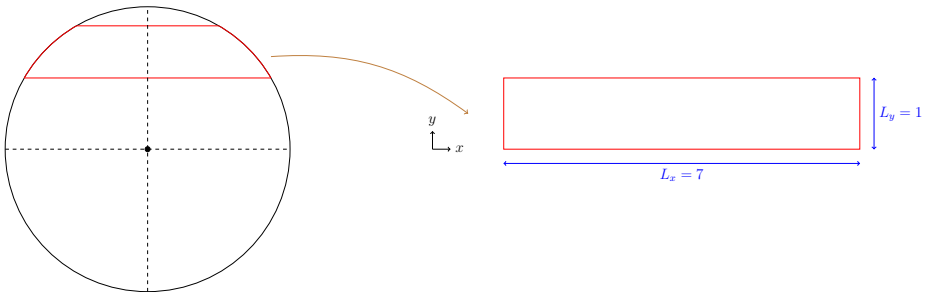

FIGURE 4.63: Schematic representation of the 2D domain (right) used for the climate model simulations.

TABLE 4.5: Grid parameters for the atmosphere and ocean components of the climate model

Parameters	**Fine grid**	**Coarse grid**
Number of elements, $N_x \times N_y$	896×128	224×32
Smallest element size, Δx	$1/128$ (~ 30 km)	$1/32$ (~ 120 km)
Time-step size, Δt	0.010 (~ 8 min.)	0.04 (~ 32 min.)
Eddy viscosity, ν^a, ν^o	$1/(8 \times 10^4)$	$1/10^4$
Diffusion coefficient, η^a, η^o	$1/(8 \times 10^4)$	$1/10^4$

key non-dimensional parameters in the model have the form

$$Ro^a = Ro^o = \frac{U}{Lf}, \; C^a = \frac{U^2}{\kappa\Theta}, \; \kappa = c_v \left(\frac{R}{p_0}\right)^{\frac{2}{7}}$$

where $f = 2\Omega_e \sin\varphi_e$ is the Coriolis parameter and Θ is a reference temperature.

Based on typical geophysical scales, we assume: $L = 3891$ km, $U = 80$ m/s, $T = 300$ K, $\varphi = 27.5°$, and compute the non-dimensional parameters: $Ro^a = Ro^o = 0.3$, $C^a = 0.02$. The variables ν^a, ν^o and η^a, η^o denote eddy viscosity and diffusion coefficient terms, respectively. These variables depend on the spatial resolution of the domain.

Free-slip conditions are applied for velocity in both the ocean and atmosphere:

$$u_2 = 0, \quad \frac{\partial u_1}{\partial y} = 0.$$

For temperature, insulated boundary conditions are imposed:

$$\frac{\partial \theta}{\partial y} = 0.$$

We consider two different mesh configurations for our experiments: the fine grid consists of 896×128 elements whereas the coarse grid has 224×32 elements. Table 4.5 displays the parameters used in the numerical simulations for these grids.

4.3.1 Fine grid simulation

We solve the deterministic climate model (4.9) on a fine grid with 896×128 elements. The initial atmospheric velocity is set to represent a zonal jet in the northern hemisphere, with profile

$$u_1^a(x, y, t = 0) = \begin{cases} 0 & \text{for } y \leq y_0, \\ \exp\left(\dfrac{\alpha^2}{(y - y_0)(y - y_1)}\right) \exp\left(\dfrac{4\alpha^2}{(y_1 - y_0)^2}\right) & \text{for } y_0 < y < y_1, \\ 0 & \text{for } y \geq y_1, \end{cases}$$

$$u_2^a(x, y, t = 0) = 0.$$

where $\alpha = 1.64$, $y_0 = 1/14$, and $y_1 = 13/14$. This formulation generates a smooth, localized jet centered in the meridional direction. The initial atmospheric temperature is given by

$$\theta^a(x, y, t = 0) = 1 + \theta_0,$$

where θ_0 is obtained by solving the balance equations

$$\frac{\partial \theta_0}{\partial y} = -\frac{C^a}{Ro^a} u_1^a, \quad \frac{\partial \theta_0}{\partial x} = 0.$$

The ocean is set to be at rest at $t = 0$: $u^o(x, y, t = 0) = (0, 0)$. We choose the initial ocean temperature to be

$$\theta^o = 1 + \theta_0 + \hat{\theta} \cos\left(\frac{\pi y}{2}\right) e^{-c_1(x - x_0)^2} e^{-c_2(y - y_2)^2}, \tag{4.10}$$

where $\hat{\theta} = 0.01$, $c_1 = 4$, $c_2 = 81$, $x_0 = 3.5$, and $y_2 = 0.5$. Equation (4.10) represents a perturbation in the ocean temperature above the initial atmosphere temperature profile. Figure 4.64 shows the plots of initial conditions for the test on 896×128 grid .

We set the coupling coefficients to $\gamma = 10$, $\sigma = -0.1$, and run the deterministic model until $t = 45$ (approximately 27 days). Figure 4.65 presents the time series of atmospheric kinetic energy. After an initial spin-up phase of around 20 time units, the kinetic energy stabilizes, indicating that the model has reached a statistically steady state.

Figure 4.66 displays the velocity and temperature fields for both the atmosphere and ocean at $t = 25$. Both velocity fields exhibit multiscale structures, with a range of eddies and filaments. This is further illustrated by Figure 4.67, which shows the corresponding vorticity fields. The presence of diverse flow features, from large-scale eddies to fine filaments, suggests that the system has entered a dynamically rich regime.

To further investigate the temporal evolution of the flow, Figure 4.68 shows snapshots of the atmospheric vorticity field from $t = 30$ to $t = 45$. Over this time interval, the spatial structure of flow is fairly maintained: the eddies move around in the domain

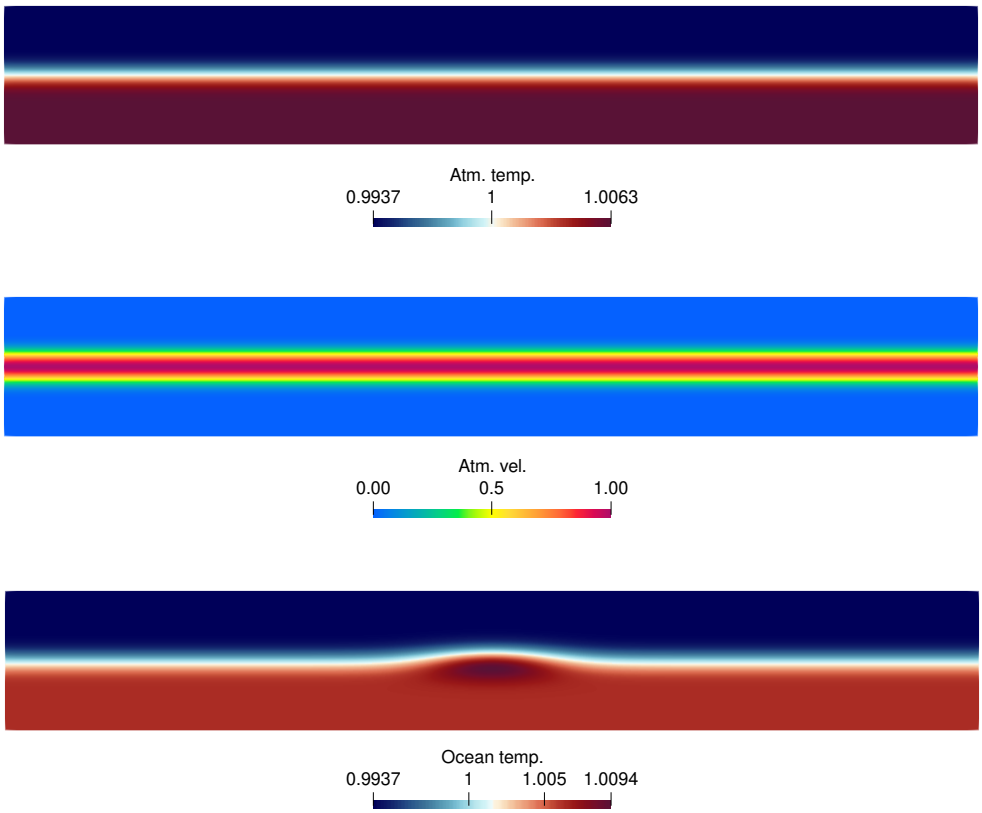

FIGURE 4.64: Initial atmospheric temperature (top), atmospheric velocity (middle), and ocean temperature (bottom) fields at $t = 0$. The ocean velocity is set to zero at $t = 0$.

without exhibiting much dissipation. We conclude that the flow has achieved a state of statistical equilibrium between $t = 25$ and $t = 45$. We use the atmosphere velocity data from this period to calibrate the stochastic model.

Stochastic model calibration

We use the difference between the Lagrangian trajectories generated by the high-resolution (896×128 grid) velocity field $\mathbf{u}$ and its coarse-grained version $\overline{\mathbf{u}}$ at different time-instances to estimate $\boldsymbol{\xi}_i$. The coarse-grained velocity is evaluated for the grid of size 224×32. A singular value decomposition (SVD) analysis of $(\mathbf{u} - \overline{\mathbf{u}})\Delta t$ reveals that the first 53, 20 and 10 empirical orthogonal functions (EOFs) explain 99%, 90%, and 70% of the total variance, respectively in the data. Figure 4.69 shows some of the estimated $\boldsymbol{\xi}_i$ for the coarse grid of size 224×32. The scale of flow structures exhibited by $\boldsymbol{\xi}_i$ decreases with increasing i. Relative to $\boldsymbol{\xi}_1$ which contains large-scale structures, $\boldsymbol{\xi}_{10}$ contains small-scale structures. This trend is also shown by the $\boldsymbol{\xi}_i$ that we obtained for the stochastic Navier-Stokes and stochastic atmosphere models.

The time series corresponding to each $\boldsymbol{\xi}$ is generally modeled as a Gaussian process. However, the autocorrelation function (ACF) of these time series reveal that the data (particularly corresponding to the first few $\boldsymbol{\xi}_i$) are highly correlated (see Figures 4.70

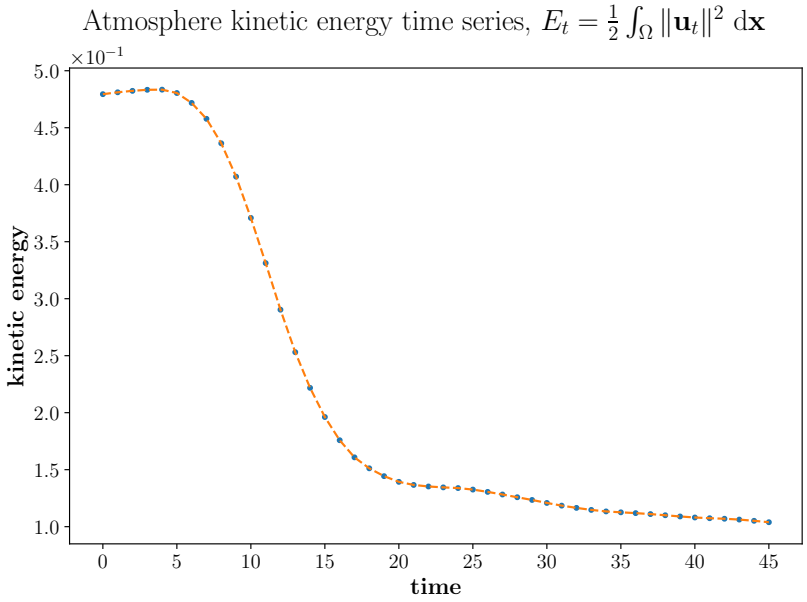

FIGURE 4.65: Time series of kinetic energy for the atmospheric component of the climate model over 45 time units.

and 4.71). The decorrelation time for the time series corresponding to first three $\boldsymbol{\xi}_i$ is between 50 to 150 time steps. Therefore, modeling these time series using standard normal distributions (which assume a decorrelation time of 1 time step) is not correct. We model the time series data using the OU processes (see Algorithm 3).

4.3.2 Stochastic model simulation

We run the stochastic climate model on a coarse grid of size 224×32 with the coarse-grained velocity and temperature fields (Figure 4.72 and 4.73) corresponding to $t = 25$ as initial conditions. Figure 4.72 displays the initial velocity and temperature fields for the stochastic climate model. Coarse graining procedure has led to a smoothening of these fields. In comparison to the high-resolution fields (Figure 4.66), the coarse-grained fields have lost sharp gradients (both for velocity and temperature) in the flow. Moreover, the filaments present in the high-resolution atmosphere vorticity field (Figure 4.67) can no longer be seen in the coarse-grained vorticity field (Figure 4.73).

The stochastic climate model is simulated for 20 time units (from $t = 25$ to $t = 45$). We use 53 EOFs (which explains 99% of the total variance) for the simulation. Each realization of the SPDE starts from the same initial condition.

Figure 4.74 shows the atmosphere vorticity fields obtained from three independent realizations/particles of the SPDE after 10 time units i.e., at $t = 35$. These particles, although starting from same initial condition, have developed different vortical structures over time due to the stochastic parameterization. Figure 4.74 also displays the results obtained from a deterministic model simulation (without any parameterization) and the coarse-grained high-resolution solution (henceforth denoted as the truth). It can

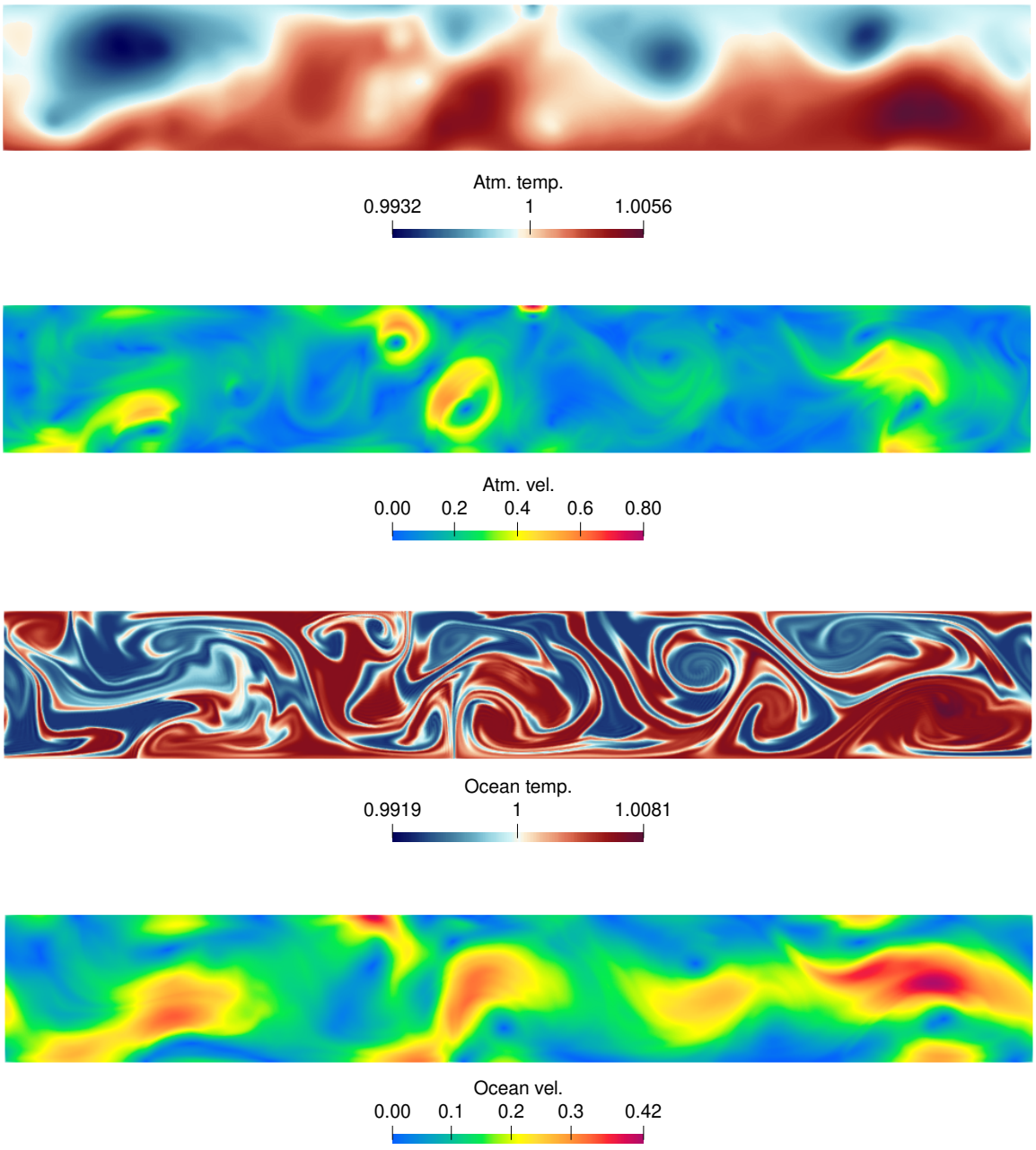

FIGURE 4.66: Atmospheric (top two) and oceanic (bottom two) velocity and temperature fields at $t = 25$ for the deterministic climate model simulation on the 896×128 grid.

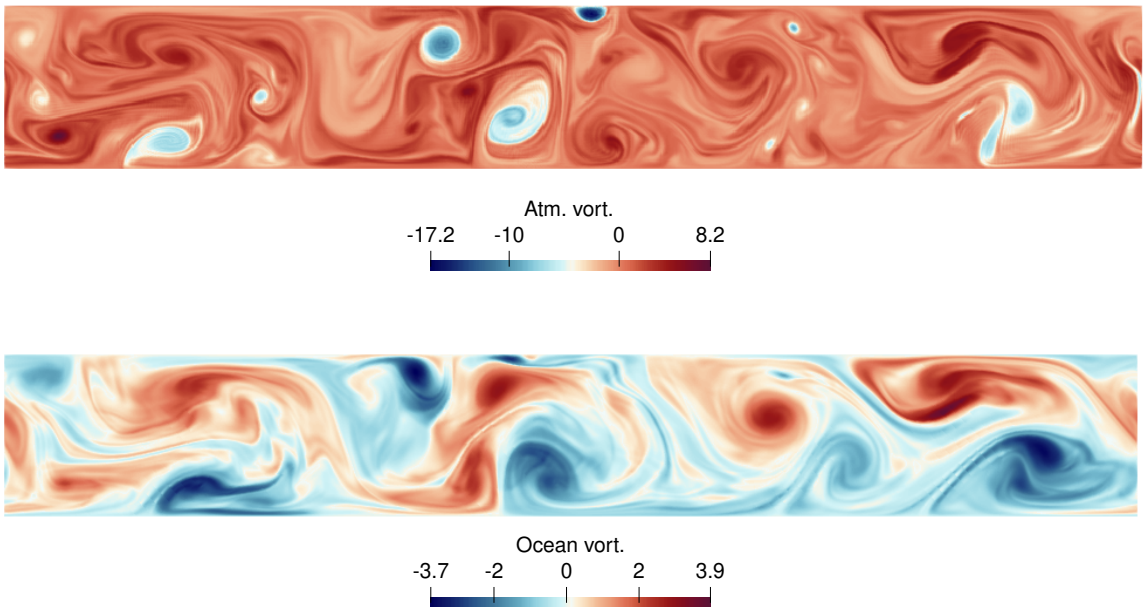

FIGURE 4.67: Atmospheric vorticity (top) and ocean vorticity (bottom) fields at $t = 25$ for the deterministic model simulation on the 896×128 grid.

be observed that the stochastic solutions closely match the truth at all the locations except the central region. This observation is also true for the deterministic solution. However, the advantage of stochastic solutions lie in their capability of representing the uncertainty. The stochastic solutions exhibit a lot of variability and hence spread in the vorticity fields near the central region. This indicates that one should be less confident about the results provided by the SPDE solution in this region. Interestingly, the correlation fields $\boldsymbol{\xi}_i$ (Figure 4.69) also capture more flow structures in the central region than elsewhere, suggesting that unresolved scales predominantly influence this region.

In order to quantify the uncertainty in the SPDE solution, we monitor the velocity and temperature fields at 84 uniformly distributed observation points in the grid (see Figure 4.75). Figures 4.76 and 4.77 show the stochastic simulation results. We compare the velocity and temperature values between the truth and the deterministic solution at six observation points. The stochastic ensemble captures the truth for a few time units before diverting. In general, the ensemble spread increases over time, suggesting increased uncertainty in the stochastic model solution as time progresses.

We analyze the SPDE results further by using ensemble mean, ensemble standard deviation (also called spread) and ensemble root mean square error (RMSE). We denote different realizations of an SPDE variable at a particular time instance by X_i, where $i = 1, 2, \ldots, N_p$ denotes the particle number. The ensemble mean is defined as

$$\hat{\mathbb{E}}(X_i) = \frac{1}{N_p} \sum_{i=1}^{N_p} X_i,$$

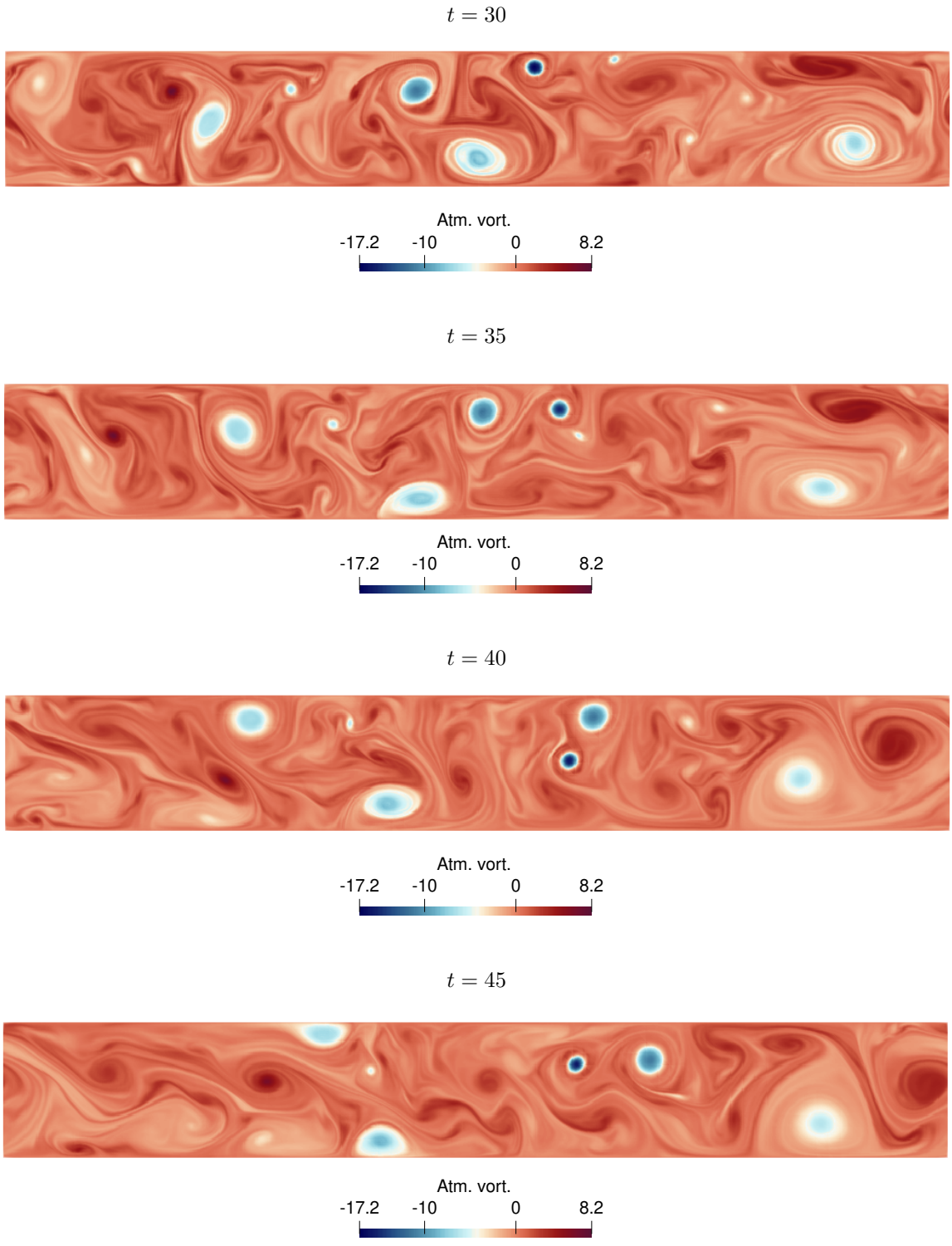

FIGURE 4.68: Evolution of atmosphere vorticity field over time. The number of small, medium, and large eddies remains roughly constant over the time interval.

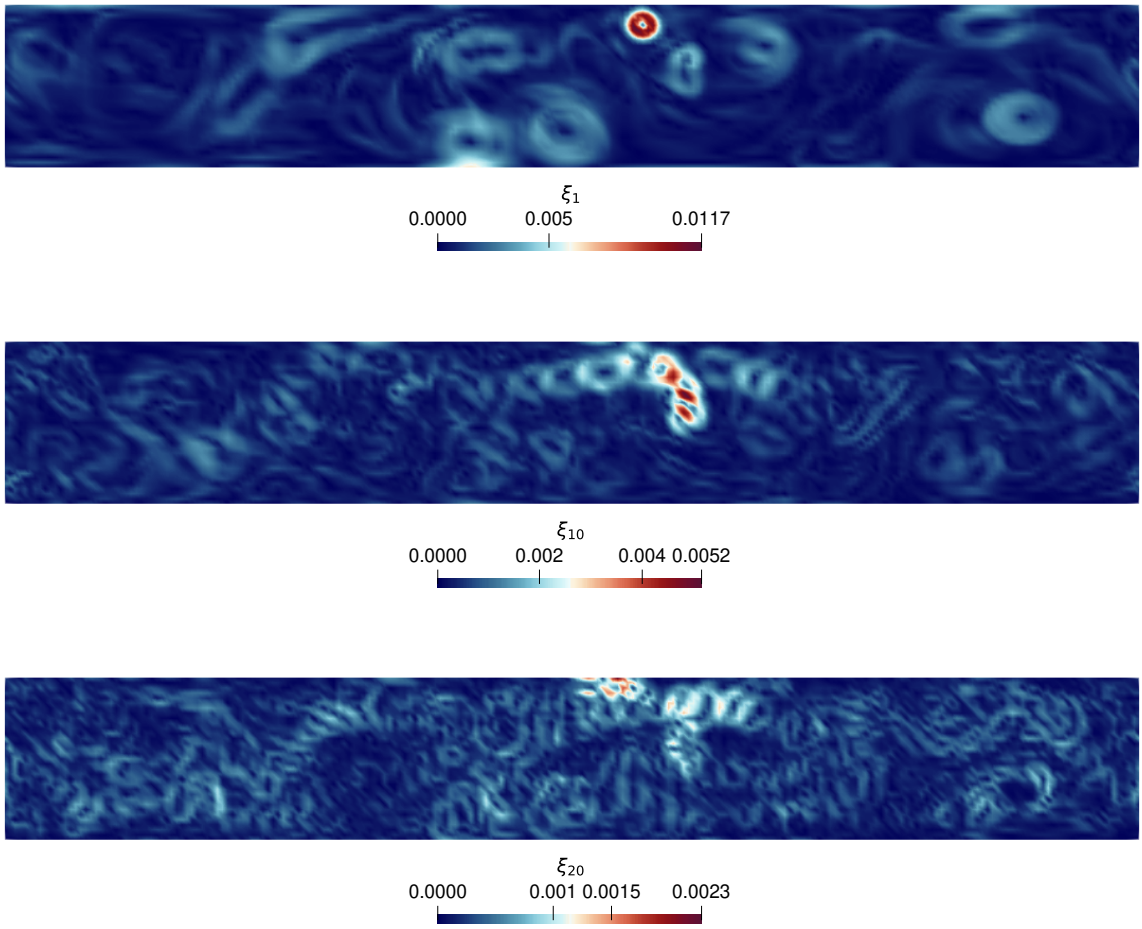

FIGURE 4.69: Estimated $\boldsymbol{\xi}_i$ for the coarse grid (224×32). The 1st (top), 10th (middle), and 20th (bottom) $\boldsymbol{\xi}_i$ are shown. The first 20 EOFs explain 90% of the total variance.

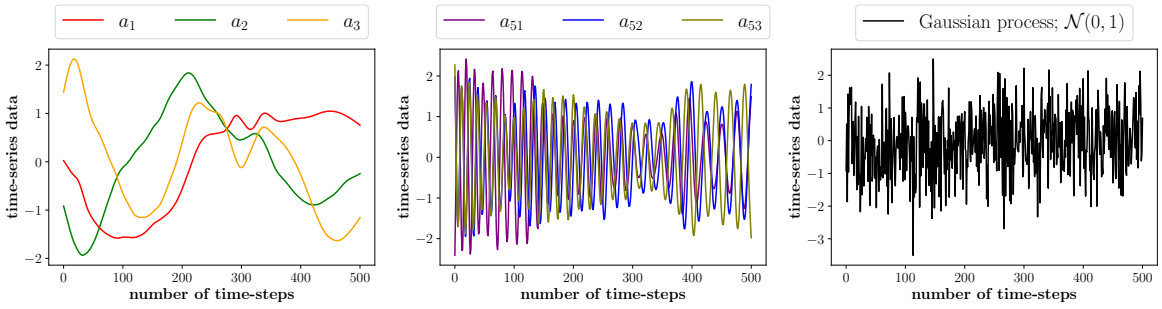

FIGURE 4.70: Time series plots corresponding to $\boldsymbol{\xi}_1$, $\boldsymbol{\xi}_2$, $\boldsymbol{\xi}_3$ (left) and $\boldsymbol{\xi}_{51}$, $\boldsymbol{\xi}_{52}$, $\boldsymbol{\xi}_{53}$ (center) for the coarse grid of size 224×32. For comparison, the time series generated by a Gaussian process is also shown (right).

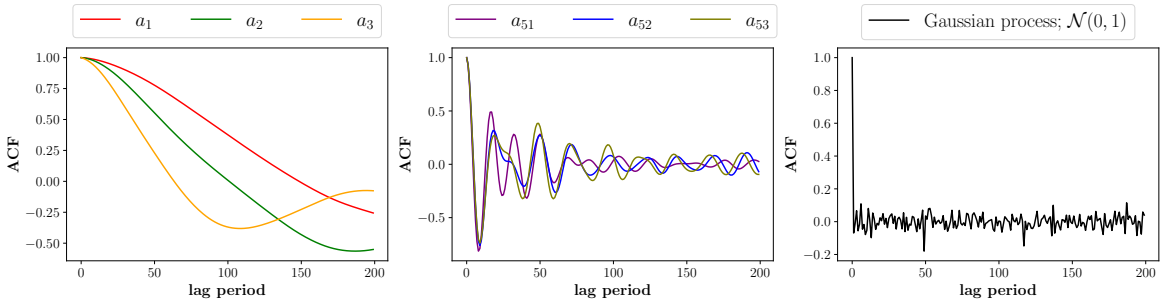

FIGURE 4.71: Autocorrelation function (ACF) plots for time series corresponding to $\boldsymbol{\xi}_1$, $\boldsymbol{\xi}_2$, $\boldsymbol{\xi}_3$ (left) and $\boldsymbol{\xi}_{51}$, $\boldsymbol{\xi}_{52}$, $\boldsymbol{\xi}_{53}$ (center) for the coarse grid of size 224×32. For comparison, the ACF plot for time series generated by a Gaussian process is also shown (right).

TABLE 4.6: Parameter values for different configurations of the stochastic climate model

Configuration	**Ensemble size,** N_p	**Variance level in** %
1	50	70
2	50	99
3	100	70
4	100	99

the ensemble spread is defined as

$$\text{Spread}(X_i) = \sqrt{\frac{1}{N_p}\sum_{i=1}^{N_p}\left(X_i - \hat{\mathbb{E}}(X_i)\right)^2},$$

and the ensemble RMSE with respect to truth X_{truth} is defined as

$$\text{RMSE}(X_i, X_{\text{truth}}) = \sqrt{\frac{1}{N_p}\sum_{i=1}^{N_p}(X_i - X_{\text{truth}})^2}$$

where X_{truth} represents the coarse-grained high-resolution field.

Figures 4.78 and 4.79 display the plots for the evolution of ensemble spread and RMSE at six different locations on the grid. It can be observed that the size of ensemble spread is proportional to the RMSE (for at least 15 time units) at all the locations. This suggests that the error in the stochastic solution can be estimated by its own spread. This property makes the SPDE solution suitable for data assimilation methods (Resseguier et al., 2017).

Uncertainty quantification

We compare the impact of using different ensemble sizes and different number of $\boldsymbol{\xi}_i$ on the ensemble spread and RMSE. Four different model configurations are considered in the analysis (see Table 4.6).

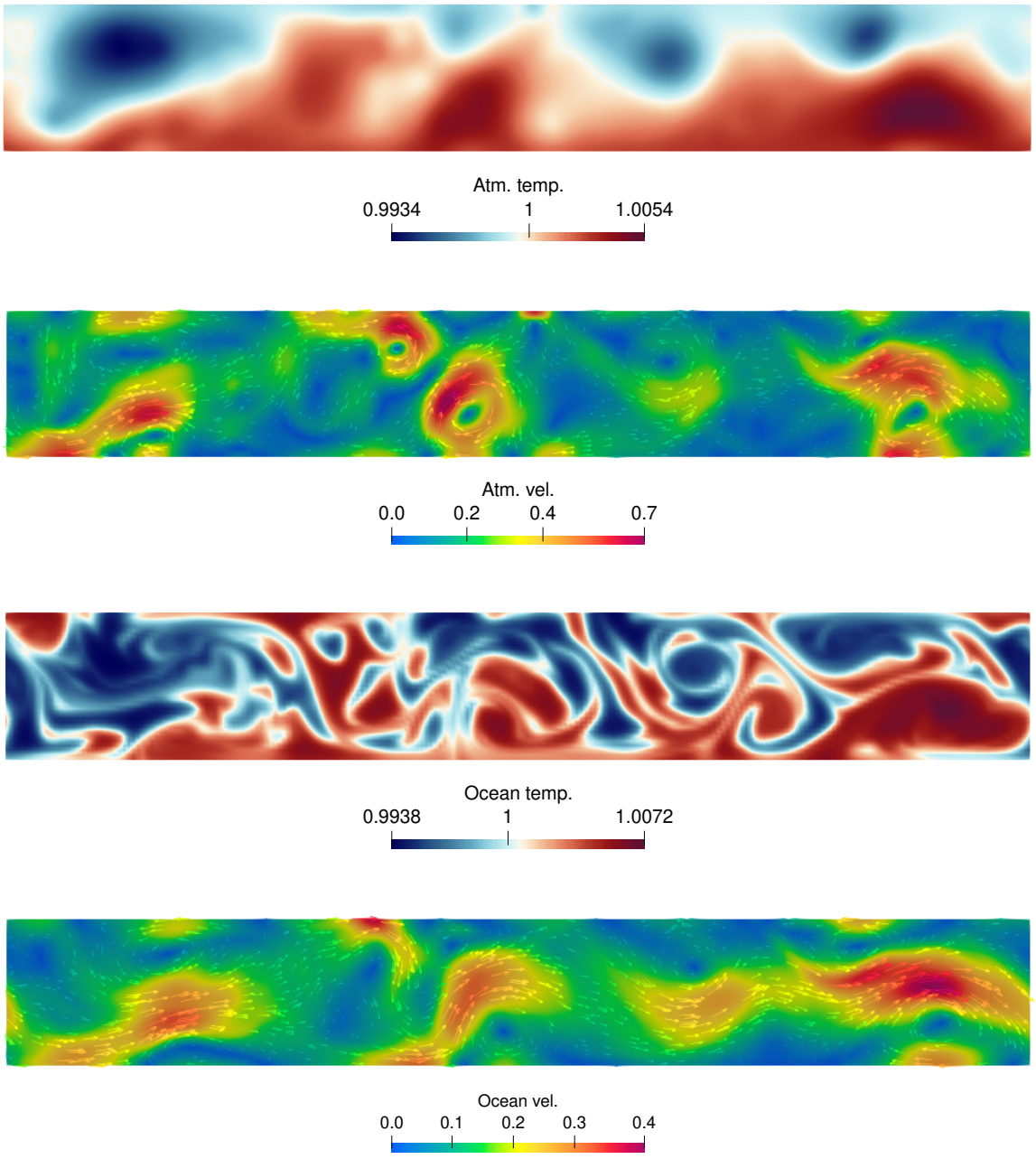

FIGURE 4.72: Coarse-grained velocity and temperature fields of the atmosphere (top two) and ocean (bottom two) at $t = 25$. These fields are obtained by filtering high-resolution (896×128) fields onto a grid of size 224×32.

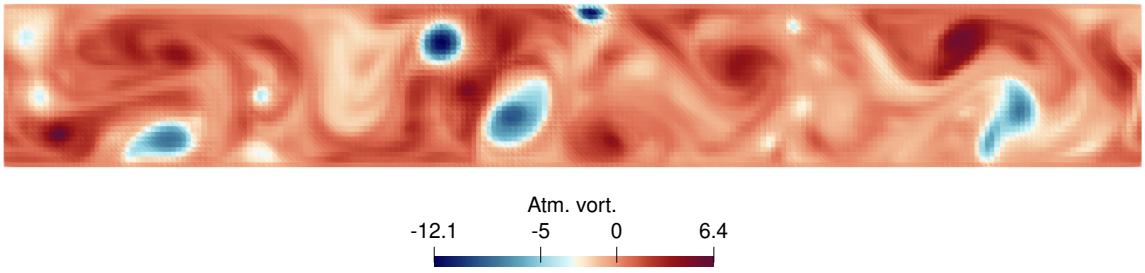

FIGURE 4.73: Initial vorticity field for the stochastic model simulations. This corresponds to the coarse-grained vorticity field at $t = 25$.

We calculate the averages of ensemble spread and RMSE over all the observation points (Figure 4.75) for different choices of ensemble sizes and different number of EOFs/$\boldsymbol{\xi}_i$. The results are plotted in Figure 4.80. In the initial phase of the simulation, the spread sizes are similar for all configurations. However, in the later stages, the effect of stochastic parameterization kicks in and we clearly see differences in the spread sizes. Maximum spread is generated when $N_p = 100$ and $n_\xi \equiv 0.99$ (99% variance level). The ensemble spread size increases with increase in the number of particles or the variance level captured by the EOFs. This confirms that our stochastic parameterization methodology is consistent with the ensemble size and the number of EOFs.

The effect of using different model parameters is less prominent on the RMSE in comparison to the spread size. Differences in RMSE for different model configurations only develop near the end of simulation time window. The average of ensemble spread size over the whole domain seems to develop in proportion to average RMSE only for 10 to 15 time units. After that, the RMSE keeps on growing unlike the spread size which stabilizes. In terms of RMSE, best results are obtained when $N_p = 50$ and $n_\xi \equiv 0.99$.

Stochastic versus deterministic ensemble

We perturb the atmosphere velocity field at $t = 25$ to create an ensemble of initial conditions

$$\mathbf{u}_{\text{pert}} = \mathbf{u}_0 + 0.2 \times r \times \mathbf{u}_0,$$

where $\mathbf{u}_0$ denotes the coarse-grained velocity field and $r \in \mathcal{N}(0, 1)$ is a random variable from a Gaussian distribution. The deterministic climate model is simulated on the coarse grid with these initial conditions to generate an ensemble of solutions. The same (perturbed) initial conditions are also used to run the stochastic climate model. We compare the results for 50 independent realizations of the deterministic and the stochastic model.

Figures 4.81 and 4.82 compare the evolution of stochastic and deterministic ensembles for the atmospheric velocity and temperature at six different locations within the computational domain. Visual inspection of these figures reveals that the stochastic

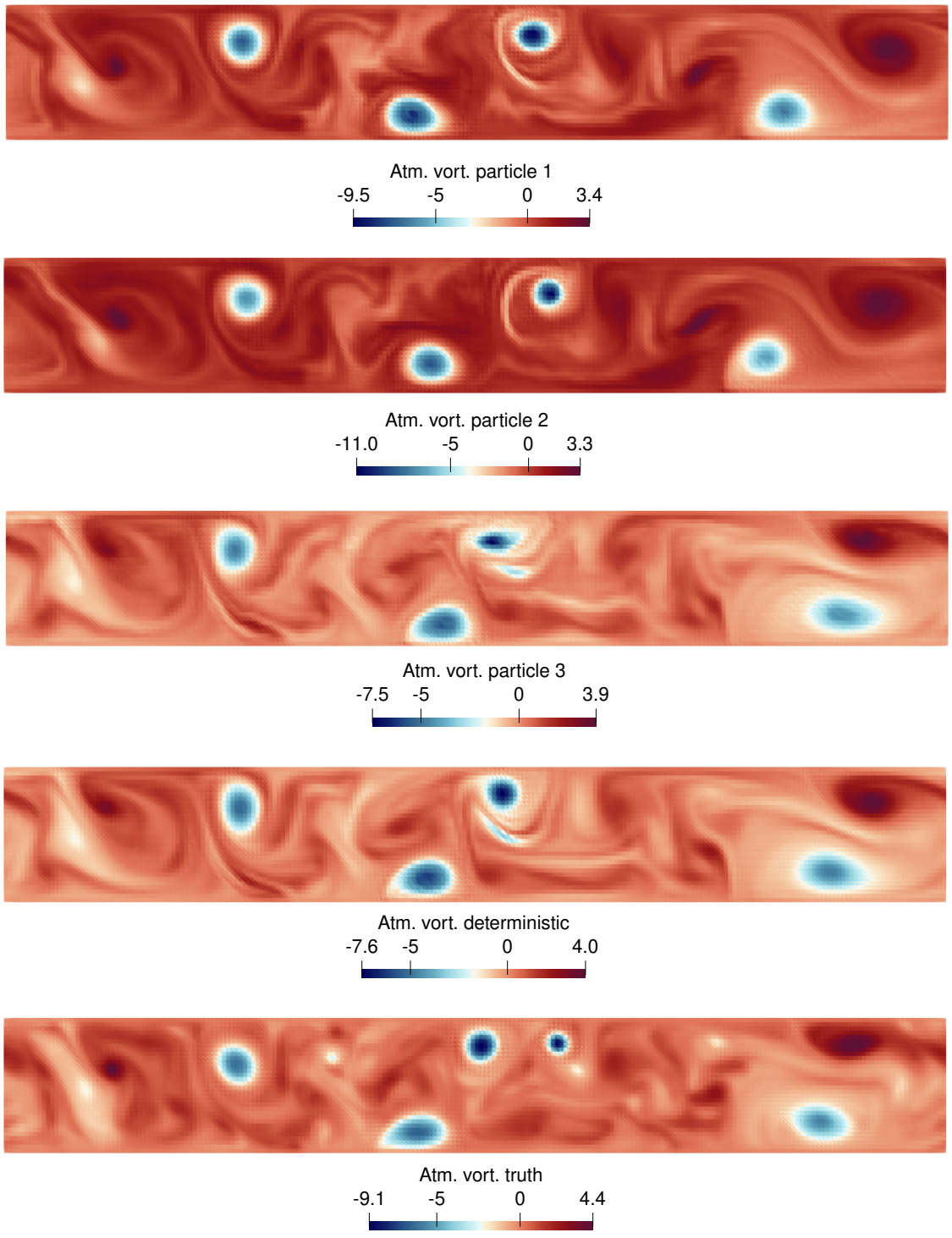

FIGURE 4.74: Atmospheric vorticity fields from three independent realizations of the SPDE on the 224×32 grid at $t = 35$ (top three plots), compared with the deterministic model result (fourth plot) and the coarse-grained high-resolution solution (last plot).

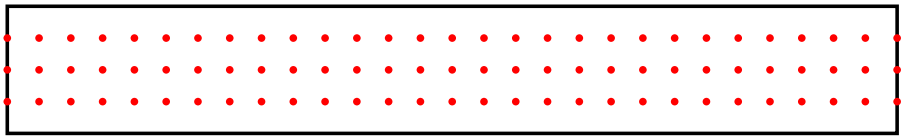

FIGURE 4.75: Observation points (red dots) within the domain where the SPDE solution is analyzed for uncertainty quantification.

model exhibits bigger spreads/one-standard-deviation regions than the deterministic model at all times. Due to a bigger spread size, true solution stays inside the spread of stochastic model solution for a longer time than the spread of deterministic model solution.

In order to do a more quantitative comparison, we compare the ensemble spread and root mean square error of solutions produced by these two models at the same six locations. The results are plotted in Figures 4.83 and 4.84. Ensemble spread sizes of the stochastic model solution are indeed larger than the deterministic model solution. Interestingly, the RMSE of the stochastic model solution is also higher than the deterministic model solution. For both models, the spread pattern resembles the RMSE pattern for at least 10 to 15 time units. This suggests that both models have good uncertainty quantification skills. However, these findings are limited to only six locations on the grid. To get a global picture, we compute the average spread size and average RMSE over all observation points in the grid.

Figure 4.85 displays the plots of average spread size and average RMSE values for both the stochastic and deterministic models. The stochastic model consistently produces a bigger spread than the deterministic model. The RMSE values corresponding to both models follow similar trends: for the x component of velocity, the error continuously increases over time, for the y component, the error increases for the first 10 time units, stays constant for roughly the next 5 time units and then increases again until the end of simulation. The ensemble spread of the stochastic model solution is able to match the RMSE trend for the first 10 to 12 time units. On the other hand, the ensemble spread of the deterministic model solution could match the RMSE trend only for 6 to 8 time units. These observations indicate that the stochastic model has better uncertainty quantification skills than the deterministic model. In terms of model accuracy, however, the deterministic model (with perturbed initial conditions) outperforms the stochastic model; it has lower RMSE values. Since both models have their own strengths—the stochastic model is better at uncertainty quantification while the deterministic model is closer to the true solution—it is difficult to say which model is better. We need a metric which can evaluate the performance of an ensemble forecast based on both the uncertainty quantification skill and the RMSE. Continuous ranked probability score (CRPS) is one such metric.

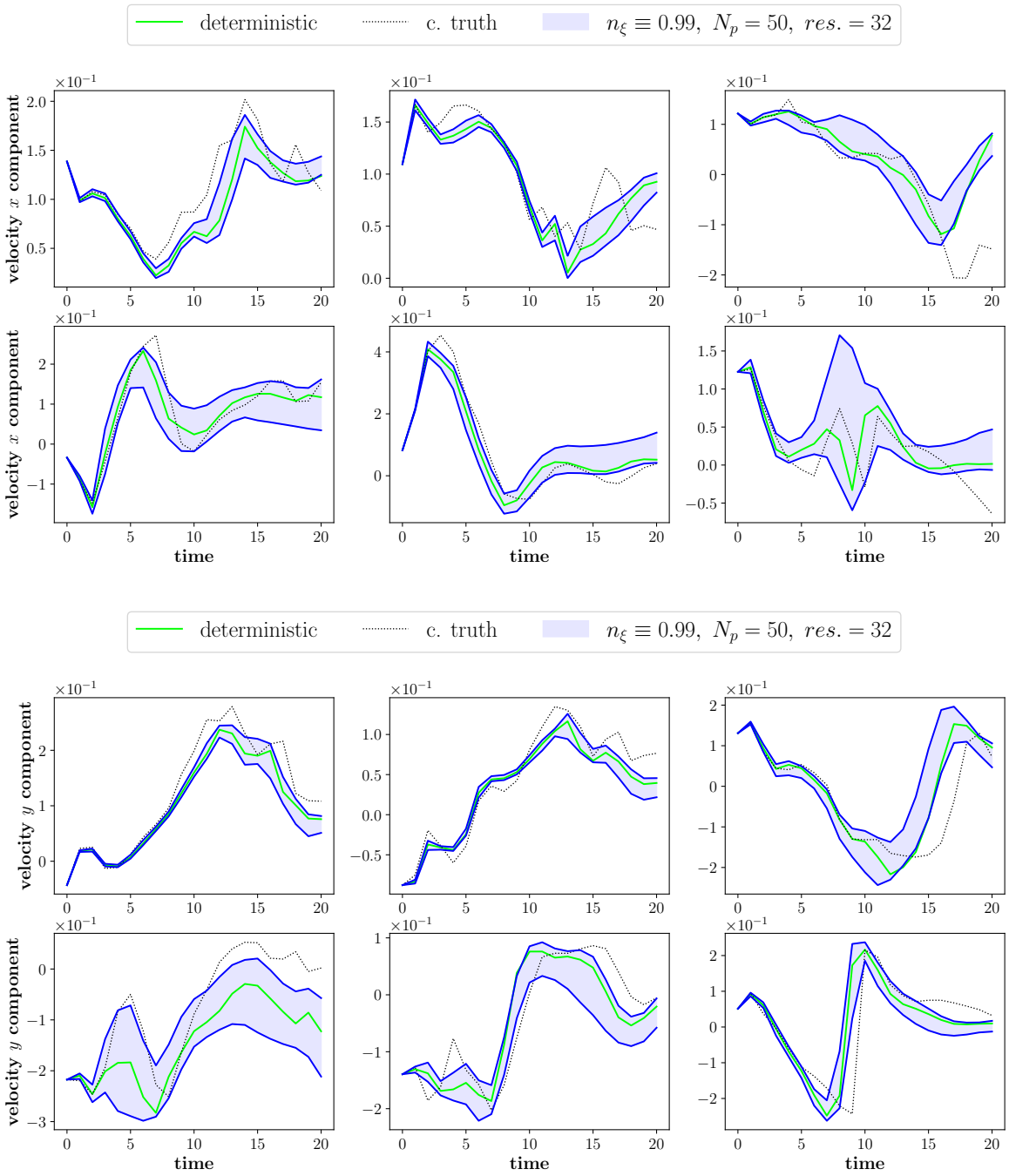

FIGURE 4.76: Evolution of atmospheric velocity (x and y components) at six observation points on the grid over time ($t = 25$ to $t = 45$). The solution from the stochastic model is compared with the coarse-grained high-resolution solution (truth) and the deterministic model solution.

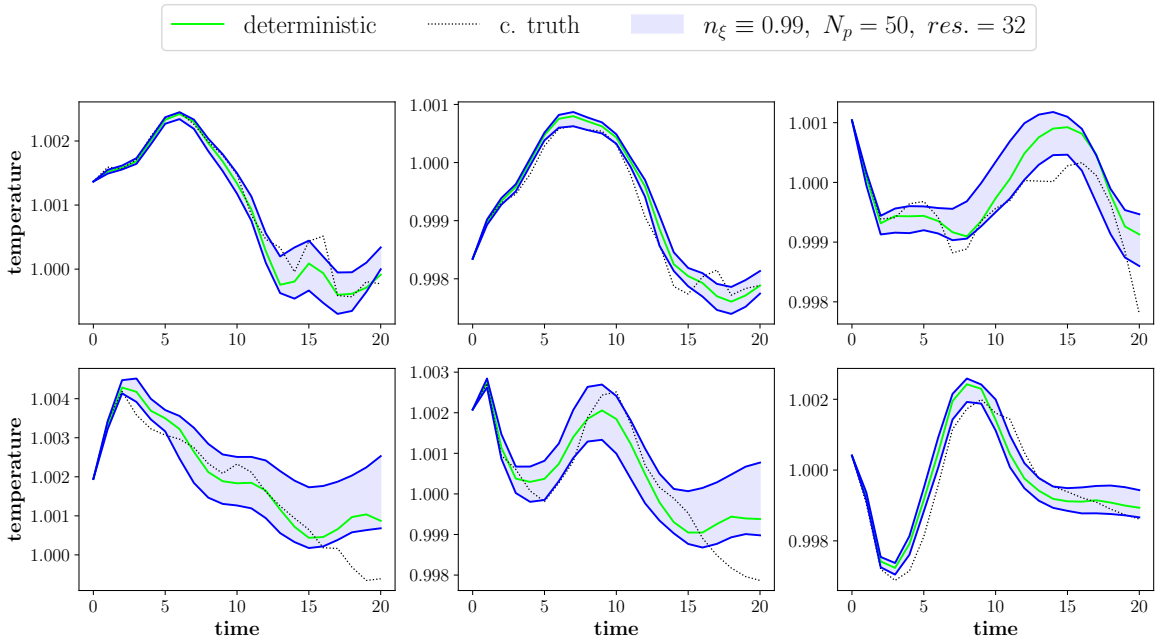

FIGURE 4.77: Evolution of atmospheric temperature at six observation points on the grid over time ($t = 25$ to $t = 45$). The solution from the stochastic model is compared with the coarse-grained high-resolution solution (truth) and the deterministic model solution.

Continuous ranked probability score

Continuous Ranked Probability Score (CRPS) is a widely recommended metric for evaluating ensemble forecasts (Hersbach, 2000; Zamo and Naveau, 2018). CRPS is a strictly proper scoring rule which rewards forecasts that provide an accurate representation of the true underlying distribution. This ensures that the metric encourages improvements in both the probabilistic accuracy and sharpness of forecasts (Gneiting and Raftery, 2007). Metrics like RMSE or Mean Absolute Error (MAE), on the other hand, can measure the average magnitude of errors but they do not reflect the distributional properties of forecasts, such as variability, spread, or confidence intervals. CRPS applies to probabilistic forecasts and considers both the spread and bias of the forecast distribution.

CRPS is defined as a quadratic discrepancy measure between the forecast cumulative distribution function (CDF) $F(x)$ and the empirical CDF $\mathbb{1}(x \geq y)$ of the observation y:

$$\mathrm{crps}(F, y) = \int_{-\infty}^{\infty} (F(x) - \mathbb{1}(x \geq y))^2 \, \mathrm{d}x,$$

where $\mathbb{1}$ is the Heaviside step function that equals 1 if $x \geq y$ and 0 otherwise (Gneiting and Raftery, 2007).

When F is known only through N_p ensemble particles $x_{i=1,\ldots,N_p}$, an estimator is used to approximate CRPS. We use a CRPS estimator known as the $\widehat{\mathrm{crps}}_{\mathrm{PWM}}$ (where the subscript PWM stands for probability weighted moment) to evaluate forecasts

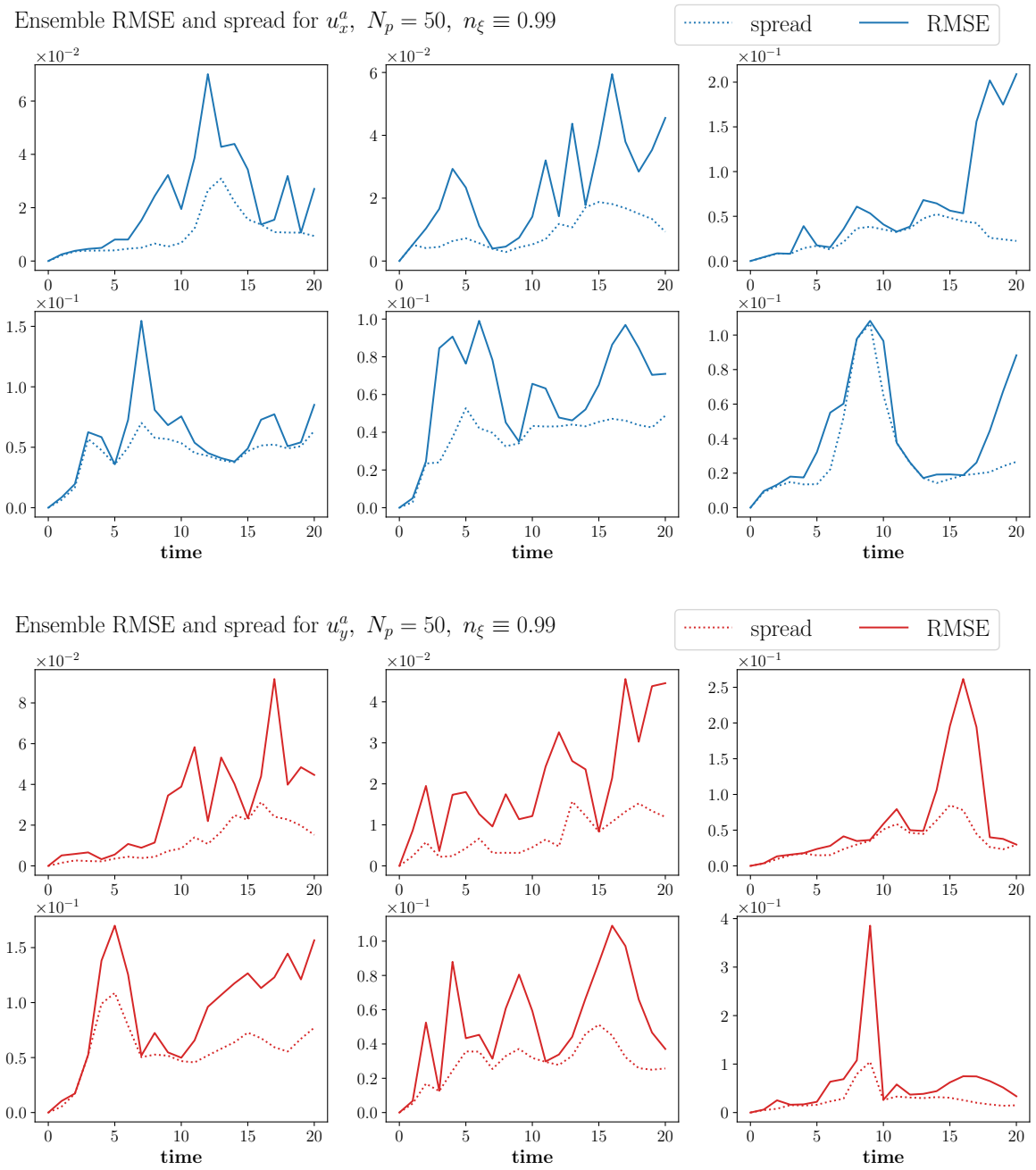

FIGURE 4.78: Ensemble RMSE and spread of velocity (x and y components) values at six observation points in the grid over time.

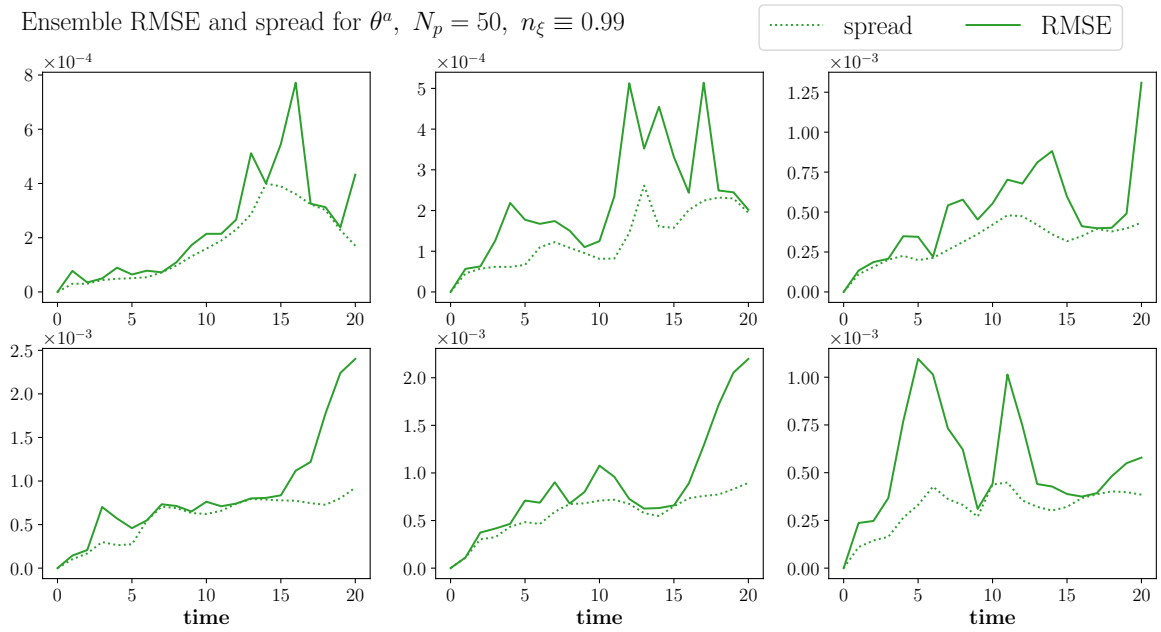

FIGURE 4.79: Ensemble RMSE and spread of temperature (x and y components) values at six observation points in the grid over time.

obtained from the stochastic model and the deterministic model. The expression for $\hat{\text{crps}}_{\text{PWM}}$ is given by

$$\hat{\text{crps}}_{\text{PWM}}(N_p, y) = \frac{1}{N_p}\sum_{i=1}^{N_p}|x_i - y| + \frac{1}{N_p}\sum_{i=1}^{N_p} x_i - \frac{2}{N_p(N_p-1)}\sum_{i=1}^{N_p}(i-1)x_i,$$

where it is assumed that the ensemble particles x_i are sorted in increasing order (Zamo and Naveau, 2018). A lower CRPS value indicates a better forecast accuracy while a higher CRPS value suggests a poor probabilistic forecast.

Figure 4.86 compares the CRPS values of the stochastic ensemble and the deterministic ensemble for atmospheric variables (velocity and temperature). The CRPS values displayed are obtained by taking the average of CRPS over all the observations points (84 in total, see Figure 4.75) at an interval of 1 time unit from $t = 25$ to $t = 45$. The stochastic ensemble corresponds to the configuration: $N_p = 50, n_\xi \equiv 0.99$. The deterministic ensemble consists of 50 particles. Unlike the RMSE plots (Figure 4.85), where we observed a significant difference between the stochastic and deterministic ensembles, the CRPS values for both models are very close to each other.

For the y component of velocity u_y^a and the temperature θ^a, the CRPS values of stochastic model are consistently lower than the CRPS values of deterministic model. For the x component of velocity u_x^a, the CRPS values of both models are similar. However, near the end of simulation, a clear difference between the CRPS values can be noticed. These observations suggest that the stochastic model predictions is more accurate than the deterministic model predictions.

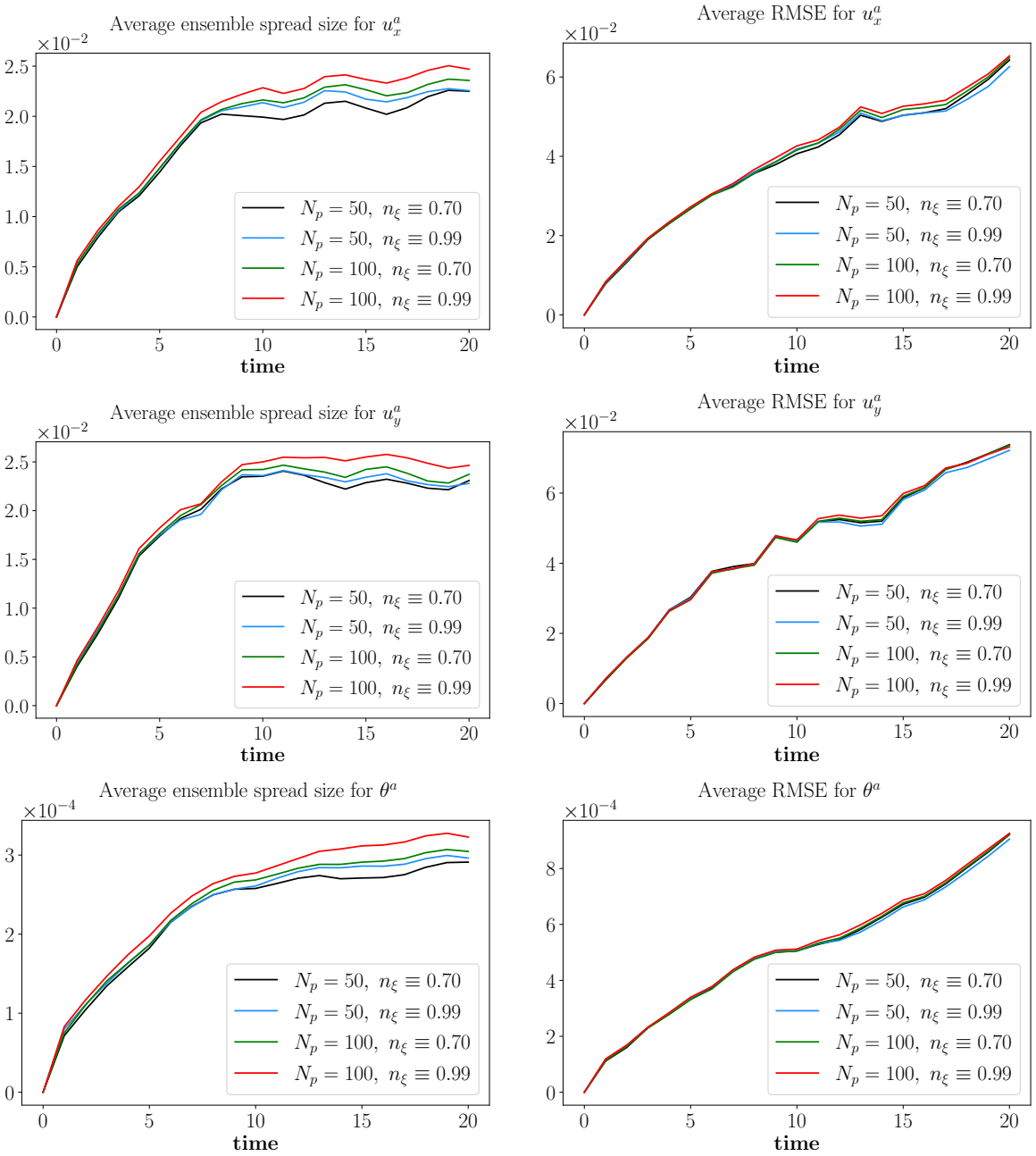

FIGURE 4.80: Uncertainty quantification plots comparing the average spread and average RMSE for different configurations of the stochastic model.

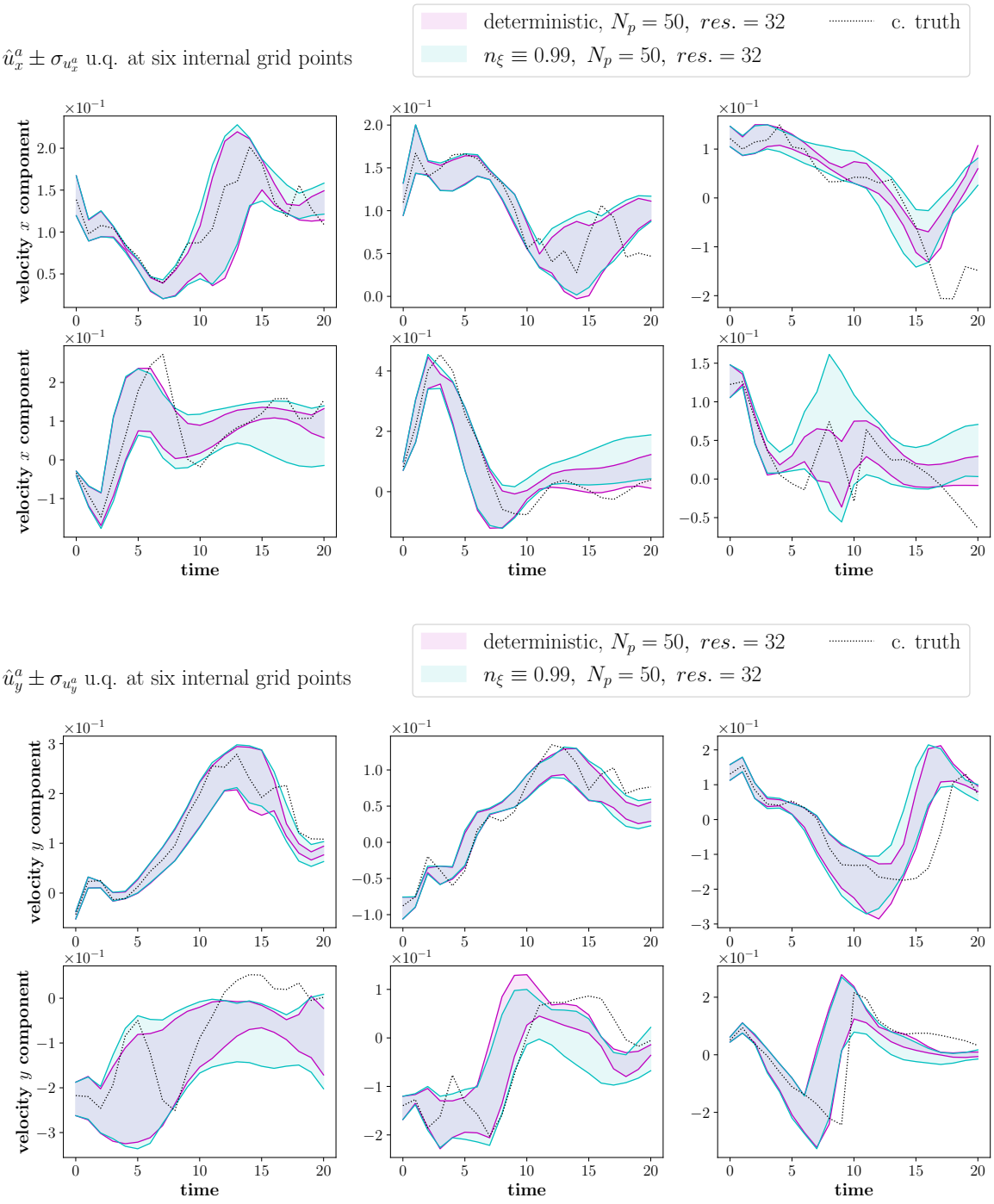

FIGURE 4.81: Comparison of atmospheric velocity generated by the stochastic ensemble and the deterministic ensemble. Both ensembles start with same initial conditions (perturbed velocity fields at $t = 25$). The stochastic model is parameterized using SALT.

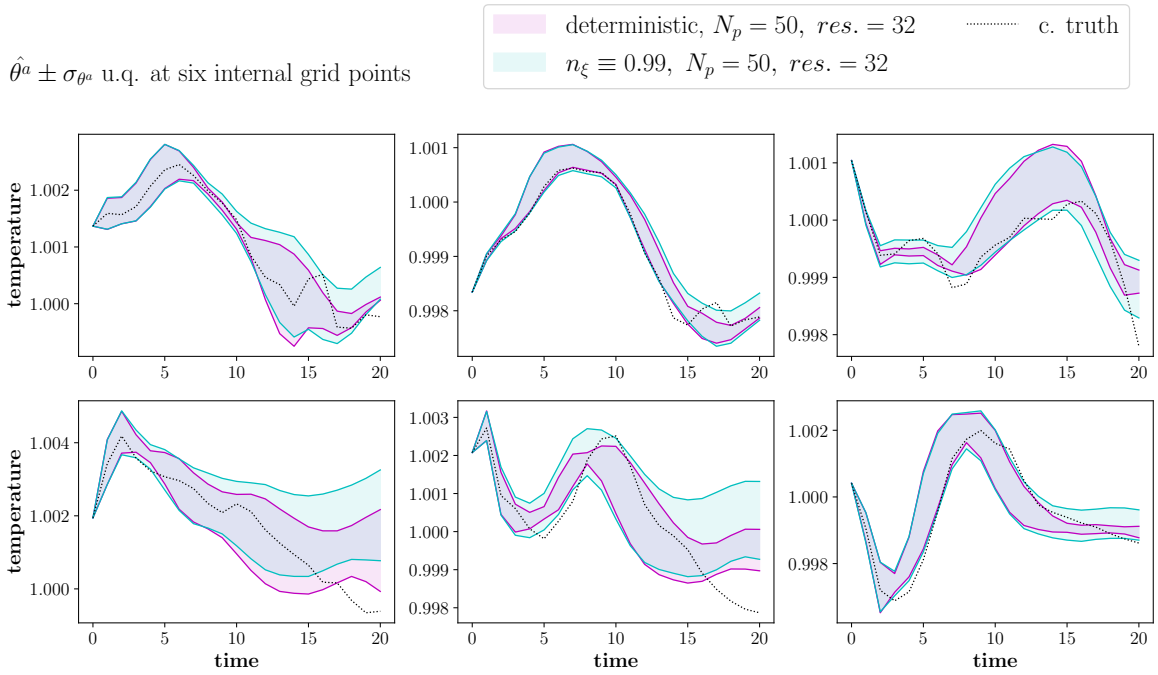

FIGURE 4.82: Comparison of atmospheric temperature generated by the stochastic ensemble and the deterministic ensemble. Both ensembles start with same initial conditions (perturbed velocity fields at $t = 25$). The stochastic model is parameterized using SALT.

4.3.3 Concluding remarks

Uncertainty quantification tests for the coupled ocean-atmosphere model have shown promising results. The stochastic parameterization methodology was found to be consistent with respect to both the number of EOFs/$\boldsymbol{\xi}_i$ (denoted by n_ξ) and the number of ensemble particles (denoted by N_p): an increase in either N_p or n_ξ led to a larger ensemble spread. More importantly, the stochastic spread demonstrated favorable reliability properties. At certain locations on the grid, the spread in the solution closely matched the actual error during the first 5 to 10 time units. This property enables the stochastic model ensemble to estimate the magnitude of its own errors.

One approach to quantifying uncertainty due to unresolved small-scale processes involves running the deterministic model with randomly perturbed initial conditions. However, this method is known to produce insufficient ensemble spread (Resseguier et al., 2021), leading to underestimation of error and a lack of variability in the solution. In our study, this behavior was observed in the deterministic climate model ensembles. In contrast, the stochastic model (also initialized with perturbed conditions) exhibited significantly bigger spread. However, the stochastic model was found to be less accurate: the RMSE of the stochastic ensemble was consistently larger than that of the deterministic ensemble. These contrasting results complicate the assessment of ensemble forecast quality. To address this, we employed the CRPS (continuous ranked probability score) metric, which evaluates an ensemble based on its ability to represent

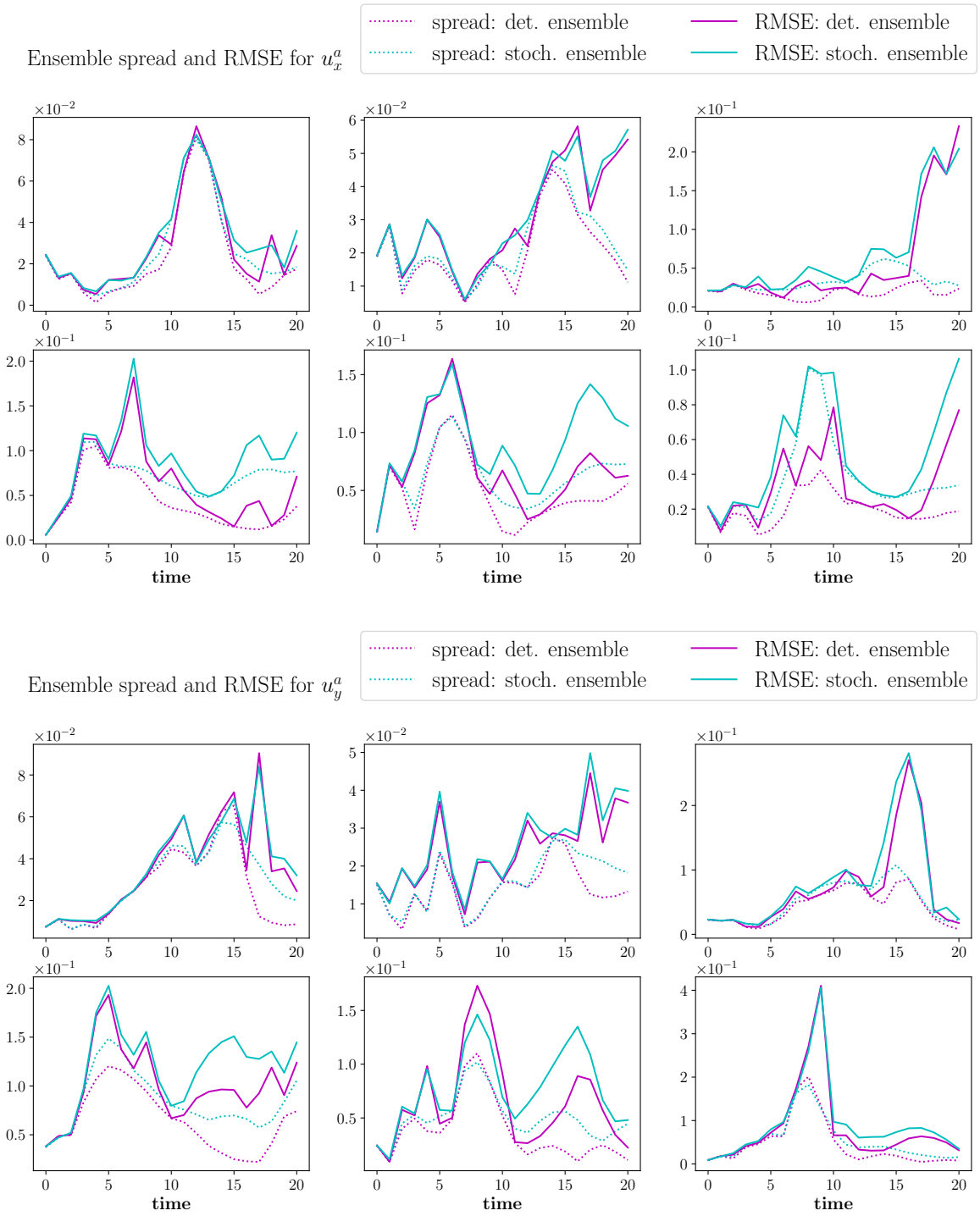

FIGURE 4.83: Comparison of ensemble spreads and RMSE for atmospheric velocity (x and y component) generated by the deterministic model and the stochastic model at six locations on the grid. The ensemble consists of 50 particles.

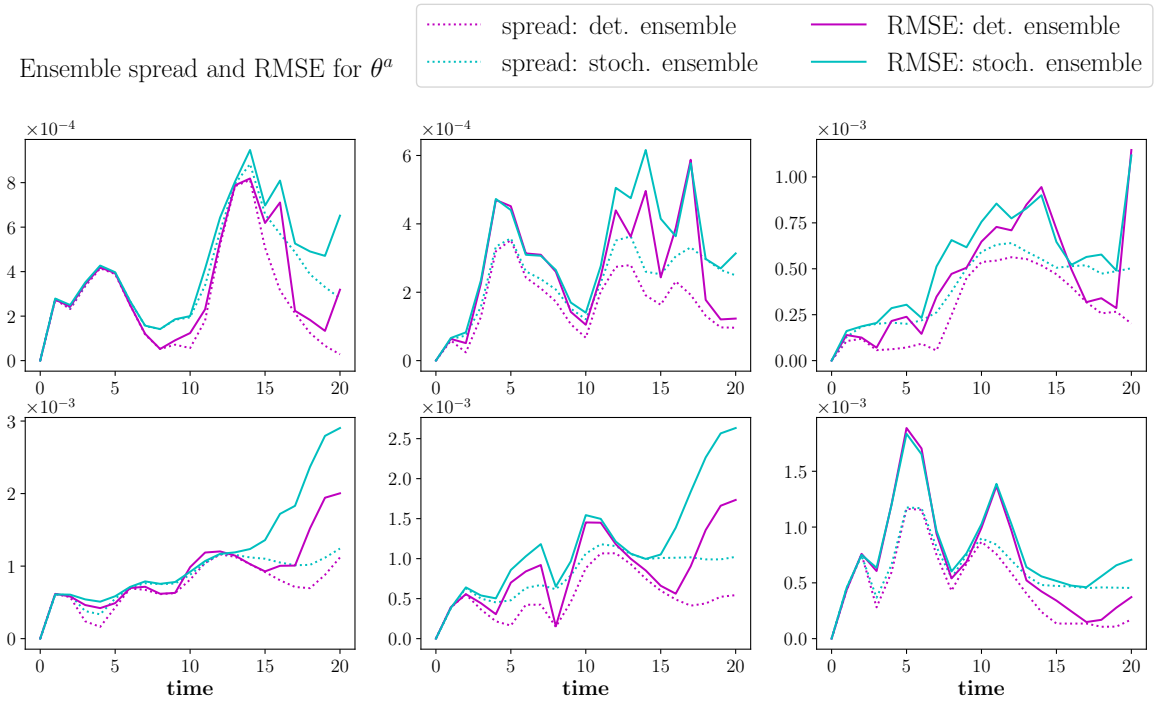

FIGURE 4.84: Comparison of ensemble spreads and RMSE for atmospheric velocity (x and y component) generated by the deterministic model and the stochastic model at six locations on the grid. The ensemble consists of 50 particles.

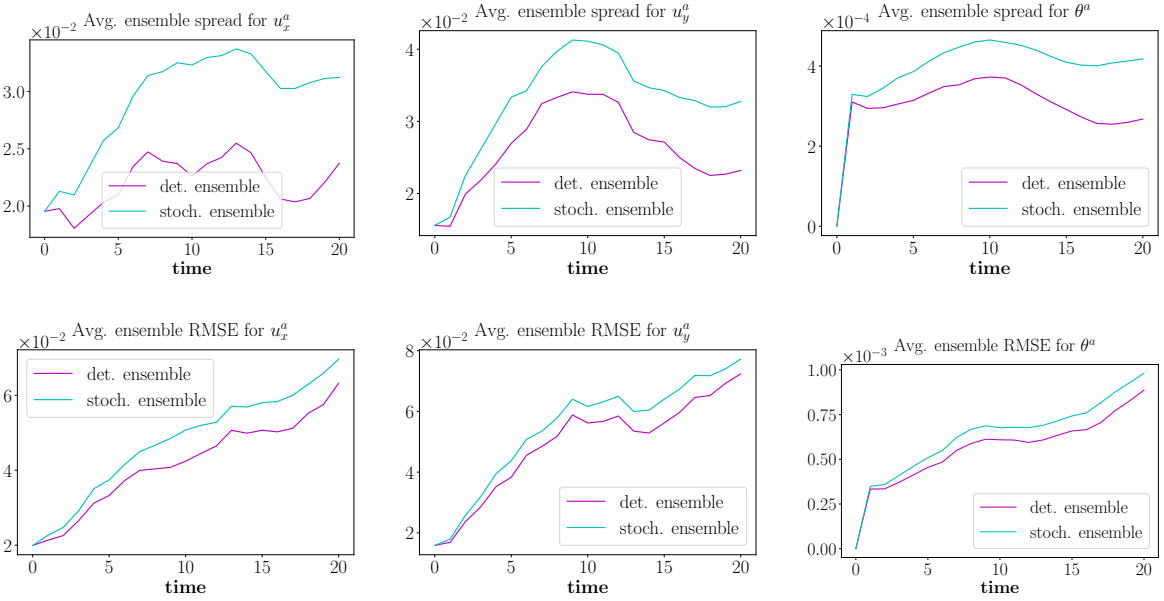

FIGURE 4.85: Uncertainty quantification plots comparing the average spread size and average RMSE for ensembles generated by the deterministic model and the stochastic model.

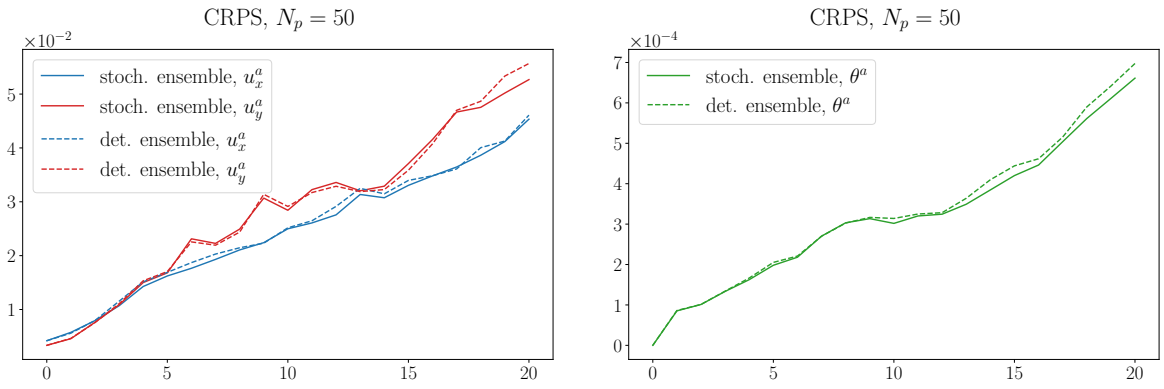

FIGURE 4.86: CRPS plots comparing the performance of the stochastic ensemble and the deterministic ensemble.

the true underlying distribution. A comparison of CRPS values revealed that the stochastic parameterization produced better forecast accuracy than the deterministic approach.

The analysis presented here for the stochastic climate model is limited in scope. There are several opportunities for improvement and further exploration. In our simulations, we considered only a single coarse grid mesh of size 224×32 for the stochastic model. As a result, our study lacks an analysis of consistency with respect to mesh refinement. It would be valuable to investigate the performance of the stochastic parameterization on finer meshes, such as the 448×64 grid.

In our analysis, we did not explore the evolution of ocean dynamics in detail. An interesting research direction would be to examine how ocean dynamics evolve over time due to the stochastic nature of the atmosphere. Comparing these results with those from a deterministic climate model could help assess whether atmospheric stochasticity impacts the long-term behavior of the oceanic flow. Another possible direction is to extend the current framework by coupling a stochastic atmosphere model with a stochastic ocean model.

The reliability tests presented in this work are not comprehensive. We compared ensemble spread (interpreted as the estimated error) with true error (measured by the ensemble RMSE) only at selected grid points. Although, comparing average ensemble spread to average RMSE offers a general indication of reliability, it may not be sufficient to assess ensemble performance comprehensively. A more informative approach would involve comparing spatial plots of ensemble spread and true error. This would make it easier to identify regions in the domain where the ensemble performs particularly well or poorly.

The literature offers several methods for assessing the reliability of probabilistic forecasts. For instance, Resseguier et al. (2020) and Resseguier et al. (2017) compare absolute bias with 1.96 times the ensemble standard deviation at each grid point. In Cotter et al. (2020a), the spatial average of RMSE of the ensemble mean is compared to the spatial average of the ensemble standard deviation. Crisan et al. (2023b), on

the other hand, compared ensemble RMSE and bias with ensemble spread at selected locations. Incorporating such approaches into our study would offer a more robust evaluation of reliability in the stochastic climate model.

In the future, we plan to address the issues discussed above and conduct a more comprehensive numerical investigation of the stochastic climate model.

Chapter 5

Summary and outlook

The goal of this thesis was to numerically simulate a stochastic coupled ocean-atmosphere climate model and investigate the effectiveness of SALT in representing the influence of unresolved scales on resolved flow dynamics, as well as in quantifying the uncertainty induced by these unresolved small scales. We approached this problem by breaking it into simpler subproblems, analyzing them thoroughly before progressing to the more complex coupled model. Our methodology consisted of three phases. First, we developed numerical schemes for the ocean component and solved the stochastic incompressible Navier–Stokes equations. Next, we conducted a numerical investigation of an idealized stochastic atmosphere model. Finally, we integrated these approaches to solve the coupled ocean–atmosphere model. Below, we summarize our main findings and suggest directions for future research.

Section 2.1 addressed the numerical discretization of the ocean model equations. This model comprises the 2D incompressible Navier–Stokes equations and an advection–diffusion equation for temperature. We used the Finite Element Method (FEM) to solve these equations, employing the Scott–Vogelius finite element pair $\mathbb{P}_2$–$\mathbb{P}_1^{\text{disc}}$ (with $\mathbf{u} \in \mathbb{P}_2$ and $p \in \mathbb{P}_1^{\text{disc}}$) on barycentrically refined meshes for spatial discretization of the Navier–Stokes equations. We selected this pair over alternatives such as Taylor–Hood and Raviart–Thomas due to its favorable accuracy, ease of implementation, and excellent mass conservation properties. For time discretization, we used a second-order implicit Crank–Nicolson scheme. The advection–diffusion equation was discretized spatially using the standard Galerkin FEM ($\theta \in \mathbb{P}_1$) and temporally using the same Crank–Nicolson method. Both the Navier–Stokes and advection–diffusion equations are known to produce numerical artifacts when advection dominates diffusion. We addressed this issue by choosing mesh sizes capable of resolving steep solution gradients, thereby avoiding instability.

Section 4.1 presented the numerical simulation results for the stochastic Navier-Stokes equations. We used high-resolution (256×256) deterministic simulations to generate data for calibrating the stochastic model. The calibration involved several steps: (1) computing differences between Lagrangian trajectories obtained from the high-resolution velocity field $\mathbf{u}$ and its coarse-grained version $\overline{\mathbf{u}}$ at multiple time

instances to form a space–time matrix of measurements; (2) applying singular value decomposition (SVD) to decompose the matrix into empirical orthogonal functions (EOFs) and corresponding time series; and (3) using the EOFs as correlation vectors $\boldsymbol{\xi}_i$ in the stochastic model, while modeling the time series using Gaussian distributions. To evaluate the model performance, a new reference solution was generated by using the exact time series of the EOFs, thus creating a deterministic benchmark that included time-accumulated discretization errors absent in the coarse-grained solution. The stochastic model was then solved on coarser grids (64×64 and 32×32), and uncertainty quantification (UQ) tests were performed. The stochastic parameterization was found to be consistent with mesh refinement: the SPDE solution on the 64×64 grid captured the reference solution for a longer period and showed significantly lower L^2 error compared to the 32×32 case. However, increasing the number of particles or the number of EOFs $\boldsymbol{\xi}_i$ had no observable effect on ensemble spread size or mean ensemble L^2 error.

Section 2.2 focused on the numerical discretization of the deterministic version of an idealized stochastic atmosphere model. We developed spatial and temporal discretization schemes for the atmosphere model equations, using $\mathbf{u} \in P_1$ and $\theta \in P_1$ along with the Crank–Nicolson method. The accuracy of this discretization was evaluated using the Galewsky test case. Although originally designed for shallow-water models, this test case was suitable for our purposes due to similarities in governing dynamics. Our numerical model successfully reproduced key features of the test case: geostrophic balance was maintained for 120 hours with unperturbed initial conditions, gravity waves appeared during the adjustment phase, and complex vortical structures developed in the long term.

In Section 4.2, we investigated the idealized stochastic atmosphere model. A modified version of the Galewsky initial conditions was used for numerical experiments. As in the Navier–Stokes case, Lagrangian trajectory data was used to estimate the correlation vectors $\boldsymbol{\xi}_i$. Two approaches were considered for modeling the associated time series: Gaussian distributions and Ornstein–Uhlenbeck (OU) processes. Replacing Gaussian noise with OU processes resulted in marked improvements: relative L^2 errors decreased, and temperature fields were free of spurious oscillations or numerical artifacts. Subsequent UQ tests using the OU-based stochastic model yielded results consistent with those from the stochastic Navier–Stokes case. The parameterization remained consistent under mesh refinement but was insensitive to changes in the number of ensemble members or the number of EOFs. To further assess the impact of stochastic parameterization, we compared the stochastic ensemble to a deterministic model without any parameterization. While the mean L^2 error of the stochastic ensemble was comparable to that of the deterministic model, some individual ensemble members achieved lower L^2 errors and successfully captured large-scale flow features absent in the deterministic solution.

Section 4.3 discussed the numerical simulation of the full stochastic climate model. High-resolution deterministic simulations on a 896×128 grid were used to calibrate the

EOFs $\boldsymbol{\xi}_i$ for stochastic simulations on a coarser 224×32 grid. The temporal component of the noise was modeled using an OU process. The calibration was validated through standard UQ tests. Unlike the stochastic Navier–Stokes and atmosphere models, where ensemble spread size showed no dependence on particle number N_p or the number of EOFs n_ξ, here the parameterization was found to be consistent: increases in N_p or n_ξ led to larger ensemble spread, especially during the later stages of the simulation. The parameterization also demonstrated good reliability: the ensemble root mean square error (RMSE) was proportional to the spread size for at least 10 time units. Forecast performance of the stochastic model was further evaluated by comparison with a deterministic model initialized from randomly perturbed initial conditions. The continuous ranked probability score (CRPS) of the stochastic ensemble was consistently lower than that of the deterministic ensemble for both velocity and temperature fields, indicating improved forecast accuracy.

Outlook

In this thesis, we presented simulation results for the stochastic incompressible Navier – Stokes equations and an idealized stochastic atmosphere model. The numerical investigation of these models aided in the development of a discretization scheme for the idealized stochastic climate model, which constituted our main objective. Uncertainty quantification (UQ) tests for all three models produced promising results. However, further work is needed to address some of the limitations of the approaches presented in this thesis. Doing so will deepen our understanding of these models and improve their predictive capabilities. Below, we outline potential improvements and propose directions for future research.

In the analysis of the stochastic incompressible Navier–Stokes equations, the temporal component of the noise should be modeled using an Ornstein–Uhlenbeck (OU) process rather than a Gaussian distribution due to the strong correlations observed in the time series data. The UQ tests could be enhanced by incorporating additional reliability diagnostics, such as spread versus bias or root mean square error (RMSE), and by conducting comparative studies between stochastic and deterministic model ensembles.

For the stochastic atmosphere model, the impact of parameterization terms associated with rotation requires further investigation. It remains unclear why these terms induce spurious oscillations in the temperature fields. One potential research direction is the use of high-order time-discretization schemes, such as strong stability preserving Runge–Kutta (SSPRK) methods of order 3 or 4 (Hansen and Penland, 2006; Rüemelin, 1982). The ensemble study can also be expanded through additional reliability assessments and comparisons with deterministic ensemble forecasts.

The SALT parameterization of the coupled ocean–atmosphere model yielded strong ensemble performance, providing a solid foundation for the implementation of data assimilation techniques. We plan to explore this direction in our future work.

Our contribution

Our work has made scientific contributions in the following key areas:

Stochastic incompressible Navier–Stokes equations

We presented, to the best of our knowledge, the first numerical investigation of two-dimensional incompressible Navier–Stokes equations parameterized by SALT. We proposed a calibration technique capable of extracting spatial correlations of unresolved small-scale features from Lagrangian trajectory data, applicable to both compressible and incompressible fluids. We conducted tests demonstrating the effectiveness of SALT in quantifying uncertainties arising from unresolved transport dynamics and discussed methods to further improve the accuracy of solutions obtained from stochastic models.

Stochastic atmosphere model

We performed an extensive numerical analysis of the atmospheric component of an idealized stochastic climate model. Our study identified significant limitations, in terms of both uncertainty quantification and solution accuracy, when the temporal component of the stochastic noise was modeled using a Gaussian process rather than an Ornstein–Uhlenbeck process. In addition to quantifying uncertainty, we compared stochastic model solutions directly against deterministic counterparts. Furthermore, we highlighted specific challenges introduced by fluid compressibility and parameterization effects associated with the Coriolis force in the stochastic modeling of atmospheric dynamics.

Stochastic climate model

We conducted the first numerical simulations of an idealized coupled ocean–atmosphere climate model derived using the SALT methodology. Numerical tests were performed to assess SALT's effectiveness in quantifying uncertainties due to unresolved small-scale processes within the coupled climate model setting. Additionally, the impact of SALT parameterization on forecast skill was evaluated by directly comparing stochastic model outcomes with results from the corresponding non-parameterized deterministic model.

Publications and conference contributions

The doctoral studies resulted in the following publications and conference contributions:

Publications

- Kamal Sharma and Peter Korn. Numerical Simulation of an idealized coupled Ocean-Atmosphere Climate Model. In *Modeling, Simulation and Optimization of Fluid Dynamic Applications*, pages 113–130. Springer, Cham, 2023. DOI: 10.1007/978-3-031-45158-4_7

Conference contributions

- Workshop on Stochastic Transport in Upper Ocean Dynamics, French Research Institute for Exploitation of the Sea (IFREMER), Brest, France, *contributed talk* (2023).
- Conference on Mathematical and Computational Issues in the Geosciences, Society for Industrial and Applied Mathematics (SIAM), Bergen, Norway, *contributed talk* (2023).
- Conference on Computational Science and Engineering, Society for Industrial and Applied Mathematics (SIAM), Amsterdam, Netherlands, *contributed talk* (2023).
- Firedrake User and Developer Workshop, University of Exeter & Imperial College London, Totnes, England, *contributed talk* (2023).
- Workshop on Modeling, Simulation & Optimization of Fluid Dynamic Applications, Groß Schwansee, Germany, *contributed talk* (2022).
- Workshop on Modeling, Simulation & Optimization of Fluid Dynamic Applications, Groß Schwansee, Germany, *contributed talk and poster* (2021).

Declaration of contribution

- Except for Figure 1.2, all tables and figures in this thesis were created by the candidate.
- Some of the text used in Chapter 1 corresponds to the paper Sharma and Korn (2023). Modified versions of the numerical schemes presented in Sharma and Korn (2023) are used in this thesis.
- The selection of test cases for the numerical experiments presented in Section 2.2 was a joint effort between Peter Korn and the candidate. All numerical code used to solve the equations in this section was written by the candidate and is publicly available on GitHub.

- The idea behind the calibration methodology in Chapter 3 was proposed by Wei Pan. Its implementation was carried out solely by the candidate. The time discretization scheme for the stochastic partial differential equations in this chapter was developed in collaboration with James Woodfield.
- A Python package (bary.py), written by Patrick Farrell, was used to create the barycentrically refined meshes in Section 4.1. Algorithm 3 was developed in collaboration with Sagy Ephrati.
- The code for solving the three stochastic models in Chapter 4 was written entirely by the candidate. The section about the continuous ranked probability score (CRPS) is the result of discussions between James Woodfield and the candidate.
- Section 4.3 is expected to lead to a publication co-authored with Peter Korn; the manuscript is currently in preparation.

Data availability statement

The computational code, data, and post-processing scripts used in this thesis are available on Github.

- 2D viscous shallow water equations (Subsection 2.2.2): https://github.com/sharma-kk/viscous_shallow_water_2d.
- Stochastic Navier-Stokes equations (Section 4.1): https://github.com/sharma-kk/NS_free_slip_SALT.
- Stochastic atmosphere model (Section 4.2): https://github.com/sharma-kk/atmo_semi_periodic_SALT.
- Stochastic climate model (Section 4.3): https://github.com/sharma-kk/coupled_OA_model

Numerical implementation is done using the open-source Python Finite Element package Firedrake (Rathgeber et al. 2016). The simulation results are visualized using the ParaView application (Ahrens et al. 2005). All post-processing is done in Jupyter Notebook.

Bibliography

Geoffrey K. Vallis. *Atmospheric and Oceanic Fluid Dynamics*. Cambridge University Press, June 2017.

Baylor Fox-Kemper. Notions for the Motions of the Oceans. In *New Frontiers in Operational Oceanography*. GODAE OceanView, August 2018. DOI: 10.17125/gov2018.ch02.

Paul D Williams. Modelling climate change: The role of unresolved processes. *Philosophical Transactions of the Royal Society A: Mathematical, Physical and Engineering Sciences*, 363:2931–2946, October 2005. DOI: 10.1098/rsta.2005.1676.

William R. Holland. The Role of Mesoscale Eddies in the General Circulation of the Ocean—Numerical Experiments Using a Wind-Driven Quasi-Geostrophic Model. *Journal of Physical Oceanography*, 8:363–392, May 1978. DOI: 10.1175/1520-0485(1978)008<0363:TROMEI>2.0.CO;2.

John C. Wyngaard. *Turbulence in the Atmosphere*. Cambridge University Press, Cambridge, 2010. DOI: 10.1017/CBO9780511840524.

Roland B. Stull. *Practical Meteorology: An Algebra-Based Survey of Atmospheric Science*. UBC, Vancouver, 2017.

Laure Zanna, PierGianLuca Porta Mana, James Anstey, Tomos David, and Thomas Bolton. Scale-aware deterministic and stochastic parametrizations of eddy-mean flow interaction. *Ocean Modelling*, 111:66–80, March 2017. DOI: 10.1016/j.ocemod.2017.01.004.

T. N. Palmer. Towards the probabilistic Earth-system simulator: A vision for the future of climate and weather prediction. *Quarterly Journal of the Royal Meteorological Society*, 138:841–861, 2012. DOI: 10.1002/qj.1923.

Judith Berner, Ulrich Achatz, Lauriane Batté, Lisa Bengtsson, Alvaro de la Cámara, Hannah M. Christensen, Matteo Colangeli, Danielle R. B. Coleman, Daan Crommelin, Stamen I. Dolaptchiev, Christian L. E. Franzke, Petra Friederichs, Peter Imkeller, Heikki Järvinen, Stephan Juricke, Vassili Kitsios, François Lott, Valerio Lucarini, Salil Mahajan, Timothy N. Palmer, Cécile Penland, Mirjana Sakradzija, Jin-Song von Storch, Antje Weisheimer, Michael Weniger, Paul D. Williams, and Jun-Ichi

Yano. Stochastic Parameterization: Toward a New View of Weather and Climate Models. *Bulletin of the American Meteorological Society*, 98:565–588, March 2017. DOI: 10.1175/BAMS-D-15-00268.1.

Darryl D. Holm. Variational principles for stochastic fluid dynamics. *Proceedings of the Royal Society A: Mathematical, Physical and Engineering Sciences*, 471:20140963, April 2015. DOI: 10.1098/rspa.2014.0963.

J. Berner, T. Jung, and T. N. Palmer. Systematic Model Error: The Impact of Increased Horizontal Resolution versus Improved Stochastic and Deterministic Parameterizations. *Journal of Climate*, 25:4946–4962, July 2012. DOI: 10.1175/JCLI-D-11-00297.1.

Rüdiger Brecht, Long Li, Werner Bauer, and Etienne Mémin. Rotating Shallow Water Flow Under Location Uncertainty With a Structure-Preserving Discretization. *Journal of Advances in Modeling Earth Systems*, 13:e2021MS002492, 2021. DOI: 10.1029/2021MS002492.

C. J. Cotter, G. A. Gottwald, and D. D. Holm. Stochastic partial differential fluid equations as a diffusive limit of deterministic Lagrangian multi-time dynamics. *Proceedings of the Royal Society A: Mathematical, Physical and Engineering Sciences*, 473:20170388, September 2017. DOI: 10.1098/rspa.2017.0388.

Etienne Mémin. Fluid flow dynamics under location uncertainty. *Geophysical & Astrophysical Fluid Dynamics*, 108:119–146, March 2014. DOI: 10.1080/03091929.2013.836190.

Jonathan M. Lilly. jLab: A data analysis package for Matlab, v. 1.7.3. https://jmlilly.net/doc/about_drifters.html, 2024.

Dan Crisan, Franco Flandoli, and Darryl D. Holm. Solution Properties of a 3D Stochastic Euler Fluid Equation. *Journal of Nonlinear Science*, 29:813–870, June 2019. DOI: 10.1007/s00332-018-9506-6.

D Crisan, D D Holm, and P Korn. An implementation of Hasselmann's paradigm for stochastic climate modelling based on stochastic Lie transport*. *Nonlinearity*, 36: 4862–4903, September 2023a. DOI: 10.1088/1361-6544/ace1ce.

Dan Crisan and Oana Lang. Well-Posedness Properties for a Stochastic Rotating Shallow Water Model. *Journal of Dynamics and Differential Equations*, 36:3175–3205, December 2024. DOI: 10.1007/s10884-022-10243-1.

François Gay-Balmaz and Darryl D. Holm. Stochastic Geometric Models with Non-stationary Spatial Correlations in Lagrangian Fluid Flows. *Journal of Nonlinear Science*, 28:873–904, June 2018. DOI: 10.1007/s00332-017-9431-0.

Colin Cotter, Dan Crisan, Darryl D. Holm, Wei Pan, and Igor Shevchenko. Numerically Modeling Stochastic Lie Transport in Fluid Dynamics. *Multiscale Modelling & Simulation*, 17:192–232, 2019. DOI: 10.1137/18M1167929.

Colin Cotter, Dan Crisan, Darryl Holm, Wei Pan, and Igor Shevchenko. Modelling uncertainty using stochastic transport noise in a 2-layer quasi-geostrophic model. *Foundations of Data Science*, 2:173–205, 2020a. DOI: 10.3934/fods.2020010.

Sagy R. Ephrati, Paolo Cifani, Erwin Luesink, and Bernard J. Geurts. Data-Driven Stochastic Lie Transport Modeling of the 2D Euler Equations. *Journal of Advances in Modeling Earth Systems*, 15:e2022MS003268, January 2023. DOI: 10.1029/2022MS003268.

Dan Crisan, Oana Lang, Alexander Lobbe, Peter-Jan Van Leeuwen, and Roland Potthast. Noise calibration for SPDEs: A case study for the rotating shallow water model. *Foundations of Data Science*, 0:0–0, 2023b. DOI: 10.3934/fods.2023012.

Valentin Resseguier, Wei Pan, and Baylor Fox-Kemper. Data-driven versus self-similar parameterizations for stochastic advection by Lie transport and location uncertainty. *Nonlinear Processes in Geophysics*, 27:209–234, April 2020. DOI: 10.5194/npg-27-209-2020.

Colin Cotter, Dan Crisan, Darryl D. Holm, Wei Pan, and Igor Shevchenko. A Particle Filter for Stochastic Advection by Lie Transport: A Case Study for the Damped and Forced Incompressible Two-Dimensional Euler Equation. *SIAM/ASA Journal on Uncertainty Quantification*, 8:1446–1492, January 2020b. DOI: 10.1137/19M1277606.

Colin Cotter, Dan Crisan, Darryl Holm, Wei Pan, and Igor Shevchenko. Data Assimilation for a Quasi-Geostrophic Model with Circulation-Preserving Stochastic Transport Noise. *Journal of Statistical Physics*, 179:1186–1221, June 2020c. DOI: 10.1007/s10955-020-02524-0.

Oana Lang, Peter Jan van Leeuwen, Dan Crisan, and Roland Potthast. Bayesian inference for fluid dynamics: A case study for the stochastic rotating shallow water model. *Frontiers in Applied Mathematics and Statistics*, 8, October 2022. DOI: 10.3389/fams.2022.949354.

M. A. Cane and S. E. Zebiak. A theory for el nino and the southern oscillation. *Science (New York, N.Y.)*, 228:1085–1087, May 1985. DOI: 10.1126/science.228.4703.1085.

S.G. Philander. El Niño Southern Oscillation (Enso) Models. In *Encyclopedia of Ocean Sciences*, pages 827–832. Elsevier, 2001. DOI: 10.1006/rwos.2001.0401.

Julian P. McCreary Jr. and David L. T. Anderson. An overview of coupled ocean-atmosphere models of El Niño and the Southern Oscillation. *Journal of Geophysical Research: Oceans*, 96:3125–3150, 1991. DOI: 10.1029/90JC01979.

K. Hasselmann. Stochastic climate models Part I. Theory. *Tellus*, 28:473–485, 1976. DOI: 10.1111/j.2153-3490.1976.tb00696.x.

Valerio Lucarini and Mickaël D. Chekroun. Theoretical tools for understanding the climate crisis from Hasselmann's programme and beyond. *Nature Reviews Physics*, 5:744–765, December 2023. DOI: 10.1038/s42254-023-00650-8.

Volker John. *Finite Element Methods for Incompressible Flow Problems*, volume 51 of *Springer Series in Computational Mathematics*. Springer International Publishing, Cham, 2016. DOI: 10.1007/978-3-319-45750-5.

Philipp W. Schroeder and Gert Lube. Pressure-robust analysis of divergence-free and conforming FEM for evolutionary incompressible Navier–Stokes flows. *Journal of Numerical Mathematics*, 25:249–276, December 2017. DOI: 10.1515/jnma-2016-1101.

Patrick E. Farrell, Lawrence Mitchell, L. Ridgway Scott, and Florian Wechsung. A Reynolds-robust preconditioner for the Scott-Vogelius discretization of the stationary incompressible Navier-Stokes equations. *The SMAI journal of computational mathematics*, 7:75–96, March 2021. DOI: 10.5802/smai-jcm.72.

Sven Gross and Arnold Reusken. *Numerical Methods for Two-phase Incompressible Flows*, volume 40 of *Springer Series in Computational Mathematics*. Springer, Berlin, Heidelberg, 2011. DOI: 10.1007/978-3-642-19686-7.

Volker John, Petr Knobloch, and Julia Novo. Finite elements for scalar convection-dominated equations and incompressible flow problems: A never ending story? *Computing and Visualization in Science*, 19:47–63, December 2018. DOI: 10.1007/s00791-018-0290-5.

Tobias Gelhard, Gert Lube, Maxim A. Olshanskii, and Jan-Hendrik Starcke. Stabilized finite element schemes with LBB-stable elements for incompressible flows. *Journal of Computational and Applied Mathematics*, 177:243–267, May 2005. DOI: 10.1016/j.cam.2004.09.017.

E. Burman and A. Linke. Stabilized finite element schemes for incompressible flow using Scott–Vogelius elements. *Applied Numerical Mathematics*, 58:1704–1719, November 2008. DOI: 10.1016/j.apnum.2007.11.001.

Leopoldo P. Franca, Guillermo Hauke, and Arif Masud. Revisiting stabilized finite element methods for the advective–diffusive equation. *Computer Methods in Applied Mechanics and Engineering*, 195:1560–1572, February 2006. DOI: 10.1016/j.cma.2005.05.028.

Alexander N. Brooks and Thomas J. R. Hughes. Streamline upwind/Petrov-Galerkin formulations for convection dominated flows with particular emphasis on the incompressible Navier-Stokes equations. *Computer Methods in Applied Mechanics and Engineering*, 32:199–259, September 1982. DOI: 10.1016/0045-7825(82)90071-8.

Pavel B. Bochev, Max D. Gunzburger, and John N. Shadid. Stability of the SUPG finite element method for transient advection–diffusion problems. *Computer Methods in Applied Mechanics and Engineering*, 193:2301–2323, June 2004. DOI: 10.1016/j.cma.2004.01.026.

Erik Burman and Peter Hansbo. Edge stabilization for Galerkin approximations of convection–diffusion–reaction problems. *Computer Methods in Applied Mechanics and Engineering*, 193:1437–1453, April 2004. DOI: 10.1016/j.cma.2003.12.032.

Thomas J. R. Hughes, Leopoldo P. Franca, and Gregory M. Hulbert. A new finite element formulation for computational fluid dynamics: VIII. The galerkin/least-squares method for advective-diffusive equations. *Computer Methods in Applied Mechanics and Engineering*, 73:173–189, May 1989. DOI: 10.1016/0045-7825(89)90111-4.

Blanca Ayuso and L. Donatella Marini. Discontinuous Galerkin Methods for Advection-Diffusion-Reaction Problems. *SIAM Journal on Numerical Analysis*, 47:1391–1420, January 2009. DOI: 10.1137/080719583.

Joseph Galewsky, Richard K. Scott, and Lorenzo M. Polvani. An initial-value problem for testing numerical models of the global shallow-water equations. *Tellus A: Dynamic Meteorology and Oceanography*, 56:429, January 2004. DOI: 10.3402/tellusa.v56i5.14436.

A. Hannachi, I. T. Jolliffe, and D. B. Stephenson. Empirical orthogonal functions and related techniques in atmospheric science: A review. *International Journal of Climatology*, 27:1119–1152, July 2007. DOI: 10.1002/joc.1499.

Daniel Goodair and Dan Crisan. On the 3D Navier-Stokes Equations with Stochastic Lie Transport. In *Stochastic Transport in Upper Ocean Dynamics II*, volume 11, pages 53–110. Springer Nature Switzerland, Cham, 2024. DOI: 10.1007/978-3-031-40094-0_4.

Zhongqiang Zhang, Xiu Yang, Guang Lin, and George Em Karniadakis. Numerical solution of the Stratonovich- and Ito–Euler equations: Application to the stochastic piston problem. *Journal of Computational Physics*, 236:15–27, March 2013. DOI: 10.1016/j.jcp.2012.11.017.

Darryl D. Holm and Erwin Luesink. Stochastic Wave–Current Interaction in Thermal Shallow Water Dynamics. *Journal of Nonlinear Science*, 31:29, April 2021. DOI: 10.1007/s00332-021-09682-9.

Kun Il Park. *Fundamentals of Probability and Stochastic Processes with Applications to Communications*. Springer International Publishing, Cham, 2018. DOI: 10.1007/978-3-319-68075-0.

Marco Toboga. Autocorrelation, Lectures on probability theory and mathematical statistics. https://www.statlect.com/fundamentals-of-statistics/autocorrelation, 2021.

Ross A. Maller, Gernot Müller, and Alex Szimayer. Ornstein–Uhlenbeck Processes and Extensions. In *Handbook of Financial Time Series*, pages 421–437. Springer Berlin Heidelberg, Berlin, Heidelberg, 2009. DOI: 10.1007/978-3-540-71297-8_18.

V. Resseguier, E. Mémin, and B. Chapron. Geophysical flows under location uncertainty, Part II Quasi-geostrophy and efficient ensemble spreading. *Geophysical & Astrophysical Fluid Dynamics*, 111:177–208, May 2017. DOI: 10.1080/03091929.2017.1312101.

Hans Hersbach. Decomposition of the Continuous Ranked Probability Score for Ensemble Prediction Systems. *Weather and Forecasting*, 15:559–570, October 2000. DOI: 10.1175/1520-0434(2000)015<0559:DOTCRP>2.0.CO;2.

Michaël Zamo and Philippe Naveau. Estimation of the Continuous Ranked Probability Score with Limited Information and Applications to Ensemble Weather Forecasts. *Mathematical Geosciences*, 50:209–234, February 2018. DOI: 10.1007/s11004-017-9709-7.

Tilmann Gneiting and Adrian E Raftery. Strictly Proper Scoring Rules, Prediction, and Estimation. *Journal of the American Statistical Association*, 102:359–378, March 2007. DOI: 10.1198/016214506000001437.

V. Resseguier, L. Li, G. Jouan, P. Dérian, E. Mémin, and B. Chapron. New Trends in Ensemble Forecast Strategy: Uncertainty Quantification for Coarse-Grid Computational Fluid Dynamics. *Archives of Computational Methods in Engineering*, 28: 215–261, January 2021. DOI: 10.1007/s11831-020-09437-x.

James A. Hansen and Cecile Penland. Efficient Approximate Techniques for Integrating Stochastic Differential Equations. *Monthly Weather Review*, 134:3006–3014, October 2006. DOI: 10.1175/MWR3192.1.

W. Rüemelin. Numerical Treatment of Stochastic Differential Equations. *SIAM Journal on Numerical Analysis*, 19:604–613, June 1982. DOI: 10.1137/0719041.

Kamal Sharma and Peter Korn. Numerical Simulation of an idealized coupled Ocean-Atmosphere Climate Model. In *Modeling, Simulation and Optimization of Fluid Dynamic Applications*, pages 113–130. Springer, Cham, 2023. DOI: 10.1007/978-3-031-45158-4_7.

Florian Rathgeber, David A. Ham, Lawrence Mitchell, Michael Lange, Fabio Luporini, Andrew T. T. Mcrae, Gheorghe-Teodor Bercea, Graham R. Markall, and Paul H. J. Kelly. Firedrake: Automating the Finite Element Method by Composing Abstractions. *ACM Trans. Math. Softw.*, 43:24:1–24:27, December 2016. DOI: 10.1145/2998441.

James Ahrens, Berk Geveci, and Charles Law. ParaView: An End-User Tool for Large-Data Visualization. In *Visualization Handbook*, pages 717–731. Elsevier, 2005. DOI: 10.1016/B978-012387582-2/50038-1.

Declaration of authorship

I hereby declare and affirm that this doctoral dissertation is my own work and that I have not used any aids and sources other than those indicated. If electronic resources based on generative artificial intelligence (gAI) were used in the course of writing this dissertation, I confirm that my own work was the main and value-adding contribution and that complete documentation of all resources used is available in accordance with good scientific practice. I am responsible for any erroneous or distorted content, incorrect references, violations of data protection and copyright law or plagiarism that may have been generated by the gAI.

Hamburg, 02.10.2025

Kamal Kishor Sharma